Atomically Precise Gold Nanoclusters: Syntheses, Properties and Applications

By

ZEHUA GAO

B.Sc. University of Science and Technology of China, 2017

M.A. Brown University, 2019

A Dissertation Submitted in Partial Fulfillment of the Requirements for the Degree of Doctor of Philosophy in the Department of Chemistry at Brown University

Providence, Rhode Island

February 2023

This dissertation by Zehua Gao is accepted in its present form by the Department of Chemistry as satisfying the dissertation requirement for the degree of Doctor of Philosophy.

Date_____ _____

Lai-Sheng Wang, Advisor

Recommended to the Graduate Council

Date_____ _____

Shouheng Sun, Reader

Date_____ _____

Jerome R. Robinson, Reader

Approved by the Graduate Council

Date_____ _____

Thomas A. Lewis, Dean of the Graduate School

CURRICULUM VITAE

Zehua Gao grew up in Wuhan, China. He graduated from Huangpi No.1 High School from Hubei Province of China in 2013 and began his undergraduate study in the University of Science and Technology of China later the same year. While fulfilling all the requirements of the chemistry major, Zehua started researching on the syntheses and catalytic applications of noble-metal nanoparticles under the supervision of Prof. Jie Zeng from 2014 to 2017. Zehua graduated from University of Science and Technology of China in 2017 and enrolled as a graduate student in the department of chemistry at Brown University later that year. Zehua started his PhD research in Prof. Ou Chen's group and then switched to Prof. Lai-Sheng Wang's group in 2019, focusing on atomically precise gold nanoclusters. His PhD research included exploring the syntheses, properties and applications of phosphine protected gold nanoclusters. Zehua had lots of experiences in the syntheses and characterizations of photophysical or chemical properties of gold nanocluster materials, resulting in the discovery of several novel gold nanoclusters. Apart from this, he had some experiences and collaborations in the exploration of catalytic properties as well as DFT calculations with other groups. He also attended and presented posters at two GRC conferences during his time at Brown.

PUBLICATIONS

1. Dong, J., Jerome, R., **Gao, Z. H.**, Wang, L. S. Selective semihydrogenation of polarized alkynes by a gold hydride nanocluster. *J. Am. Chem. Soc*. 2022, 144, 27, 12501–12509

2. **Gao, Z. H.**, Wei, K., Wu, T., Dong, J., Jiang, D. E., Sun, S., Wang, L. S. A Heteroleptic Gold Hydride Nanocluster for Efficient and Selective Electrocatalytic Reduction of CO_2 to CO. *J. Am. Chem. Soc*. 2022, 144, 12, 5258–5262

3. Dong, J., **Gao, Z. H.**, Wang, L. S. The synthesis and characterization of a new diphosphine-protected gold hydride nanocluster. *J. Chem. Phys*. 2022, 155(3), 034307.

4. Dong, J., **Gao, Z. H.**, Zhang, Q. F., Wang, L. S. The Synthesis, Bonding, and Transformation of a Ligand-Protected Gold Nanohydride Cluster. *Angew. Chem. Int. Ed*. 2021,60(5), 2424-2430.

5. **Gao, Z. H.**, Dong, J., Zhang, Q. F., Wang, L. S. Halogen effects on the electronic and optical properties of Au 13 nanoclusters. *Nanoscale Adv.* 2020, 2(10), 4902-4907.

6. Yuan, Y., Zhu, H., Wang, X., Cui, D., **Gao, Z. H.**, Su, D., Zhao, J., Chen, O. Cu-catalyzed synthesis of CdZnSe–CdZnS alloy quantum dots with highly tunable emission. *Chem. Mater*. 2019, 31(7), 2635-2643.

7. Wang, L., Zhang, W., Wang, S., **Gao, Z. H.**, Luo, Z., Wang, X., Zeng, R., Li, A., Li, H., Wang, M., Zheng, X., Zhu, J., Zhang, W., Ma, C., Si, R., Zeng, J. Atomic-level insights in optimizing reaction paths for hydroformylation reaction over Rh/CoO single-atom catalyst. *Nat. Commun*. 2016, 7(1), 1-8.

8. Khan, M.U., Wang, L., Liu, Z., **Gao, Z. H.**, Wang, S., Li, H., Zhang, W., Wang, M., Wang, Z., Ma, C. and Zeng, J. Pt_3Co octapods as superior catalysts of CO_2 hydrogenation. *Angew. Chem. Int. Ed.* 2016, 55(33), 9548-9552.

Conferences

1. 2020 Gordon Research Conference, Feb 2020.

Poster Presentation: Phosphine-Protected Gold Nanoclusters: Reactivity and Optical Properties.

2. 2022 Gordon Research Conference, Oct 2022.

Poster Presentation: A Heteroleptic Gold Hydride Nanocluster for Efficient and Selective Electrocatalytic Reduction of CO_2 to CO.

Teaching Experience

Served as a teaching assistant for the following courses and semesters:

CHEM 0330 (Equilibrium, Rate and Structure)	Fall 2019, Spring 2021, Summer 2021
CHEM 0350 (Organic Chemistry I)	Spring 2019, Spring 2020, Spring 2022
CHEM 0360 (Organic Chemistry II)	Fall 2018

ACKNOWLEDGEMENTS

"*Not hammer-strokes, but dance of the water, sings the pebbles into perfection.*" - Rabindranath Tagore. The past five years is not an easy journey for me, especially when thinking about all the difficulties that I came across in my research. It's impossible for me to achieve anything without the help from all these wonderful people. And I'd like to express my sincere gratitude to those who helped me during my PhD study.

Firstly, I would like to express my greatest gratitude to my advisor Prof. Lai-Sheng Wang, who has strongly supported me and offered me numerous valuable comments and suggestions with great patience throughout my PhD study. I am always so impressed by his sharp insights and thoughtful ideas into many different areas of chemistry. His continuous pursuit of knowledge and meticulous attitude towards every research detail really set a good example for me.

Then, I must thank my committee members Prof. Shouheng Sun and Prof. Jerome R. Robinson. They are always welcome for my questions and provide me with invaluable comments and suggestions on my research projects.

I would like to give special thanks to my lab member who is also my friend, Jia Dong. We work the most closely in the synthetic lab and he is always willing to discuss all the problems and discoveries that arise during my experiments. He helps me a lot during these years in developing purification methods as well as theoretical calculations.

My following thanks go to all my collaborators for offering great support in my research projects. I want to thank Prof. Shouheng Sun, Dr. Kecheng Wei and Yuliang Chen for their

help with the catalytic properties of gold clusters. I want to thank Prof. De-en Jiang and Dr. Tao Wu for their help with theoretical calculations. I want to thank Prof. Ou Chen for the help with the photophysical property measurements for gold clusters, Dr. Russell E. Hopson for helping with the NMR instrument and Dr. Lisa Chen for helping with the mass spectrometry. I would also like to express my sincere gratitude to Dr. Tun-Li Shen, who not only trained me patiently on the knowledge and operating mass spectrometry, but also offered me invaluable career advice.

I would also like to thank all the current and previous members from the Wang group for being a great bunch of people in and out of the lab. They help me so much throughout my graduate study and support me with lots of useful suggestions. I also should thank all my professors, friends, and classmates that I met here.

Last but not least, I would like to thank my parents as well as my girlfriend, who support me all the time in my life and study.

Abstract of "Atomically Precise Gold Nanoclusters: Syntheses, Properties and Applications" by Zehua Gao, Brown University, Dec 2022

Atomically precise gold nanoclusters have attracted much attention over the past decade due to their well-defined structures which allow fundamental studies of structure-property relationships. They can serve as ideal models of nanoparticles and establish the bridge between metal complexes and conventional nanoparticles. The tetrahedral Au_{20} pyramidal cluster, discovered to be highly stable in the gas phase with different types of surface sites, has long been our pursuit as the perfect model catalyst. Towards this aim, many interesting clusters have been discovered and their structure-property relationships have been uncovered. This thesis mainly focuses on the syntheses of phosphine-protected gold clusters and the elucidation of ligand-Au interactions, optical and electronic properties as well as the application of atomically precise gold nanoclusters as model catalysts to understand catalytic reactions from the atomical level.

Chapter 1 provides a general introduction to the scope of atomically precise gold nanoclusters, the predicament of gold clusters in the gas phase and the discovery of the T_d Au_{20} pyramid cluster. Then, the development of gold clusters in solution phase will be briefly discussed, followed by our previous efforts towards the ligand selection and the solution synthesis of the Au_{20} cluster.

Chapter 2 discusses the syntheses and ligand exchange of different halogen-coordinated Au_{13} clusters. The halogen effect on the photophysical properties, Au-halogen interactions, as well as the electronic structures of the clusters will be studied.

Chapter 3 describes the study of two interesting hydride-containing $[Au_{22}H_4(dppo)_6]^{2+}$ and $[Au_{22}H_3(dppb)_7]^{3+}$ clusters. A series of characterization techniques will be included to verify the existence of H atoms, Au-H interactions and reveal the properties of these hydrogens. The synthesis as well as the importance of reducing agent will be highlighted in producing the $[Au_{22}H_3(dppb)_7]^{3+}$ cluster.

Chapter 4 presents the synthesis of a unique heteroleptic $[Au_{22}H_3(dppe)_3(PPh_3)_8]^{3+}$ hydride nanocluster through a combination of two phosphine ligands. The hydride properties and surface redox properties are thoroughly studied. The cluster is then prepared as a catalyst towards the electrochemical CO_2 reduction reaction with surprisingly high selectivity and activity. DFT calculations are performed to explore the reaction mechanisms. This cluster is established as a model catalyst to provide atomical insights into the CO_2 reduction reaction.

Chapter 5 summarizes all the projects during my PhD study and provides my insight and outlook for future directions of gold nanoclusters including the synthesis of Au_{20} pyramid cluster or other gold clusters with uncoordinated active sites, as well as the potential applications in other catalytic reactions.

Table of Contents

List of Abbreviations

Key Abbreviation	Definition
Au NC	Gold nanocluster
Au NP	Gold nanoparticle
TEM	Transmission electron microscopy
SC-XRD	Single crystal X-ray diffraction
PES	Photoelectron spectroscopy
ESI	Electrospray ionization
NMR	Nuclear magnetic resonance
XPS	X-ray photoelectron spectroscopy
PL	Photoluminescence
FCC	Face-centered cubic
T_d	Tetrahedral
NHC	N-heterocyclic carbene
PLQY	Photoluminescent quantum yield
DFT	Density functional theory
MALDI	Matrix-assisted laser desorption/ionization
DCM	Dichloromethane

HOMO	Highest occupied molecular orbital
LUMO	Lowest unoccupied molecular orbital
PLE	Photoluminescent excitation
HER	Hydrogen evolution reaction
CID	Collision-induced dissociation
CO_2RR	CO_2 reduction reaction
FE	Faradaic efficiency

List of Figures

List of Tables

Chapter 1 Introduction to Gold Nanoclusters

1.1 Gold nanomaterials

Gold is the 79th element in the periodic table and has been used in coinage or jewelry for millennia due to its chemical stability and shiny metallic color in bulk phase. However, when gold is reduced to sizes between 2-100 nm, the physical and chemical properties of the resulting gold nanoparticles (Au NPs) can change dramatically from those of the bulk, due to the quantum confinement effects as well as the higher ratio of low-coordinated surface atoms.[1] In 1857, Michael Faraday reported the formation of deep red solutions of colloidal gold by reduction of chloroaurate ($AuCl_4^-$) using phosphorus in a well-known work, as shown in Figure 1.1.[2] Faraday's work laid the foundation for later colloid science and since then tremendous works have been done on the syntheses of Au NPs with extensive characterizations on their morphology features,[3, 4] optical and electronic properties,[5] as well as catalytic[6] and biological applications.[7] Despite the fact that excellent control of size and shape of Au NPs have been achieved after more than 150 years of scientific research, two major issues impede the further understanding in nanoscience research. First, the polydispersity and heterogeneity of nanoparticles prevents the correct interpretation of the size/shape dependent properties. Second, the interaction of surface layers with the metal cores remains poorly understood due to the limitation of transmission electron microscope (TEM) in resolving light atoms and the coexistence of various surface structures on the NPs. The poorly-defined compositions and structures

could also give rise to problems of reproducibility. Therefore, solution syntheses of well-defined atomically-precise Au NPs were highly desirable.

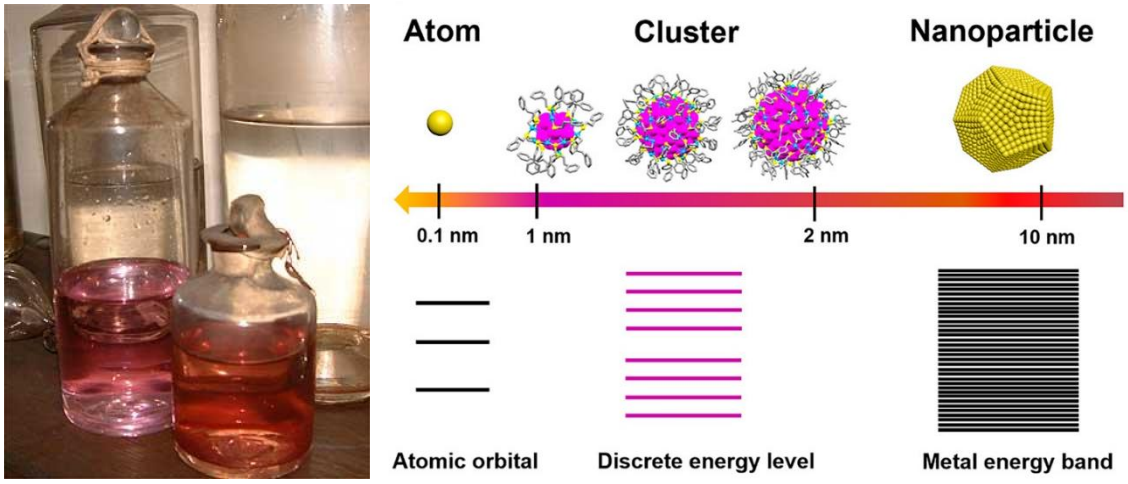

Figure 1.1 Left. Colloidal solutions of gold prepared by Faraday at the Royal Institution.[2] Copyright © 1857 The Royal Society of Chemistry. Right. The scope of nanocluster science.[8] Copyright © 2022 American Chemical Society

The atomically precise nanocluster (NC) is a special class of nanoparticles with 1-2 nm diameter that can be placed in between metal complexes and metal nanoparticles (Figure 1.1 Right).[8] They can serve as ideal models of nanoparticles and establish the bridge between metal complexes and conventional nanoparticles.[9] With the help of single crystal X-ray crystallography (SC-XRD) technique, the structures as well as the metal-organic bonding modes that are unknown in nanoparticles become distinct in the scope of nanoclusters.[10] Therefore, this advance makes NCs possible to overcome the greatest weakness to achieve atomic precision study and atomic-level control over the synthesis. Apart from the well-defined structures, due to such small size, strong quantum size effects in nanoclusters are manifested in their chemical and physical characteristic such as discrete energy levels of electronic and multiple absorption bands arising from molecular-like

electronic transitions.[11] With new synthetic methods and the adoption of modern separation methodologies, a large number of unique Au NCs have been successfully synthesized and characterized. As shown in Figure 1.2, over 5000 research publications in this area suggests an explosion of investigations into this field.[12] The unique features associated with both crystal structure and electronic structure also provide NCs great potential for applications in energy conversion,[13-15] catalysis,[8, 16, 17] biology,[18] and so on.[19, 20]

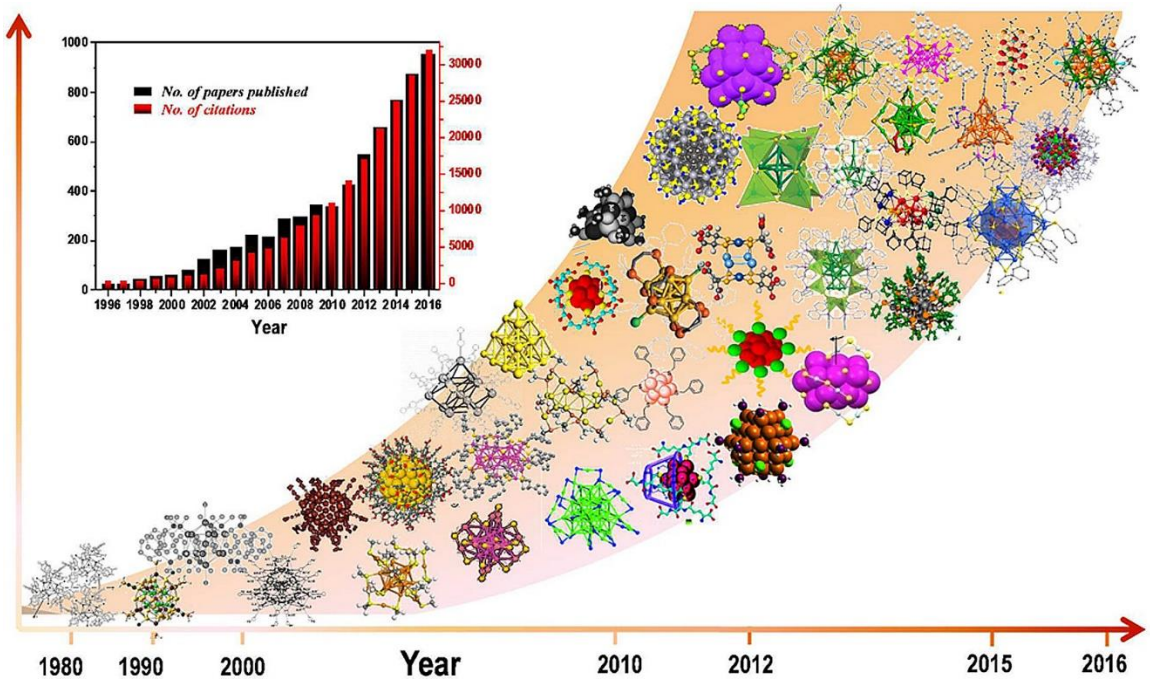

Figure 1.2 Evolution of Au NCs with respect to time. Insert shows the number of papers published and citations in each year till 2017.[12] Copyright © 2017 American Chemical Society

1.2 Gas phase study on Au NCs

The predicament of the Au NCs in solution could be resolved readily by the research of Au NCs generated in the gas phase.[21] Without the complexity that associated with solvent molecules as well as surface ligands, the cluster in the gas phase is much easier to investigate than in the solution phase. Also, every cluster is atom-precise because the cluster sizes can be accurately selected by mass spectrometry and the cluster structures can be determined through combined spectroscopic techniques (photoelectron spectroscopy, Infrared spectroscopy, ion mobility spectroscopy, Raman spectroscopy, etc.) and quantum mechanical calculations.[22] To date, the structures of small Au NCs have been well established.[23-27] Studies have shown that gold anion clusters exhibit two dimensional structures up to the size of Au_{12}^-, followed by flat-cage and hollow-cage structures up to Au_{18}^- and then pyramidal structures from Au_{18}^- to Au_{20}^- (Figure 1.3).[24]

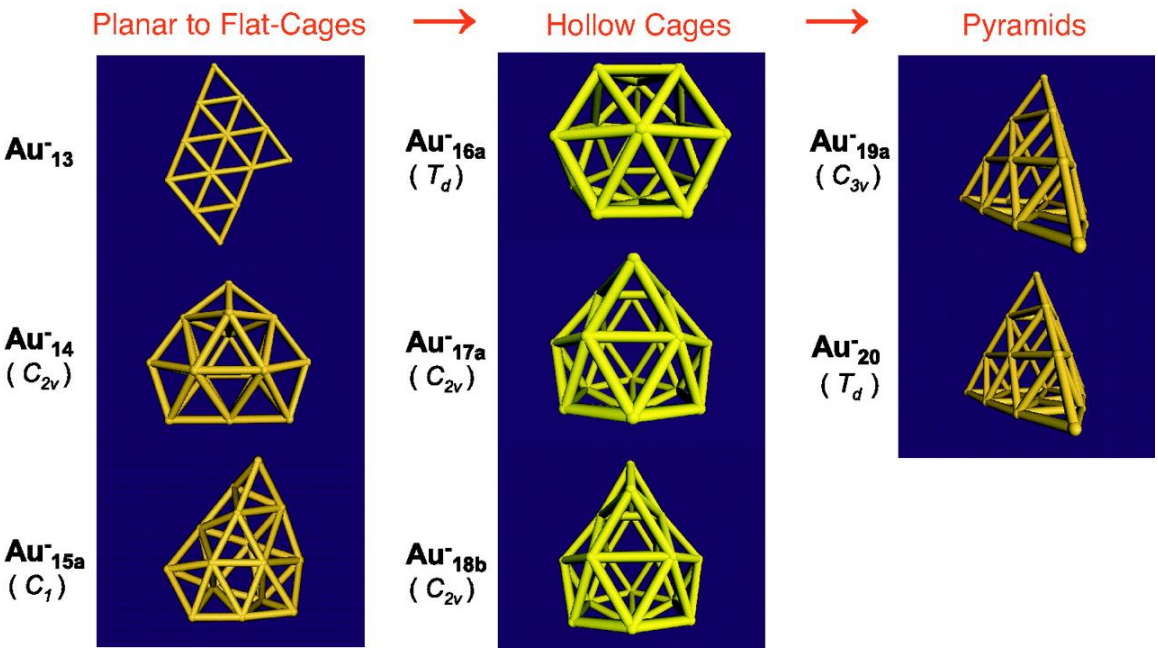

Figure 1.3 Structural evolution of mid-sized gold anion clusters from Au_{13}^- to Au_{20}^-.[24] Copyright © 2006 The National Academy of Sciences of the USA.

Among all these gas-phase Au NCs, the tetrahedral Au_{20} was the most remarkable one.[28] Its large HOMO-LUMO gap (1.77 eV) as revealed by photoelectron spectroscopy (PES) of the negatively charged Au_{20}^- (Figure 1.4) suggested that neutral Au_{20} upon electron detachment is a highly stable electronic and chemical system. The joint PES and theoretical study revealed that it has a tetrahedral (T_d) structure as shown in Figure 1.4b. The 1.77 eV energy gap indicates the Au_{20} cluster is a semiconductor with blue color. Most interestingly, the Au_{20} pyramid consists of four triangle Au(111) facets and can be viewed

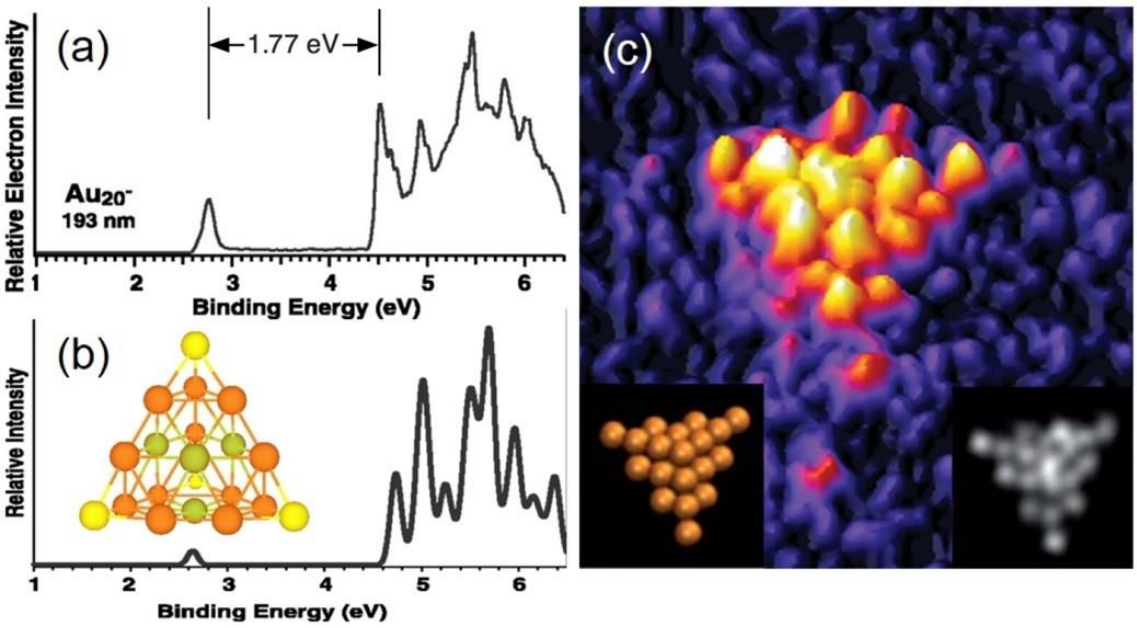

Figure 1.4 (a) Experimental photoelectron spectrum of the Au_{20}^- anion, the energy gap of 1.77 eV is labeled. (b) The tetrahedral structure of the Au_{20}^- cluster (insert) and its simulated photoelectron spectrum.[28] Copyright © 2003 The American Association for the Advancement of Science. (c) HAADF-STEM image (2.8 x 2.8 nm) of a Au_{20} cluster (left inset shows the orientation of the Au_{20} cluster; the right inset is the simulated STEM image).[29] Copyright © 2012 The Royal Society of Chemistry.

as a fragment of the face-centered cubic (fcc) structure of bulk gold. All the atoms of the Au_{20} pyramid are on the cluster surface with a large fraction of corner sites with low coordination number. Three different kinds of atoms exist in the T_d structure: 4 at the apexes, 4 at the center of each face and 12 along the edges. Its structure has also been confirmed by high-angle annular dark-field scanning transmission electron microscopy (Figure 1.4c).[29] Many interesting catalytic[30, 31] and optical[32] properties have been revealed for the Au_{20} pyramid over the past decade.

However, the bare Au_{20} pyramid can only be produced in a very small quantity in molecular beams in the gas phase, which limits the further application. Therefore, it's of great importance to develop a solution phase synthetic route to produce this nanocluster.

1.3 Solution phase syntheses of ligand-protected Au NCs

Au NCs are featured with small size and high surface/volume ratio. As is shown in Figure 1.5, by decreasing the number of atoms in closed-pack full-shell cluster from 561 to 13, the percentage of surface atoms can dramatically increase from 45% to 92%.[33] The

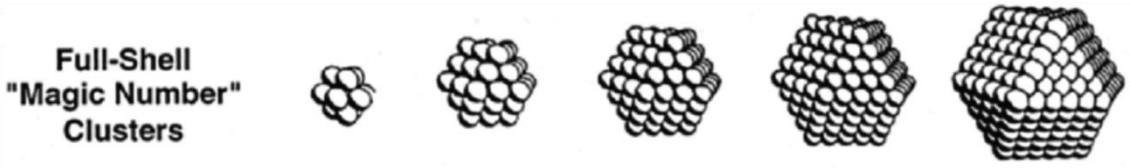

Number of shells	1	2	3	4	5
Number of atoms in cluster	M_{13}	M_{55}	M_{147}	M_{309}	M_{561}
Percentage surface atoms	92%	76%	63%	52%	45%

Figure 1.5 Idealized representation of close-packed full-shell clusters.[33] Copyright © 2019 Elsevier B.V.

low coordinated surface atoms with high surface energies tends to interact or aggregate with the contiguous NC to stabilize, therefore ligand passivation is necessary.

The selection and design of surface ligands is crucial for ligand-protected Au NCs. Apart from providing protection to the low coordinated surface atoms, the surface ligands also play two important roles: 1. Interact with the exterior environment which influences Au NCs towards different applications. 2. The interfacial chemistry between ligands and gold atoms can alternate the structures as well as the physical and chemical properties of Au NCs.[34] Various organic ligands have been employed to protect Au NCs and the most common ligands are phosphines, thiolates, and halide ions.[10, 35, 36] In 1970, a phosphine and halide co-protected $Au_{11}I_3[P(C_6H_4\text{-}p\text{-}Cl)_3]_7$ NC with crystal structure was firstly reported, where the central gold atom is surrounded by 10 other gold atoms to form an incomplete icosahedron structure (Figure 1.6a).[37] A decade later, Mingos et al. successfully crystallized an icosahedral $[Au_{13}(PPhMe_2)_{10}Cl_2]^{3+}$ cluster that had been predicted by theoretical analysis in 1976.[38] As shown in Figure 1.6b, the cluster is featured with one gold atom in the center surrounded by twelve other gold atoms, giving rise to a five-fold symmetry. Many researchers have also studied this cluster extensively after that.[39, 40] With the development in colloidal gold chemistry, in 1994 Brust et al. designed methods to synthesize thiolate protected Au NPs with a narrow size distribution via a two-phase system.[41] Then the Brust-Schiffrin method was quickly adapted to produce thiolate-protected Au NCs. However, challenge remains regarding growing single crystals of thiolate protected Au NCs. In 2007, Kornberg et al. succeeded with a Au_{102}(*p*-mercaptobenzoic acid)$_{44}$ thiolate cluster that was crystallographically determined.[42] The cluster has a 49-atom Marks decahedral core which could also be interpreted as a five-

twinned face-centered cubic or hexagonal close-packed core (Figure 1.6c). One year later, Jin et al. reported a unusual single crystal structure of a phenylethanethiol-capped $Au_{25}(SR)_{18}$ cluster (Figure 1.6d).[43] X-ray crystallographic analysis shows that the Au_{25} cluster is based on an icosahedral Au_{13} kernel, which is capped by six extended "staple" motif where three sulfur and two Au atoms are arranged in a 'V-shaped' -S-Au-S-Au-S-

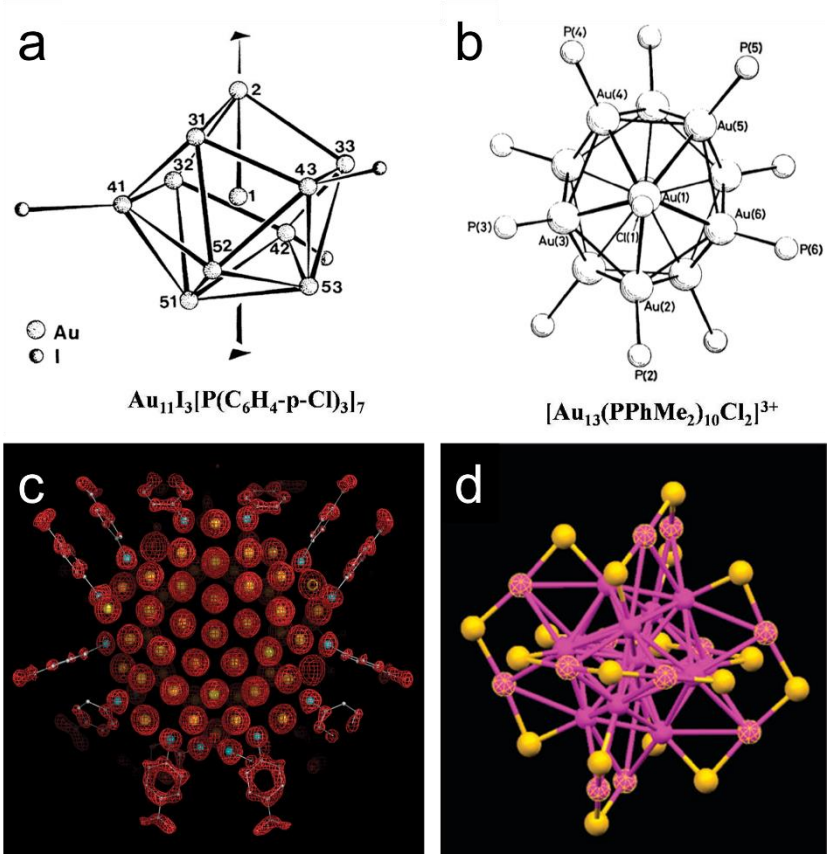

Figure 1.6 a) Crystal structure of $Au_{11}I_3[P(C_6H_4\text{-}p\text{-}Cl)_3]_7$ cluster.[37] Copyright © 1970 The Royal Society of Chemistry. b) Crystal structure of $[Au_{13}(PPhMe_2)_{10}Cl_2]^{3+}$ ion.[38] Copyright © 1981 The Royal Society of Chemistry. c) Crystal structure of $Au_{102}(p\text{-}MBA)_{44}$ cluster (Au: yellow, S: cyan, C: gray, O: red).[42] Copyright © 2007 The American Association for the Advancement of Science. d) Crystal structure of $Au_{25}(SR)_{18}$ cluster (Au: magenta, S: yellow).[43] Copyright © 2008 American Chemical Society

pattern. The smaller size of Au_{25} cluster makes it possible to correlate the cluster structure and optical properties with the help of theoretical calculations. These pioneer works open the door for all the other atomically precise Au NCs and their properties study.

1.4 Previous efforts towards Au_{20} pyramid cluster

Although recent research has let to detailed characterization of numerous thiolate protected atom-precise Au NCs.[10] The interface between the thiolate ligands and the cluster surface was found to be complex due to the strong Au-S bond , which usually leads to compact structures with staple motifs.[44] Therefore, thiolate ligands are not suitable for the purpose of pursuing the Au_{20} pyramid. Jin et al. reported the crystal structure of a thiolate ligated $Au_{20}(TBBT)_{16}$ (TBBT = SPh-*t*-Bu) cluster, and it comprises a bi-tetrahedral Au_7 kernel with an $Au_8(SR)_8$ octameric ring and a trimeric and dimeric staple motif, which distinguish from the tetrahedral shape.[45] To maintain the pyramidal structure of Au_{20} cluster, a neutral ligand with moderate strength of bonding to gold is preferable and phosphine ligands are better candidate for this purpose. In addition to mild binding strength, the zero-valent phosphine ligands only have one lone pair and form dative bonding to gold, while thiolates or alkynes have two lone pairs and carry one unit of negative charge, which give rise to different electronic structures and ligand-shell configurations.[17, 46]

Starting from monodentate ligand, the bulky PPh_3 ligand was selected for the syntheses of the Au_{20} pyramid. Triphenylphosphine has been widely used in the studies of phosphine-coordinated clusters.[47, 48] The PPh_3-protected Au_{20} was prepared by reducing $Au(PPh_3)Cl$ with $NaBH_4$ solution, and followed by characterizing with high-resolution transmission electron microscopy (HRTEM).[49] The observed isotopic pattern from

electrospray ionization mass spectroscopy (ESI-MS) was identical to the simulated isotopic pattern of the $[Au_{20}(PPh_3)_8]^{2+}$. All the results together indicate the formation of a $[Au_{20}(PPh_3)_8]^{2+}$ cluster which agree well with the theoretical prediction that the four apex sites and four face-centered gold sites were coordinated by eight PPh_3 ligands (Figure 1.7). The 18-electron $[Au_{20}(PPh_3)_8]^{2+}$ core also fulfills the closed-shell electronic structure, suggesting the high stability. Nevertheless, the selectivity and the yield of this reaction is too low with difficulties in obtaining pure Au_{20} cluster or growing into single crystals. Therefore, better synthetic strategies, including ligand modification and reaction conditions, need more investigations.

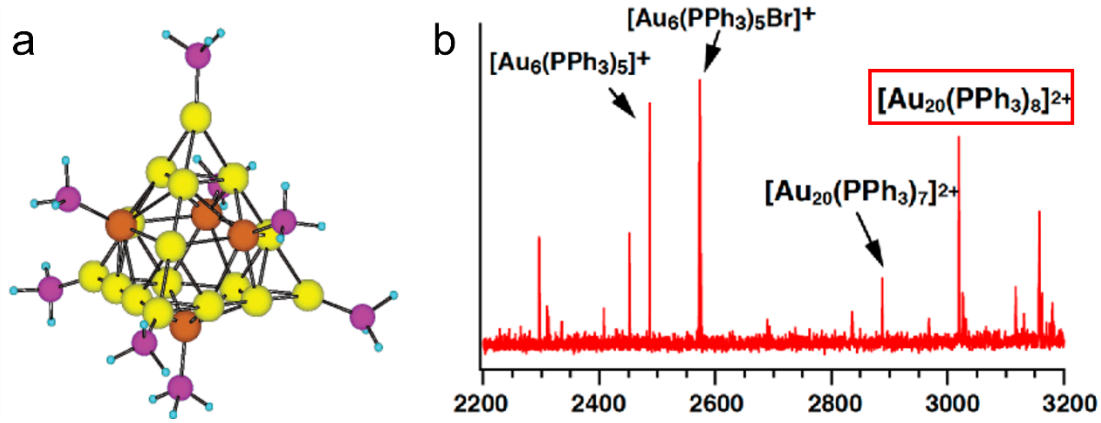

Figure 1.7 Au_{20} pyramid in solution: a) Computed structure of $Au_{20}(PH_3)_8$, Au: yellow and orange, P: purple. b) ESI-MS of Au clusters produced from $Au(PPh_3)Cl$ precursor.[49] Copyright © 2004 American Chemical Society

In a continuing effort towards the Au_{20} pyramid, bidentate and multidentate diphosphine ligands were also employed. As shown in Figure 1.8a, a series of α,ω-bis(diphenylphosphino) alkanes of the general formula, $P(Ph)_2(CH_2)_nP(Ph)_2$ (abbreviated as L^n) were selected. Compared to PPh_3 ligand, these ligands in principle can provide the targeted Au_{20} pyramid cluster with more rigidity as well as different stereo-effects by

tuning the carbon chain length. Although the optimized conditions towards T_d Au_{20} haven't been achieved, it's observed that the diphosphine ligands with n > 2 exhibit a degree of size selectivity, giving rise to a simple method to synthesize other Au NCs.[50] The joint characterizations with ESI-MS and UV-vis absorption spectroscopy confirm that monodispersed Au_{11} cluster is obtained with n = 3, whereas n = 5/6 yield Au_{10} and Au_8 cluster. When n = 8, a dichloromethane solution of $Au_2L^8Cl_2$ could be reduced by $NaBH_4$ to yield a unique $Au_{22}(L^8)_6$ cluster.[51] Single crystal of the cluster was obtained after purifying by column chromatography and the structure was successfully determined by SC-XRD (Figure 1.8a). The Au_{22} core is composed of two icosahedral Au_{11} units through sharing a square face with inversion symmetry. The two Au_{11} units are clipped together by four L^8 diphosphine ligands, giving the cluster good stability. Therefore, such coordination mode leaves behind eight undercoordinated Au sites in the center, which were later found to be highly active towards CO oxidation reaction.[52] The synthesis with a tetradentate phosphine ligand gives rise to a novel $[Au_{20}(PP_3)_4]Cl_4$ cluster (PP_3 = tris[2-(diphenylphosphino)-ethyl]phosphine).[53] As shown in Figure 1.8b, the Au_{20} cluster

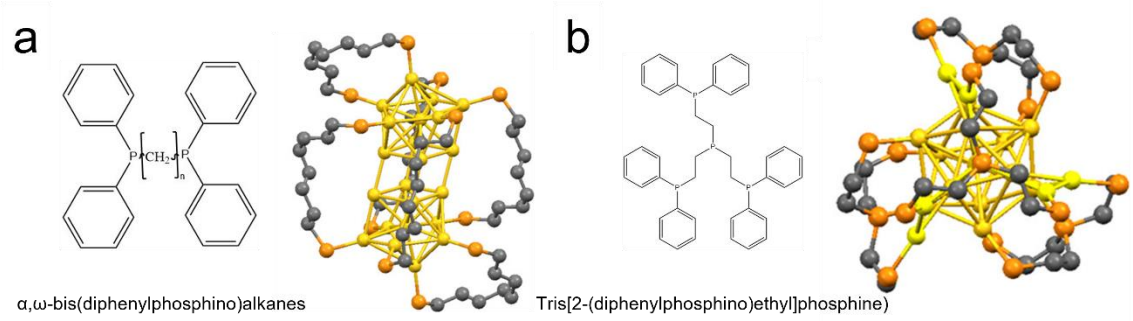

Figure 1.8 a) Diphosphine ligands and $[Au_{22}(L^8)_6]$ cluster.[51] Copyright © 2013 American Chemical Society. b) Tetradentate PP_3 ligand and $[Au_{20}(PP_3)_4]Cl_4$ cluster.[53] Au: yellow, P: orange, P: gray. Copyright © 2014 American Chemical Society.

consists of an icosahedral Au_{13} kernel and a seven-Au-atom partial outer shell arranged in a C_3 symmetry. All the sixteen surface atoms in the Au_{20} core were coordinated, resulting in a very stable cluster.

The previous efforts towards T_d Au_{20} cluster, although not successful, have suggested that small changes in synthesizing can lead to drastic changes in structural and the properties of gold-phosphine clusters. The changes include different phosphine ligands (chain length, coordination mode), reducing agent, temperature, etc. The nature of phosphine ligands determines the core size nuclearity, geometrical structure, stability and electronic structure, leading to the rich chemistry of phosphine-ligated Au NCs.

1.5 Overview of the dissertation

The atomically precise Au NCs have attracted much attention over the past decade due to their well-defined structures which allow for the in-depth study of structure-property relationships. They can serve as perfect models of nanoparticles and establish the bridge from metal complexes to conventional nanoparticles. Instead of synthesizing novel phosphine ligands to create novel clusters, my PhD study has mainly focused on understanding the ligand-Au interactions, properties study as well as the application of atomically precise Au NCs as model catalyst to demonstrate some important chemical reactions from atomical level.

In the following chapters, several aspects of the atomically precise Au NCs will be thoroughly discussed. Firstly, the properties of different halogen coordinated Au_{13} NCs are investigated, including the halide exchange reaction as well as halogen effect on the photophysical properties of the Au_{13} NCs and the importance of halogen ligands in the

electronic structures of Au NCs. Secondly, two novel diphosphine protected Au nanohydride clusters will be discussed. The Au-H interactions are experimentally verified and the existence as well as the properties of these H atoms are studied with the help of a series of spectroscopic tools. Also, on the aspect of synthesis, the effect of reducing power and the ratio of reducing agent on the formation of Au NCs will be studied with several pairs of controlled experiments. Although the reaction mechanism hasn't been figured out completely, some results from this part will lead to the discovery of more novel hydride containing Au NCs. Thirdly, the combination of both monodentate and bidentate phosphine ligands results in a highly stable heteroleptic trihydride Au NC. This cluster is demonstrated as a very efficient catalyst towards electrochemical CO_2 reduction reaction. The mechanism study of this process suggests that the H atoms on the cluster can participate in the catalytic cycle and lower the activation barrier for important intermediate species. Therefore, this cluster successfully realizes our aim to control and identify the active sites for catalytic reactions. Finally, some perspectives on the future will be put forward.

References

(1) Daniel, M. C.; Astruc, D. Gold nanoparticles: assembly, supramolecular chemistry, quantum-size-related properties, and applications toward biology, catalysis, and nanotechnology. *Chem. Rev.* **2004**, *104* (1), 293-346.

(2) Faraday, M. On the relations of gold and other metals to light. *Proc. R. Soc. Lond.* **1857**, (8), 356-361.

(3) Sun, Y.; Xia, Y. Shape-controlled synthesis of gold and silver nanoparticles. *Science* **2002**, *298* (5601), 2176-2179.

(4) Jana, N. R.; Gearheart, L.; Murphy, C. J. Seed-mediated growth approach for shape-controlled synthesis of spheroidal and rod-like gold nanoparticles using a surfactant template. *Adv. Mater.* **2001**, *13* (18), 1389-1393.

(5) Elghanian, R.; Storhoff, J. J.; Mucic, R. C.; Letsinger, R. L.; Mirkin, C. A. Selective colorimetric detection of polynucleotides based on the distance-dependent optical properties of gold nanoparticles. *Science* **1997**, *277* (5329), 1078-1081.

(6) Corma, A.; Garcia, H. Supported gold nanoparticles as catalysts for organic reactions. *Chem. Soc. Rev.* **2008**, *37* (9), 2096-2126.

(7) Giljohann, D. A.; Seferos, D. S.; Daniel, W. L.; Massich, M. D.; Patel, P. C.; Mirkin, C. A. Gold nanoparticles for biology and medicine. *Angew. Chem. Int. Ed.* **2010**, *49* (19), 3280-3294.

(8) Cai, X.; Li, G.; Hu, W.; Zhu, Y. Catalytic Conversion of CO_2 over Atomically Precise Gold-Based Cluster Catalysts. *ACS Catal.* **2022**, *12* (17), 10638-10653.

(9) Kang, X.; Li, Y.; Zhu, M.; Jin, R. Atomically precise alloy nanoclusters: syntheses, structures, and properties. *Chem. Soc. Rev.* **2020**, *49* (17), 6443-6514.

(10) Jin, R.; Zeng, C.; Zhou, M.; Chen, Y. Atomically precise colloidal metal nanoclusters and nanoparticles: fundamentals and opportunities. *Chem. Rev.* **2016**, *116* (18), 10346-10413.

(11) Schmid, G. Large clusters and colloids. Metals in the embryonic state. *Chem. Rev.* **1992**, *92* (8), 1709-1727.

(12) Chakraborty, I.; Pradeep, T. Atomically precise clusters of noble metals: emerging link between atoms and nanoparticles. *Chem. Rev.* **2017**, *117* (12), 8208-8271.
(13) Zhang, H.; Liu, H.; Tian, Z.; Lu, D.; Yu, Y.; Cestellos-Blanco, S.; Sakimoto, K. K.; Yang, P. Bacteria photosensitized by intracellular gold nanoclusters for solar fuel production. *Nat. Nanotechnol.* **2018**, *13* (10), 900-905.
(14) Abbas, M. A.; Kamat, P. V.; Bang, J. H. Thiolated gold nanoclusters for light energy conversion. *ACS Energy Lett.* **2018**, *3* (4), 840-854.
(15) Negishi, Y. Metal-nanocluster science and technology: my personal history and outlook. *Phys. Chem. Chem. Phys.* **2022**, *24* (13), 7569-7594.
(16) Yamazoe, S.; Koyasu, K.; Tsukuda, T. Nonscalable oxidation catalysis of gold clusters. *Acc. Chem. Res.* **2014**, *47* (3), 816-824.
(17) Adnan, R. H.; Madridejos, J. M. L.; Alotabi, A. S.; Metha, G. F.; Andersson, G. G. A Review of State of the Art in Phosphine Ligated Gold Clusters and Application in Catalysis. *Adv. Sci.* **2022**, 2105692.
(18) Lin, C. A. J.; Yang, T. Y.; Lee, C. H.; Huang, S. H.; Sperling, R. A.; Zanella, M.; Li, J. K.; Shen, J. L.; Wang, H. H.; Yeh, H. I. Synthesis, characterization, and bioconjugation of fluorescent gold nanoclusters toward biological labeling applications. *ACS Nano* **2009**, *3* (2), 395-401.
(19) Zhang, M. M.; Dong, X. Y.; Wang, Y. J.; Zang, S. Q.; Mak, T. C. Recent progress in functional atom-precise coinage metal clusters protected by alkynyl ligands. *Coord. Chem. Rev.* **2022**, *453*, 214315.
(20) Kang, X.; Zhu, M. Tailoring the photoluminescence of atomically precise nanoclusters. *Chem. Soc. Rev.* **2019**, *48* (8), 2422-2457.
(21) Wang, L. M.; Wang, L. S. Probing the electronic properties and structural evolution of anionic gold clusters in the gas phase. *Nanoscale* **2012**, *4* (14), 4038-4053.
(22) Häkkinen, H. Atomic and electronic structure of gold clusters: understanding flakes, cages and superatoms from simple concepts. *Chem. Soc. Rev.* **2008**, *37* (9), 1847-1859.
(23) Ji, M.; Gu, X.; Li, X.; Gong, X.; Li, J.; Wang, L. S. Experimental and theoretical investigation of the electronic and geometrical structures of the Au_{32} cluster. *Angew. Chem. Int. Ed.* **2005**, *44* (43), 7119-7123.

(24) Bulusu, S.; Li, X.; Wang, L.S.; Zeng, X. C. Evidence of hollow golden cages. *Proc. Natl. Acad. Sci. U.S.A.* **2006**, *103* (22), 8326-8330.

(25) Bulusu, S.; Li, X.; Wang, L. S.; Zeng, X. C. Structural Transitions from Pyramidal to Fused Planar to Tubular to Core/Shell Compact in Gold Clusters: Au_n^- (n= 21− 25). *J. Phys. Chem. C* **2007**, *111* (11), 4190-4198.

(26) Shao, N.; Huang, W.; Gao, Y.; Wang, L. M.; Li, X.; Wang, L. S.; Zeng, X. C. Probing the Structural Evolution of Medium-Sized Gold Clusters: Au_n^- (n= 27− 35). *J. Am. Chem. Soc.* **2010**, *132* (18), 6596-6605.

(27) Pande, S.; Huang, W.; Shao, N.; Wang, L. M.; Khetrapal, N.; Mei, W. N.; Jian, T.; Wang, L. S.; Zeng, X. C. Structural Evolution of Core–Shell Gold Nanoclusters: Au_n^-(n= 42–50). *ACS Nano* **2016**, *10* (11), 10013-10022.

(28) Li, J.; Li, X.; Zhai, H. J.; Wang, L. S. Au_{20}: a tetrahedral cluster. *Science* **2003**, *299* (5608), 864-867.

(29) Wang, Z.; Palmer, R. Direct atomic imaging and dynamical fluctuations of the tetrahedral Au_{20} cluster. *Nanoscale* **2012**, *4* (16), 4947-4949.

(30) Molina, L.; Hammer, B. The activity of the tetrahedral Au_{20} cluster: charging and impurity effects. *J. Catal.* **2005**, *233* (2), 399-404.

(31) Gao, Y.; Shao, N.; Pei, Y.; Chen, Z.; Zeng, X. C. Catalytic activities of subnanometer gold clusters (Au_{16}–Au_{18}, Au_{20}, and Au_{27}–Au_{35}) for CO oxidation. *ACS Nano* **2011**, *5* (10), 7818-7829.

(32) Yu, C.; Harbich, W.; Sementa, L.; Ghiringhelli, L.; Aprá, E.; Stener, M.; Fortunelli, A.; Brune, H. Intense fluorescence of Au_{20}. *J. Chem. Phys.* **2017**, *147* (7), 074301.

(33) Chen, S.; Xiong, F.; Huang, W. Surface chemistry and catalysis of oxide model catalysts from single crystals to nanocrystals. *Surf. Sci. Rep.* **2019**, *74* (4), 100471.

(34) Zhang, B.; Chen, J.; Cao, Y.; Chai, O. J. H.; Xie, J. Ligand Design in Ligand-Protected Gold Nanoclusters. *Small* **2021**, *17* (27), 2004381.

(35) Konishi, K.; Iwasaki, M.; Shichibu, Y. Phosphine-ligated gold clusters with core+ exo geometries: Unique properties and interactions at the ligand–cluster interface. *Acc. Chem. Res.* **2018**, *51* (12), 3125-3133.

(36) Zeng, J. L.; Guan, Z. J.; Du, Y.; Nan, Z. A.; Lin, Y. M.; Wang, Q. M. Chloride-promoted formation of a bimetallic nanocluster $Au_{80}Ag_{30}$ and the total structure determination. *J. Am. Chem. Soc.* **2016**, *138* (25), 7848-7851.

(37) Albano, V.; Bellon, P.; Manassero, M.; Sansoni, M. Intermetallic pattern in metal-atom clusters. Structural studies on $Au_{11}X_3(PR_3)_7$ species. *J. Chem. Soc. D* **1970**, (18), 1210-1211.

(38) Briant, C. E.; Theobald, B. R.; White, J. W.; Bell, L. K.; Mingos, D. M. P.; Welch, A. J. Synthesis and X-ray structural characterization of the centred icosahedral gold cluster compound $[Au_{l3}(PMe_2Ph)_{10}Cl_2](PF_6)_3$; the realization of a theoretical prediction. *J. Chem. Soc., Chem. commun.* **1981**, (5), 201-202.

(39) Shichibu, Y.; Konishi, K. HCl-Induced Nuclearity Convergence in Diphosphine-Protected Ultrasmall Gold Clusters: A Novel Synthetic Route to "Magic-Number" Au_{13} Clusters. *Small* **2010**, *6* (11), 1216-1220.

(40) Shichibu, Y.; Suzuki, K.; Konishi, K. Facile synthesis and optical properties of magic-number Au_{13} clusters. *Nanoscale* **2012**, *4* (14), 4125-4129.

(41) Brust, M.; Walker, M.; Bethell, D.; Schiffrin, D. J.; Whyman, R. Synthesis of thiol-derivatised gold nanoparticles in a two-phase liquid–liquid system. *J. Chem. Soc., Chem. commun.* **1994**, (7), 801-802.

(42) Jadzinsky, P. D.; Calero, G.; Ackerson, C. J.; Bushnell, D. A.; Kornberg, R. D. Structure of a thiol monolayer-protected gold nanoparticle at 1.1 A resolution. *Science* **2007**, *318* (5849), 430-433.

(43) Zhu, M.; Aikens, C. M.; Hollander, F. J.; Schatz, G. C.; Jin, R. Correlating the crystal structure of a thiol-protected Au25 cluster and optical properties. *J. Am. Chem. Soc.* **2008**, *130* (18), 5883-5885.

(44) Pei, Y.; Wang, P.; Ma, Z.; Xiong, L. Growth-rule-guided structural exploration of thiolate-protected gold nanoclusters. *Acc. Chem. Res.* **2018**, *52* (1), 23-33.

(45) Zeng, C.; Liu, C.; Chen, Y.; Rosi, N. L.; Jin, R. Gold–thiolate ring as a protecting motif in the $Au_{20}(SR)_{16}$ nanocluster and implications. *J. Am. Chem. Soc.* **2014**, *136* (34), 11922-11925.

(46) Zhang, Q. F.; Chen, X.; Wang, L. S. Toward solution syntheses of the tetrahedral Au_{20} pyramid and atomically precise gold nanoclusters with uncoordinated sites. *Acc. Chem. Res.* **2018**, *51* (9), 2159-2168.

(47) Teo, B. K.; Shi, X.; Zhang, H. Pure gold cluster of 1: 9: 9: 1: 9: 9: 1 layered structure: a novel 39-metal-atom cluster $[(Ph_3P)_{14}Au_{39}Cl_6]Cl_2$ with an interstitial gold atom in a hexagonal antiprismatic cage. *J. Am. Chem. Soc.* **1992**, *114* (7), 2743-2745.

(48) Kenzler, S.; Schnepf, A. Metalloid gold clusters–past, current and future aspects. *Chem. Sci.* **2021**, *12* (9), 3116-3129.

(49) Zhang, H. F.; Stender, M.; Zhang, R.; Wang, C.; Li, J.; Wang, L. S. Toward the solution synthesis of the tetrahedral Au_{20} cluster. *J. Phys. Chem. B* **2004**, *108* (33), 12259-12263.

(50) Bertino, M. F.; Sun, Z. M.; Zhang, R.; Wang, L. S. Facile syntheses of monodisperse ultrasmall Au clusters. *J. Phys. Chem. B* **2006**, *110* (43), 21416-21418.

(51) Chen, J.; Zhang, Q. F.; Bonaccorso, T. A.; Williard, P. G.; Wang, L. S. Controlling gold nanoclusters by diphospine ligands. *J. Am. Chem. Soc.* **2014**, *136* (1), 92-95.

(52) Wu, Z.; Hu, G.; Jiang, D. E.; Mullins, D. R.; Zhang, Q. F.; Allard Jr, L. F.; Wang, L. S.; Overbury, S. H. Diphosphine-protected Au_{22} nanoclusters on oxide supports are active for gas-phase catalysis without ligand removal. *Nano Lett.* **2016**, *16* (10), 6560-6567.

(53) Chen, J.; Zhang, Q. F.; Williard, P. G.; Wang, L. S. Synthesis and structure determination of a new Au_{20} nanocluster protected by tripodal tetraphosphine ligands. *Inorg. Chem.* **2014**, *53* (8), 3932-3934.

Chapter 2 Halogen effects on the electronic and optical properties of Au_{13} nanoclusters

Portions of this chapter are adapted and/or reprinted from the following work. Copyright belongs to the publisher.

Gao, Z. H., Dong, J., Zhang, Q. F., Wang, L. S. Halogen effects on the electronic and optical properties of Au 13 nanoclusters. *Nanoscale Adv.* 2020, 2(10), 4902-4907.

2.1 Introduction

Even though bulk gold displays the beautiful golden color, the photophysical properties of nanogold are size-dependent due to quantum confinement of the conducting electrons.[1,2] Specifically, gold nanoclusters with dimensions in the subnanometer size regime possess unique and molecular characteristics, allowing for precise structure determination and applications in photoluminescence (PL),[3-6] catalysis,[7-9] and biomedicine.[10-12] With the availability of single crystal X-ray structures,[13,14] extensive attentions have been paid to the role of the ligands in the syntheses and photophysical properties of gold nanoclusters with different nuclearities.[15-16]

To obtain novel gold clusters with different photophysical properties, organic ligands such as thiols, phosphines and alkynes have been widely exploited in the syntheses of gold nanoclusters (Au_n) such as Au_8,[17] Au_9,[18] Au_{11},[19,20] Au_{13},[21-25] Au_{18},[26] Au_{20},[27,28]

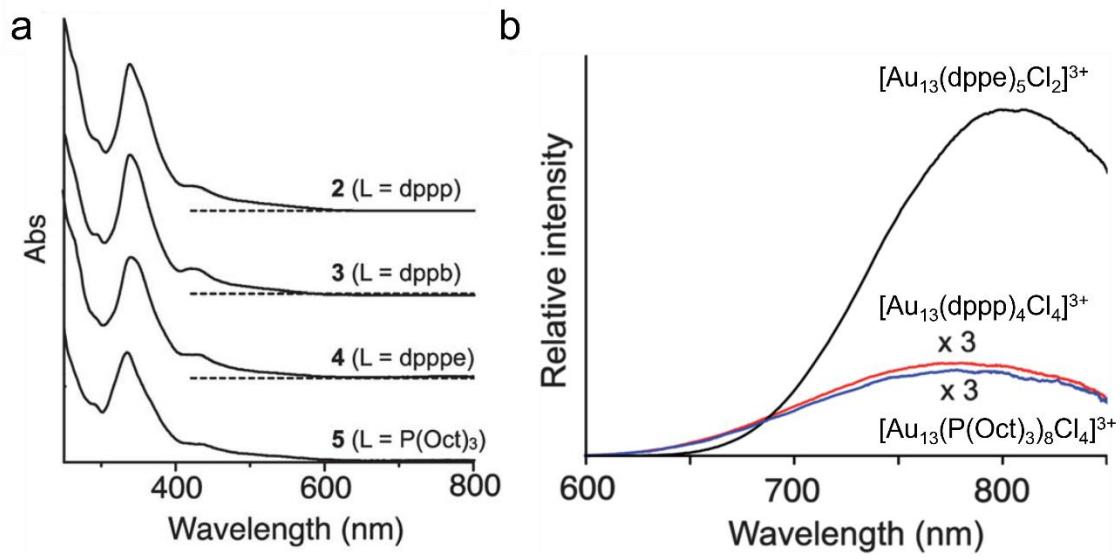

Figure 2.1 a) Absorption spectra of phosphine ligated Au_{13} clusters and b) PL spectra of the Au_{13} clusters.[24] Copyright © 2012 The Royal Society of Chemistry.

Au_{22},[29,30] Au_{23},[31] Au_{24},[32] Au_{25},[33,34] Au_{32},[35] Au_{37},[36] Au_{44},[37] Au_{52},[38] Au_{55},[39] and Au_{102}.[13] Among all of gold nanoclusters that have been structurally characterized, the icosahedral Au_{13} nanocluster has been more extensively studied due to its highly symmetrical structure and prominent photoluminescent properties. For example, the bis(diphenylphosphino)ligands (Ph_2P-(CH_2)m-PPh_2, m = 2,3,4) protected $[Au_{13}P_{10}Cl_2]^{3+}$ or $[Au_{13}P_8Cl_4]^+$ clusters have been reported to exhibit near infrared PL by Konish et al.[24,25] As is shown in Figure 2.1, the absorption spectra of different phosphine ligated Au_{13} NC have nearly identical absorption features, meaning that the phosphine ligands may have little participation in the electronic structures of the icosahedral cluster. However, by examining the PL spectra of these clusters (Figure 2.1b), the cluster that contains five dppe ligands and two chloride anions is much more emissive than the other two clusters with four chloride anions. Based on these results, they concluded that the optical properties of Au NCs are dependent also on the numbers of Cl/neutral phosphine ligands. Thus, to figure out the roles of halogen atoms and phosphine ligands on the electronic structure of the cluster is very meaningful.

In addition, N-heterocyclic carbene (NHC) was employed by Crudden and co-workers to synthesize $[Au_{13}(NHC)_9Cl_3]^{2+}$, which possesses enhanced stability.[40] The cluster contains three chlorine atoms in its crystal structure (Figure 2.2) and exceptionally high PL quantum yield (PLQY) (16.0%) is also measured for this cluster. The icosahedral Au_{13} was also identified as the kernels in the structures of larger gold clusters such as Au_{25}, Au_{37} and Au_{60}.[23] Furthermore, density function theory (DFT) calculations indicated the metallic $(Au_{13})^{5+}$ core can be viewed as a superatom with a closed electron configuration

of $(1S)^2(1P)^6$.[41] Despite the extensive studies, the effects of the halide ligands on the PL properties or electronic structures of the Au_{13} cluster has not been examined.

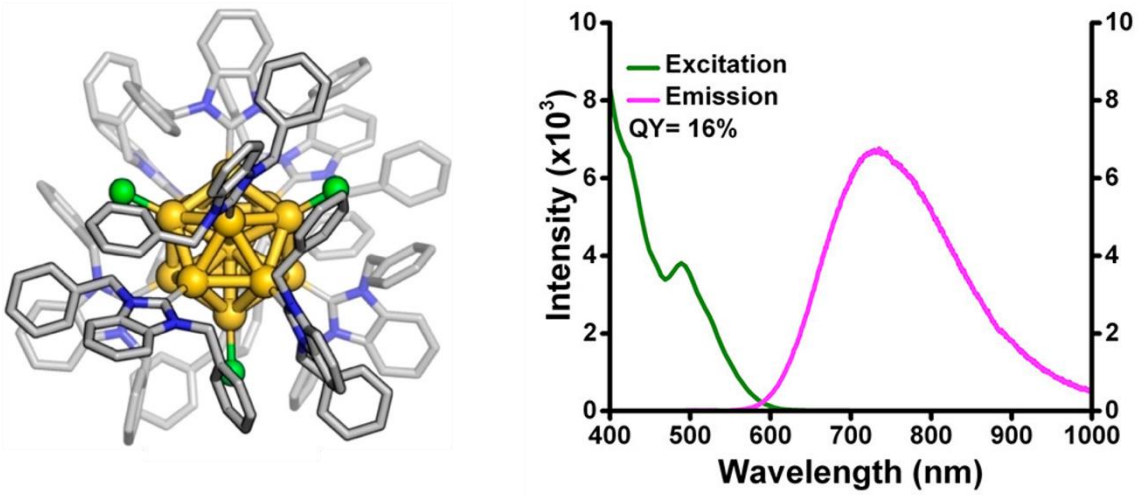

Figure 2.2 The crystal structure of $[Au_{13}(NHC)_9Cl_3]^{2+}$ cluster and PL spectrum.[40] Copyright © 2019 American Chemical Society.

Apart from understanding the influence of halide ions on the photophysical properties of Au NCs, the investigation on halogen ligands is of great importance to our ultimate purpose which is the solution synthesis of Au_{20} pyramid cluster. The synthesis of diverse gold phosphine precursor always starts from the stoichiometric reaction between phosphine ligands and AuCl-$S(CH_3)_2$ (chloro(dimethylsulfide)gold(I)), leading to the formation of chlorine-contained precursor. Therefore, halide ions unavoidably take part in the reduction reaction of gold precursor towards larger Au NCs and this also explains the participation of halide ions in the crystal structures of so many Au NCs (Figure 2.3).

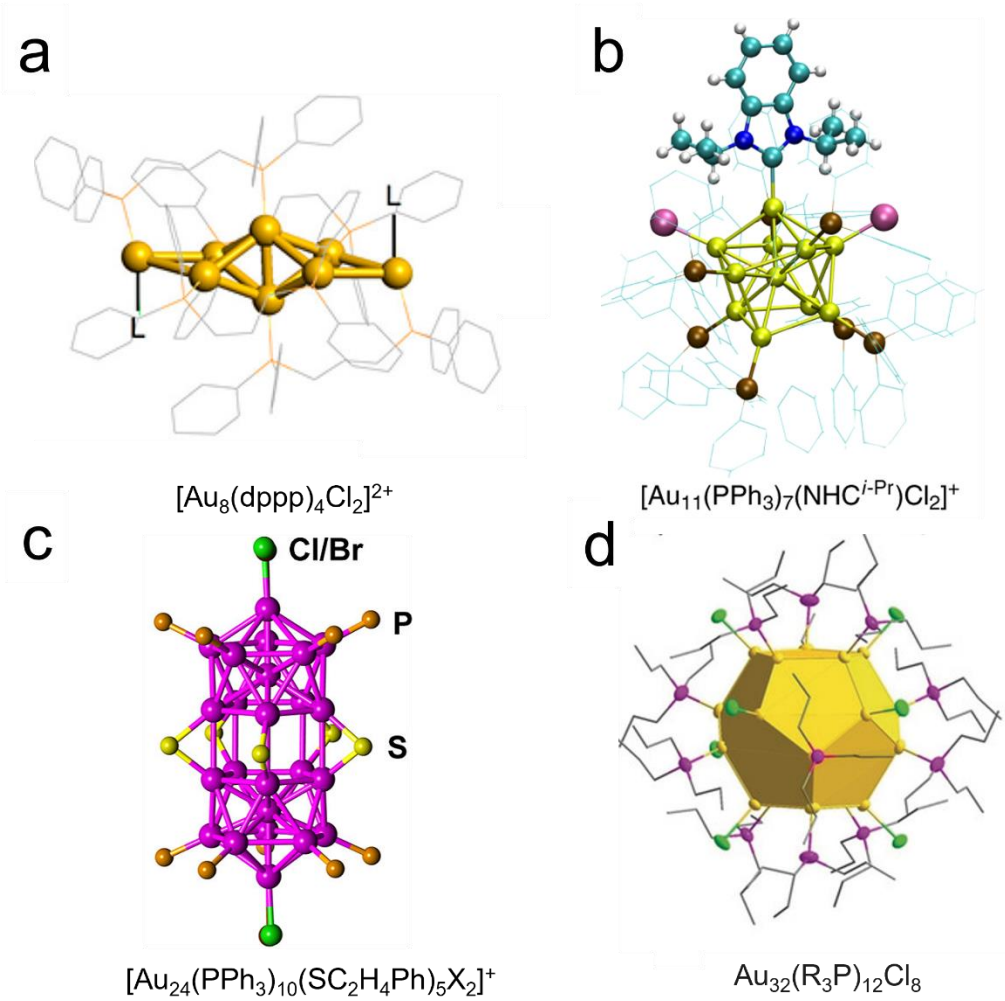

Figure 2.3 Examples of halogen containing clusters: a) Au_8 cluster.[17] Copyright © 2017 American Chemical Society. b) Au_{11} cluster.[20] Copyright © 2019 Springer Nature. c) Au_{24} cluster.[32] Copyright © 2012 American Chemical Society. d) Au_{32} cluster.[35] Copyright ©2019 Wiley-VCH Verlag GmbH & Co. KGaA, Weinheim.

However, the Au-halogen interactions in a series of Au compounds in the gas phase, including $[AuX_2]^-$ (X=halogens) and $[XAuCN]^-$, have been investigated by photoelectron spectroscopy previously.[42,43] Periodic trends were found in the bond lengths and covalent nature of the Au-X bond.[42] In addition, halogens have been found to take an active role in

the synthesis of nanoparticles (NPs) for morphology control[44-46] and PL.[47,48] Although there have been sophisticated characterization methods and theoretical calculations, it is a challenge to understand the halogen effects due to the large size and inhomogeneity of NPs.

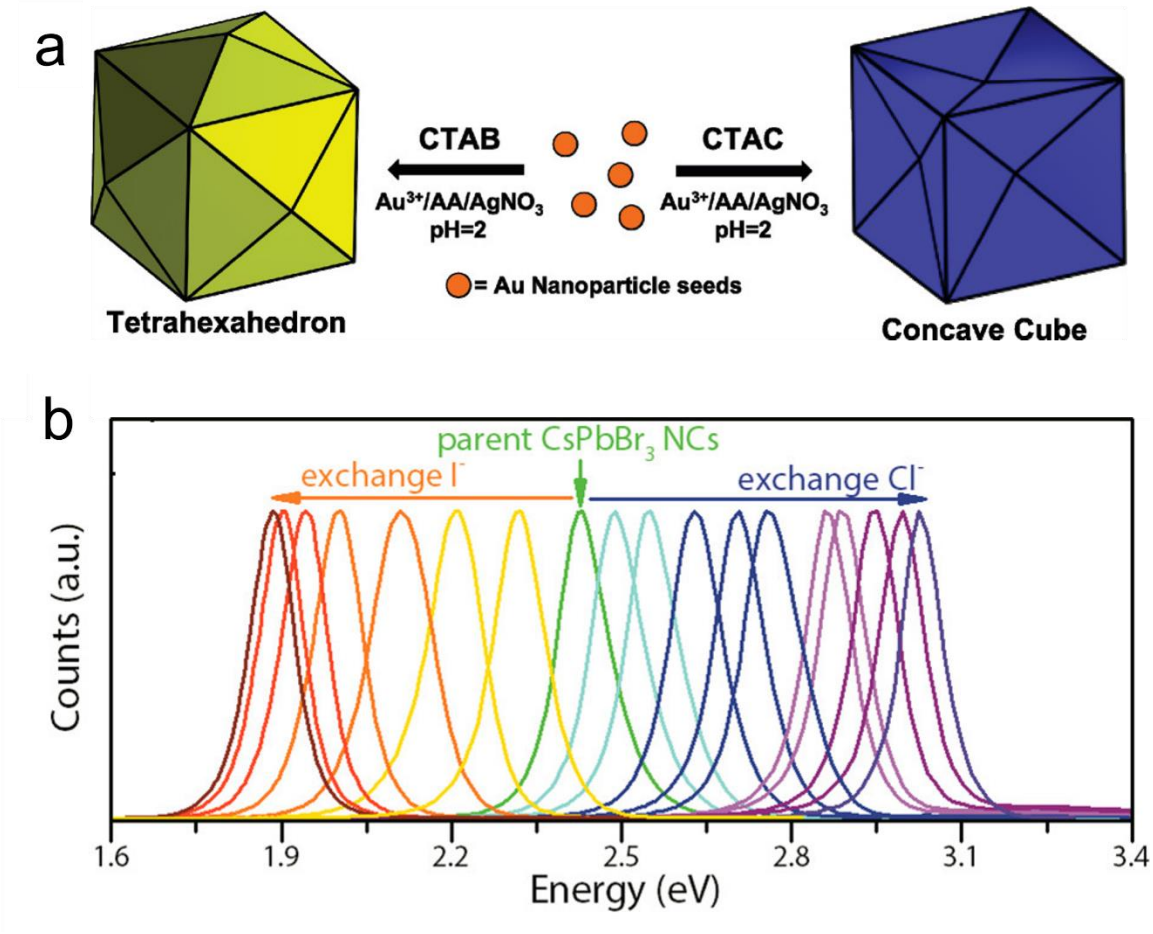

Figure 2.4 Halogen effect on the a) morphology of NPs,[45] Copyright © 2010 American Chemical Society. And b) PL spectra.[47] Copyright © 2015 American Chemical Society.

Therefore, small nanoclusters with atomically precise structure and molecular-like size are more suitable systems to study the halogen effects. Relatively few studies have been done on gold clusters with different halogen ligands. The transformation of halogen-stabilized Au_8 to Au_{11} was investigated by Yam et al.[18] Wang and co-workers determined the structure of a large $Au_{80}Ag_{30}$ bimetallic nanocluster, as is shown in Figure 2.5a, it has

a concentric four-shell arrangement: $Au_6@Au_{35}@Ag_{30}Au_{18}@Au_{21}$ with all chlorines are coordinated to Ag atoms.[49] More interestingly, they performed controlled experiments to illustrate the importance of chloride during the formation of bimetallic cluster (Figure 2.5b). In matrix-assisted laser desorption/ionization (MALDI) mass spectra, the pure cluster has a peak at 23.4 kDa. However, the preparation under similar reaction conditions without chloride source led to the formation of a much smaller cluster with mass peak around 9.3 kDa and no peak from the $Au_{80}Ag_{30}$ can be observed. With the reduction of precursors by $NaBH_4$ in the presence of NH_4Cl or AgCl, the targeted cluster peak can be detected and larger species at around 32 kDa were also generated. Thus, there results indicate that the chloride is essential in stabilizing larger clusters. Similarly, the reaction has also been achieved by replacing chloride with bromide and it suggested that the halide ions functioned more than counterions in the formation of large clusters.

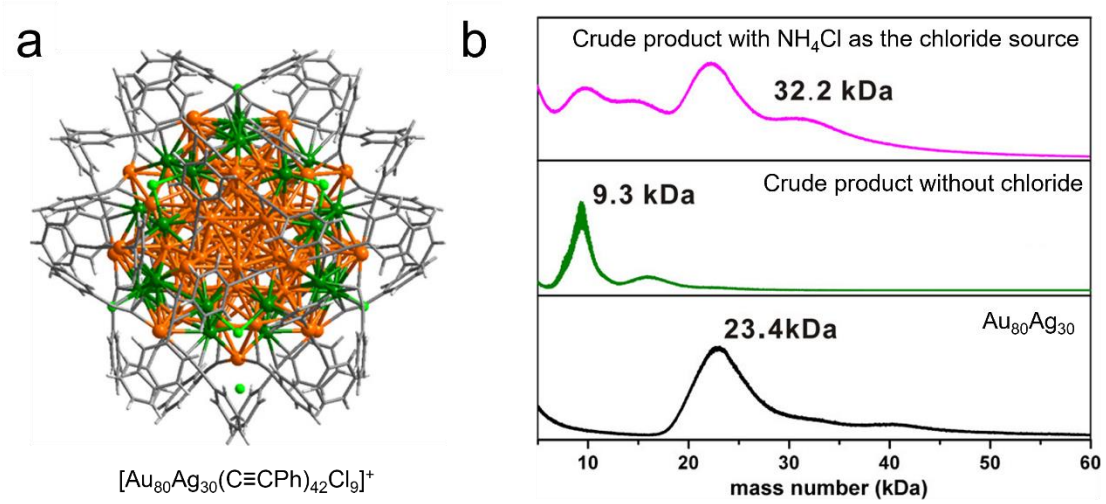

Figure 2.5 a) Crystal structure of $[Au_{80}Ag_{30}(C{\equiv}CPh)_{42}Cl_9]^+$ cluster. b) MALDI mass spectra in positive-ion mode of $Au_{80}Ag_{30}$ and the crude products of control experiments.[49]

To the best of our knowledge, there has been no research regarding the influence of the electronic structure of gold nanoclusters by halogens. Chloride is usually the *de facto* ligand in gold cluster syntheses, probably because of the easy availability of the $ClAuPPh_3$ starting material. There are no simple methods to synthesize bromide- or iodide-coordinated gold clusters. Furthermore, the intrinsic photophysical properties of the gold clusters and their influence by large organic ligands instead of halogens have been the focus.

In the current study we report a systematical study about the halogen effects on the Au13 nanocluster. We used both direct syntheses and halide exchanges to obtain three halogen-coordinated clusters, $[Au_{13}(dppe)_5X_2]X_3$ (X = Cl, Br, I) (abbreviated as $[Au_{13}\text{-}X_2]$ hereafter). Both methods are facile enough to obtain $[Au_{13}\text{-}Br_2]$ and $[Au_{13}\text{-}I_2]$; the latter is the first I-coordinated gold cluster. All three clusters have been fully characterized by electrospray ionization mass spectroscopy (ESI-MS) and NMR spectroscopy. Both experimental and theoretical results show that the $[Au_{13}\text{-}Br_2]$ and $[Au_{13}\text{-}I_2]$ clusters retain the same icosahedral Au_{13} kernel as the original $[Au_{13}\text{-}Cl_2]$ cluster. The photophysical properties of the $[Au_{13}\text{-}X_2]$ clusters are systematically studied by UV-vis absorption spectroscopy, PL and photoluminescent excitation spectroscopy (PLE). We have observed that both the first absorption peak and the emission peak show consistently red shift from X = Cl to I. However, we observed an unusual PLE spectrum for the I-ligated cluster. Theoretical calculations confirmed that the p-orbitals of the halogen ligands contribute to the HOMO $\rightarrow$ LUMO transition. Additional non-radiative transitions in the $[Au_{13}\text{-}I_2]$ cluster resulted in lower PL intensities. These findings provide further insights into the ligand-to-metal charge transfer process. Finally, the synthetic methods and the knowledge

about halogen-gold cluster interactions will be useful to guide future designs on halogen-ligated gold clusters.

2.2 The syntheses of [Au_{13}-X_2] (X = Cl, Br, I)

2.1.1 Chemicals and preparations

[1,2-Bis(diphenylphosphino)ethane]dichlorodigold(I) ($Au_2(dppe)Cl_2$, 96%), hydrochloric acid (HCl, 12 M), hydrobromic acid (HBr, 8.9 M), hydroiodic acid (HI, 7.57 M), Potassium thiocyanate (KSCN, 99%) and other chemicals were obtained from Sigma-Aldrich and were used as received unless further noted. All solvents were technical grade. All glasswares were washed with aqua regia and cleaned thoroughly before use.

2.1.2 Two synthetic methods of $[Au_{13}(dppe)_5X_2]X_3$

Direct synthesis of $[Au_{13}(dppe)_5X_2]X_3$: The method is based on a previous method with some modifications and can be divided into two following steps.[25] Step 1: $Au_2(dppe)Cl_2$ (30.2 mg, 0.035 mmol) was dissolved in 24 mL dichloromethane in a 50 mL flask, 1mL suspended $NaBH_4$ solution (33.2 mg fresh $NaBH_4$ in 5mL ethanol) was rapidly injected to the flask under 900 rpm stirring. The mixture quickly turned into dark red color upon injection and was stirred at room temperature for 3h. After that, the solvent was removed by rotary evaporator and the residue was re-suspended in dichloromethane and centrifuged to remove insoluble precipitates. The solute was then evaporated to dryness to give a dark-brown solid. Step 2: The dark-brown solid was dissolved in 5 mL ethanol to give deep red color solution. 0.1 mL 12 M HCl (or 0.14 mL 8.9 M HBr, or 0.16 mL 7.57 M HI) was added to the solution at the speed of 5 seconds per drop (The adding of concentrated acid must be performed very slowly with extra caution). The vial was then

shaded from light by aluminum foil covering, especially for [Au_{13}-I_2], and stirred at room temperature for 24 h. After that, the volatiles were evaporated and the residue was washed with acetone, dried again, suspended in ethanol and centrifuged to remove precipitates. Red (deep red for HBr and brown for HI) solids were obtained after evaporation and the total yield was nearly 30% based on the gold precursor. The solvent wash process could be repeated if the final product is not pure enough.

[Au_{13}-X_2] (X=Br, I) were also obtained through a ligand exchange method: By adding excess amounts (typically with a ratio of Br/Cl or I/Cl equal to three) of potassium bromide (KBr) (2.8 mg, 0.024 mmol) or potassium iodide (KI) (3.9 mg, 0.024 mmol) to 5 mL methanol solution of [Au_{13}-Cl_2] (20 mg, 0.004 mmol), the color immediately turned from red to deep red (Br) or brown (I), respectively. After the evaporation of the volatiles, products were purified by acetone and methanol as in the step 2 of the direct method. The yield was nearly 60% for both. [Au_{13}-I_2] could be produced by introducing KI to [Au_{13}-Br_2] similarly. The reverse reactions were not successful. Similar experiment using KF was also performed, Au_{13} clusters decomposed instead of forming [Au_{13}-F_2].

The syntheses of the three [Au_{13}-X_2] clusters were carried out at ambient conditions. The [Au_{13}-X_2] clusters could all be synthesized by an acid-assisted two-step method (Figure 2.6) according to a previously reported method with some modifications. Halide exchanges could also be used to obtain the Br- or I-ligated clusters (Figure 2.6). Briefly, a CH_2Cl_2 solution of $Au_2(dppe)Cl_2$ was reduced by $NaBH_4$. After purification, halogen acids were added and the corresponding [Au_{13}-X_2] clusters were obtained. It should be noted that light shading is essential for the successful synthesis of the I-coordinated cluster. The

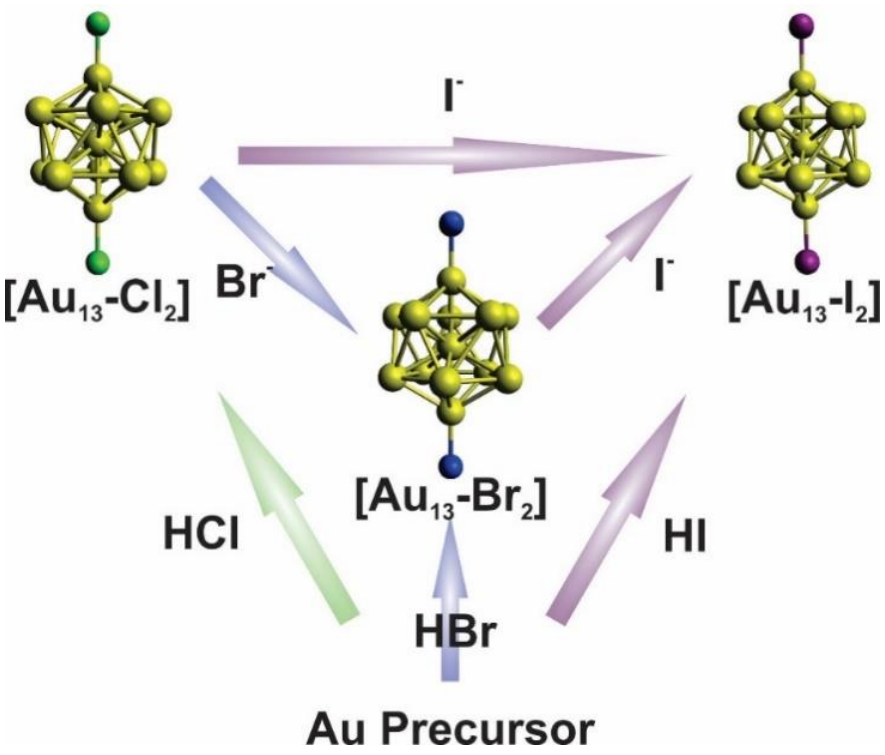

Figure 2.6 Schematic illustration of the direct synthesis (bottom up) and halide exchange (left to right) for [Au_{13}-X_2].

halide exchange method was also performed between clusters as shown in the top of Figure 2.6. By introducing stoichiometric amounts of KBr or KI salts into a methanol solution of [Au_{13}-Cl_2], exchange reactions rapidly happened with significant color change. We should point out that the reactions only occurred from Cl to Br to I, the reverse reactions were not observed. This result indicated that the Au-X bond strength increases from Cl to I, due to the increased Au-X covalency.[42,43]

2.1.3 Characterization

Nuclei magnetic resonance (NMR) spectra were recorded on a 400 MHz Bruker Ultrashield spectrometer using MeOD as solvent. Chemical shifts are reported in ppm and are referenced to tetramethylsilane (internal) for ^{1}H and 85% H_3PO_4 (external) for ^{31}P-

NMR. Unless further noted, all NMR spectra were measured at 298 K. The mass spectra were measured in the positive ionization mode. The methanol solution of AuNCs (≈0.5 mg mL^{-1}) was introduced into an Agilent 6530 Accurate Mass Q-TOF LC-MS system (with Agilent 1260 HPLC) via flow injection. The ESI mobile phase was made of acetonitrile/water (50/50) with ≈0.05% formic acid at a flow rate of 200 μL·min^{-1}. The gas temperature of the ESI source was 130 °C at a flow rate of 8 L·min^{-1}. The fragmentor voltage was set at 50 V, skimmer at 65 V, and the capillary voltage (Vcap) at 3500 V. The mass range measured was up to 20,000 for MS. The assignments were based on high

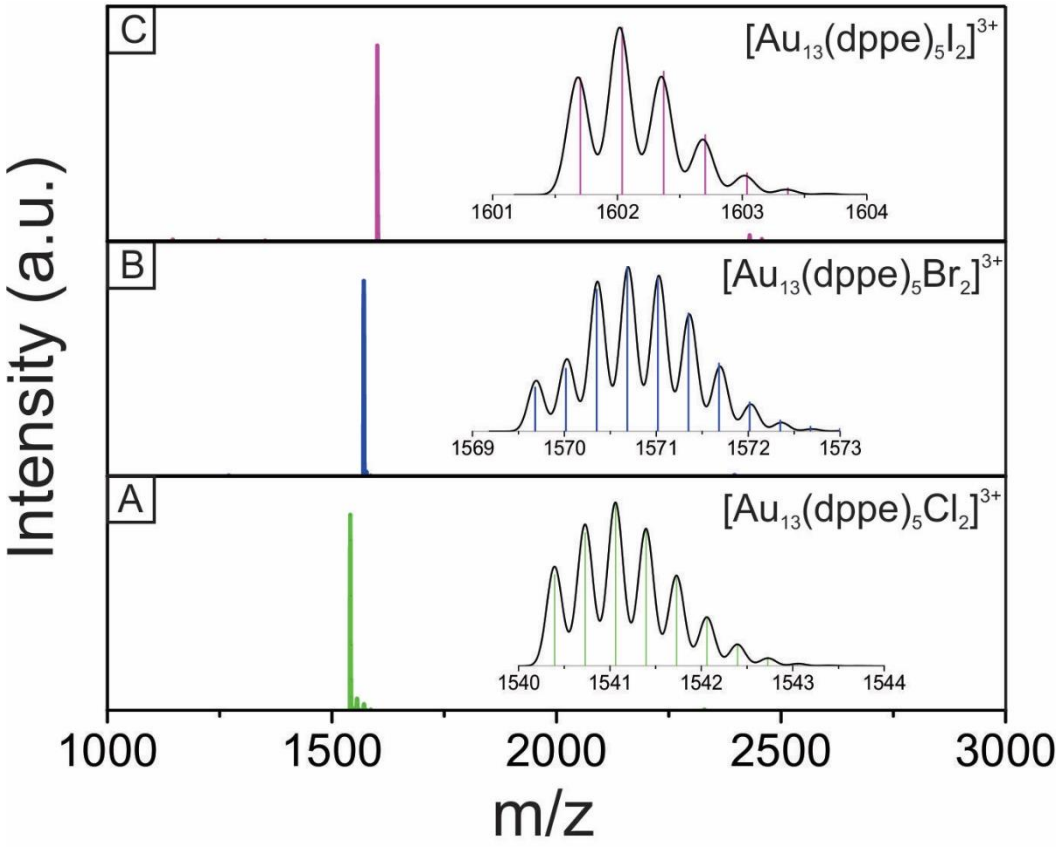

Figure 2.7 Positive-mode ESI mass spectra of the triply charged $[Au_{13}\text{-}X_2]^{3+}$ cluster ions. A) $[Au_{13}\text{-}Cl_2]$, B) $[Au_{13}\text{-}Br_2]$, C) $[Au_{13}\text{-}I_2]$. The inset in panel shows the simulated isotopic distribution pattern (black curve) for each cluster.

resolution m/z values and isotopic distributions. UV-Vis-NIR spectra were measured in methanol solution of [Au_{13}-X_2] on an Agilent Technologies Cary 5000 UV-Vis Spectrophotometer. The solution PL and QY measurements were performed on an Edinburgh Instruments Fluorescence Spectrometer FS5. [Au_{13}-X_2] were dissolved in methanol for measurements. The PL QYs were measured by FS5 Spectrometer with a built-in integrating sphere.

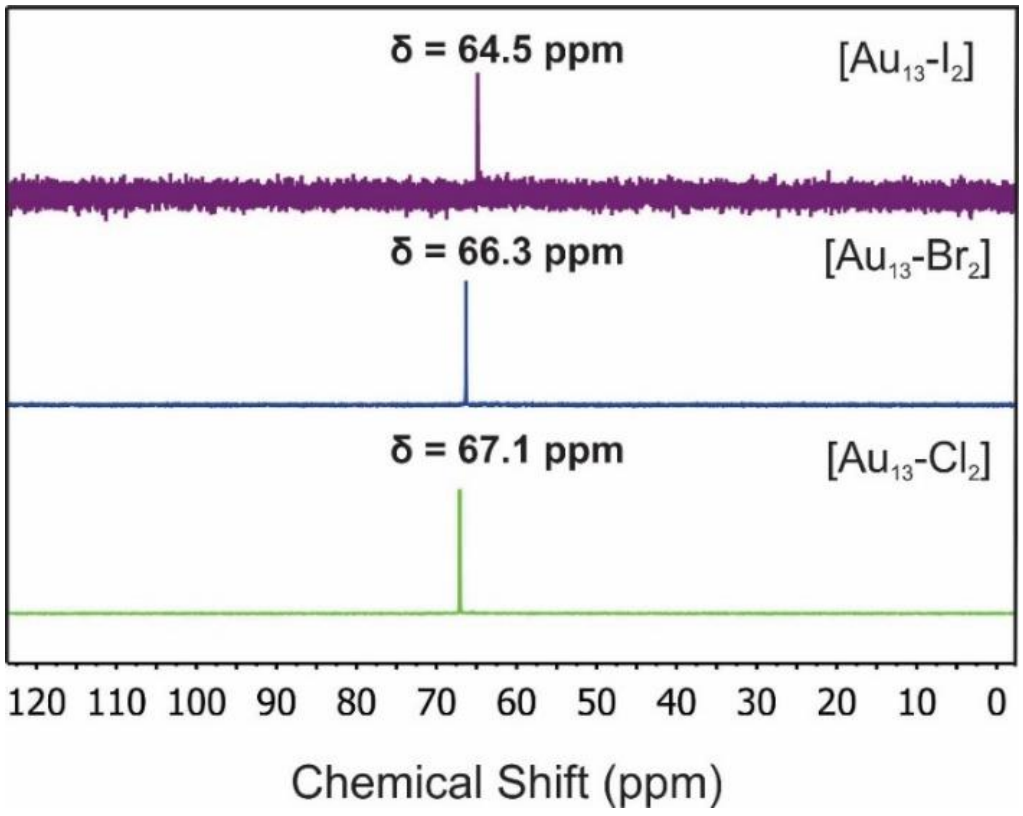

Figure 2.8 ^{31}P-NMR spectra of the [Au_{13}-X_2] clusters.

We used electrospray mass spectrometry and NMR spectroscopy to verify the composition and purity of the [Au_{13}-X_2] clusters after the purification process. The positive-ion ESI mass spectra of all three species exhibited a single peak in the mass-charge ratio range from 0 to 8000 (Figure 2.7). Comparison with the simulated isotopic

distributions (insets in Figure 2.7) confirmed the triply charged $[Au_{13}(dppe)_5X_2]^{3+}$ cation in each case. Therefore, with the same charge state, gold nuclearity and diphosphine

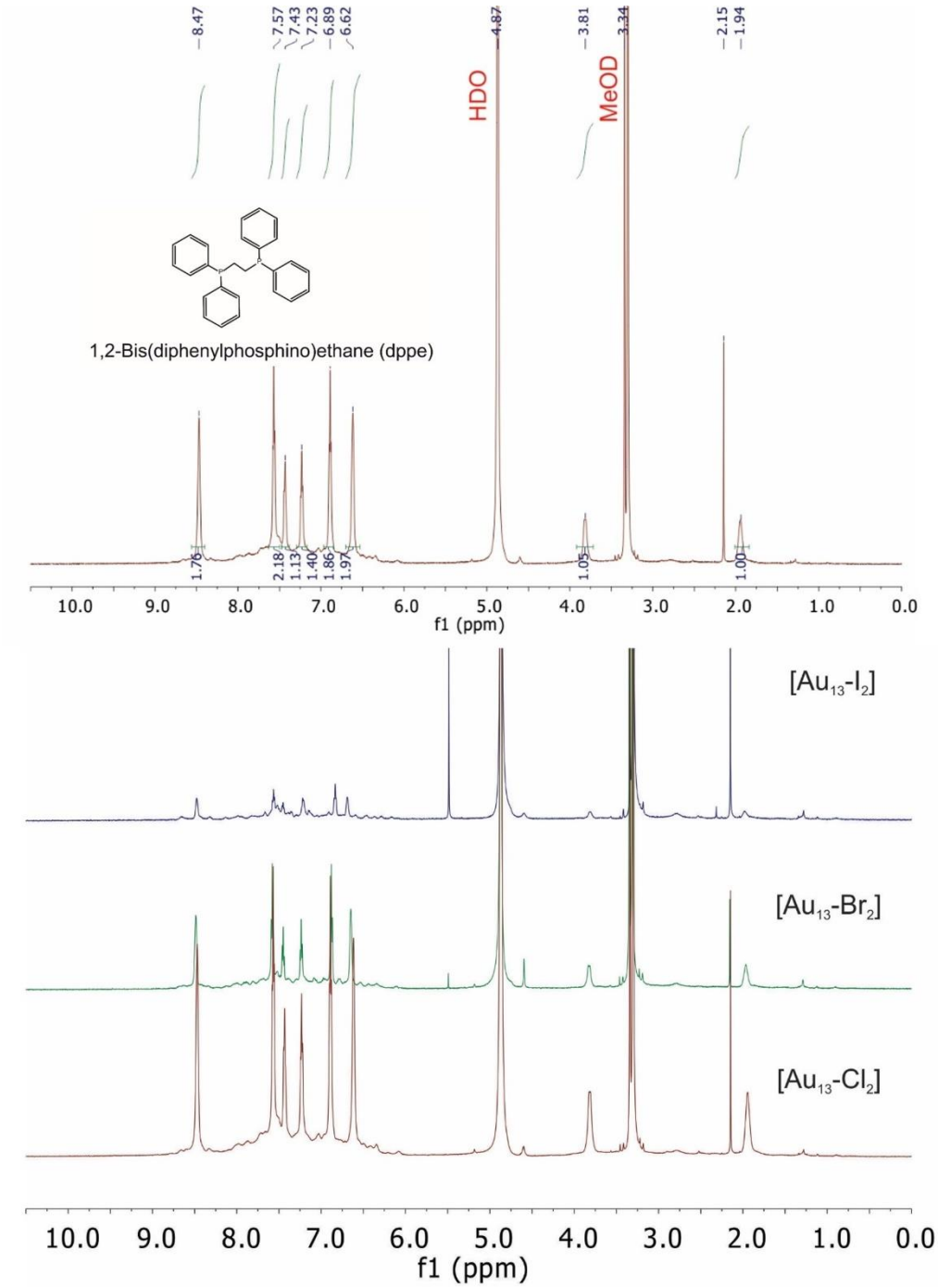

Figure 2.9 ^{1}H-NMR spectrum of $[Au_{13}\text{-}Cl_2]$ (top) and compiled ^{1}H-NMR spectra of the three clusters (bottom) (MeOD, 400MHz).

ligands, these three species showed good composition consistency in the mass spectroscopy.

The ^{31}P-NMR spectra of all three clusters are shown in Figure 2.8. The existence of a single peak in the spectra at around 67 ppm indicated the similar chemical environments of all phosphorus atoms in the three clusters. The heavier halogen atoms shifted the peak towards upfield. Both the ESI mass spectra and the ^{31}P-NMR data showed that the three [Au_{13}-X_2] clusters we obtained were pure enough for further spectroscopy analyses. Furthermore, we also measured the ^{1}H-NMR spectra for all the clusters to evaluate the proton environments on the cluster samples. The ^{1}H-NMR result for the [Au_{13}-Cl_2] (Figure 2.9 top) showed two sets of peaks in aromatic region (6.5~8.5 ppm) and alkyl region (1.5~4 ppm). The ratio of peak areas can be calculated as $H_{aromatic}/H_{alkyl}$ with a experimental result of 5/1 in good agreement with that in dppe ligand. Also, by compiling the spectra for the three clusters as in Figure 2.9 bottom suggest the structural similarity. Overall, the ^{31}P- and ^{1}H-NMR data confirmed the highly symmetric structures and identical ligand configurations in all three [Au_{13}-X_2] clusters.

With the pure samples of three clusters, we can move forward to measuring the photophysical properties to evaluate the halogen effects on these features. We obtained the absorption and PL emission spectra for the [Au_{13}-X_2] clusters. As is shown in Figure 2.10a, the absorption features for the three clusters at around 310 nm, 365 nm and shoulder peak at around 490 nm indicate the electronic structures are similar. Both the absorption and emission spectra for [Au_{13}-Cl_2] are consistent with those reported previously by Konish et al.[25] The UV-Vis and PL results again confirm that the as-synthesized [Au_{13}-Br_2] and [Au_{13}-I_2] clusters possess the same structure as [Au_{13}-Cl_2], which was known to adopt an

icosahedral Au_{13} core with the two chlorine atoms coordinated to the two polar gold atoms and the five bidentate dppe ligand coordinated to the ten equatorial gold atoms.

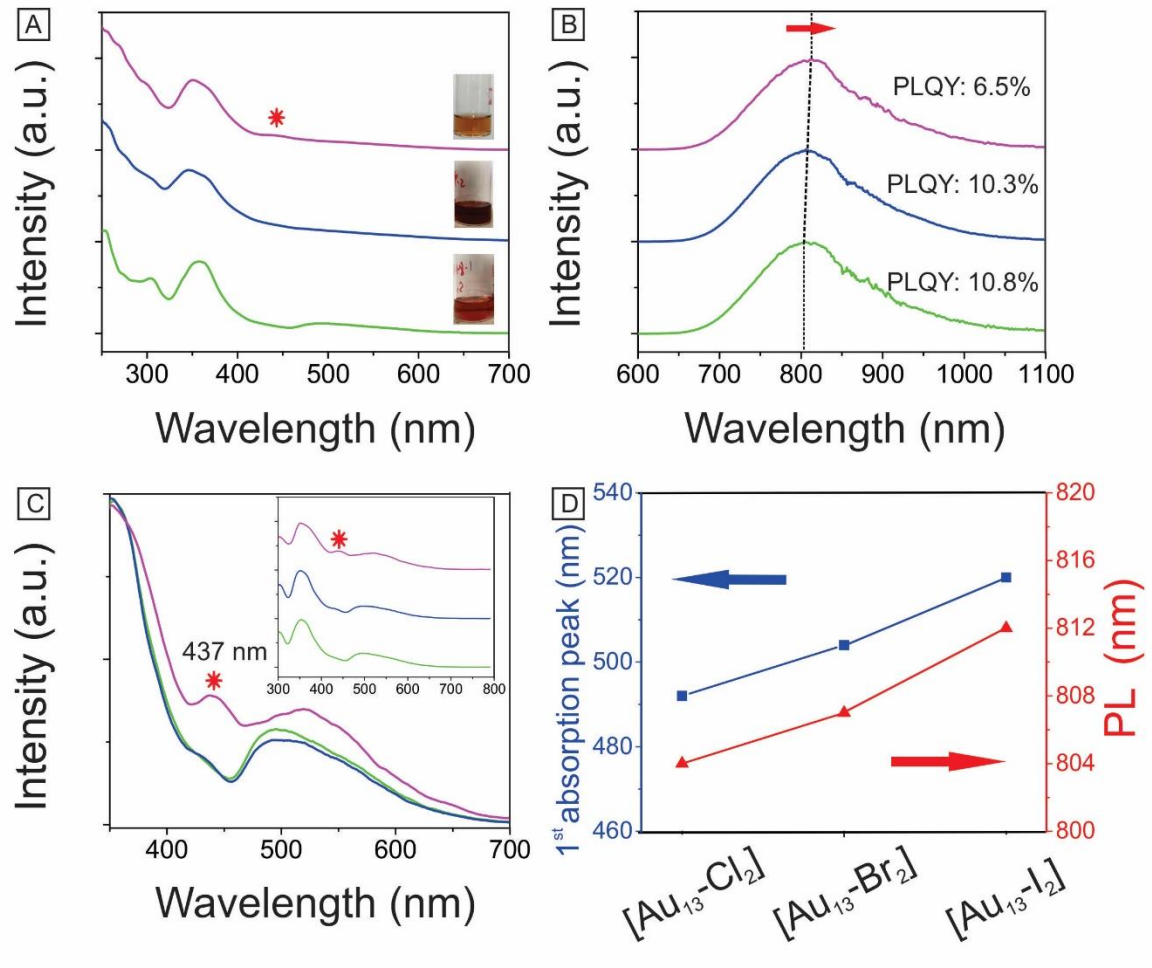

Figure 2.10 Photophysical properties of $[Au_{13}\text{-}X_2]$ in CH_3OH: (A) Absorption spectra. Inset: pictures of cluster solutions. Red star: absorption feature at 437 nm. (B) PL spectra and absolute PL QYs. (C) PLE spectra ($\lambda = 800$ nm). Red star: the second excitation feature at 437 nm. (D) Evolutions of the first absorption peak and PL position for the three clusters. For A, B and C, $[Au_{13}\text{-}Cl_2]$ (bottom), $[Au_{13}\text{-}Br_2]$ (middle), $[Au_{13}\text{-}I_2]$ (top).

2.3 Photophysical properties of the $[Au_{13}\text{-}X_2]$ clusters

There are subtle differences in the UV-vis absorption and emission spectra of the three clusters due to the halogen effects (Figure 2.10). Although the colors of three cluster solutions changed from red ($[Au_{13}\text{-}Cl_2]$) to dark red ($[Au_{13}\text{-}Br_2]$) to brown ($[Au_{13}\text{-}I_2]$) (inset in Figure 2.10a), their absorption features are similar. The corresponding PL peaks showed a slight red shift from 804 nm to 814 nm and the absolute PLQYs dropped from 10.8% to 6.5% (Figure 2.10b). The PL intensities are stronger than those reported previously for gold clusters.[6,16-19]

We further employed PLE spectroscopy to obtain higher signal-to-noise ratio on the band features of the $[Au_{13}\text{-}X_2]$ clusters, as shown in Figure 2.10c. We focused on the PL excitations that result in the PL peaks around 800 nm. The PLE spectra resembled the absorption spectra, but provided much clearer details in the electronic transitions responsible for the PL. The PLE spectra of $[Au_{13}\text{-}Cl_2]$ and $[Au_{13}\text{-}Br_2]$ are similar, but that of $[Au_{13}\text{-}I_2]$ seems quite different. The first absorption peaks of the clusters were red-shifted from 491 nm for $[Au_{13}\text{-}Cl_2]$ to 520 nm for $[Au_{13}\text{-}I_2]$. The red shifts in the PLE and PL spectra are due to a decrease in the bandgaps of the clusters. It should be pointed out that these changes in optical properties are more pronounced compared with the influence of the phosphine ligand structures on the Au_{13} clusters reported by Konishi et al.[3,24] Their experiments on different phosphine ligands showed no significant changes on the UV-vis and PL spectra, which led to the conclusion that the optical properties of the gold clusters were mainly influenced by the cluster nuclearity, not so much by the coordinated ligands. The current study illustrated that the coordinated halogens did have strong influence on the photophysical properties, probably due to the strong Au-halogen electronic interactions. The UV-Vis absorption spectra were also measured at lower temperature, as is shown in

Figure 2.11. Despite the peaks at 195 K become a little narrower, no more new features could be observed and the peak positions as well as relative peak intensities for all the main features remain the same.

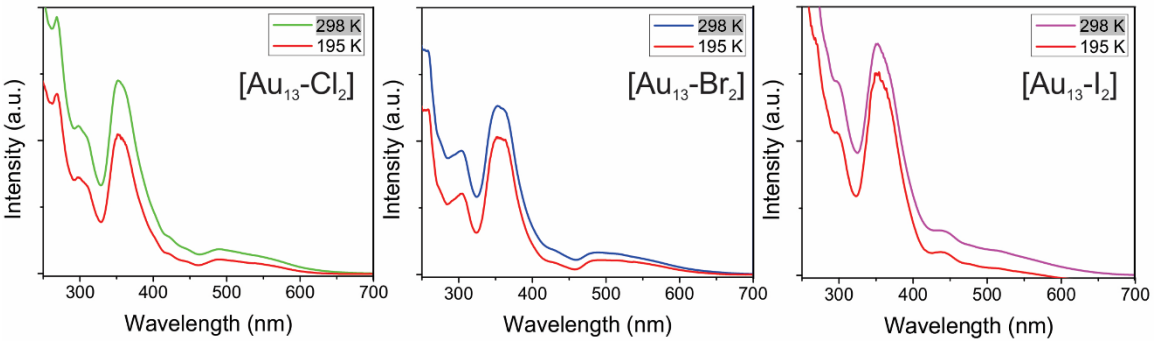

Figure 2.11 Temperature-dependent UV-Vis spectra of [Au_{13}-X_2] at 298 K and 195 K. From left to right: [Au_{13}-Cl_2], [Au_{13}-Br_2], [Au_{13}-I_2].

It is interesting to note that the red shifts of the PLE and PL features (Figure 2.10d) by tuning the halogens are in agreement with those observed in halide perovskites.[50] In addition to the red shift, we noticed the appearance of an absorption band at 437 nm for

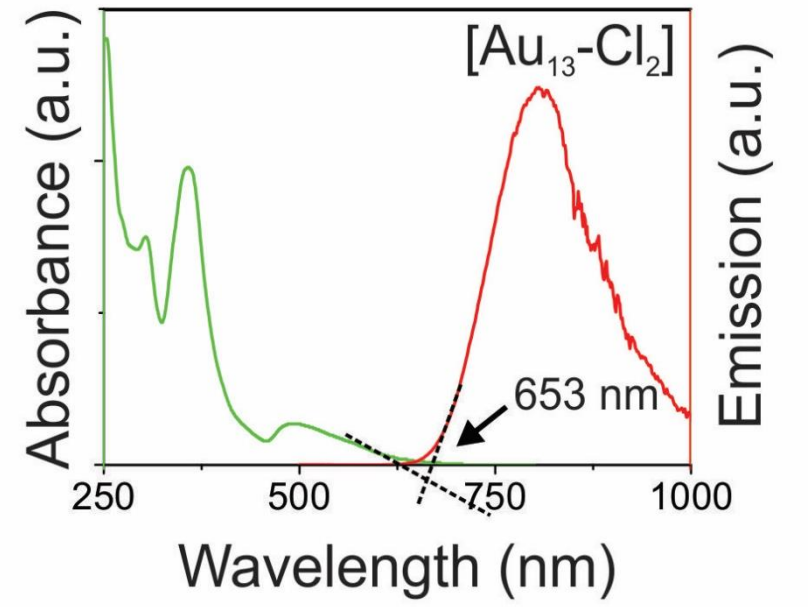

Figure 2.12 Tauc plot for [Au_{13}-Cl_2] cluster.

[Au_{13}-I_2] in the UV-vis absorption spectrum, as marked by * in Figure 2.10a. This feature is much more pronounced in the PLE spectra. A similar second absorption feature also seemed to exist in the [Au_{13}-Cl_2] and [Au_{13}-Br_2] PLE spectra, albeit with much lower relative intensities.

With the absorption and PL spectra, we can also use Tauc plot to determine the optical energy gaps for the clusters. Take the [Au_{13}-Cl_2] cluster as an example, by plotting the UV-Vis absorption and PL spectra together, the HOMO-LUMO gap could be determined at the intersection of absorption and emission spectra which is around 1.90 eV (653 nm) (Figure 2.12). Similarly, the HOMO-LUMO gaps could be measured for [Au_{13}-Br_2]: 1.85 eV and [Au_{13}-I_2]: 1.79 eV. Therefore, from Cl to I, the HOMO-LUMO gap becomes smaller.

2.4 The optimized structures of the [Au_{13}-X_2] clusters

2.4.1 Computational methods

The structures of [Au_{13}-X_2] (X = Cl, Br, I) were optimized based on the crystal structure reported previously using the B3PW91 hybrid density functional. The 6-31G(d) basis set was employed for C, H, P, and LANL2DZ basis set was employed for Au. The harmonic vibrational frequencies were also calculated to confirm that the optimized structures are global minima with no imaginary frequencies. Time-dependent DFT (TD-DFT) calculations were conducted to get the simulated UV-vis absorption spectra. All calculations were carried out using the Gaussian 09 package.[52]

2.4.2 Theoretical results

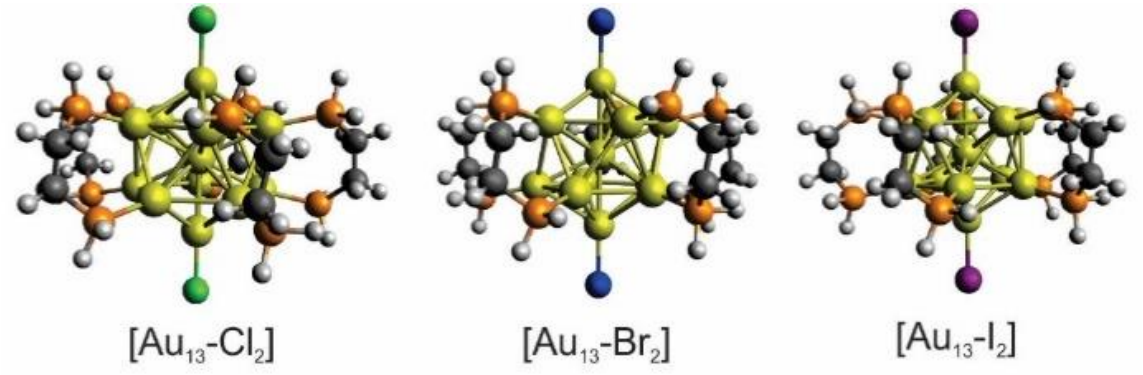

Figure 2.13 Optimized structures of [Au_{13}-X_2].

To obtain further insights into the electronic and optical properties of the different halogen Au_{13} clusters, we performed DFT calculations. The $[Au_{13}(PH_2CH_2CH_2PH_2)_5X_2]^{3+}$ clusters were modeled by replacing the phenyl rings with hydrogen atoms to simplify the calculations. All structures were fully optimized as shown in Figure 2.13. The Au-X bond length increased from 2.335 Å for Cl to 2.629 Å for I (Table 1), consistent with the previously reported Au-X bond lengths for halide-Au(I) complexes.[42,34] The average Au-Au distances were nearly identical for the three clusters as summarized in Table 1 and Table S1, indicating the stability of the Au_{13} core. The two halogens on the polar sites of the icosahedron also align perfectly with the five-fold axis.

Table 2.1 Structure properties of the simulated [Au_{13}-X_2] clusters.

[Au_{13}-X_2]	Au-X (Å)	Central Au-Au-X angle (°)	Central Au-Au (Å)	Average Au-Au (Å)
Cl	2.335	180.0	2.841	2.948
Br	2.435	180.0	2.842	2.949
I	2.629	179.1	2.843	2.949

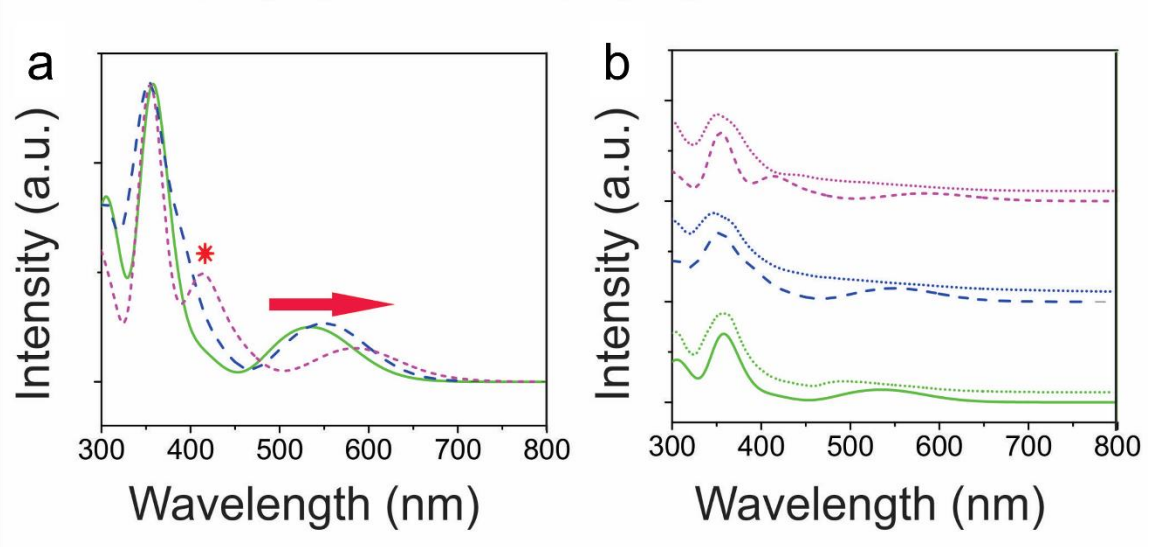

Figure 2.14 Calculated optical absorption spectra for [Au_{13}-X_2]. (C) Comparison of the experimental (dash line) and theoretical absorption spectra (solid line). [Au_{13}-Cl_2] (bottom, green), [Au_{13}-Br_2] (middle, blue [Au_{13}-I_2] (top, purple).

We conducted TD-DFT analyses to compare with the absorption spectra. As shown in Figure 2.14, the theoretical absorption spectra were in good agreement with the experimental data. The theoretical first absorption peak also indicates a red shift from Cl to I ligated Au_{13} clusters. The most obvious absorption features were also well reproduced at very similar position for all three clusters. In particular for the [Au_{13}-I_2] cluster, the calculations revealed three bands located at 370 nm, 413 nm, 600 nm were in excellent agreement with the three bands in both the absorption and PLE spectra (Figure 2.15). The lowest energy optical transition should come from the HOMO→LUMO transition. The experimental optical gaps were determined (see Figure 2.12) to decrease from 1.9 eV for Cl to 1.85 eV for Br to 1.79 eV for I. The experimental energy gaps are reproduced well from the theoretical HOMO-LUMO gaps which are similarly generated from the Tauc plot of the theoretical absorption spectra, as compared in Table 2.1 The 1.9 eV gap for [Au_{13}-

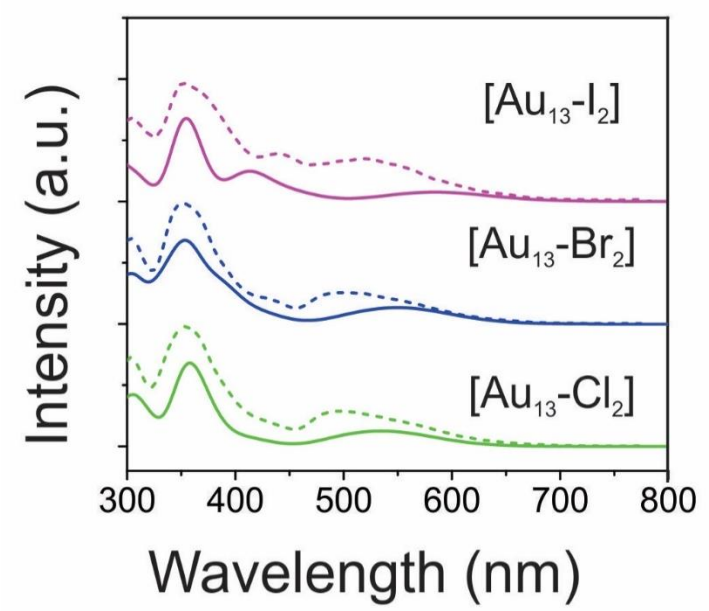

Figure 2.15 Comparison of theoretical absorption spectra (solid lines) and experimental PLE spectra (dotted lines).

Cl_2] has been confirmed by the result from Zhang et al.[51] The large energy gaps reflect the expected electronic stability of the Au_{13} core.

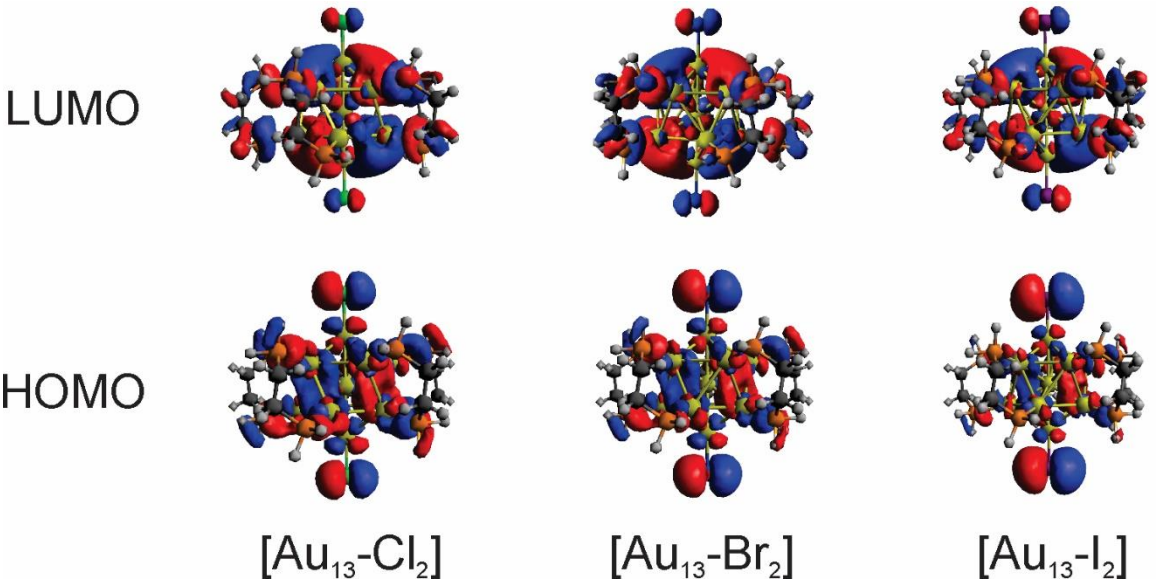

Figure 2.16 Pictures of the HOMO and LUMO orbitals for the [Au_{13}-X_2] clusters.

To understand the electronic interactions between the ligands and Au_{13} core, we show the pictures of the HOMOs and LUMOs for the three clusters in Figure 2.16. Although there are two types of ligands (halogen ligands and diphenylphosphines) on the cluster surface, the HOMOs for the three clusters are mainly derived from the p orbitals of the halogens, while the LUMOs are mainly delocalized orbitals on the Au_{13} cores. The phosphines don't participate in any HOMO or LUMO orbitals. The frontier orbitals explain why the halogens have significant influences on the electronic and optical properties of the [Au_{13}-X_2] clusters, whereas the diphosphine ligands have minimal effects. The negligible influence of phosphine ligand on absorption spectra agrees well with what was observed in the absorption spectra for Au_{13} clusters protected with different diphosphine ligands by Konish et al.[24]

Table 2.2 Geometrical parameters of the ground-state structures of [Au_{13}-X_2] and comparison of DFT-predicted HOMO-LUMO gap with the observed optical gap.

[Au_{13}-X_2]	Au-X (Å)	Average Au-Au (Å)	Optical gap (eV)	Calculated gap (eV)
Cl	2.335	2.948	1.90	1.94
Br	2.435	2.949	1.85	1.89
I	2.629	2.949	1.79	1.80

Therefore, the HOMO→LUMO transitions in the [Au_{13}-X_2] clusters correspond to ligand-to-metal charge transfers (LMCT). The LMCT process was studied by Jin and co-workers on thiolate-ligated $Au_{25}(SR)_{18}$ clusters.[6] They found that by strengthening the

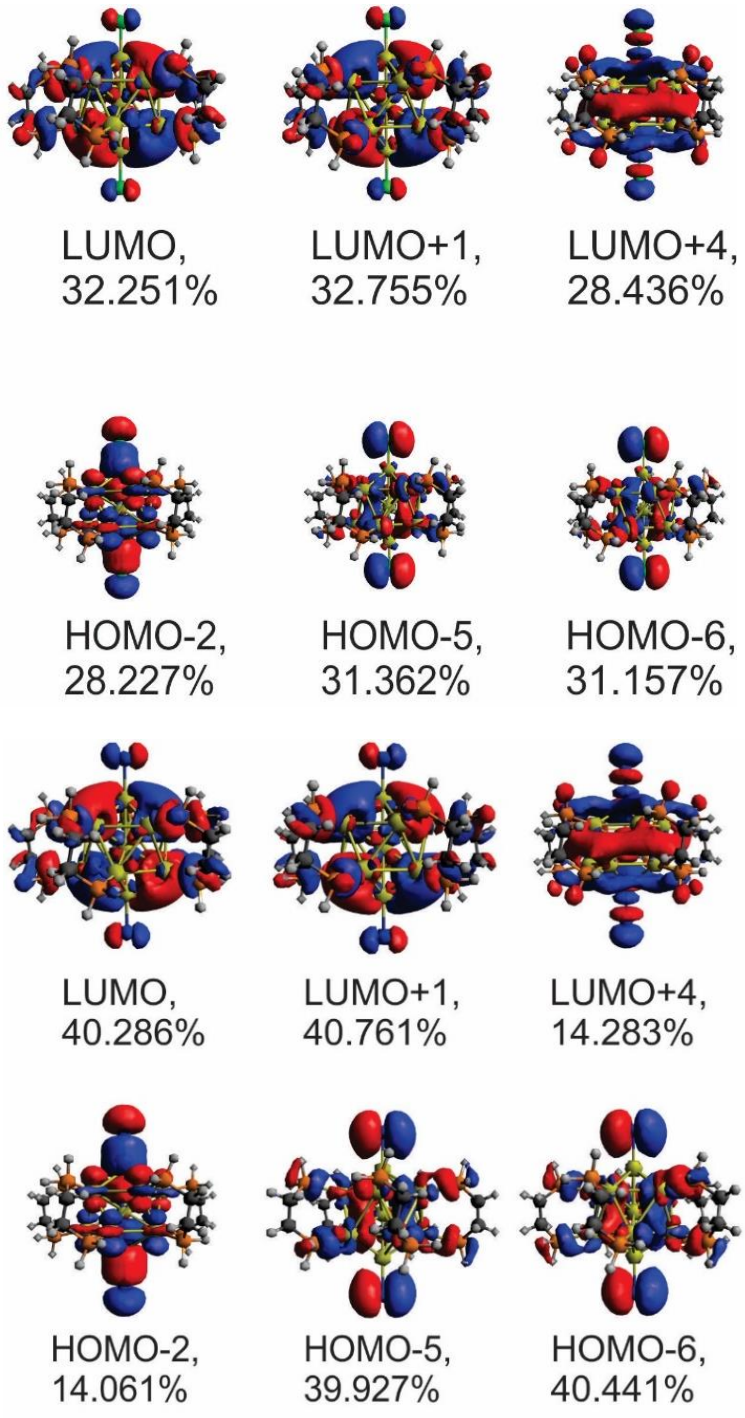

Figure 2.17 Compositions of the second absorption peak for [Au_{13}-Cl_2] with contribution larger than 5%.(top) Compositions of the second absorption peak for [Au_{13}-Br_2] with contribution larger than 5%.(bottom)

electron donation capability of the capped ligands, the PL intensity or the degree of LMCT on gold cluster was enhanced. However, from chlorine to iodine, the stronger electron donation capability from the halogen ligands seemed to result in lower PL intensities. The theoretical calculations provided some hints about the lower PL intensity in the [Au_{13}-I_2] cluster. The higher intensity on the second main absorption peak for the [Au_{13}-I_2] cluster indicated a stronger electronic excitation at this wavelength.

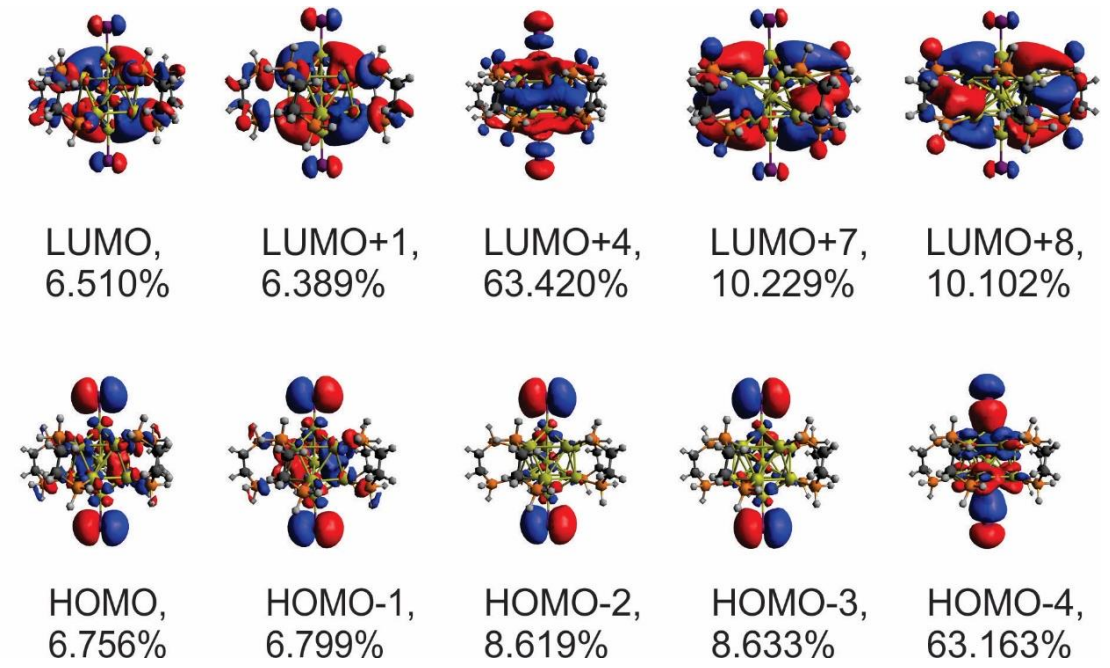

Figure 2.18 Compositions of the second absorption peak for [Au_{13}-I_2] with contribution larger than 5%.

To obtain the components in the second main absorption peak, we considered the orbital transitions related to the 413 nm peak in the calculated absorption spectra. As shown in Figure 2.17-2.18, all these peaks contained multiple HOMOs and LUMOs. Three similar sets of HOMOs and LUMOs accounted for the second main absorption feature in both the [Au_{13}-Cl_2] and [Au_{13}-Br_2] clusters, consistent with the similar PLE and absorption spectra

for these two clusters. For the [Au_{13}-I_2] cluster, five sets of HOMOs and LUMOs were found to be involved in the second absorption peak. However, not all these transitions might have ended up in radiative recombination, which caused the lower PL intensity in the I-coordinated clusters.

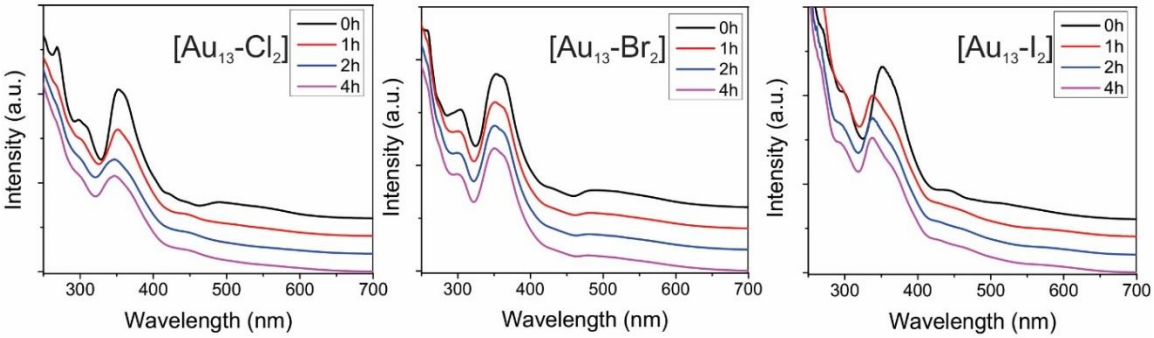

Figure 2.19 Thermal stability of [Au_{13}-X_2] at 50 ^{o}C. From left to right: [Au_{13}-Cl_2], [Au_{13}-Br_2], [Au_{13}-I_2].

We also measured the thermal stability of these clusters in the solution as shown in Figure 2.19. The [Au_{13}-I_2] cluster was observed to have the poorest stability upon heating to 50 ^{o}C. The strongest absorption peak at 370 nm blue shifted to 345 nm after one hour and the second absorption peak gradually became smooth. The [Au_{13}-Cl_2] cluster was more stable: the strongest absorption peak remains after 1h and gradually shifted to 351 nm after 4h. And the [Au_{13}-Br_2] cluster was the more stable among these three without any noticeable change in absorption spectra even after heating for four hours. Therefore, the result indicates that the thermal stability doesn't correlate with the binding energy of Au NCs and halogens.

2.5 Extended experiments with [Au_{13}-X_2] clusters

We also tried the reaction with pseudohalide anion by reacting [Au_{13}-Cl_2] cluster with KSCN in ethanol solution. As is shown in Figure 2.20, the adding of excess amounts of KSCN into [Au_{13}-Cl_2] solution leads to the color change from red to brown. The ESI-MS spectrum of the crude product indicates the formation of the [Au_{13}-$(SCN)_4$] cluster with peak positions at 2164 m/z for 2+ cation and 4386 m/z for 1+ charge state. And the experimental isotope distribution patterns match well with the simulated results. At the same time, the original [Au_{13}-Cl_2] cluster peak at 1543 m/z disappeared completely with a dominant peak at 993 m/z that can be assigned to $[Au(dppe)_2]^+$ compound. Therefore, the

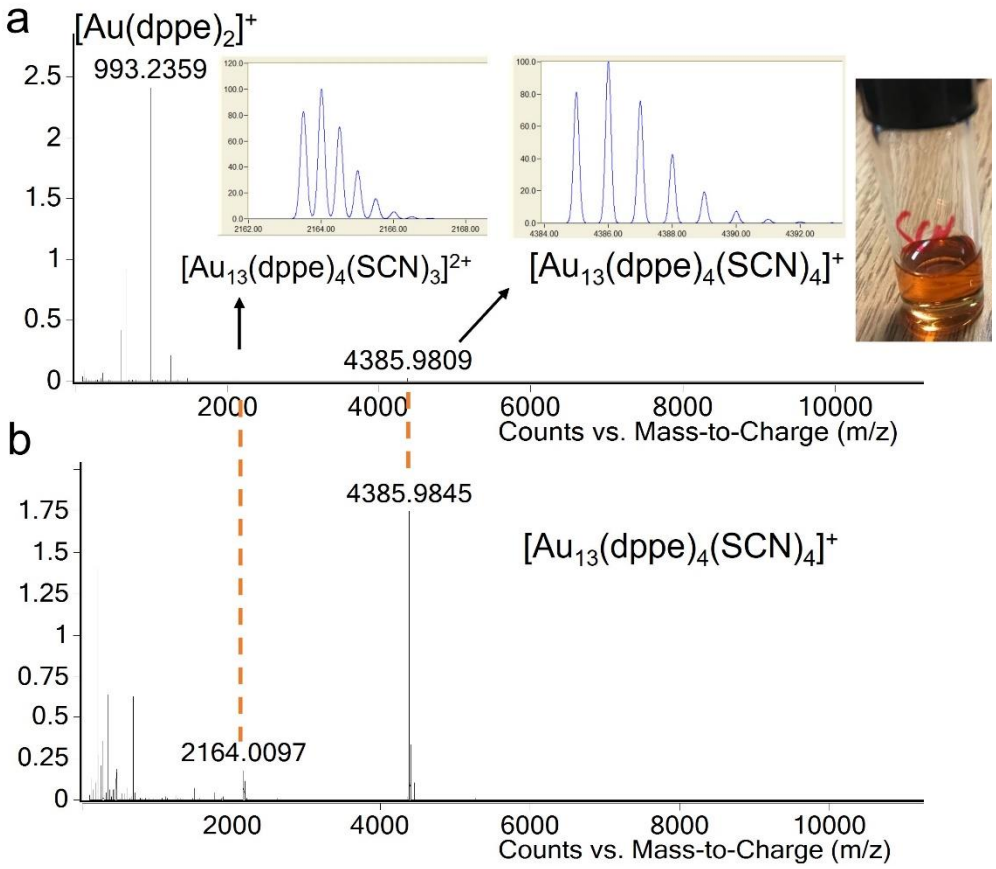

Figure 2.20 a) ESI-MS spectrum of crude products after the ligand exchange with [Au_{13}-Cl_2] clusters. Inserts: isotope patterns of simulated results. b) After purification.

addition of KSCN into [Au_{13}-Cl_2] cluster solution can induce ligand exchange as well as cluster decomposition. Even though the yield is very low for the [Au_{13}-$(SCN)_4$] cluster, similar solvent extraction methods (as described in the experimental part) can be performed to purify the cluster sample from the initial crude product. The purified sample shows a very strong cluster peak at 4386 m/z and the valence electron of the cluster can be counted as 13-4-1=8 (+ charge state) or 13-3-2=8 (2+ charge state) which is the same as other halogen-ligated Au_{13} clusters. We also measured the absorption and PL spectra of this cluster, as shown in Figure. 2.21. The cluster sample shows similar absorption features as the other Au_{13} clusters, and more features could be resolved in the PLE spectrum which indicate more electronic transitions exist for this cluster. The PL spectrum has a peak that centered at 814 nm which is between the emission peaks of [Au_{13}-Br_2] and [Au_{13}-I_2] clusters.

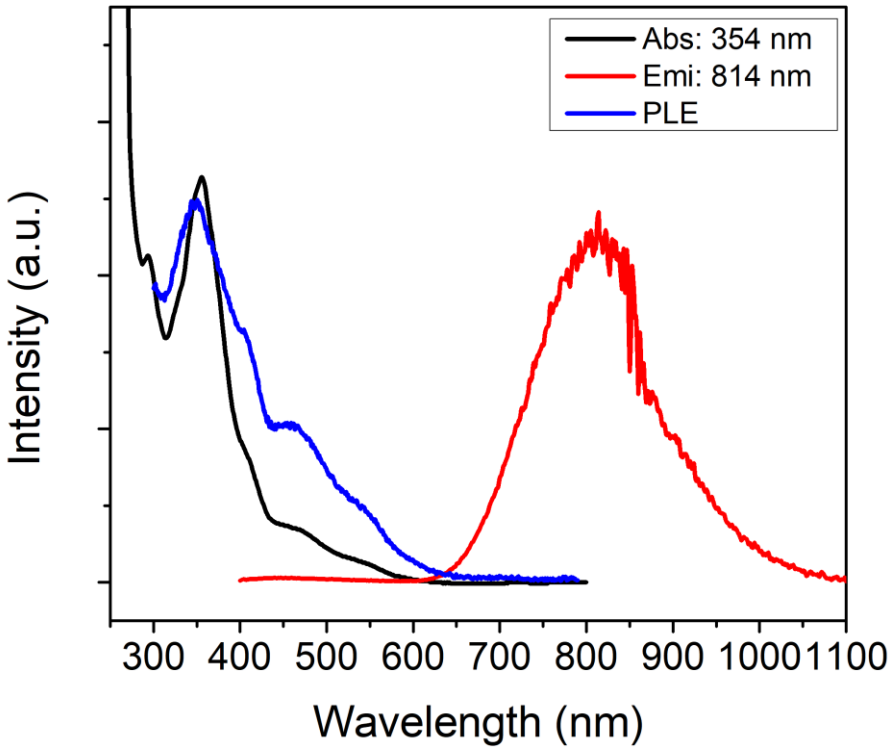

Figure 2.21 Absorption, PL and PLE spectra of the [Au_{13}-$(SCN)_4$] cluster.

2.5 Summary

In summary, we have synthesized three halogen-ligated Au_{13} clusters [Au_{13}-X_2] (X = Cl, Br, I) and investigated the effects of the halogen ligands on the electronic structures and photophysical properties of the clusters. The icosahedral Au_{13} core structure is preserved during the ligand exchange reactions from Cl to Br to I. The HOMO-LUMO gaps of the clusters are slightly decreased, as well as the PL intensities along the same direction. Theoretical studies indicated that these clusters all have similar electronic structures. The HOMOs of the clusters are mainly of halogen p characters and the LUMOs are mainly on the Au_{13} core. The different absorption features in the I-coordinated cluster are understood based on the electronic structure calculations. We have found that different halogens have some subtle effects on the electronic structures and photophysical properties of the clusters due to the different Au-X interactions.

References

(1) Daniel, M. C.; Astruc, D. Gold nanoparticles: assembly, supramolecular chemistry, quantum-size-related properties, and applications toward biology, catalysis, and nanotechnology. *Chem. Rev*. **2004**, *104* (1), 293-346.

(2) Jin, R.; Zeng, C.; Zhou, M.; Chen, Y. Atomically precise colloidal metal nanoclusters and nanoparticles: fundamentals and opportunities. *Chem. Rev.* **2016**, *116* (18), 10346-10413.

(3) Shichibu, Y.; Kamei, Y.; Konishi, K. Unique [core+ two] structure and optical property of a dodeca-ligated undecagold cluster: critical contribution of the exo gold atoms to the electronic structure. *Chem. Commun*. **2012**, *48* (61), 7559-7561.

(4) Qu, X.; Li, Y.; Li, L.; Wang, Y.; Liang, J.; Liang, J. Fluorescent gold nanoclusters: synthesis and recent biological application. *J. Nanomater.* **2015**, 2015.

(5) Pyo, K.; Thanthirige, V. D.; Kwak, K.; Pandurangan, P.; Ramakrishna, G.; Lee, D. Ultrabright luminescence from gold nanoclusters: rigidifying the Au (I)–thiolate shell. *J. Am. Chem. Soc.* **2015**, *137* (25), 8244-8250.

(6) Wu, Z.; Jin, R. On the ligand's role in the fluorescence of gold nanoclusters. *Nano Lett*. **2010**, *10* (7), 2568-2573.

(7) Yamazoe, S.; Koyasu, K.; Tsukuda, T. Nonscalable oxidation catalysis of gold clusters. *Acc. Chem. Res*. **2014**, *47* (3), 816-824.

(8) Zhang, Y.; Song, P.; Chen, T.; Liu, X.; Chen, T.; Wu, Z.; Wang, Y.; Xie, J.; Xu, W. Unique size-dependent nanocatalysis revealed at the single atomically precise gold cluster level. *Proc. Natl. Acad. Sci. U.S.A.* **2018**, *115* (42), 10588-10593.

(9) De Silva, N.; Ha, J. M.; Solovyov, A.; Nigra, M. M.; Ogino, I.; Yeh, S. W.; Durkin, K. A.; Katz, A. A bioinspired approach for controlling accessibility in calix [4] arene-bound metal cluster catalysts. *Nat. Chem.* **2010**, *2* (12), 1062.

(10) Valden, M.; Lai, X.; Goodman, D. W. Onset of catalytic activity of gold clusters on titania with the appearance of nonmetallic properties. *Science* **1998**, *281* (5383), 1647-1650.

(11) Giljohann, D. A.; Seferos, D. S.; Daniel, W. L.; Massich, M. D.; Patel, P. C.; Mirkin, C. A. Gold nanoparticles for biology and medicine. *Angew. Chem. Int. Ed*. **2010**, *49* (19), 3280-3294.

(12) Yougbare, S.; Chang, T.K.; Tan, S.H.; Kuo, J.C.; Hsu, P.H.; Su, C.Y.; Kuo, T.R. Antimicrobial Gold Nanoclusters: Recent Developments and Future Perspectives. *Int. J. Mol. Sci.* **2019**, *20* (12), 2924.

(13) Jadzinsky, P. D.; Calero, G.; Ackerson, C. J.; Bushnell, D. A.; Kornberg, R. D. Structure of a thiol monolayer-protected gold nanoparticle at 1.1 Å resolution. *Science* **2007**, *318* (5849), 430-433.

(14) Yan, N.; Xia, N.; Liao, L.; Zhu, M.; Jin, F.; Jin, R.; Wu, Z. Unraveling the long-pursued Au144 structure by x-ray crystallography. *Sci. Adv.* **2018**, *4* (10), eaat7259.

(15) Kang, X.; Zhu, M. Tailoring the photoluminescence of atomically precise nanoclusters. *Chem. Soc. Rev*. **2019**, *48* (8), 2422-2457.

(16) Sugiuchi, M.; Maeba, J.; Okubo, N.; Iwamura, M.; Nozaki, K.; Konishi, K. Aggregation-induced fluorescence-to-phosphorescence switching of molecular gold clusters. *J. Am. Chem. Soc.* **2017**, *139* (49), 17731-17734.

(17) Kamei, Y.; Shichibu, Y.; Konishi, K. Generation of Small Gold Clusters with Unique Geometries through Cluster-to-Cluster Transformations: Octanuclear Clusters with Edge-sharing Gold Tetrahedron Motifs. *Angew. Chem. Int. Ed.* **2011**, *50* (32), 7442-7445.

(18) Yao, L.Y.; Yam, V. W. W. Diphosphine-Stabilized Small Gold Nanoclusters: From Crystal Structure Determination to Ligation-Driven Symmetry Breaking and Anion Exchange Properties. *J. Am. Chem. Soc.* **2016**, *138* (48), 15736-15742.

(19) Tomihara, R.; Hirata, K.; Yamamoto, H.; Takano, S.; Koyasu, K.; Tsukuda, T. Collision-induced dissociation of undecagold clusters protected by mixed ligands $[Au_{11}(PPh_3)_8X_2]^+$ (X= Cl, C≡ CPh). *ACS omega* **2018**, *3* (6), 6237-6242.

(20) Narouz, M. R.; Osten, K. M.; Unsworth, P. J.; Man, R. W.; Salorinne, K.; Takano, S.; Tomihara, R.; Kaappa, S.; Malola, S.; Dinh, C.T. N-heterocyclic carbene-functionalized magic-number gold nanoclusters. *Nat. Chem.* **2019**, *11* (5), 419-425.

(21) Briant, C. E.; Theobald, B. R.; White, J. W.; Bell, L. K.; Mingos, D. M. P.; Welch, A. J. Synthesis and X-ray structural characterization of the centred icosahedral gold cluster compound $[Au_{13}(PMe_2Ph)_{10}Cl_2](PF_6)_3$; the realization of a theoretical prediction. *J. Chem. Soc., Chem. Commun*. **1981**, (5), 201-202.

(22) Zhang, S. S.; Feng, L.; Senanayake, R. D.; Aikens, C. M.; Wang, X.P.; Zhao, Q.Q.; Tung, C.H.; Sun, D. Diphosphine-protected ultrasmall gold nanoclusters: opened icosahedral Au_{13} and heart-shaped Au_8 clusters. *Chem. Sci.* **2018**, *9* (5), 1251-1258.

(23) Jin, S.; Wang, S.; Zhu, M. Insight into the Geometric and Electronic Structures of Gold/Silver Superatomic Clusters Based on Icosahedron M13 Units and Their Alloys. *Chem. Asian J.* **2019**, *14* (19), 3222-3231.

(24) Shichibu, Y.; Suzuki, K.; Konishi, K. Facile synthesis and optical properties of magic-number Au 13 clusters. *Nanoscale* **2012**, *4* (14), 4125-4129.

(25) Shichibu, Y.; Konishi, K. HCl-Induced Nuclearity Convergence in Diphosphine-Protected Ultrasmall Gold Clusters: A Novel Synthetic Route to “Magic-Number” Au13 Clusters. *Small* **2010**, *6* (11), 1216-1220.

(26) Zhang, S. S.; Senanayake, R. D.; Zhao, Q. Q.; Su, H. F.; Aikens, C. M.; Wang, X. P.; Tung, C.H.; Sun, D.; Zheng, L.S. $[Au_{18}(dppm)_6Cl_4]^{4+}$: a phosphine-protected gold nanocluster with rich charge states. *Dalton Trans.* **2019**, *48* (11), 3635-3640.

(27) Chen, J.; Zhang, Q. F.; Williard, P. G.; Wang, L. S. Synthesis and structure determination of a new Au_{20} nanocluster protected by tripodal tetraphosphine ligands. *Inorg. Chem.* **2014**, *53* (8), 3932-3934.

(28) Zhang, H. F.; Stender, M.; Zhang, R.; Wang, C.; Li, J.; Wang, L. S. Toward the solution synthesis of the tetrahedral Au20 cluster. *J. Phys. Chem. B.* **2004**, *108* (33), 12259-12263.

(29) Chen, J.; Zhang, Q. F.; Bonaccorso, T. A.; Williard, P. G.; Wang, L.S. Controlling gold nanoclusters by diphospine ligands. *J. Am. Chem. Soc.* **2014**, *136* (1), 92-95.

(30) Zhang, Q. F.; Williard, P. G.; Wang, L. S. Polymorphism of Phosphine-Protected Gold Nanoclusters: Synthesis and Characterization of a New 22-Gold-Atom Cluster. *Small* **2016**, *12* (18), 2518-2525.

(31) Guan, Z. J.; Hu, F.; Li, J. J.; Wen, Z. R.; Lin, Y. M.; Wang, Q. M. Isomerization in Alkynyl-Protected Gold Nanoclusters. *J. Am. Chem. Soc.* **2020**, *142* (6), 2995-3001.

(32) Das, A.; Li, T.; Nobusada, K.; Zeng, Q.; Rosi, N. L.; Jin, R. Total structure and optical properties of a phosphine/thiolate-protected Au_{24} nanocluster. *J. Am. Chem. Soc.* **2012**, *134* (50), 20286-20289.

(33) Li, J. J.; Guan, Z. J.; Lei, Z.; Hu, F.; Wang, Q. M. Same Magic Number but Different Arrangement: Alkynyl-Protected Au_{25} with D_3 Symmetry. *Angew. Chem.* **2019**, *131* (4), 1095-1099.

(34) Zhu, M.; Lanni, E.; Garg, N.; Bier, M. E.; Jin, R. Kinetically controlled, high-yield synthesis of Au_{25} clusters. *J. Am. Chem. Soc.* **2008**, *130* (4), 1138-1139.

(35) Kenzler, S.; Fetzer, F.; Schrenk, C.; Pollard, N.; Frojd, A. R.; Clayborne, A. Z.; Schnepf, A. Synthesis and Characterization of Three Multi-Shell Metalloid Gold Clusters $Au_{32}(R_3P)_{12}Cl_8$. *Angew. Chem. Int. Ed.* **2019**, *58* (18), 5902-5905.

(36) Jin, R.; Liu, C.; Zhao, S.; Das, A.; Xing, H.; Gayathri, C.; Xing, Y.; Rosi, N. L.; Gil, R. R.; Jin, R. Tri-icosahedral gold nanocluster $[Au_{37}(PPh_3)_{10}(SC_2H_4Ph)_{10}X_2]^+$: Linear assembly of icosahedral building blocks. *ACS Nano* **2015**, *9* (8), 8530-8536.

(37) Liao, L.; Zhuang, S.; Yao, C.; Yan, N.; Chen, J.; Wang, C.; Xia, N.; Liu, X.; Li, M.-B.; Li, L. Structure of chiral Au_{44}(2, 4-DMBT)$_{26}$ nanocluster with an 18-electron shell closure. *J. Am. Chem. Soc.* **2016**, *138* (33), 10425-10428.

(38) Zeng, C.; Chen, Y.; Liu, C.; Nobusada, K.; Rosi, N. L.; Jin, R. Gold tetrahedra coil up: Kekulé-like and double helical superstructures. *Sci. Adv.* **2015**, *1* (9), e1500425.

(39) Schmid, G. The relevance of shape and size of Au_{55} clusters. *Chem. Soc. Rev*. **2008**, *37* (9), 1909-1930.

(40) Narouz, M. R.; Takano, S.; Lummis, P. A.; Levchenko, T. I.; Nazemi, A.; Kaappa, S.; Malola, S.; Yousefalizadeh, G.; Calhoun, L. A.; Stamplecoskie, K. G. Robust, Highly Luminescent Au_{13} Superatoms Protected by N-Heterocyclic Carbenes. *J. Am. Chem. Soc.* **2019**, *141* (38), 14997-15002.

(41) Weerawardene, K. D. M.; Pandeya, P.; Zhou, M.; Chen, Y.; Jin, R.; Aikens, C. M. Luminescence and Electron Dynamics in Atomically Precise Nanoclusters with Eight Superatomic Electrons. *J. Am. Chem. Soc.* **2019**, *141* (47), 18715-18726.

(42) Xiong, X. G.; Wang, Y. L.; Xu, C. Q.; Qiu, Y. H.; Wang, L. S.; Li, J. On the gold–ligand covalency in linear $[AuX_2]^-$ complexes. *Dalton trans.* **2015**, *44* (12), 5535-5546.

(43) Liu, H. T.; Xiong, X. G.; Dau, P. D.; Wang, Y. L.; Li, J.; Wang, L. S. The mixed cyanide halide Au(i) complexes,$[XAuCN]^-$ (X= F, Cl, Br, and I): evolution from ionic to covalent bonding. *Chem. Sci.* **2011**, *2* (11), 2101-2108.

(44) Rai, A.; Singh, A.; Ahmad, A.; Sastry, M. Role of halide ions and temperature on the morphology of biologically synthesized gold nanotriangles. *Langmuir* **2006**, *22* (2), 736-741.

(45) Zhang, J.; Langille, M. R.; Personick, M. L.; Zhang, K.; Li, S.; Mirkin, C. A. Concave cubic gold nanocrystals with high-index facets. *J. Am. Chem. Soc.* **2010**, *132* (40), 14012-14014.

(46) Himstedt, R.; Hinrichs, D.; Sann, J.; Weller, A.; Steinhauser, G.; Dorfs, D. Halide ion influence on the formation of nickel nanoparticles and their conversion into hollow nickel phosphide and sulphide nanocrystals. *Nanoscale* **2019**, *11* (32), 15104-15111.

(47) Akkerman, Q. A.; D'Innocenzo, V.; Accornero, S.; Scarpellini, A.; Petrozza, A.; Prato, M.; Manna, L. Tuning the optical properties of cesium lead halide perovskite nanocrystals by anion exchange reactions. *J. Am. Chem. Soc.* **2015**, *137* (32), 10276-10281.

(48) Shamsi, J.; Urban, A. S.; Imran, M.; De Trizio, L.; Manna, L. Metal halide perovskite nanocrystals: synthesis, post-synthesis modifications, and their optical properties. *Chem. Rev.* **2019**, *119* (5), 3296-3348.

(49) Zeng, J. L.; Guan, Z. J.; Du, Y.; Nan, Z. A.; Lin, Y. M.; Wang, Q. M. Chloride-promoted formation of a bimetallic nanocluster $Au_{80}Ag_{30}$ and the total structure determination. *J. Am. Chem. Soc.* **2016**, *138* (25), 7848-7851.

(50) Protesescu, L.; Yakunin, S.; Bodnarchuk, M. I.; Krieg, F.; Caputo, R.; Hendon, C. H.; Yang, R. X.; Walsh, A.; Kovalenko, M. V. Nanocrystals of cesium lead halide perovskites ($CsPbX_3$, X= Cl, Br, and I): novel optoelectronic materials showing bright emission with wide color gamut. *Nano Lett*. **2015**, *15* (6), 3692-3696.

(51) Zhang, J.; Zhou, Y.; Zheng, K.; Abroshan, H.; Kauffman, D. R.; Sun, J.; Li, G. Diphosphine-induced chiral propeller arrangement of gold nanoclusters for singlet oxygen photogeneration. *Nano Res.* **2018**, *11* (11), 5787-5798.

(52) M. J. Frisch, G. W. Trucks, H. B. Schlegel, G. E. Scuseria, M. A. Robb, J. R. Cheeseman, G. Scalmani, V. Barone, B. Mennucci, G. A. Petersson, H. Nakatsuji, M. Caricato, X. Li, H. P. Hratchian, A. F. Izmaylov, J. Bloino, G. Zheng, J. L. Sonnenberg, M. Hada, M. Ehara, K. Toyota, R. Fukuda, J. Hasegawa, M. Ishida, T. Nakajima, Y. Honda, O. Kitao, H. Nakai, T. Vreven, J. A. Montgomery, Jr., J. E. Peralta, F. Ogliaro, M. Bearpark, J. J. Heyd, E. Brothers, K. N. Kudin, V. N. Staroverov, T. Keith, R. Kobayashi, J. Normand, K. Raghavachari, A. Rendell, J. C. Burant, S. S. Iyengar, J. Tomasi, M. Cossi, N. Rega, J. M. Millam, M. Klene, J. E. Knox, J. B. Cross, V. Bakken, C. Adamo, J. Jaramillo, R. Gomperts, R. E. Stratmann, O. Yazyev, A. J. Austin, R. Cammi, C. Pomelli, J. W. Ochterski, R. L. Martin, K. Morokuma, V. G. Zakrzewski, G. A. Voth, P. Salvador, J. J. Dannenberg, S. Dapprich, A. D. Daniels, O. Farkas, J. B. Foresman, J. V. Ortiz, J. Cioslowski, and D. J. Fox. Gaussian 09, Revision D.01, Gaussian, Inc., Wallingford CT, **2013**.

Chapter 3 The study of the hydride-containing clusters

Portions of this chapter are adapted and/or reprinted from the following works. Copyright belongs to the publisher.

Dong, J., **Gao, Z. H.**, Zhang, Q. F., Wang, L. S. The Synthesis, Bonding, and Transformation of a Ligand-Protected Gold Nanohydride Cluster. *Angew. Chem. Int. Ed*. 2021,60(5), 2424-2430.

3.1 Introduction

The interaction of hydrogen with coinage metals, copper, silver, gold, has been of great interest to the chemistry society due to the unique bonding features, broad applications in catalytic reactions, and potential use in the design of hydrogen storage materials.[1, 2] The coinage metal hydrides stands on the interface between transition metal and main group metal hydrides. The relatively high electronegativity of these metals leads to the formation of more covalent metal hydrogen bonds, especially for Au which is the most electronegativity metal element. Strong covalent bonding between Au and H has been found with PES and theoretical calculations.[3, 4] Also in the gas phase study, the comparison between the photoelectron spectra of Au_n^- and $Au_{n-1}H^-$ clusters indicate the single hydrogen atoms behave like metal atoms in an Au cluster.[5]

In the bulk phase, no metal hydride has ever been discovered for gold and silver even at elevated temperature and pressure.[6] In contrast, copper hydride was one of the very first coinage metal hydrides to be discovered. The first coinage metal hydride was discovered in 1844, Wurtz reacted hypophosphorous acid with copper sulphate in aqueous solution and a hexagonal wurtzite-type copper hydride was formed.[7] Despite the inertness of gold in bulk phase, Au NPs have been found to display remarkable activities in various reactions, such as CO oxidation, hydrogenation, photocatalytic hydrogenation, etc.[8, 9] And among many of these reactions, gold hydride is believed to be a key intermediate.[10, 11] For example, Au NPs exhibit unique catalytic activity and selectivity towards hydrogenation reactions and several possible hydrogenation pathways have been proposed on an Au NP

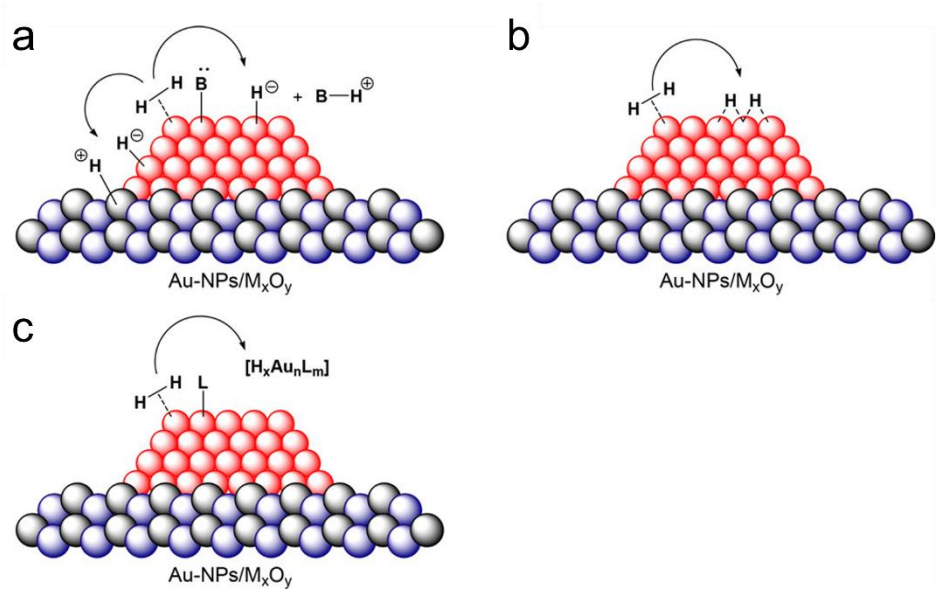

Figure 3.1 Possible hydrogenation mechanisms operating at the Au NP surfaces: a) Heterolytic H_2 activation; b) Homolytic H_2 activation; c) Generation of Au active species.[12] Copyright © 2017 American Chemical Society.

surface (in Figure 3.1): a) The ionic hydrogenation mechanism describes the collaboration of the support, additive and substrate producing direct heterolytic activation of H_2 and the transfer of proton to substrate, with formation of the gold hydride. b) The dissociative chemisorption of H_2 by the low-coordinated Au sites results in the formation of bridging H atoms. c) The activation of H_2 with the ejection of subnanometer Au-H clusters as catalytically active species.[12] All of these mechanisms include the formation of transient Au-H or hydride containing cluster species. Also, the status of surface ligands on Au NPs catalysts for the reduction of 4-nitrophenol to 4-aminophenol by $NaBH_4$ was investigated with the real-time UV-vis spectroscopic measurements. And the interaction of hydride with surface gold atoms was identified with changing in localized surface plasmon resonance.[13] Although some indirect or direct spectroscopic evidences were included, the difficulty in

isolating these Au-H or hydride containing cluster species calls for deeper understanding of hydride containing gold compounds or clusters.

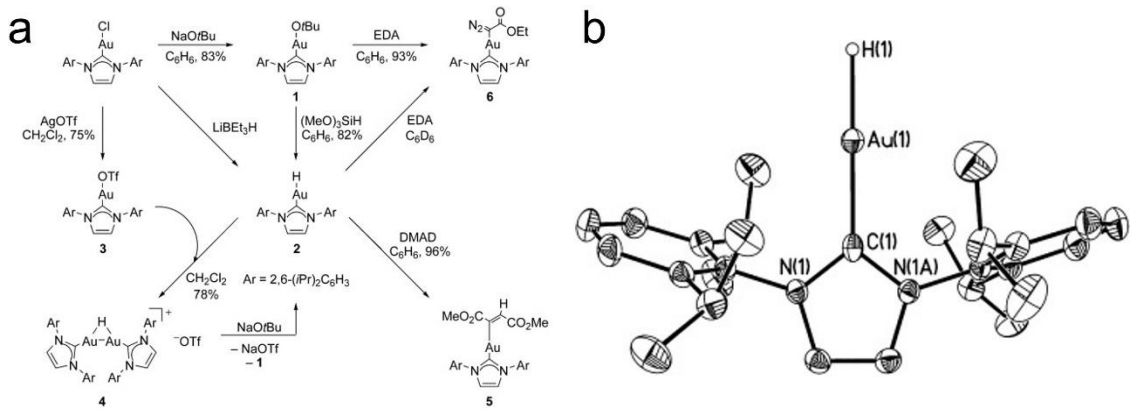

Figure 3.2 a) Preparation and reactions of [(IPr)AuH] compound, b) Solid-state structure of [(IPr)AuH].[14] Copyright © 2008 American Chemical Society.

The first stable gold hydride compound to be isolated under preparative conditions was the NHC ligated (IPr)AuH (IPr=1,3-bis(2,6-diisopropylphenyl)imidazol-2-ylidene) in 2008.[14] As shown in Figure 3.2, several methods can lead to the yield of the gold hydride compound which was confirmed with SC-XRD and ^{1}H-NMR spectroscopy. And it was also demonstrated that the compound was effective for carbene transfer catalysis. One year later, another neutral diphosphine-supported gold hydride was reported with crystal structure analysis.[15] The data permitted refinement of the hydride location, giving Au-H bond distance of 1.70(3) Å. When moving to larger hydride-containing system, while many Ag and Cu clusters have been characterized with hydrides in crystal structures,[1, 16] the investigation on polynuclear gold hydride nanoclusters only starts recently.

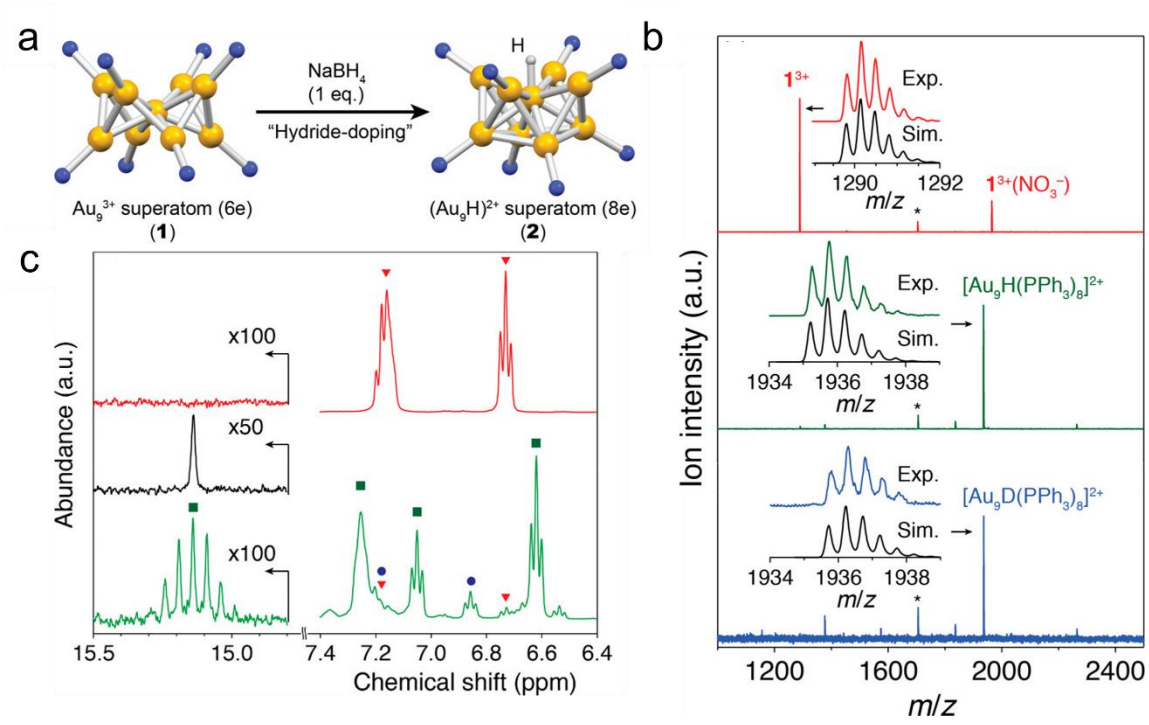

Figure 3.3 a) The formation of hydride doped Au NC. b) Positive-ion ESI-MS spectra of the Au_9 cluster and the product obtained by the addition of $NaBH_4$ or $NaBD_4$. c) ^{1}H-NMR spectra of Au_9 and Au_9H clusters.[17] Copyright © 2018 American Chemical Society.

$NaBH_4$ has been widely used as a reducing agent for coinage metal NPs and NCs due to its strong reducing power. It's also a clean hydride source for various organic reactions.[13] In 2018, Takano et al. studied the reaction between $[Au_9(PPh_3)_8]^{3+}$ cluster with $NaBH_4$, and after the addition of $NaBH_4$ solution at room temperature, the color of cluster solution changed quickly from light orange to deep red, indicating the formation of new species.[17] *In situ* ESI-MS was performed to monitor the reaction, and the original $[Au_9(PPh_3)_8]^{3+}$ peak at 1290 m/z disappeared with the appearance of a new cluster peak at 1936 m/z which could be assigned as a novel hydride $[Au_9H(PPh_3)_8]^{2+}$ cluster (Figure 3.3b). The isotope labelling experiment confirmed the source of hydride was the added BH_4^- and the hydride also gave rise to characteristic peak in ^{1}H-NMR spectrum at 15.1 ppm (Figure

3.3c). DFT calculations were performed to study the electronic structure of the new hydride cluster. The optimized structure shows that the hydride is directly bonded to the central Au with a bond length of 1.69 Å, which is very similar to length in the gold hydride compound. The electron configuration demonstrates that the hydride can mimic the Au atom in hydride cluster with a nearly spherical shape and a closed electron configuration of $(1S)^2(1P)^6$. This pioneer work provides a deeper understanding of Au-H interaction in a larger gold system. Larger hydrido Au NC was reported by Yuan et al. with a formula $[Au_{20}H_3(PPh_3)_{12}](SbF_6)_3$. Instead of hydride doping from an existed cluster, this one was synthesized directly from

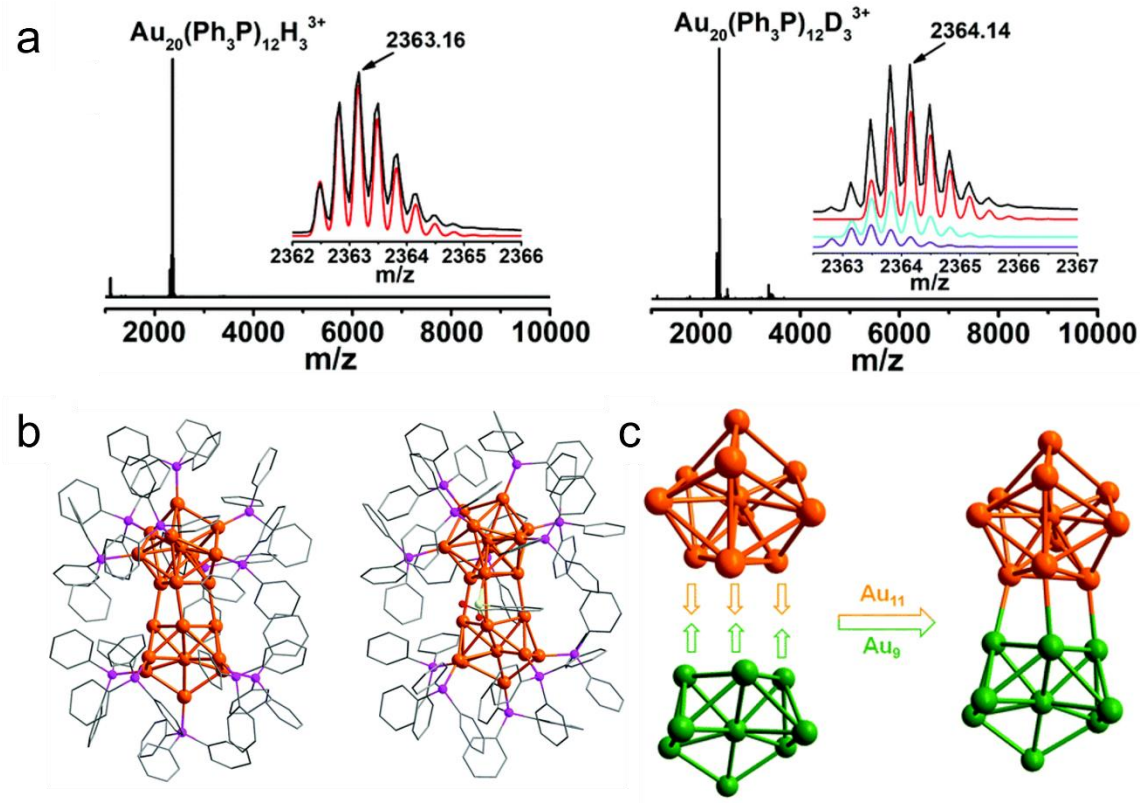

Figure 3.4 a) Mass spectra of $[Au_{20}H_3(PPh_3)_{12}]^{3+}$ and $[Au_{20}D_3(PPh_3)_{12}]^{3+}$ cluster. b) Molecular structure of $[Au_{20}H_3(PPh_3)_{12}]^{3+}$ cluster. c) The intercluster joint pattern of Au_{11} and Au_9 units. Au: organce/green, P: purple, C: grey.[18] Copyright © 2020 The Royal Society of Chemistry.

the reduction of $NaBH_4$ of phosphine ligated Au precursor.[18] The synthesized cluster was characterized by ESI-MS in positive mode with a prominent peak at 2363.16 m/z which matched perfectly with the simulated isotopic patterns (Figure 3.4a). The isotope labeling experiment was also performed and the relative height of the peaks in isotopic pattern of $[Au_{20}D_3(PPh_3)_{12}]^{3+}$ slightly deviated from the simulated value, due to the coexistence of $[Au_{20}D_2H(PPh_3)_{12}]^{3+}$ and $[Au_{20}DH_2(PPh_3)_{12}]^{3+}$ clusters. SC-XRD analysis revealed the crystal structure of the hydrido cluster as shown in Figure 3.4b, the structure consists of a Au_{20} kernel with twelve peripheral PPh_3 ligands. And the Au_{20} kernel can be constructed from a Au_9 unit and a Au_{11} unit through sharing two triangular faces. DFT calculation was performed to verify the location of hydrides in the cluster and the Au-H bond lengths were calculated as 1.744-1.798 Å. Despite the low yield of the hydrido cluster from the synthetic method, the cluster was found to be stable for six months in solid state. Still, the knowledge on the hydride containing clusters is limited and several questions remain to be answered: 1. Is it possible to synthesize other hydride-containing Au NCs and what results in the formation of hydrides in Au NCs? 2. What are the hydrogen behaviors or the properties of these hydrides in Au NCs? 3. Can we manually create the formation of these hydrides and use them as active center for some reactions? The following parts will partially answer these questions and provide a deeper insight into the hydrido Au NCs.

3.2 A $[Au_{22}H_4(dppo)_6]^{2+}$ hydride cluster

3.2.1 The discovery of the gold nanohydride cluster

Our previous focus towards synthesizing the Au_{20} pyramid in solution phase has led to the discovery of the interesting $Au_{22}(dppo)_6$ cluster (dppo=1,8-bis

(diphenylphosphino) octane, abbreviated as L^8), which contains eight uncoordinated Au sites on the interface of the two Au_{11} units. The presence of the uncoordinated sites is promising for catalysis and Jiang et al. hypothesized the cluster can be an excellent electrocatalyst for the hydrogen evolution reaction (HER).[19] They performed first-principles DFT and evaluated the Gibbes free energies of H absorption (ΔG_H) to predict the HER activity. All the possible H absorption sites on the Au_{22} cluster were tested, including eight uncoordinated bridge sites on the interface and two hollos sites on the Au_{11}

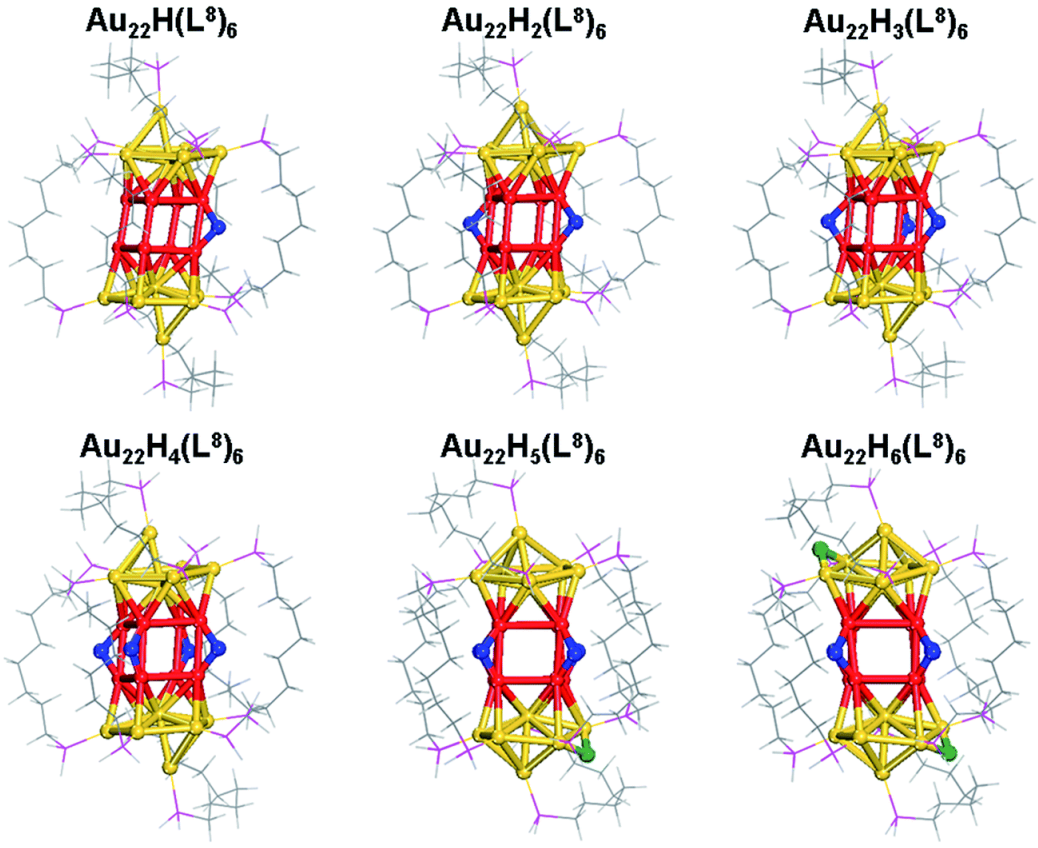

Figure 3.5 Optimized structures of the $Au_{22}H_n(L^8)_6$ cluster, n=1-6. Au: red/yellow, H: blue/green. P: magenta, C: grey.[19] Copyright © 2018 The Royal Society of Chemistry.

units. As shown in Figure 3.5, up to six H atoms can favorably absorb onto the cluster and the close-to-zero ΔG_H indicates a good potential HER catalyst that is even stronger than

Pt. The theoretical results led us to revisit this cluster and an interesting $[Au_{22}H_4(dppo)_6]^{2+}$ hydride cluster was discovered and characterized as below.

3.2.2 Chemicals and preparations

The chemicals listed below are directly used as received. Chloro(dimethylsulfide)gold(I) (≥97%, Strem), 1,8-bis(diphenylphosphino)octane (dppo, 99%, Strem), 1,4-bis(diphenylphosphino)butane (dppb, 99%, Sigma-Aldrich), sodium borohydride ($NaBH_4$, ≥98.0%, Sigma-Aldrich), sodium borodeuteride ($NaBD_4$, 98 atom % D, Sigma-Aldrich), acetone (≥99.5%, Certified ACS, Fisher Scientific), methylene chloride (≥99.5%, Certified ACS, Fisher Scientific), ethanol (≥99.5%, 200 proof, ACS reagent, Sigma-Aldrich), ethanol-OD (≥99.5% atom %D, Sigma-Aldrich), hexanes (≥98.5%, Certified ACS, Fisher Scientific), toluene (≥99.5%, Certified ACS, Fisher Scientific).

Synthesis of the $Au_2(dppo)Cl_2$ gold precursors:

A sample of 208 mg (0.43 mmol) of dppo was first added to a Schlenk flask containing 30 mL acetone. After vigorously stirring for about 15 mins, 254 mg (0.86 mmol) of chloro(dimethylsulfide)gold(I) dissolved in 50 mL acetone was quickly added. The reaction was allowed to proceed for 24 hours at room temperature in the dark. The white precipitates were filtered, dried and washed with pentane. Finally, 380.6 mg of $Au_2(dppo)Cl_2$ was obtained with a yield of 93%. ^{1}H-NMR (600.0 MHz, $CDCl_3$): δ 7.68-7.58 (m, 8H), 7.53-7.39 (m, 12H), 2.45-2.32 (m, 4H), 1.65-1.52 (m, 4H), 1.49-1.35 (m, 4H), 1.30-1.25 (m, 4H). ^{31}P-NMR (161.9 MHz, $CDCl_3$): δ 29.2 (s). ESI-MS: observed *m/z* = 911.1347, calculated *m/z* ($Au_2C_{32}H_{36}P_2Cl$) = 911.1312.

Synthesis of the $[Au_{22}H_4(dppo)_6]^{2+}$ hydride clusters:

A sample of 284 mg (0.30 mmol) of $Au_2(dppo)Cl_2$ was initially dissolved in 360 mL CH_2Cl_2. The solution was cooled down to 0 ˚C and stirred for over 30 minutes. Then, 45.4 mg (1.20 mmol) of $NaBH_4$ dissolved in 16 mL ethanol (EtOH) was quickly added to the cooled solution. During this time, the color of the solution gradually changed from light yellow to black. The reaction was carefully sealed with nitrogen and stirred at 0 ˚C for 18 hours in the dark. After the removal of all solvents by a rotary evaporator, the dark brown residue was washed by a 40 mL CH_2Cl_2/hexane (1/5 ratio) mixed solution for three times to get rid of the excess phosphine ligands. The remained solid was then dissolved into a minimum amount of CH_2Cl_2 and purified by silica-gel column chromatography. A sample of 89.6 mg brown powder was obtained after solvent evaporation. If all counter anions were assumed as chloride, a relatively high yield of 45% was obtained on the basis of the initial amount of Au in $Au_2(dppo)Cl_2$. ^{1}H-NMR (600.0 MHz, $CDCl_2$): δ 15.35-15.78 (m, 4H), 6.14-8.64 (m, 120H), 2.83-0.22 (m, 96H). ESI-MS: observed *m/z* = 3616.3344, calculated *m/z* ($Au_{22}C_{192}H_{220}P_{12}$) = 3616.3353.

Crystallization of the $[Au_{22}H_4(dppo)_6]^{2+}$ hydride clusters and the $Au_{22}(dppo)_6$ clusters:

89.6 mg as obtained $[Au_{22}H_4(dppo)_6]^{2+}$ hydride sample was subjected to a fast crystallization method by layering its CH_2Cl_2 solution with toluene in less than 1 day. Finally, 46.3 mg of $[Au_{22}H_4(dppo)_6]^{2+}$ with over ~95% purity was obtained. The quality was confirmed by full range ESI mass spectrometry. It should be noted that the slow crystallization method that was originally reported caused the transformation of the

$[Au_{22}H_4(dppo)_6]^{2+}$ hydride clusters into the large single crystals of the $Au_{22}(dppo)_6$ clusters, suitable for X-ray analyses.

3.2.3 Characterization methods

UV-vis Absorption Spectroscopy: UV-vis absorption spectra were recorded on a Varian Cary 50 Bio spectrometer with a spectral range between 300 to 800 nm at 298 K. The quartz cuvette used for all measurements had 1.0 cm optical path length. Background subtractions were done using appropriate solvents as blanks.

NMR Spectroscopy: ^{1}H, ^{2}H, ^{13}C, ^{31}P-NMR and two-dimensional NMR experiments (NOESY) were obtained on a 600 MHz Bruker Ultrashield spectrometer using CD_2Cl_2 or $CDCl_3$ as the solvent. Unless further noted, the NMR spectra were measured at 298 K. Chemical shifts (δ) are reported in ppm and referenced to internal solvent resonances for ^{1}H, ^{2}H, ^{13}C-NMR and external 85% H_3PO_4 for ^{31}P-NMR. Coupling constants (*J*) are reported in Hertz (Hz). All data were processed using the TopSpin or MestReNova software.

Fourier-Transform Infrared (FTIR) Spectroscopy:

FTIR spectra were acquired on a Bruker Tensor 27 FTIR spectrometer. The potassium bromide (KBr) pellet was used and prepared by mixing 2-3 mg of solid sample with *ca.* 100 mg of anhydrous KBr. The average number of scans was set as 20. Background subtractions were done with a blank cell.

Electrospray Ionization Mass Spectrometry (ESI-MS):

Positive ionization mode ESI mass spectra were measured on an Agilent 6530 Accurate Mass Q-TOF LC-MS system (with Agilent 1260 HPLC). The CH_2Cl_2 solution of the sample (*ca.* 1.0 mg mL^{-1}) was introduced into the system through a stainless steel needle via flow injection. Acetonitrile/water (1/1 ratio) was used as the mobile phase at a flow rate of 200 μL min^{-1}. The source temperature was kept at 130 ˚C. The fragmentor voltage was set at 50 V, skimmer at 65 V, and the capillary voltage at 3500 V. The measuring mass range was 0 to 20,000 m/z units.

The ESI-MS-CID spectra were acquired using the same system in a range of collision energy between 0 and 25 V. In the experiment, the precursor parent ion was isolated with an m/z width of ~ 4. The measuring mass range was 0 to 4000 m/z units.

All spectra were recorded at a rate of 1 spectrum s^{-1}. Different species were assigned using isotopic distributions in the high-resolution spectra by comparing with simulated spectra.

X-ray Photoelectron Spectroscopy (XPS):

XPS spectra were collected by a Thermo Scientific K-Alpha system that equipped with an Al k-Alpha excitation source (1486.6 eV). During the measurement, the analysis chamber pressure was pumped down below 10^{-7} mBar with the electron flood gun on to reduce possible sample charging. The X-ray spot size was set at 400 μm, pass energy at 50 eV and energy step size at 0.1 eV. Samples were positioned at the electron take-off angle normal to the surface relative to the analyzer.

Computational methods:

The initial structure of the $[Au_{22}H_4(dppo)_6]^{2+}$ hydride nanocluster considered in the structural optimization was based on the single-crystal structure of the $Au_{22}(dppo)_6$ cluster that was reported previously. The geometry was fully relaxed without constraints using the GGA-type BPBE density functional approximation, with the 6-31G(d) basis set for C, H, P and the LANL2DZ scalar relativistic pseudopotential basis set for Au. This functional was known to achieve a good balance between the structural accuracy and computational cost for the ligand-protected gold nanoclusters. Vibrational frequency calculations were also carried out to make sure that the fully optimized structure was a true minimum of the potential energy surface without imaginary frequencies. The calculated Infrared spectrum was smoothed with a half-width at half-maximum of 10 cm^{-1}. The linear-response time-dependent DFT calculation was performed for the relaxed structure at the PBE0 and 6-31G(d)/LANL2DZ levels, with the focus on the first 600 singlet transitions. A red-shift correction of 0.2 eV was used to compensate the systematic underestimation of the simulated spectrum, which was understandable considering the characteristics of the DFT functional used in the calculation. The calculated UV-vis spectrum was smoothed with a half-width at half-maximum of 0.15 eV. The molecular orbital calculations and chemical bonding analyses for the $[Au_{22}H_4(dppo)_6]^{2+}$ hydride cluster was done at the PBE0/6-31G(d)/LANL2DZ level and compared with the related information of the classical $[Re_2Cl_8]^{2-}$ cluster complex. The Bader charge analyses, electronic excitation analyses were performed using the Multiwfn 3.7 software. All calculations were carried out using the Gaussian 09 software package.

3.2.4 Results and discussion

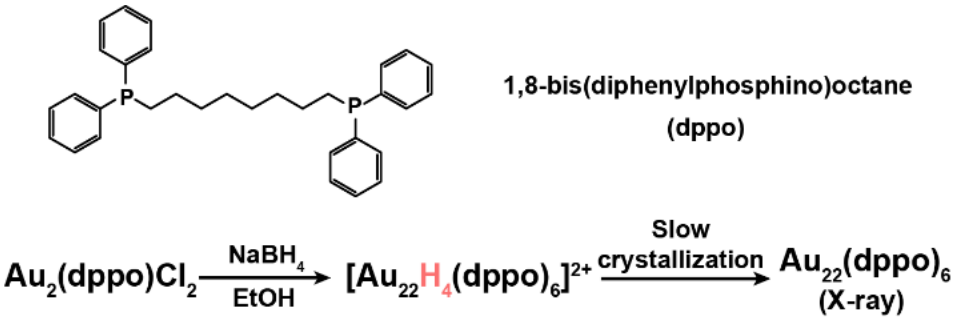

Figure 3.6 The synthetic method to the $[Au_{22}H_4(dppo)_6]^{2+}$ cluster.

The $Au_2(dppo)Cl_2$ was firstly prepared and then reacted with $NaBH_4$ to yield the $[Au_{22}H_4(dppo)_6]^{2+}$ cluster. The optimized ratio of $NaBH_4$ to Au is 2:1 and the reaction needs to be performed at 0 ^oC to ensure the highest yield. After purification by column, we noticed that the initial product was a hydride-containing cluster, as confirmed by ESI mass

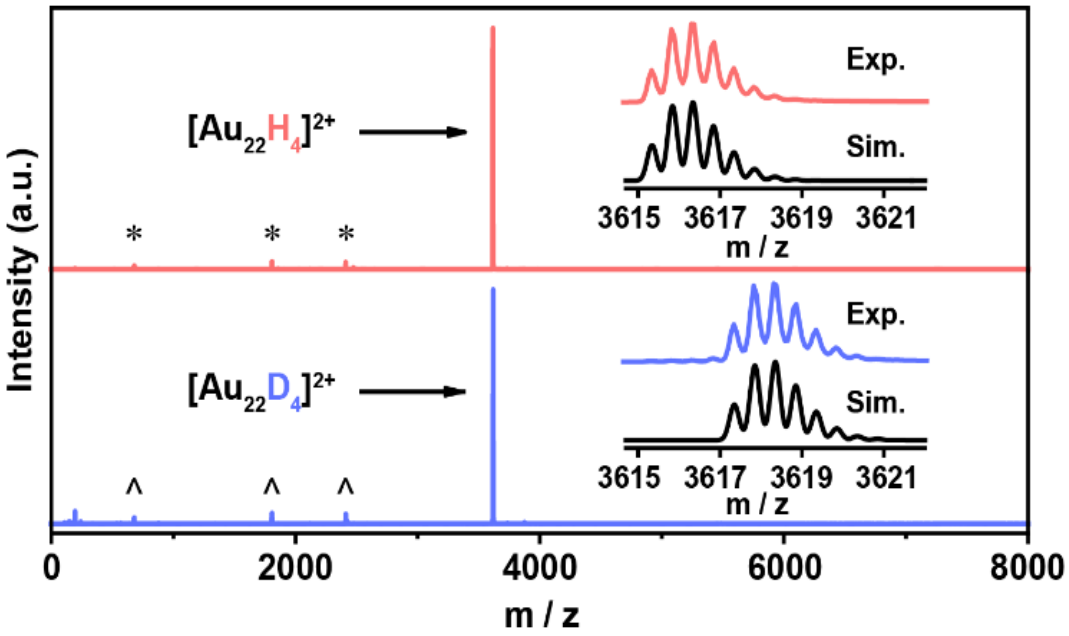

Figure 3.7 ESI-MS spectra of $[Au_{22}H_4(dppo)_6]^{2+}$ and $[Au_{22}D_4(dppo)_6]^{2+}$; the insets show the experimental and simulated isotopic distributions. The minor peaks labeled with * (from right to left) are: $[Au_{22}H(dppo)_6]^{3+}$, $[Au_{22}H_2(dppo)_6]^{4+}$, $[Au(dppo)]^+$. The minor peaks labeled with ^ (from right to left) are: $[Au_{22}D(dppo)_6]^{3+}$, $[Au_{22}D_2(dppo)_6]^{4+}$, $[Au(dppo)]^+$.

spectrometry. As is shown in Figure 3.7 top, the dominant peak in the mass spectrum was $[Au_{22}H_4(dppo)_6]^{2+}$ cluster at around 3616 m/z. By comparing with the simulated isotopic profile, we can see a good match between these two spectra.

However, the origin of these H atoms on the cluster remains a mystery. There are three possibilities: 1. They can come from the electrospray process because formic acid is used in the mobile phase of mass spectrometer to facilitate the ionization of cluster cations. 2. They can come from $NaBH_4$ which is the reducing agent or 3. They can come from the solvent ethanol. To verify the origin of H atoms, several controlled experiments have been carried out. By using $NaBD_4$ dissolved in EtOD, the same synthesis could be performed, and the resulting ESI mass spectrum could be seen in Figure 3.7 bottom: the experimental isotopic profile exhibited a shifting of 2 mass units to 3618 m/z. With the 2+ charge state, the result indicated that all the H atoms were substituted by D atoms. Therefore, the H atoms didn't come from the electrospray process. Then another controlled experiment was

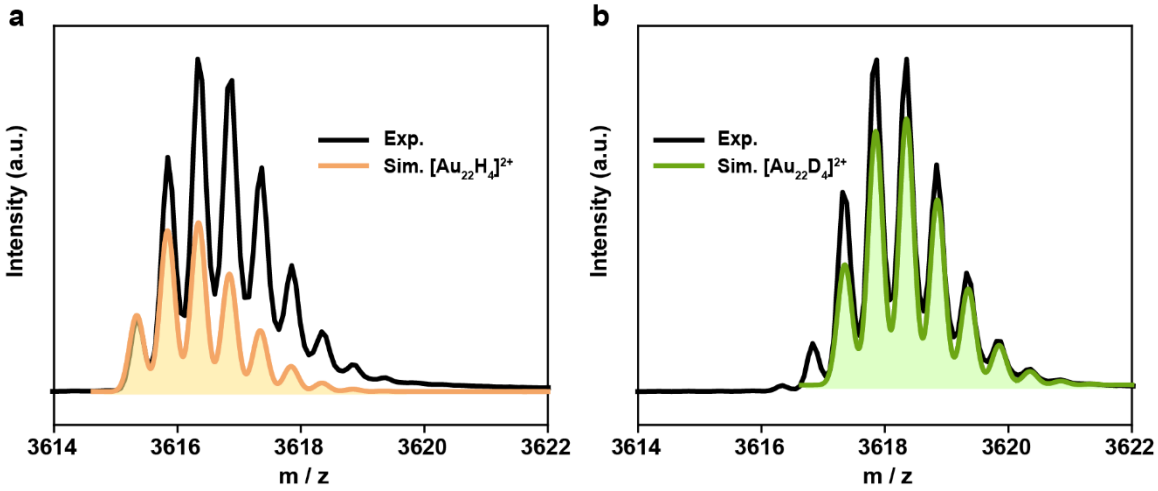

Figure 3.8 The isotopic distribution of (a) the $[Au_{22}H_4(dppo)_6]^{2+}$ clusters synthesized using $NaBH_4$ dissolved in EtOD and (b) the $[Au_{22}D_4(dppo)_6]^{2+}$ clusters synthesized using $NaBD_4$ dissolved in EtOH.

done by synthesizing using $NaBH_4$ dissolved in EtOD, it's obvious that the isotopic profile became broader which covered the range from $[Au_{22}H_4]^{2+}$ to $[Au_{22}D_4]^{2+}$. Therefore it's safe to conclude that the four H atoms on the cluster come from both the reducing agent ($NaBH_4$) and the solvent (EtOH). The third controlled experiment could be done with $NaBD_4$ dissolved in EtOH and again, a broader isotopic profile was shown in ESI mass spectrum and verified the conclusion.

To grow single crystals, a fast solvent diffusion of toluene into the CH_2Cl_2 solution of the crude product results in precipitation of high purity $[Au_{22}H_4(dppo)_6]^{2+}$ cluster sample.

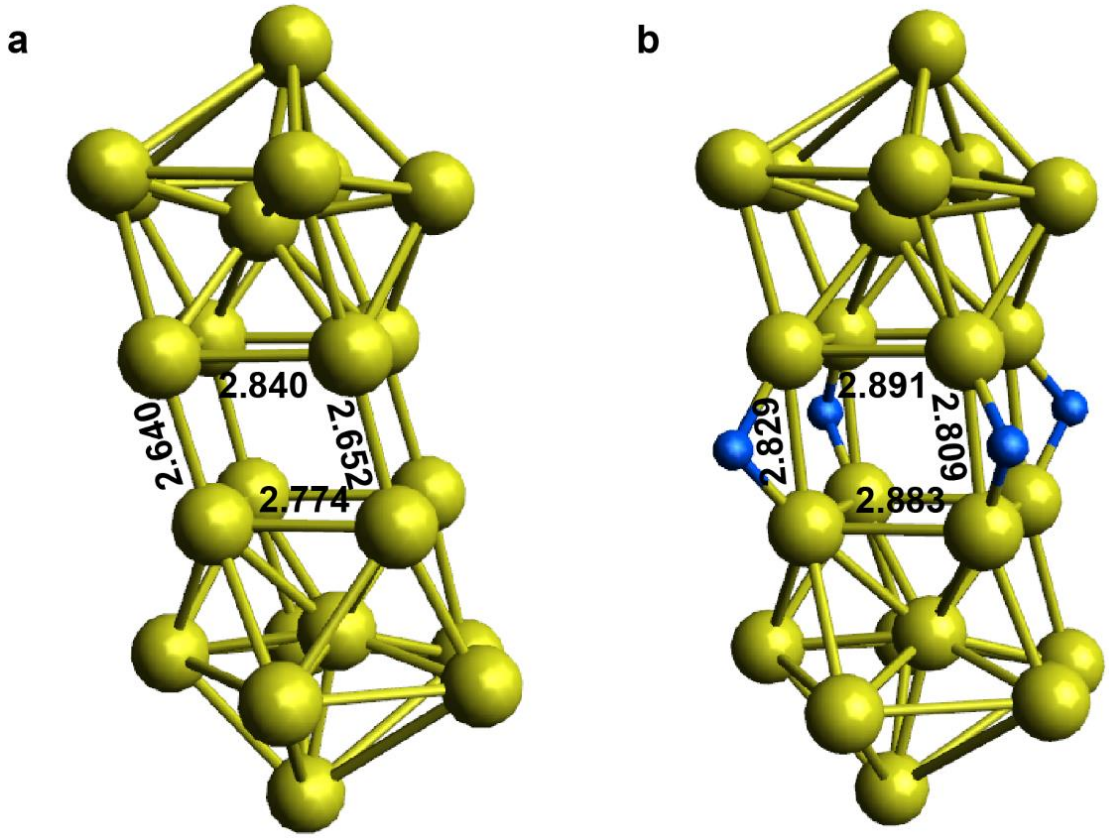

Figure 3.9 Comparison of the key Au-Au distances (Å) at the interface of the two Au_{11} units in $[Au_{22}H_4(dppo)_6]^{2+}$ and $Au_{22}(dppo)_6$. (a) The Au_{22} core in $Au_{22}(dppo)_6$ from X-ray crystallography. (b) The $Au_{22}H_4$ core in $[Au_{22}H_4(dppo)_6]^{2+}$ from DFT calculations.

However, our previous study showed that under slow crystallization conditions for several weeks, single crystals of the $Au_{22}(dppo)_6$ could be formed. As a consequence, the four H atoms on $[Au_{22}H_4(dppo)_6]^{2+}$ cluster can gradually loss to generate the neutral cluster. Thus, it's also interesting to investigate the location of H atoms with the help of theoretical calculations. The only stable structure was shown in Figure 3.9 with the four H atoms bridging the eight uncoordinated Au site of the $Au_{22}(dppo)_6$ cluster. This result agrees with that reported by Jiang et al. upon absorbing four H atoms onto the $Au_{22}(dppo)_6$ cluster. The Au_{22} cores in these two clusters are similar, except the Au-Au bond distances are lengthened in the case with bridging H atoms. The hydrogen locations could only be

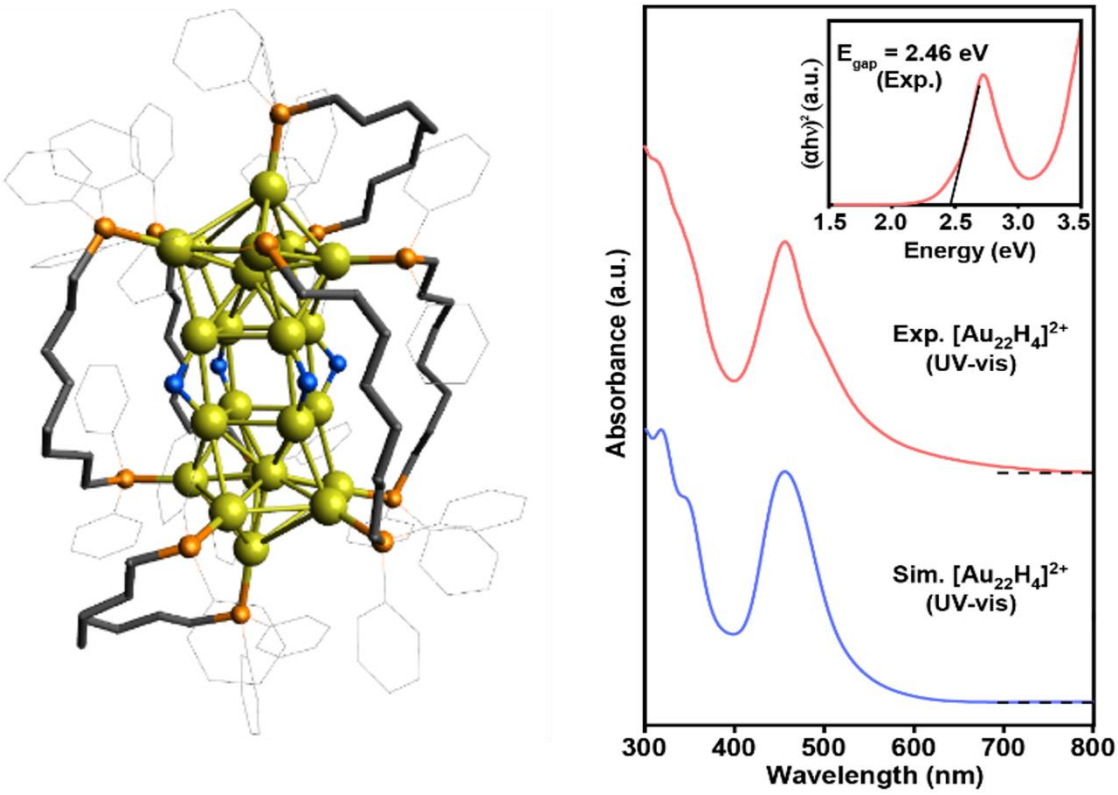

Figure 3.10 Left: The fully optimized structure of $[Au_{22}H_4(dppo)_6]^{2+}$ using DFT calculations. Right: The experimental and simulated UV-Vis absorption spectra of $[Au_{22}H_4(dppo)_6]^{2+}$cluster.

experimentally verified through neutron diffraction analysis on large size single crystals that currently cannot be achieved.

Table 3.1 The calculated electronic excitations of the $[Au_{22}H_4(dppo)_6]^{2+}$ cluster at the TD-PBE0 level of theory.

Excited state #	Wavelength (nm)	Energy (eV)	Osc. strength	Location assignments
13	534.4	2.320	0.045	Metal → metal
14	522.3	2.374	0.076	Metal → metal
28	472.9	2.622	0.362	Metal → metal
33	458.3	2.706	0.161	Metal → ligand
38	446.9	2.775	0.328	Metal → metal
43	442.0	2.805	0.366	Metal → metal
194	350.9	3.534	0.105	Metal → ligand
348	320.0	3.875	0.152	Metal → ligand

After the optimization of $[Au_{22}H_4(dppo)_6]^{2+}$ cluster, we can try to understand how these H atoms can influence the electronic structure of the gold cluster. As shown in Figure 3.10, there was a major peak at around 456 nm with a shoulder peak at ca 510 nm. The experimental result matched well with the simulated absorption spectrum. The TD-DFT calculations indicated that the peak at 456 nm was mainly due to metal→metal and metal →ligand transitions (Table 3.1). And the shoulder peak was only due to metal→metal transitions. The absorption spectrum for $[Au_{22}H_4(dppo)_6]^{2+}$ cluster was very similar to the spectrum reported previously for $Au_{22}(dppo)_6$ and this suggested that the previous spectrum might be in fact due to the tetrahydride species.

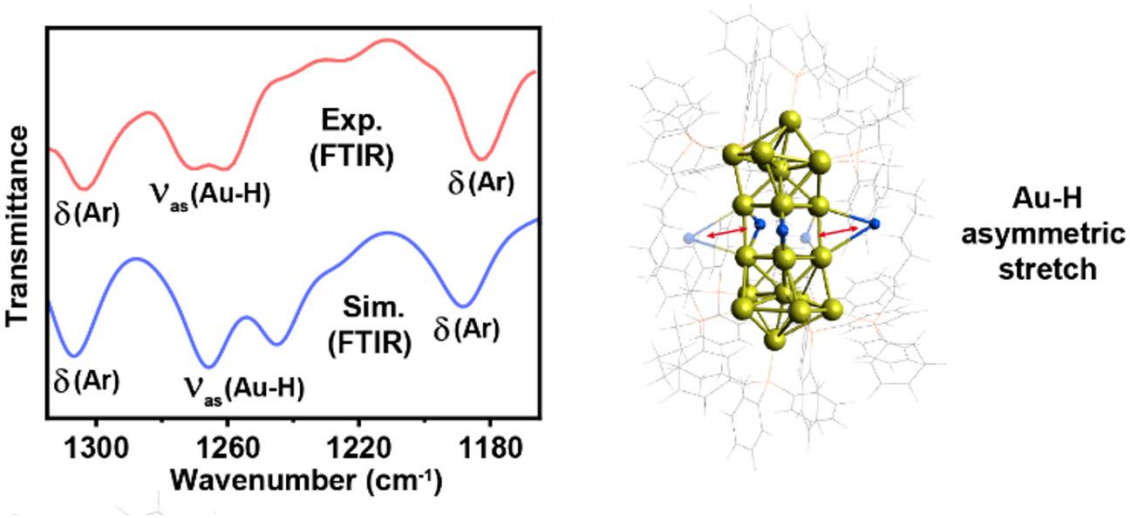

Figure 3.11 The FTIR spectra of the $[Au_{22}H_4(dppo)_6]^{2+}$ nanohydride cluster and the stretching vibration mode.

Apart from that, the infrared spectrum was also measured. The perfect match between the experimental Fourier-Transform Infrared (FTIR) spectrum and the simulated spectrum again confirmed the structure of $[Au_{22}H_4(dppo)_6]^{2+}$. The FTIR results indicated that the vibrational structure of $[Au_{22}H_4(dppo)_6]^{2+}$ contains a gold hydride asymmetric stretching mode around 1260 cm^{-1} (Figure 3.11), which is located between two aromatic ring distortion vibrations on the six dppo ligands. The asymmetric stretching mode consists of two peaks, because the four H atoms in $[Au_{22}H_4(dppo)_6]^{2+}$ are centrosymmetric and form two pairs. The FTIR spectrum of the hydride cluster was also compared with the $Au_{22}(dppo)_6$, as shown in Figure 3.12, the Au-H asymmetric stretching modes nearly disappeared in the sample of $Au_{22}(dppo)_6$ cluster. While the other peaks at around 1300 cm^{-1} and 1180 cm^{-1} remain which were due to the vibrational modes of the aromatic rings in the dppo ligands. Thus, IR spectroscopy analysis again confirms the existence of H atoms in the $[Au_{22}H_4(dppo)_6]^{2+}$ cluster as well as the theoretical predictions on the location of these hydrides.

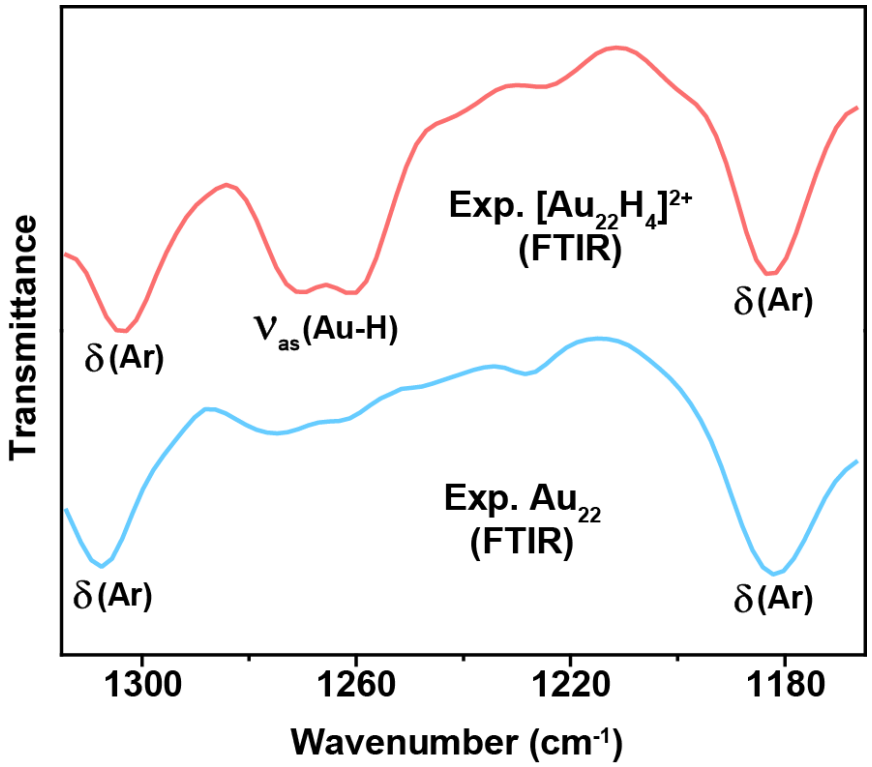

Figure 3.12 The experimental FTIR spectra of the $[Au_{22}H_4(dppo)_6]^{2+}$ and $Au_{22}(dppo)_6$ clusters. The bands assigned as the Au-H asymmetric stretching modes disappeared in the $Au_{22}(dppo)_6$ sample with only residual amount of $[Au_{22}H_4(dppo)_6]^{2+}$. The dppo ligands are omitted in the formula labels in the figure.

We further characterized $[Au_{22}H_4(dppo)_6]^{2+}$ cluster sample using ^{1}H-NMR at room temperature. As is shown in Figure 3.13, two sets of peaks could be clearly observed in the spectrum. One set was at 6.5 to 8.5 ppm which was due to the hydrogens in the aromatic rings from the dppo ligands. Another set of peaks on low field at around 15.6 ppm should be due to the four H atoms coordinated to the central eight Au atoms. It's also interesting to compare the peak position with the previously discovered $[Au_9H(PPh_3)_8]^{2+}$ hydride

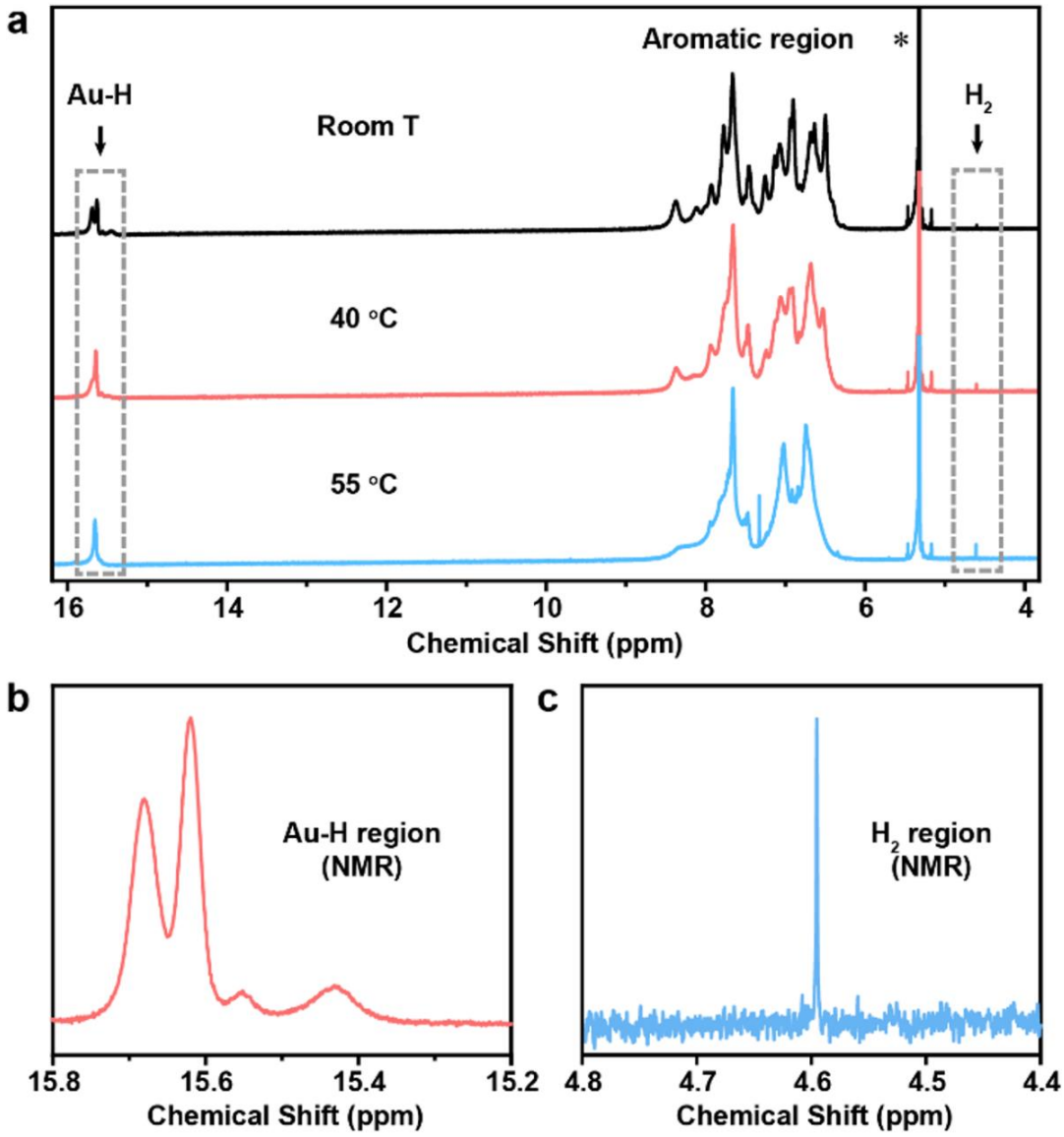

Figure 3.13 ^{1}H-NMR spectra of the $[Au_{22}H_4(dppo)_6]^{2+}$ nanohydride. (a) Variable-temperature ^{1}H-NMR spectra of the $[Au_{22}H_4(dppo)_6]^{2+}$ cluster in CD_2Cl_2. The integrated areas from the hydride region to that of the 120 aromatic H atoms on the six dppo ligands are all around 3.9:120. (b) The enlarged room temperature ^{1}H-NMR signal due to the hydrides on the Au_{22} cluster. (c) The enlarged ^{1}H-NMR signal from the H_2 molecule detected due to H-loss from the $[Au_{22}H_4(dppo)_6]^{2+}$ cluster. Note its increased intensity with temperature. The peak labeled with * is due to the solvent (CH_2Cl_2).

cluster which features with a hydride peak at around 15.1 ppm in ^{1}H-NMR spectrum. Therefore, such similarity between these two clusters indicates the chemical environments of the hydrides in these two clusters are similar. Due to the conformations of the dppo ligands at room temperature, the four H atoms may experience different chemical environments in solution, giving rise to the four NMR peaks. The number of H atoms at this region could also be calculated from the ratio of their integrated area to that of the 120 aromatic H atoms from the six dppo ligands, which is 3.91:120 based on the spectrum. Thus, the NMR characterization results match well with that from the ESI mass spectrum

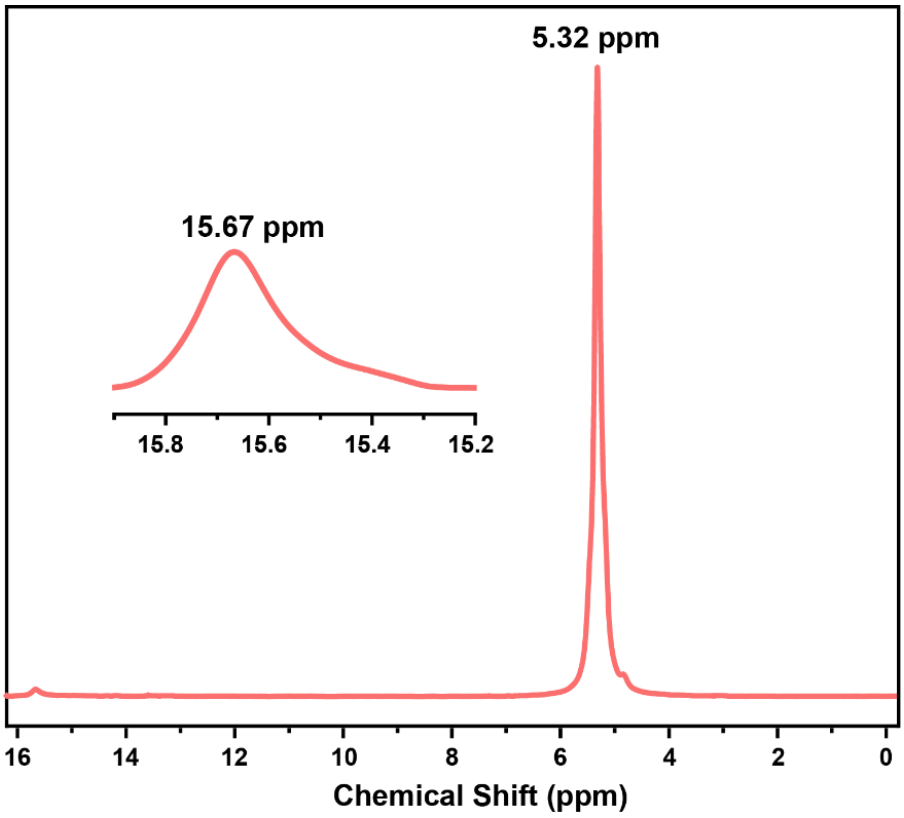

Figure 3.14 The ^{2}H-NMR spectrum of the $[Au_{22}D_4(dppo)_6]^{2+}$ cluster. The weak broad peak at 15.67 ppm is originated from the four D atoms, while the intense peak at 5.32 ppm is due to the CD_2Cl_2 solvent peak.

and confirm the four H atoms come from the cluster samples. Besides that, we can also obtain the $[Au_{22}D_4(dppo)_6]^{2+}$ clusters as aforementioned by reducing the precursor by $NaBD_4$ in EtOD solution. The ^{2}H-NMR spectrum of the $[Au_{22}D_4(dppo)_6]^{2+}$ cluster sample could be measured, as shown in Figure 3.14, only the D atoms have signals in the spectrum. Although the resolution is not as high as in the ^{1}H-NMR spectrum, a peak at 15.67 ppm could be observed for the cluster which is nearly at the same chemical shift and correlates very well with the ^{1}H-NMR spectroscopy result. Later, the temperature-dependent experiments were carried out in the ^{1}H-NMR measurement. Due to the low boiling point (39.6 ^{o}C) of the CH_2Cl_2 solvent, the sample can only be heated to 55 ^{o}C. The results showed that the peaks at 15.6 ppm gradually merged into one single peak at 55 ^{o}C (Figure 3.13b), suggesting that at elevated temperatures the dppo ligands exhibit fast dynamics on the

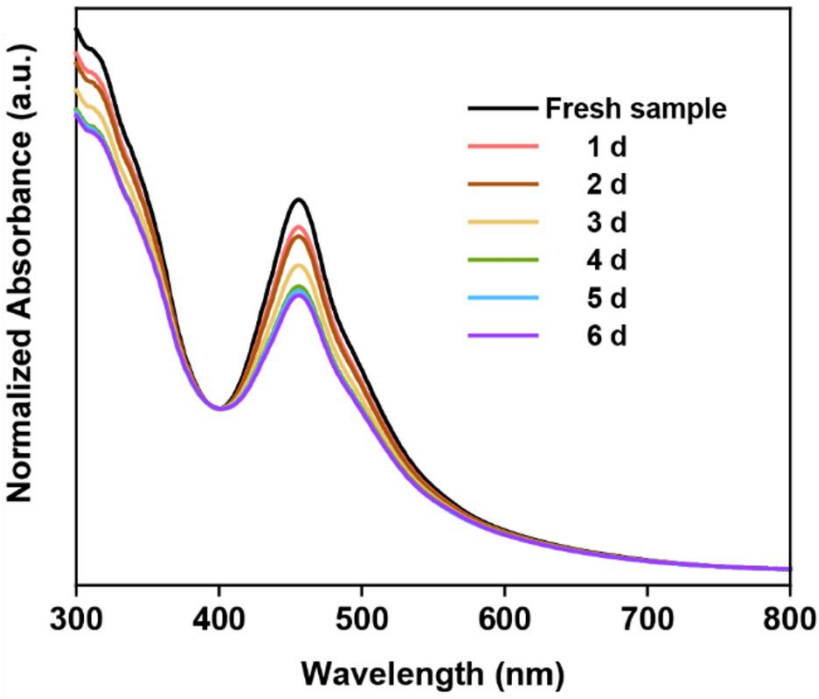

Figure **3.15** Time-dependent UV-vis absorption spectra of the $[Au_{22}H_4(dppo)_6]^{2+}$ nanohydride cluster in CH_2Cl_2 solution for six days.

NMR time scale and resulting in similar chemical environments for the four H atoms. At the same time, the H_2 gas was generated upon heating, as confirmed by the more prominent H_2 signal (δ = 4.59 ppm) at elevated temperatures.

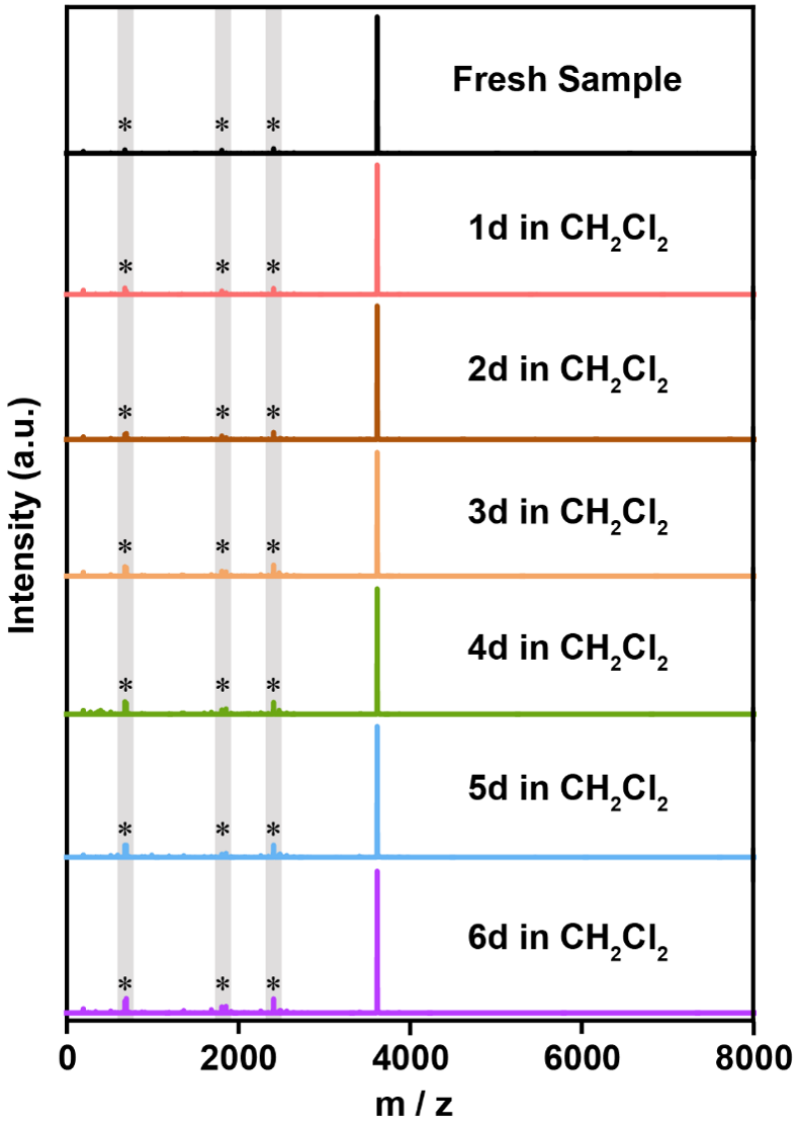

Figure 3.16 Time-dependent ESI-MS spectra of the $[Au_{22}H_4(dppo)_6]^{2+}$ cluster in CH_2Cl_2 solution for six days under ambient and dark conditions. From right to left for the minor peaks (*): $[Au_{22}H(dppo)_6]^{3+}$, $[Au_{22}H_2(dppo)_6]^{4+}$, $[Au(dppo)]^{+}$.

After the confirmation of hydrides as well as hydride positions in the $[Au_{22}H_4(dppo)_6]^{2+}$ cluster sample. We studied the stability of the $[Au_{22}H_4(dppo)_6]^{2+}$ cluster sample using a combination of UV-Vis spectrometer and ESI mass spectroscopy. Time-dependent UV-Vis absorption spectra in Figure 3.15 suggested that the fresh cluster sample gradually decomposed in the solution under ambient and dark conditions. The intensity of the main peak at 456 nm showed a slow decrease as a function of time. To understand the species that changed in solution, time-dependent ESI mass spectra were also taken as shown in Figure 3.16. The relative signal intensity of $[Au_{22}H(dppo)_6]^{3+}$ and $[Au_{22}H_2(dppo)_6]^{4+}$ increased, suggesting spontaneous and slow H loss from $[Au_{22}H_4(dppo)_6]^{2+}$ cluster. The stability of the $[Au_{22}H_4(dppo)_6]^{2+}$ cluster is between the two

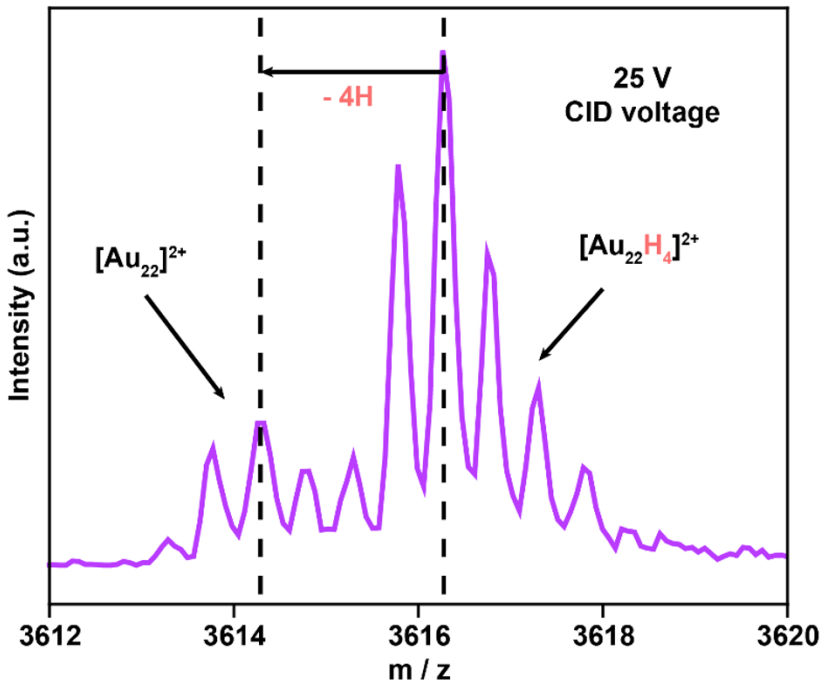

Figure 3.17. In-source CID mass spectrum of the $[Au_{22}H_4(dppo)_6]^{2+}$ cluster with a CID voltage of 25 V. The spectrum shows that the four H atoms can be completely dissociated, leading to the $[Au_{22}(dppo)_6]^{2+}$ cluster.

hydrido Au NCs, $[Au_9H(PPh_3)_8]^{2+}$ which is metastable with a half-life of only several hours[17] and $[Au_{20}(PPh_3)_{12}H_3]^{3+}$ which is stable for up to three months.[18] The collision-induced dissociation (CID) experiment also revealed that the four H atoms in the $[Au_{22}H_4(dppo)_6]^{2+}$ can be dissociated at 25 V, while the Au_{22} kernel remained intact during the process (Figure 3.18). In the solid state, the stability of the cluster sample can be greatly enhanced. Solid samples of $[Au_{22}H_4(dppo)_6]^{2+}$ are stable for more than two weeks under ambient and dark conditions, whereas $[Au_{22}H_4(dppo)_6]^{2+}$ samples stored in the dark at -40 ^oC under N_2 atmosphere are stable for at least six months. Therefore, we have discovered three H loss pathways: 1. H loss through slow crystallization and $[Au_{22}H_4(dppo)_6]^{2+}$ will convert into $Au_{22}(dppo)_6$ cluster. 2. H loss under light (ambient conditions) and characterized by ESI mass spectra. 3. H loss upon heating which has been confirmed with

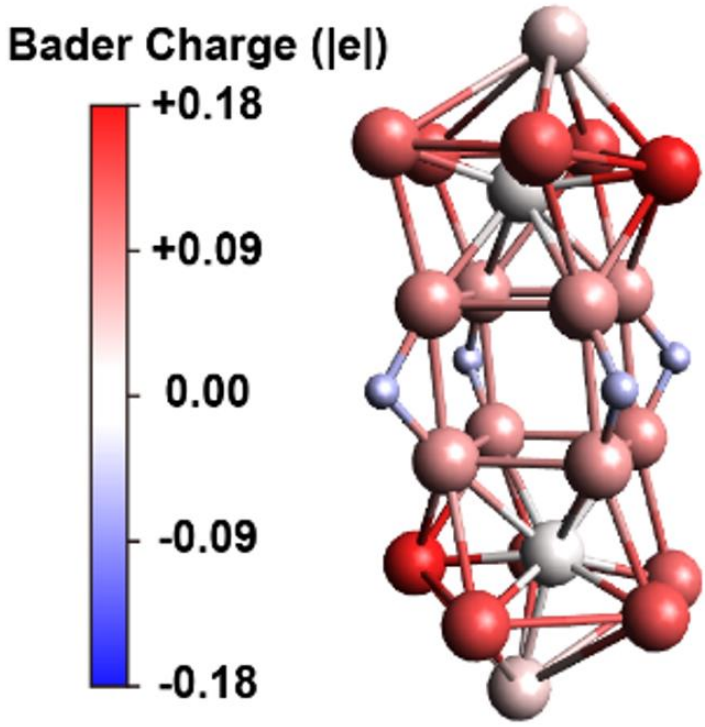

Figure 3.18 The Bader charge analysis for the metal core of $[Au_{22}H_4(dppo)_6]^{2+}$.

^{1}H-NMR spectroscopy with enhancing H_2 signal. Bader charge analysis was performed to understand the charge distributions on the Au_{22} kernel, as shown in Figure 3.18. The two Au atoms in the center of two Au_{11} units and two polar Au atoms didn't carry any charge, whereas the eight central Au atoms that are connected by H atoms carried a little positive charge. And the charge states for the four H atoms were a little negative, the close-to-zero

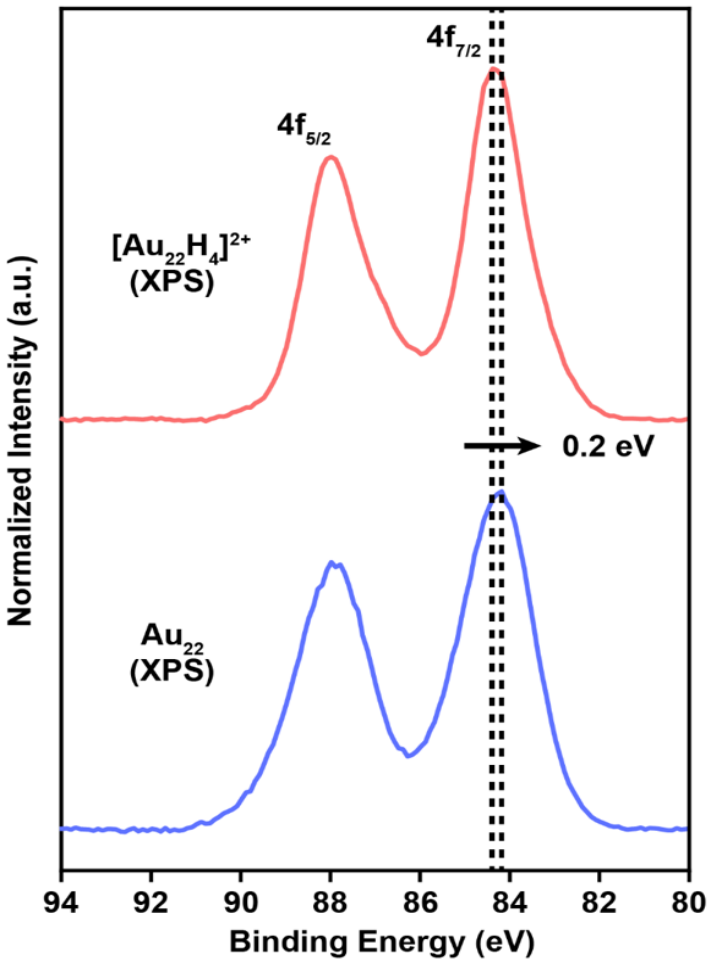

Figure 3.19 XPS spectra of the $[Au_{22}H_4(dppo)_6]^{2+}$ cluster and its hydrogen loss product in the Au 4f region. The Au $4f_{7/2}$ binding energy was slightly smaller after the hydrogen loss (~0.2 eV), suggesting the formation of neutral $Au_{22}(dppo)_6$ cluster through a disproportionation reaction.

charge on these H atoms makes it interesting to investigate the H loss pathways on the $[Au_{22}H_4(dppo)_6]^{2+}$ cluster.

During the stability study of $[Au_{22}H_4(dppo)_6]^{2+}$ cluster in solution, the observations of $[Au_{22}H_2(dppo)_6]^{4+}$ or $[Au_{22}H(dppo)_6]^{3+}$ suggest redox reactions involving H^+/H^- transfers. X-ray photoelectron spectroscopy (XPS) showed that the Au $4f_{7/2}$ binding energy was slightly smaller after the hydrogen loss (~0.2 eV), suggesting the formation of neutral $Au_{22}(dppo)_6$ cluster through a disproportionation reaction (Figure 3.19). This H_2 loss channel was also confirmed by the detection of H_2 (δ = 4.59 ppm) in the room temperature NMR spectrum. We also found that H loss from $[Au_{22}H_4(dppo)_6]^{2+}$ can be accelerated by heating or in an alcohol solution. Because of its absorption in the visible part of the spectrum, the H loss process can also be accelerated under ambient light. The mechanisms can be described approximately to proceed through two stages. In fresh samples,

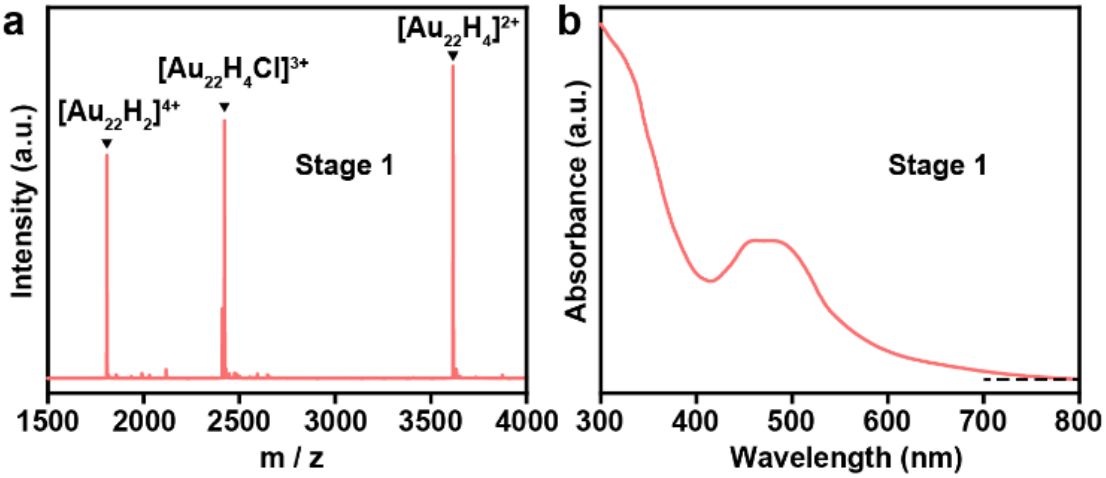

Figure 3.20 The H loss mechanisms from the $[Au_{22}H_4(dppo)_6]^{2+}$ nanohydride. (a and b) The ESI-MS spectra and the corresponding UV-vis absorption spectra in the stage 1 of hydrogen loss. The $[Au_{22}H_4Cl]^{3+}$ consists of a putative adduct between $[Au_{22}H_4]^{4+}$ and Cl^-.

$[Au_{22}H_4(dppo)_6]^{2+}$ was detected as the dominating species (Figures 3.16) and exhibited a major absorption band at around 456 nm (Figure 3.10). In the first stage of H loss, prominent signals of $[Au_{22}H_2(dppo)_6]^{4+}$ and $[Au_{22}H_4(dppo)_6]^{4+}$ (detected with a putative Cl^- adduct) were observed as shown in Figure 3.20. The UV-vis absorption spectrum at this stage showed an obvious decrease of the 456 nm peak and the appearance of a new peak at longer wavelength around 485 nm (Figure 3.20). In the second stage of H loss, $[Au_{22}H(dppo)_6]^{3+}$ was detected as the major species (Figure 3.21). At the same time, the original $[Au_{22}H_4(dppo)_6]^{2+}$ absorption peak at 456 nm was almost fully suppressed, and the major absorption peak was red-shifted to around 485 nm (Figure 3.22). The absorption spectrum of $[Au_{22}H_4(dppo)_6]^{2+}$ in the visible spectral range involves metal→metal transitions in the Au_{22} core, consistent with the spectral change induced by H loss from $[Au_{22}H_4(dppo)_6]^{2+}$. Remarkably, the UV-vis spectrum in Figure 3.22 agrees well with the absorption spectrum calculated previously for the $Au_{22}(dppo)_6$ cluster, confirming it as the major product upon H loss. At ambient and dark conditions, without heating or using

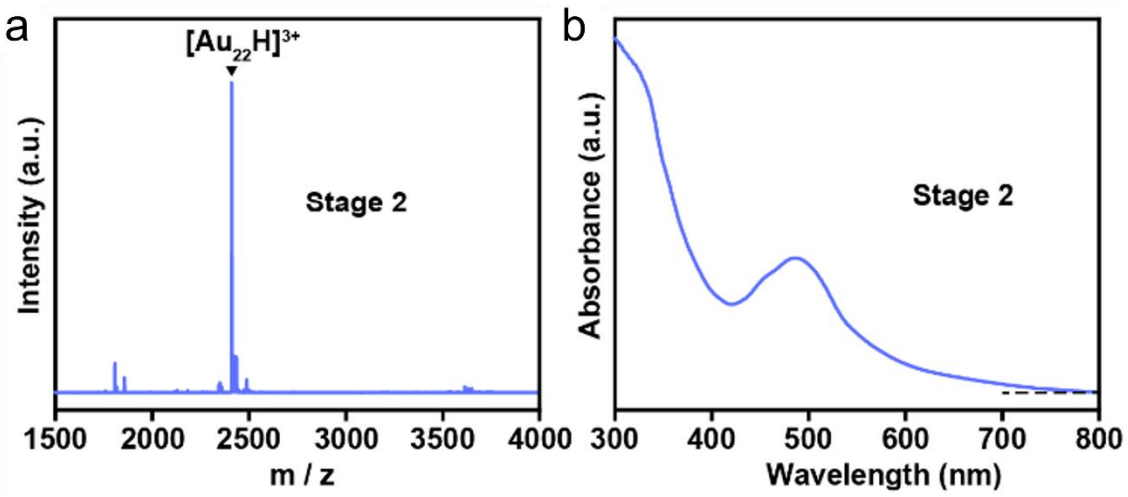

Figure 3.21 The ESI-MS spectra and the corresponding UV-vis absorption spectra in the stage 2 of hydrogen loss.

alcohol solution, the first stage can be detected in about a week and lasts for several weeks before the second stage is reached. Therefore, by combing all the experimental evidence, we can use a scheme to describe all the transformation and the intermediate species (Figure 3.22).

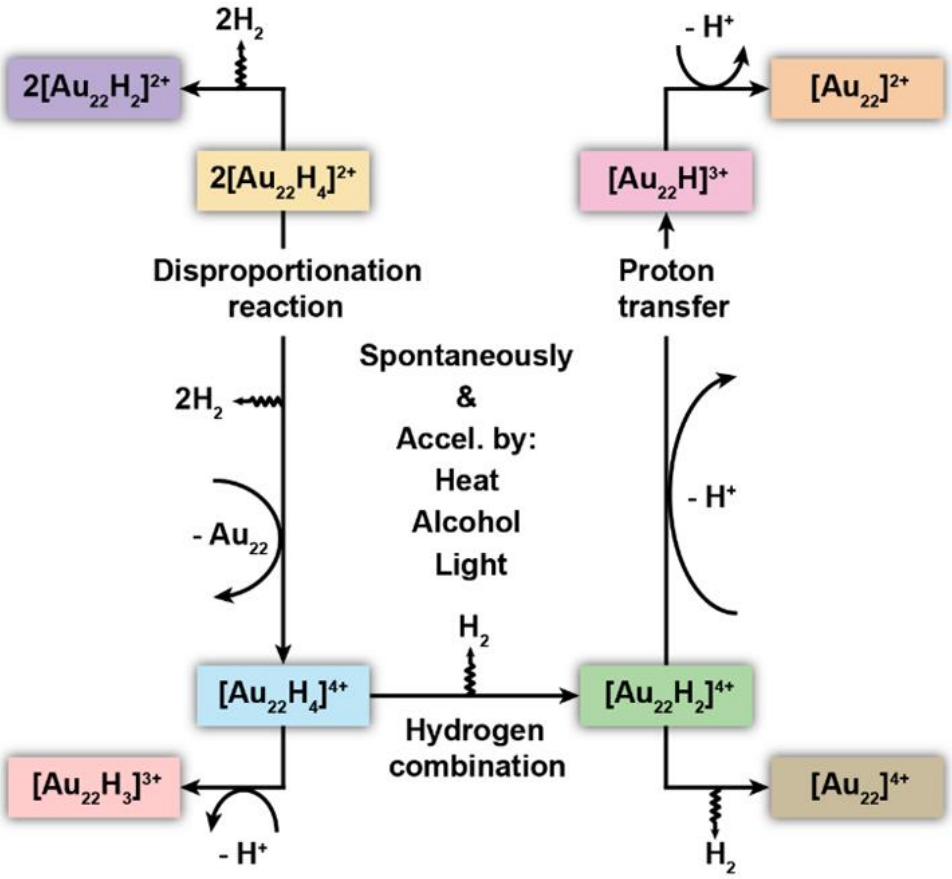

Figure 3.22 Schematics depicting the spontaneous H loss mechanisms from $[Au_{22}H_4(dppo)_6]^{2+}$ to different $[Au_{22}H_x(dppo)_6]^{n+}$ clusters (x = 0–3, n = 0, 2–4).

Apart from the proton release and hydrogen evolution of the four H atoms on $[Au_{22}H_4(dppo)_6]^{2+}$ cluster, we also noticed the existence of hydride release process. By adding an ethanol solution of $NaBD_4$ into $[Au_{22}H_4(dppo)_6]^{2+}$ cluster, five different $[Au_{22}H_{4-x}D_x(dppo)_6]^{2+}$ species (x = 1–4) could be observed in the ESI mass spectrum. As shown in

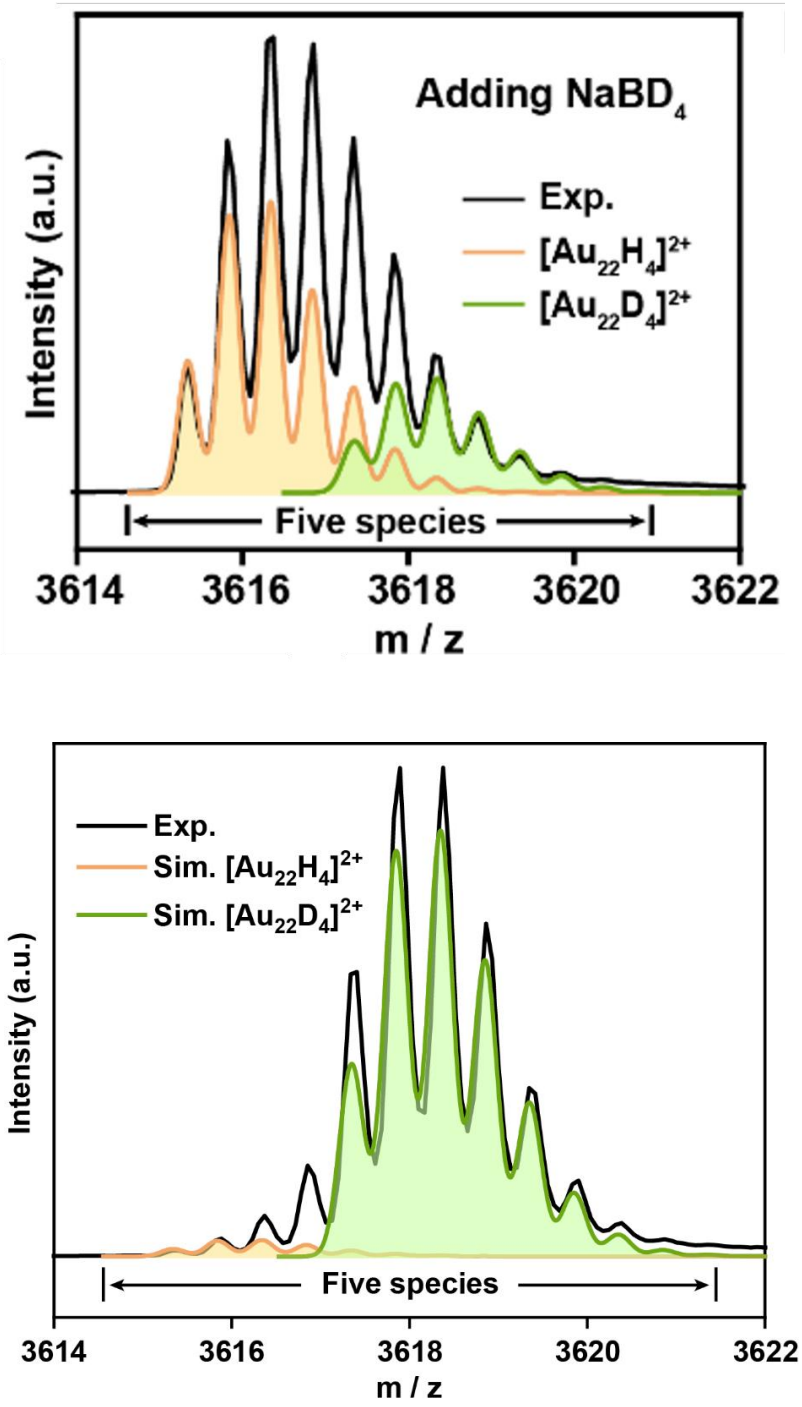

Figure 3.23 The hydride exchange experiment. Top: The isotopic distribution of $[Au_{22}H_4(dppo)_6]^{2+}$ after hydride exchange with $NaBD_4$. Bottom: The isotopic distribution of $[Au_{22}D_4(dppo)_6]^{2+}$ after hydride exchange with $NaBH_4$.

Figure 3.23 top, the isotopic scrambling was due to the rapid hydride transfers between $NaBD_4$ with $[Au_{22}H_4(dppo)_6]^{2+}$ cluster. Similarly, by adding an ethanol solution of $NaBH_4$ into $[Au_{22}D_4(dppo)_6]^{2+}$ cluster, five different $[Au_{22}H_{4-x}D_x(dppo)_6]^{2+}$ species (x = 1–4) could also be observed in the ESI mass spectrum. However, the addition of EtOD into $[Au_{22}H_4(dppo)_6]^{2+}$ solution or the addition of EtOH into $[Au_{22}D_4(dppo)_6]^{2+}$ solution doesn't lead to such hydride exchange phenomena. Therefore, the protonic H atom in ethanol cannot spontaneously exchange with the four H atoms in $[Au_{22}H_4(dppo)_6]^{2+}$ cluster. despite the fact that ethanol plays a role during the cluster synthesis or accelerates the H loss as a proton acceptor.

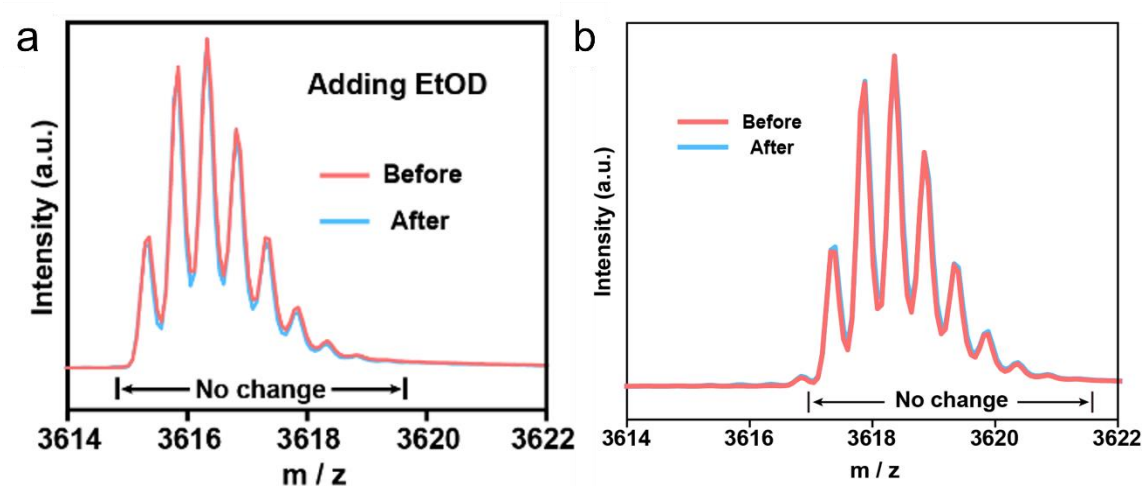

Figure 3.24 The hydride exchange experiment. a) The isotopic distribution of $[Au_{22}H_4(dppo)_6]^{2+}$ before and after the addition of EtOD. b) The isotopic distribution of $[Au_{22}D_4(dppo)_6]^{2+}$ before and after the addition of EtOH.

With the verification of hydride release as another spontaneous H loss pathway, we can summarize the three spontaneous H loss pathways on the $[Au_{22}H_4(dppo)_6]^{2+}$ cluster (Figure 3.25). In the proton release pathway, the hydrogen is released as a proton and simultaneously transferring an electron to the gold metal core, i.e. an electron-coupled

proton release process. This pathway is akin to an inverse process of the Volmer step in the hydrogen evolution reaction ($H^+ + e^- \rightarrow H$). In the hydrogen evolution pathway, two hydrogens combine intramolecularly, releasing a H_2 molecule while leaving the charge state of the gold core unchanged. This pathway is similar to the Tafel step in the hydrogen evolution reaction ($H + H \rightarrow H_2$), providing the first direct experimental evidence of this process on the surface of a gold nanocluster. In the hydride release pathway, the hydrogen comes off as a hydride by withdrawing an electron from the gold core. The diverse range of spontaneous H loss mechanisms revealed by the $[Au_{22}H_4(dppo)_6]^{2+}$ nanohydride is unprecedented, suggesting that it should be a versatile catalyst for different chemical

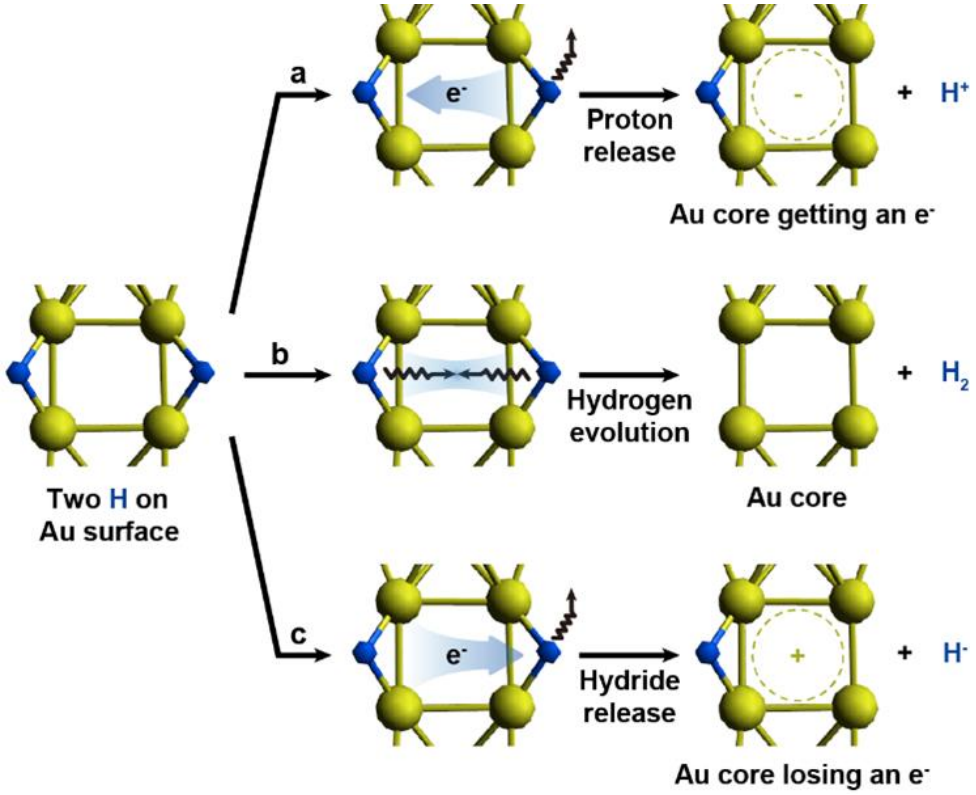

Figure 3.25 Schematic illustration of the three spontaneous hydrogen loss pathways on a nanogold surface revealed by the $[Au_{22}H_4(dppo)_6]^{2+}$ nanohydride. (a) Proton (H^+) release. (b) Hydrogen evolution. (c) Hydride (H^-) release.

reactions involving hydrogen, such as hydrogenation or hydrogen evolution reactions. More importantly, the $[Au_{22}H_4(dppo)_6]^{2+}$ nanohydride provides fundamental information about the behaviors of hydrogen on nanogold surfaces, broadening our understanding about the mechanisms of different hydrogen-related reactions catalyzed by gold nanoparticles.

3.2.5 Summary

In conclusion, we have isolated and characterized another gold nanohydride cluster $[Au_{22}H_4(dppo)_6]^{2+}$ and elucidated its chemical properties. The Au_{22} core in the nanohydride consists of two Au_{11} units bonded via eight uncoordinated gold atoms, where the four H atoms locate in the bridging positions. The properties as well as the chemical reactivity of these central H atoms has also been investigated. While the Au_{22} kernel is intact, the four H atoms are volatile. And three H loss channels are observed as proton release, H_2 evolution and hydride release, which are very important to the understanding of the catalytic mechanisms of hydrogen-related reactions on Au NPs.

3.3 A $[Au_{22}H_3(dppb)_7]^{3+}$ hydride cluster

3.3.1 The investigation of other diphosphine ligands

The success in the study of gold nanohydride cluster $[Au_{22}H_4(dppo)_6]^{2+}$ inspires us to think about whether the other diphosphine ligands [α,ω-bis(diphenylphosphino) alkanes of the general formula, $P(Ph)_2(CH_2)_mP(Ph)_2$ (abbreviated as L^m)] could be used to generate

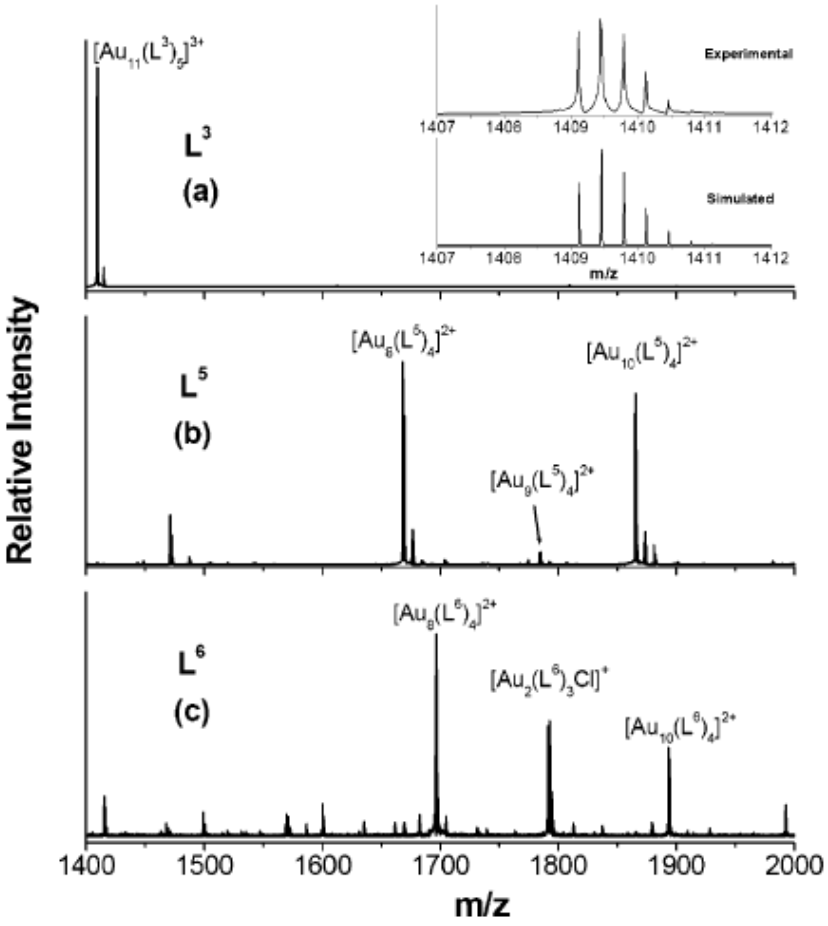

Figure 3.26 High-resolution mass spectrometry characterization of Au clusters stabilized with the indicated diphosphine ligand (L^m). The inset in (a) shows the isotopic pattern of the $[Au_{11}(L^3)_5]^{3+}$ mass peak, and the simulated isotopic pattern.[20] Copyright © 2006 American Chemical Society.

our target Au_{20} pyramid cluster or other interesting hydride-containing clusters. Our previous research on different diphenyl phosphine ligands (L^1 to L^6) has led to some important conclusions about the size selectivity on Au NCs with different chain length m of the ligand.[20] For the cases with monodentate phosphine ligand PPh_3, due to the usage of mild reducing agent borane-*tert*-butylamine complex, only some small Au_n ($n<10$) NCs could be detected within 100 min. By extending the reaction time to over 5h, the Au NC sizes increased which covered from Au_{10} to Au_{25}. And peak intensity of the desired Au_{20} cluster was not very prominent. When switching to bidentate phosphine ligands, as is shown in Figure 3.26, the L^3 ligand is highly selective towards $[Au_{11}(L^3)_5]^{3+}$ cluster and a single peak could be observed in mass spectrum. While the L^4 ligand also leads to the formation of a polydisperse mixture of clusters, the L^5 and L^6 ligand is again very selective towards Au_8 and Au_{10} clusters. Therefore, the study demonstrates that the clusters size can be varied by varying the length of the spacer separating the P atoms in the diphosphine ligands and some can be very size-selective.

When it's compared with the L^8 ligand used to synthesize $[Au_{22}H_4(dppo)_6]^{2+}$ or $Au_{22}(dppo)_6$ cluster, the distinct synthetic methods may be the cause for yielding very different clusters for the little difference between L^6 and L^8 ligands. For the synthesis of $[Au_{22}H_4(dppo)_6]^{2+}$ cluster, a stronger reducing agent $NaBH_4$ initiates the nucleation of gold precursors in just a few minutes with the color of the solution changed from light yellow to black. And the reaction is performed at 0 ^oC instead of room temperature. It's natural to think whether the reaction conditions such as different reducing agent, ratio of reducing agent to gold precursor, temperature, etc. can make a difference in yielding some interesting clusters and especially the Au_{20} pyramid cluster. The following parts focus on

the discovery of some other hydride-containing clusters from the diphosphine ligands by controlling different reaction conditions.

3.3.2 Synthesis of $[Au_{22}H_3(dppb)_7]^{3+}$ hydride cluster

Chemicals: The chemicals listed below were used as received. Chloro(dimethylsulfide)gold(I) (≥97%, Strem), 1,4-bis(diphenylphosphino)octane (dppb, 99%, Strem), sodium borohydride ($NaBH_4$, ≥98.0%, Sigma-Aldrich), sodium borodeuteride ($NaBD_4$, 98 atom % D, Sigma-Aldrich), acetone (≥99.5%, Certified ACS, Fisher Scientific), methylene chloride (≥99.5%, Certified ACS, Fisher Scientific), ethanol (≥99.5%, 200 proof, ACS reagent, Sigma-Aldrich), ethanol-OD (≥99.5% atom %D, Sigma-Aldrich).

Characterization techniques:

ESI-MS: Positive ionization mode ESI mass spectra were measured on an Agilent 6530 Accurate Mass Q-TOF LC-MS system (with Agilent 1260 HPLC). The CH_2Cl_2 solution of the sample (*ca.* 1.0 mg mL^{-1}) was introduced into the system through a stainless steel needle via flow injection. Acetonitrile/water (1/1 ratio) was used as the mobile phase at a flow rate of 200 µL min^{-1}. The source temperature was kept at 130 ˚C. The fragmentor voltage was set at 50 V, skimmer at 65 V, and the capillary voltage at 3500 V. The measuring mass range was 0 to 20,000 m/z units. All spectra were recorded at a rate of 1 spectrum s^{-1}. Different species were assigned using isotopic distributions in the high-resolution spectra by comparing with simulated spectra.

NMR Spectroscopy**:** ^{1}H, ^{31}P-NMR were obtained on a 600 MHz Bruker Ultrashield spectrometer using CD_2Cl_2 as the solvent. Unless further noted, the NMR spectra were

measured at 298 K. Chemical shifts (δ) are reported in ppm and referenced to internal solvent resonances for ^{1}H-NMR and external 85% H_3PO_4 for ^{31}P-NMR. Coupling constants (*J*) are reported in Hertz (Hz). All data were processed using the TopSpin or MestReNova software.

Synthesis and characterization of the $Au_2(dppb)Cl_2$ gold precursors:

Synthesis: A sample of 183 mg (0.43 mmol) of dppb was first added to a Schlenk flask containing 30 mL acetone. After vigorously stirring for about 15 mins, 254 mg (0.86 mmol) of chloro(dimethylsulfide)gold(I) dissolved in 50 mL acetone was quickly added. The reaction was allowed to proceed for 24 hours at room temperature in the dark. The white precipitates were filtered, dried and washed with pentane. Finally, 349 mg of $Au_2(dppb)Cl_2$ was obtained with a yield of 91%.

Characterization: The as-obtained $Au_2(dppb)Cl_2$ gold precursor was firstly characterized with ESI mass spectrometer. As is shown in Figure 3.27, one dominant peak could be observed at 855 Da which could be assigned to $[Au_2(dppb)Cl]^+$ based on the isotope distribution profile. The NMR spectra were also taken for the precursor to ensure

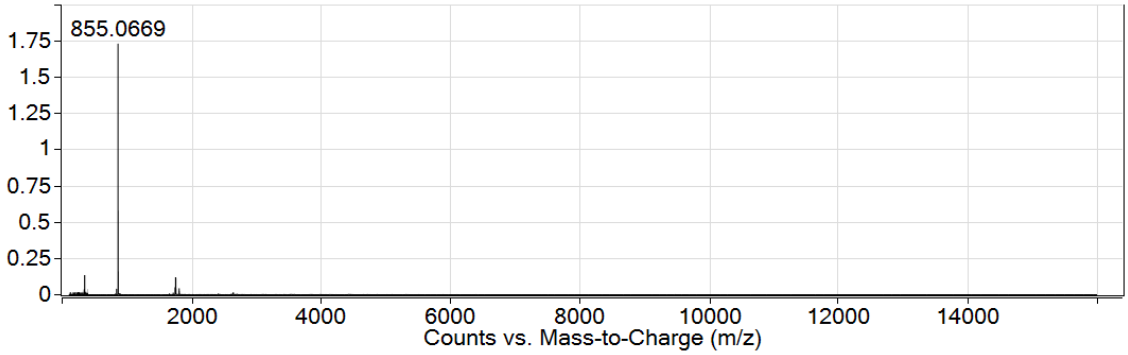

Figure 3.27 ESI-MS of the $Au_2(dppb)Cl_2$ gold precursor.

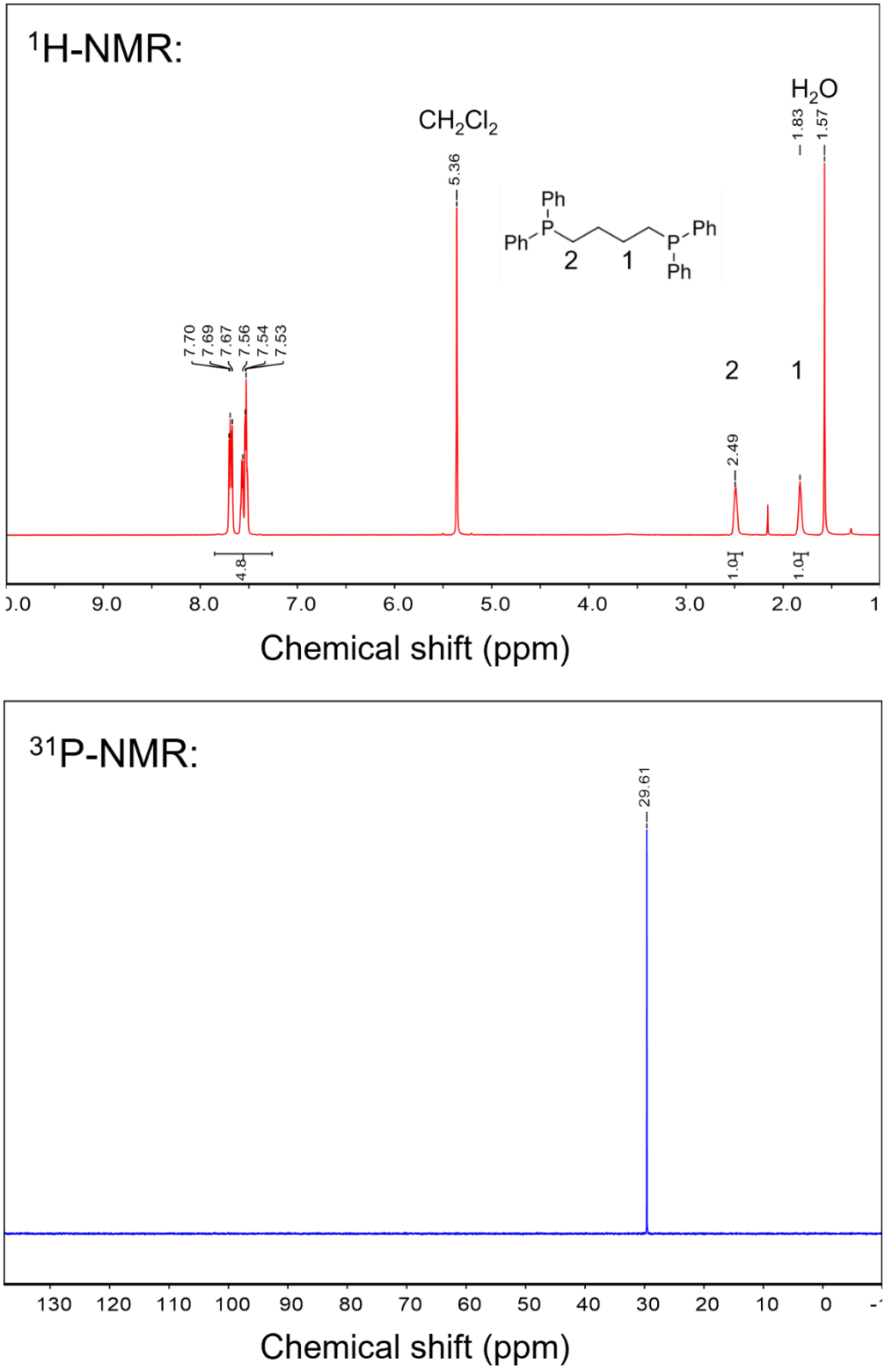

Figure 3.28 NMR spectra for the $Au_2(dppb)Cl_2$ gold precursor.

there were no other impurities that might change the results. In Figure 3.28, we can notice that the quality of the precursor was very high. The theoretical ratio of the aromatic H to alkyl H is 20:8 of the dppb ligand. The experimental ratio could be measured based on the integrated peak ratio on the NMR spectrum, which was 4.8 to 2. And only a single peak could be observed in the ^{31}P-NMR spectrum, indicating the same chemical environment of all the P atoms in the precursor.

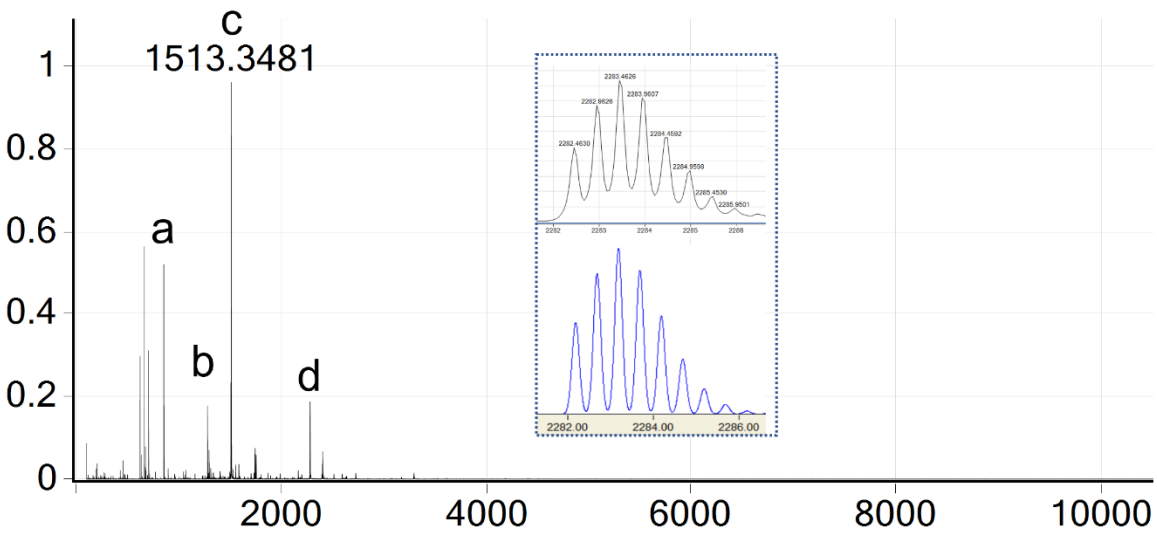

Peak Label	Experimental m/z of the peak	Charge state	Formula	Peak intensity relative to the most intense peak
a	855.17	+1	$(C_{28}H_{28}P_2)Au_2Cl$	0.56
b	1281.38	+1	$(C_{28}H_{28}P_2)_2Au_2Cl$	0.21
c	1513.35	+1	$(C_{28}H_{28}P_2)_3Au_2Cl_2$	1
d	2283.46	+2	$(C_{28}H_{28}P_2)_5Au_{12}Cl_2$	0.21

Figure 3.29 Top: ESI-MS for crude product after 2h reaction time. Bottom: Assignments for some of the peaks in the spectrum.

Experiments towards the $[Au_{22}H_3(dppb)_7]^{3+}$ hydride cluster:

The experiment employing $Au_2(dppb)Cl_2$ gold precursor starts from reducing with stoichiometry amounts of concentrated ethanol solution of $NaBH_4$ (30 mg/5 mL). To save the gold precursor, all the trials were performed with 4 mg of $Au_2(dppb)Cl_2$ (0.0045 mM) gold precursor each time. The reaction can be scaled up only after the conditions are optimized for target clusters.

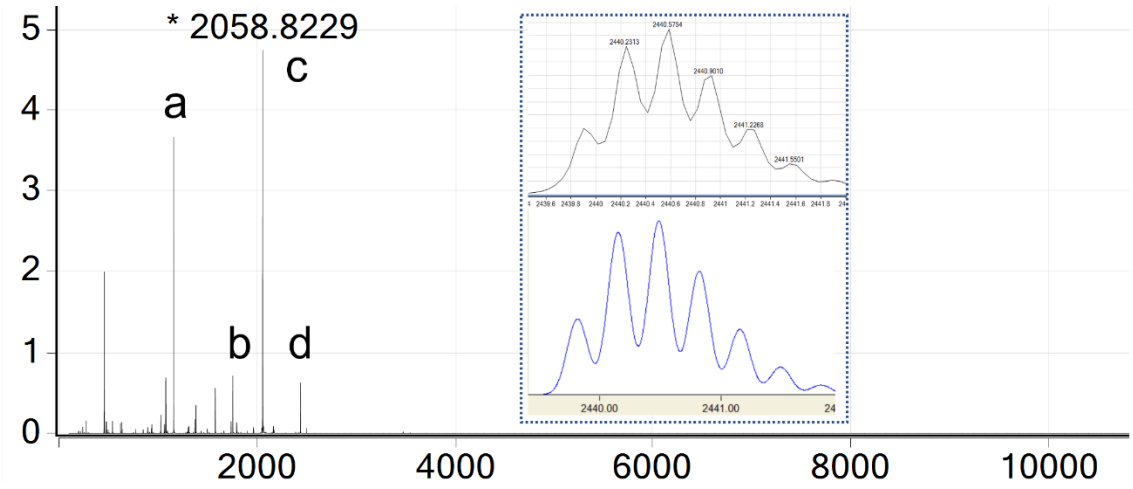

Peak Label	Experimental m/z of the peak	Charge state	Formula	Peak intensity relative to the most intense peak
a	1159.50	+3	$(C_{28}H_{28}P_2)_4Au_9$	0.79
b	1756.73	+3	$(C_{28}H_{28}P_2)_4Au_9Cl$	0.15
c	2058.82	+2	$(C_{28}H_{28}P_2)_5Au_{10}BH_4$	1
d	2440.58	+3	$(C_{28}H_{28}P_2)_7Au_{22}H_3$	0.14

Figure 3.31 Top: ESI-MS for crude product after 2h reaction time. Bottom: Assignments for some of the peaks in the spectrum.

The first reaction was done by injecting $NaBH_4$ solution (1:1 ratio to Au) into 4 mg of $Au_2(dppb)Cl_2$ in 2 mL DCM under stirring at room temperature. After 2h reaction, aliquot was taken to take ESI mass spectrum for crude product. The relative ratio of the species in the crude product is correlated to the peak intensity ratio in the spectrum. As is shown in Figure 3.29, the low ratio of $NaBH_4$ only leads to the formation of small clusters. Only a Au_{12} cluster could be observed at 2283 m/z and most of the precursor remained unreacted. Other aliquots were also taken after 6h, 1d and 2d, the spectra didn't change too much and larger cluster peak couldn't be observed. Then, I tried to increase the ratio of $NaBH_4$ from 1:1 ratio to Au to 5:1 ratio to Au, and kept other parameters the same at the same time. Very interestingly, as shown in Figure 3.30, larger clusters were obtained as a result. The most intense peaks were Au_9, Au_{10} and even a Au_{22} clusters. More experiments will be performed in the following parts to verify the origin of the hydrogens on the cluster. The other reaction conditions are nearly identical to the previous experiment in 2006, in which the reduction by borane-*tert*-butylamine complex led to the formation of polydisperse cluster solution. Therefore, the results from controlled experiment indicate that the type of reducing agent as well as the ratio matter a lot to the formation of phosphine protected Au NCs. After the discovery of this new hydride cluster, more controlled experiments were done to optimize the yield (relative ratio of peak intensity). And when the ratio of $NaBH_4$ to Au is 1.5:1, the yield of $[Au_{22}H_3(dppb)_7]^{3+}$ is the highest (Figure 3.31).

Based on this understanding, even though I didn't try different reducing reagent, I tried to add some strong base (NaOH) into the reaction to change the reduction capability. In fact, a NaOH-mediated $NaBH_4$ reduction strategy has been successfully applied for

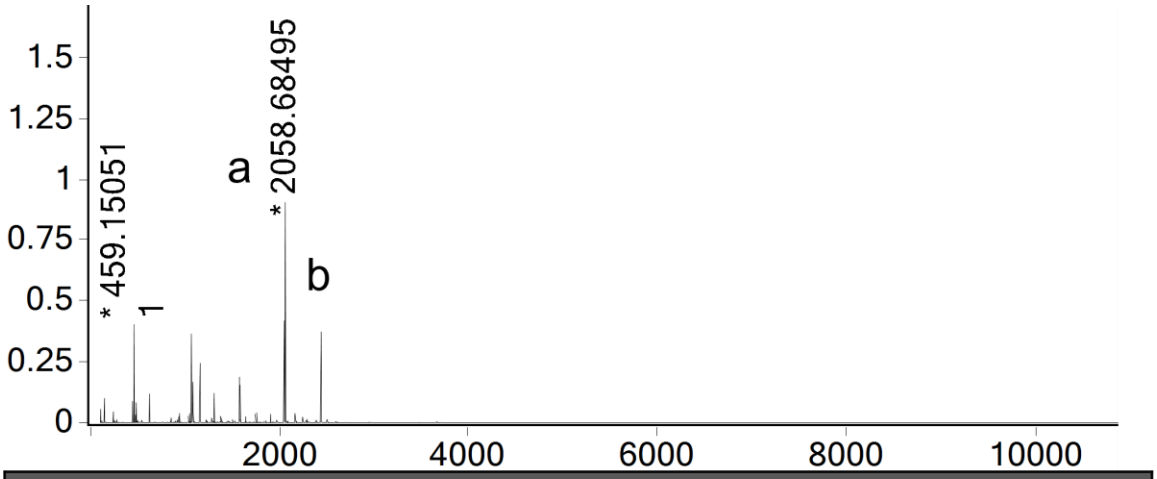

Peak Label	Experimental m/z of the peak	Charge state	Formula	Peak intensity relative to the most intense peak
a	2058.82	+2	$(C_{28}H_{28}P_2)_5Au_{10}BH_4$	1
b	2440.58	+3	$(C_{28}H_{28}P_2)_7Au_{22}H_3$	0.42

Figure 3.31 Top: ESI-MS for crude product after 2h reaction time. Bottom: Assignments for some of the peaks in the spectrum.

controlled synthesis of atomically precise thiolate Au_{25} NCs with various thiolate ligands.[21] Yuan et al. put forward that NaOH plays two roles during the synthesis: 1. It can slow down the reduction rate of Au NCs through effectively retarding the hydrolysis of $NaBH_4$. 2. NaOH can regulate the interaction between Au and thiolate ligands. It's still very challenging to study the effects NaOH during the reducing of Au precursors because the reduction is very fast and hard to capture the intermediates. I carried out some other controlled experiments to study the effect of NaOH during the reduction of $Au_2(dppb)Cl_2$ gold precursor. The NaOH was dissolved in methanol (100mg/2mL) and added by a syringe into the precursor solution. The ratio of NaOH to Au was 1:1. And after mixing thoroughly for 10min, the reducing reaction could be proceeded with the injection of

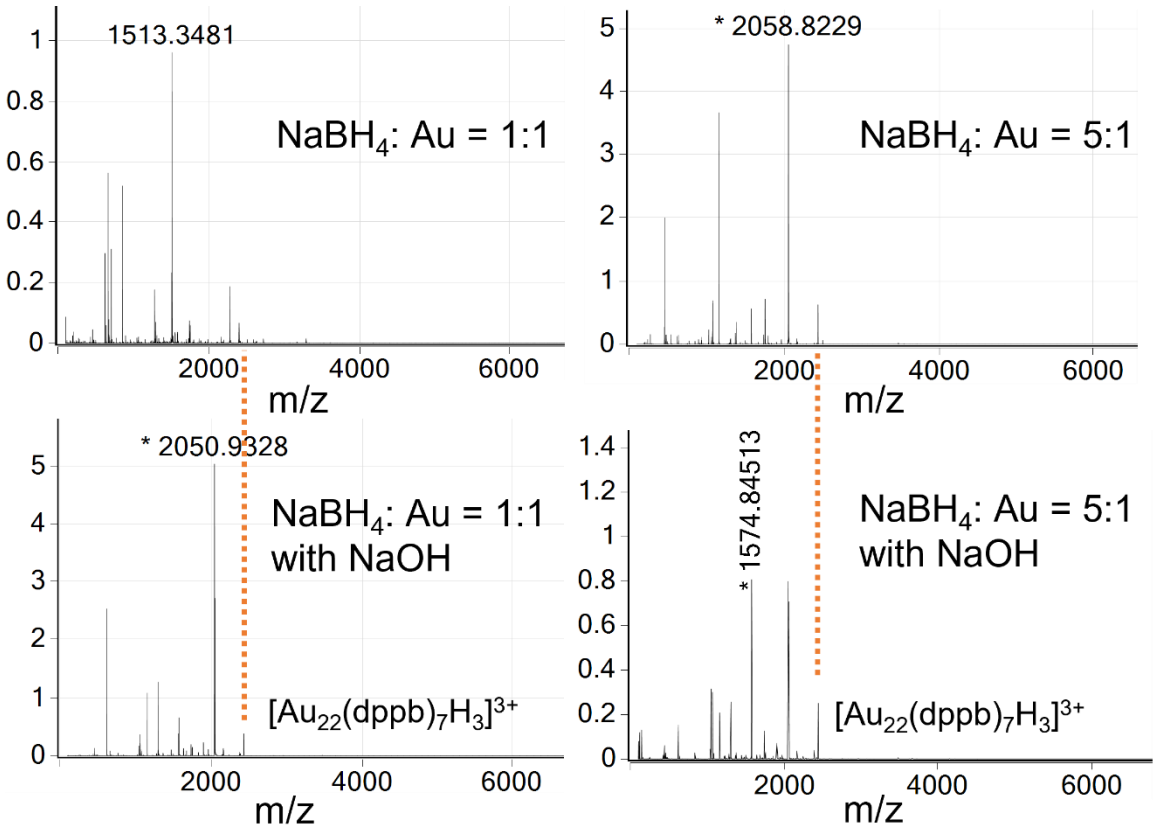

Figure 3.32 ESI-MS results for the crude products under different reaction conditions.

$NaBH_4$ solution. As is shown in Figure 3.32, when the ratio of $NaBH_4$ is 1:1 to Au, the introduction of KOH completely changed the resulting products after reduction. Most of the precursors could be converted into Au NCs, we can observe a prominent $[Au_{10}(dppb)_5]^{2+}$ cluster peak at 2050.9 Da after 2h as well as the $[Au_{22}H_3(dppb)_7]^{3+}$ hydride cluster peak. This result showed that the reducing power of the reducing reagent did make a huge difference in the formation of clusters. To exclude the effect of OH^- during the synthesis of clusters, sodium ethoxide (EtONa) was used to substitute NaOH in the controlled experiment. These two reagents have similar pKa values: 15.5 for EtONa and 15.7 for NaOH. And despite the peak intensities for some smaller clusters did show some

changes, the yield of the $[Au_{22}H_3(dppb)_7]^{3+}$ hydride cluster didn't change too much with the same amounts of these two reagents.

After these controlled experiments, I further tried to scale up the reaction in order to obtain purer $[Au_{22}H_3(dppb)_7]^{3+}$ hydride cluster sample for the following characterizations as well as potential applications. The amounts of precursor could be increased to 24 mg, but the highest yield could be achieved only when the solvent amount (DCM) remains 4 mL. And the reduction was initiated with the injection of 1.5 times of $NaBH_4$ solution under stirring. After reacting for 2h, the crude sample was dried with rotary evaporator to remove all the solvents. Finally, the solid sample was dissolved in small amounts of DCM and loaded on a silica column for purification. The combination of DCM and methanol was used, and the final pure product was collected in 4:1 ratio fraction. Aliquots could be taken during these steps and characterized with ESI mass spectrometer.

3.3.3 The characterization of $[Au_{22}H_3(dppb)_7]^{3+}$ hydride cluster

After the purification process, the ESI mass spectrum could be taken to identify the cluster species in the solution. As is shown in Figure 3.33, the final product showed a distinct peak in the ESI mass spectrum, which was centered at around 2440 m/z. The perfect match between the experimental isotope distribution profile with the simulated profile indicated the formula of the cluster was exactly $[Au_{22}H_3(dppb)_7]^{3+}$. And to ensure that the three H atoms didn't come from the electrospray process, we performed isotope labelling experiment by using $NaBH_4$ instead of $NaBD_4$ to do the synthesis again. Still, the experimental isotopic distribution profile matched well with the simulated result, which 1

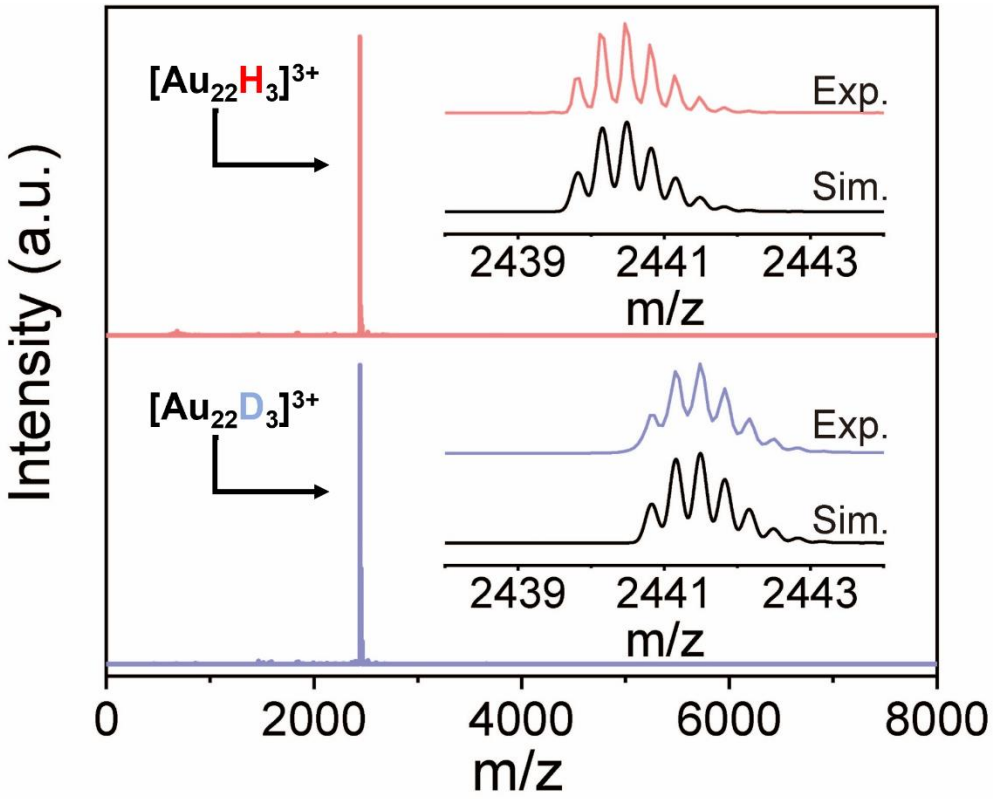

Figure 3.33 ESI-MS spectra of $[Au_{22}H_3]^{3+}$ and $[Au_{22}D_3]^{3+}$; the insets show the experimental and simulated isotopic distributions.

mass unit shift compared with the profile of the $[Au_{22}H_3(dppb)_7]^{3+}$. Therefore, this result confirmed that all three H atoms come from the reducing agent. Then the cluster sample was further characterized with NMR spectrometer. In the ^{1}H-NMR spectrum, a characteristic peak at ca 14.8 ppm could be observed, which is around the same chemical shift with the $[Au_{22}H_4(dppo)_6]^{2+}$ cluster (Figure 3.34). And the peak ratio of the aromatic H to Au-H region is around 153.3/3, similar to the theoretical ratio (140/3) based on the formula. The ^{31}P-NMR spectrum was very complicated and multiple peaks could be observed at 40 – 65 ppm region. This suggests that the phosphorus environment on the cluster is very diverse.

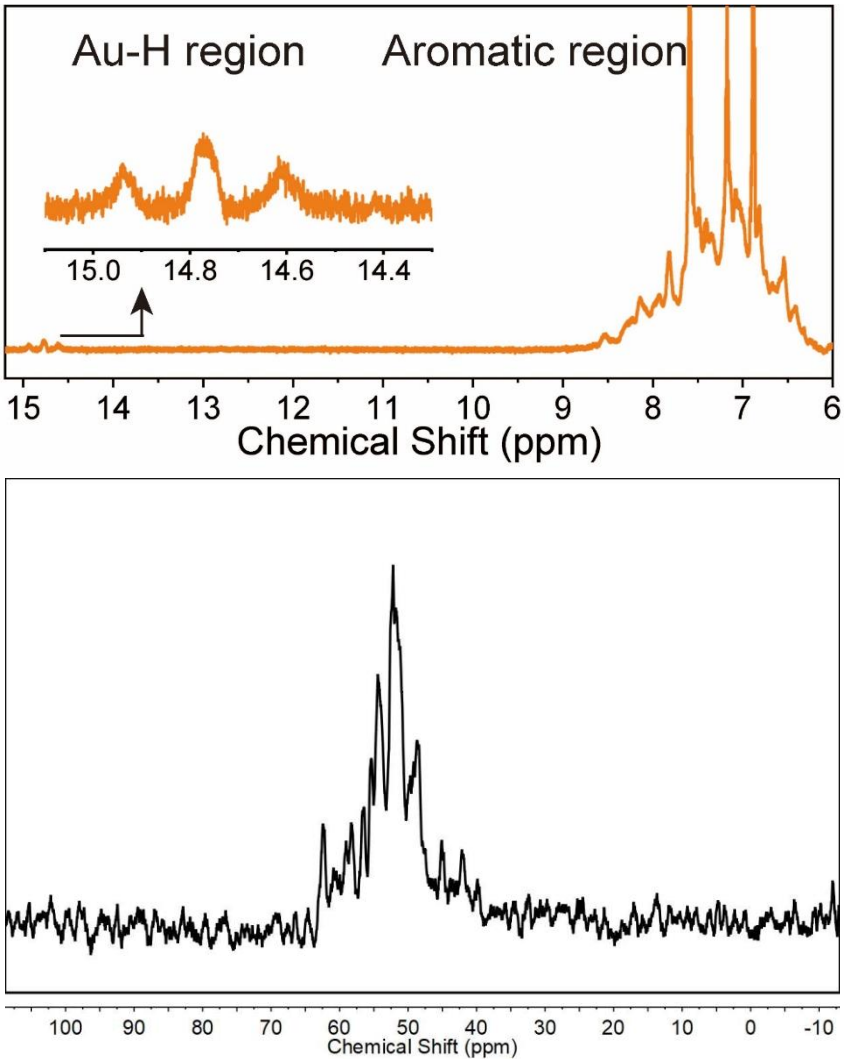

Figure 3.34 NMR spectra of the $[Au_{22}H_3(dppb)_7]^{3+}$ cluster. Top: ^{1}H-NMR spectrum. Bottom: ^{31}P-NMR spectrum.

UV-Vis absorption spectrum of the $[Au_{22}H_3(dppb)_7]^{3+}$ cluster was also taken and compared with the previously reported hydride clusters. As is shown in Figure 3.35, the $[Au_{22}H_3(dppb)_7]^{3+}$ cluster has absorption features around 315 nm, 390 nm and 475 nm. Although the absorption features of the cluster are not resemble that from $[Au_{22}H_4(dppo)_6]^{2+}$ cluster, they are nearly identical to the $[Au_{22}H_3(dppee)_7]^{3+}$ [dppee =

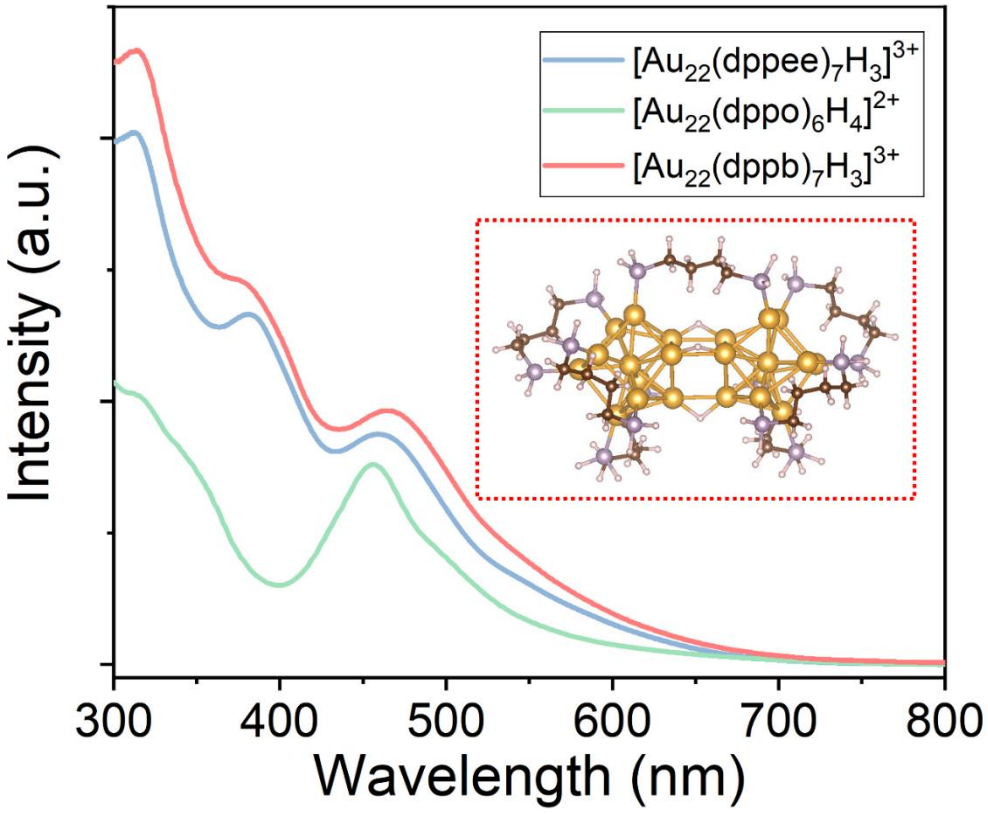

Figure 3.35 UV-Vis absorption spectra of three Au_{22} hydride clusters. Insert: Optimized structure of $[Au_{22}H_3(dppb)_7]^{3+}$.

bis(2-diphenylphosphino) ethyl ether] cluster reported by our group. Only around 5 nm red shift of the first two absorption peaks could be observed. The third one around 315 nm was in the same position. The difference between the two ligands is one extra O atom in dppee ligand. The formula of these two clusters is similar. The effort in trying to grow single crystal of this cluster was not successful. Nevertheless, based on all these similarities, DFT calculations could still be carried out to optimize the structure of the $[Au_{22}H_3(dppb)_7]^{3+}$ cluster, as is shown in Figure 3.36 Insert. Two Au_{11} units are bonded via two triangular faces, creating six uncoordinated Au sites at the interface. The three H atoms bridge the six uncoordinated Au atoms at the interface and a bridging L^4 ligand links the two units.

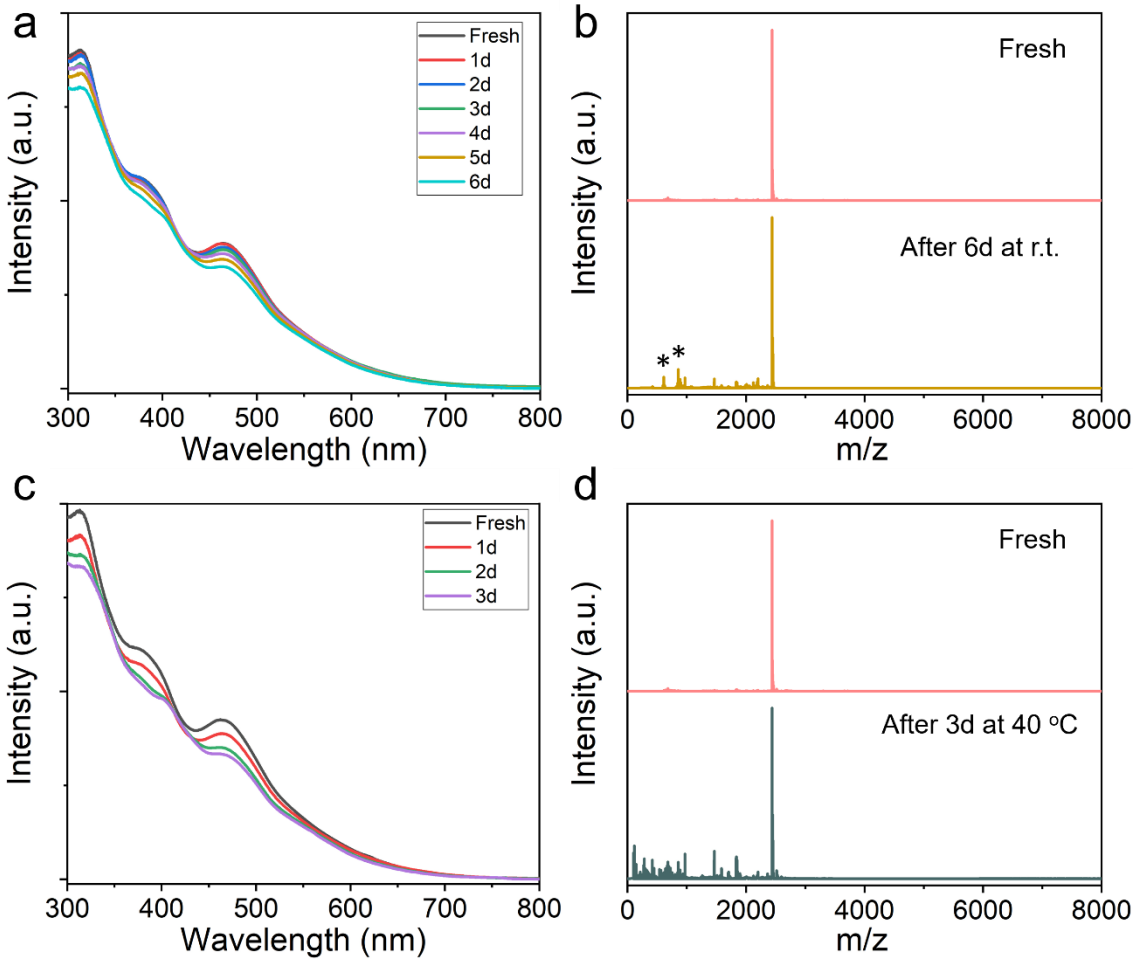

Figure 3.36 Stability test of $[Au_{22}H_3(dppb)_7]^{3+}$ cluster at room temperature and 40 °C. Time-dependent UV-Vis absorption spectra at a) r.t. and c) 40 °C. Time-dependent ESI-MS at b) r.t. and d) 40 °C. The * could be assigned to $[Audppb]^+$, $[Au_2dppbCl]^+$.

The stability of the cluster sample could be determined with the ESI-MS, UV-Vis absorption spectrometer. As is shown in Figure 3.36, the DCM solution of $[Au_{22}H_3(dppb)_7]^{3+}$ cluster is stable for 6 days under ambient conditions at room temperature with slightly decomposition. Some AuL^4 compounds showed up in the ESI-MS spectra which came from the decomposition of the cluster peak. Under 40 °C, the stability of the cluster is much worse. The absorption spectra evolution indicated that the cluster

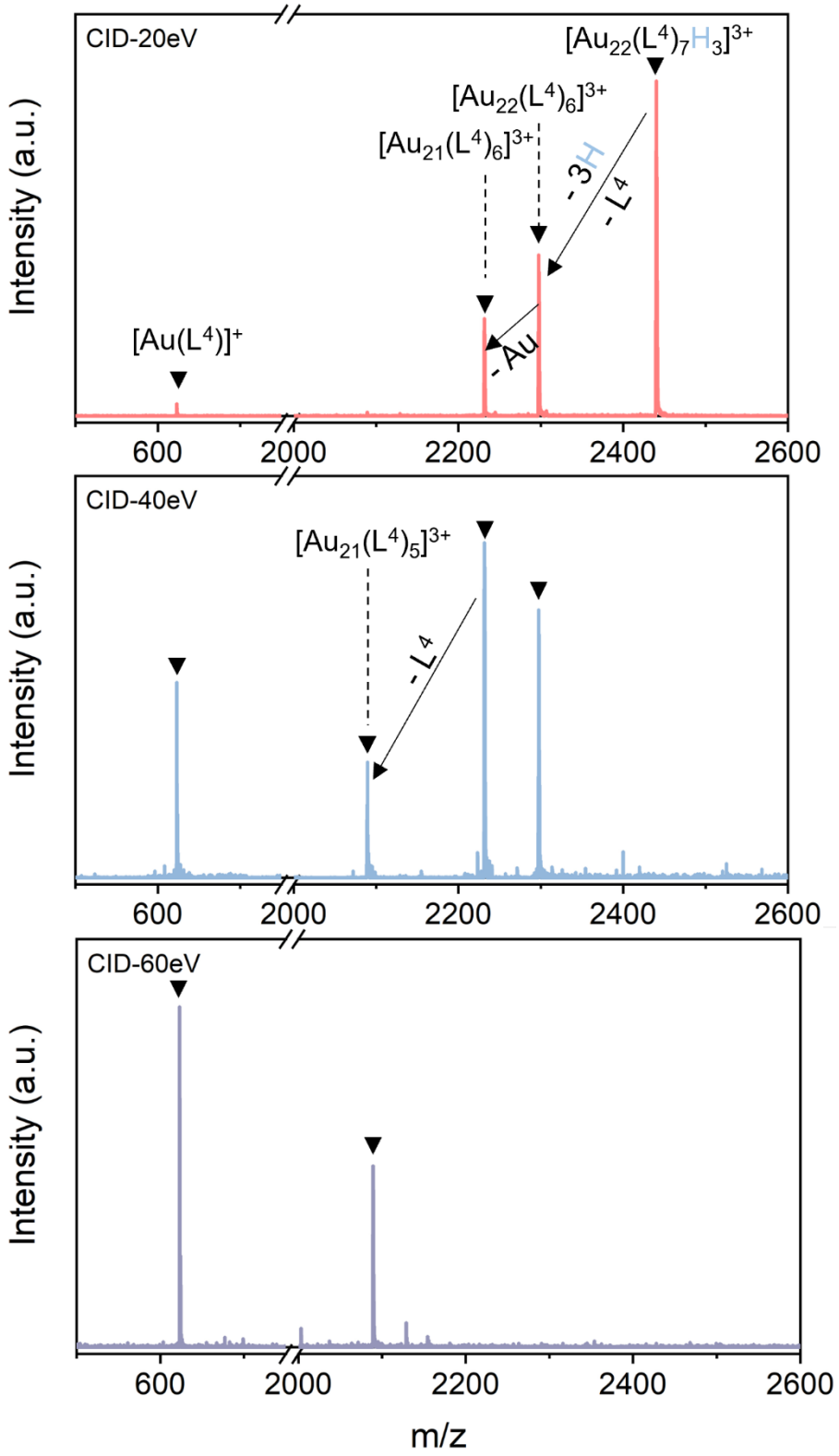

Figure 3.37 CID spectra of $[Au_{22}H_3(dppb)_7]^{3+}$ cluster under different dissociation voltages.

decomposed just in one day. And after two days, the peak at 390 nm almost disappeared in the spectra with the first absorption peak at around 475 nm became obsolete. The ESI mass spectrum after 3 days showed that multiple peaks at low mass range, indicating that the decomposition process was more complicated than that at room temperature. In the solid state, the cluster could be highly stable for over 6 months with nearly no decomposition. Collision-induced dissociation mass spectra were also taken targeting the $[Au_{22}H_3(L^4)_7]^{3+}$ cluster peak at various voltages. As we can see in Figure 3.37, the cluster peak remained intact until 20 eV, followed by slightly decomposition of losing all three H atoms and one L^4 ligand to form $[Au_{22}(L^4)_6]^{3+}$, which might be the bridging L^4 ligand from the optimized structure. Then one Au atom could leave to form $[Au_{21}(L^4)_6]^{3+}$. At around 40 eV, the original $[Au_{22}H_3(L^4)_7]^{3+}$ cluster peak completely disappeared with higher peak intensity for both $[Au_{22}(L^4)_6]^{3+}$ and $[Au_{21}(L^4)_6]^{3+}$. The $[Au_{21}(L^4)_6]^{3+}$could further lose another L^4 ligand to form $[Au_{21}(L^4)_5]^{3+}$. The $[Au(L^4)]^+$ peak intensity kept rising during this dissociation process, which should be the dissociation product from the larger clusters. At around 60 eV, both $[Au_{22}(L^4)_6]^{3+}$ and $[Au_{21}(L^4)_6]^{3+}$ cluster peak disappeared, indicating that the $[Au_{21}(L^4)_5]^{3+}$ dominated in the higher mass range. Therefore, based on the information from CID mass spectra, we can understand that the three H atoms as well as one L^4 ligand are the most volatile and the Au_{22} kernel can be stable for up to 40 eV.

It's also of great interest to study the properties of the three H atoms and make comparison with those in $[Au_{22}H_4(dppo)_6]^{2+}$ cluster. Hydride exchange experiments are carried out. With the addition of excess amounts of $NaBD_4$ (5 times to cluster), the cluster peak in the ESI mass spectrum became much broader after one hour which was due to the formation of four $[Au_{22}H_xD_{3-x}(L^4)_7]^{3+}$ (x=3,2,1,0) clusters (Figure 3.38). And after reacting

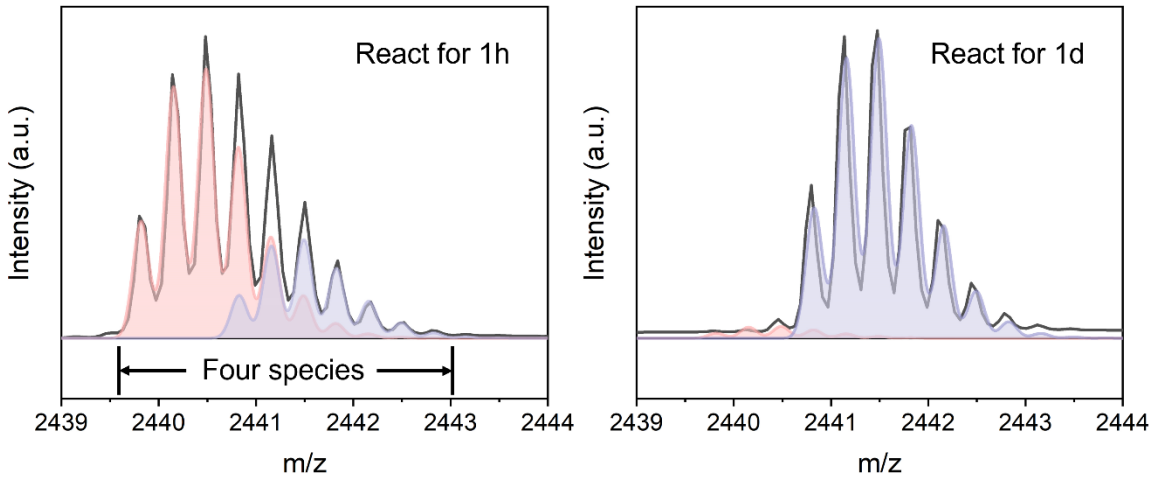

Figure 3.38 The hydride exchange experiment of $[Au_{22}H_3(L^4)_7]^{3+}$ cluster with excess $NaBD_4$ after 1h and 1d.

for one day, the peak became narrower again, which indicated the completion of hydride exchange. Similarly, the addition of excess amounts of $NaBH_4$ (5 times to cluster) into the solution of $[Au_{22}D_3(L^4)_7]^{3+}$ resulted in the formation of similar four species after 1h (Figure 3.39). And the proceeding of the reaction after 1d led to the almost completion of the deuteride exchange. However, the hydride exchange experiments of $[Au_{22}H_3(L^4)_7]^{3+}$ cluster

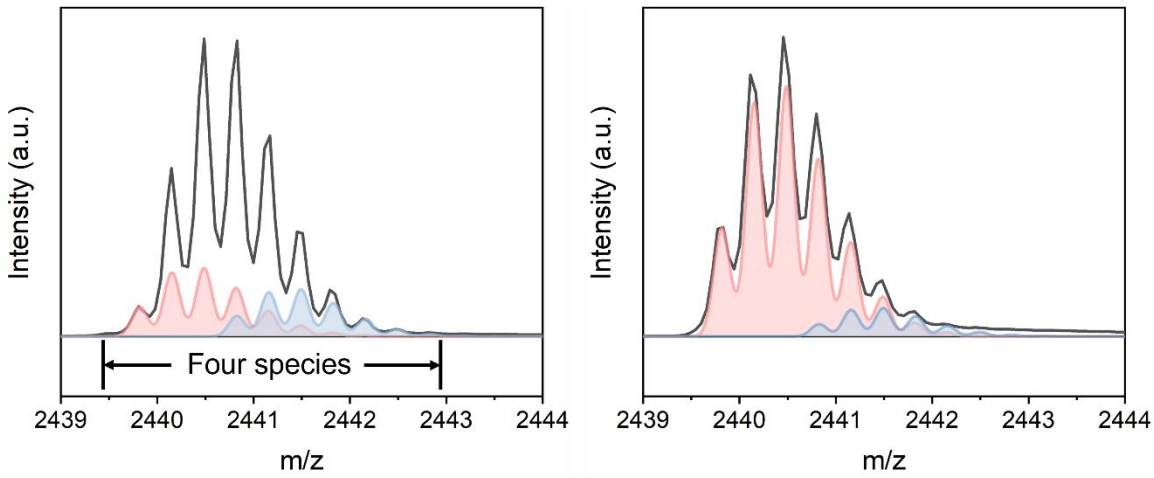

Figure 3.39 The hydride exchange experiment of $[Au_{22}D_3(L^4)_7]^{3+}$ cluster with excess $NaBH_4$ after 1h and 1d.

with EtOD or $[Au_{22}D_3(L^4)_7]^{3+}$ cluster with EtOH didn't lead to any changes in the ESI mass spectra. These experiment results were similar to those of $[Au_{22}H_4(dppo)_6]^{2+}$ cluster. The three H atoms on the cluster are only exchangeable with hydride from $NaBH_4$ instead of proton from EtOH.

3.4 Summary

To summarize, we successfully synthesized two types of hydride-containing Au_{22} clusters: a tetrahydride $[Au_{22}H_4(dppo)_6]^{2+}$ cluster and a trihydride $[Au_{22}H_3(dppb)_7]^{3+}$ cluster. The controlled experiments in the synthesis indicated that the reducing power as well as the ratio of the reducing agent did result in a huge difference in the final products. Both clusters have been subjected to thorough characterizations with ESI-MS, UV-Vis absorption, NMR spectroscopy. The comparisons have also been made between these two clusters. And all the results confirm the existence of H atoms on the cluster samples and the hydride exchange experiments on both clusters indicate that these H atoms are only exchangeable with hydrides in reducing agent instead of protons from the solvent. The stability of the clusters is also studied under ambient condition, elevated temperature, and solid state. The study of these novel hydride containing Au_{22} clusters could lead to more ongoing investigations into the effect of synthetic conditions as well as the discovery of more phosphine protected gold hydride NCs.

References

(1) Sun, C.; Teo, B. K.; Deng, C.; Lin, J.; Luo, G. G.; Tung, C. H.; Sun, D. Hydrido-coinage-metal clusters: Rational design, synthetic protocols and structural characteristics. *Coord. Chem. Rev.* **2021**, *427*, 213576.

(2) Jordan, A. J.; Lalic, G.; Sadighi, J. P. Coinage metal hydrides: synthesis, characterization, and reactivity. *Chem. Rev.* **2016**, *116* (15), 8318-8372.

(3) Liu, H. T.; Wang, Y. L.; Xiong, X G.; Dau, P. D.; Piazza, Z. A.; Huang, D. L.; Xu, C.-Q.; Li, J.; Wang, L S. The electronic structure and chemical bonding in gold dihydride: AuH_2^- and AuH_2. *Chem.Sci.* **2012**, *3* (11), 3286-3295.

(4) Schmidbaur, H.; Raubenheimer, H. G.; Dobrzańska, L. The gold–hydrogen bond, Au–H, and the hydrogen bond to gold, Au··· H–X. *Chem. Soc. Rev.* **2014**, *43* (1), 345-380.

(5) Buckart, S.; Ganteför, G.; Kim, Y. D.; Jena, P. Anomalous behavior of atomic hydrogen interacting with gold clusters. *J. Am. Chem. Soc.* **2003**, *125* (46), 14205-14209.

(6) Donnerer, C.; Scheler, T.; Gregoryanz, E. High-pressure synthesis of noble metal hydrides. *J. Chem. Phys.* **2013**, *138* (13), 134507.

(7) Wurtz, A. On copper hydride (Translated from French). *Cr Hebd Acad Sci* **1844**, *18*, 702-704.

(8) Daniel, M. C.; Astruc, D. Gold nanoparticles: assembly, supramolecular chemistry, quantum-size-related properties, and applications toward biology, catalysis, and nanotechnology. *Chem. Rev.* **2004**, *104* (1), 293-346.

(9) Haruta, M. Size-and support-dependency in the catalysis of gold. *Catal. Today* **1997**, *36* (1), 153-166.

(10) Conte, M.; Miyamura, H.; Kobayashi, S.; Chechik, V. Spin trapping of Au−H intermediate in the alcohol oxidation by supported and unsupported gold catalysts. *J. Am. Chem. Soc.* **2009**, *131* (20), 7189-7196.

(11) Mitsudome, T.; Noujima, A.; Mikami, Y.; Mizugaki, T.; Jitsukawa, K.; Kaneda, K. Supported gold and silver nanoparticles for catalytic deoxygenation of epoxides into alkenes. *Angew. Chem., Int. Ed.* **2010**, *49* (32), 5545-5548.

(12) Luza, L.; Rambor, C. P.; Gual, A.; Alves Fernandes, J.; Eberhardt, D.; Dupont, J. Revealing hydrogenation reaction pathways on naked gold nanoparticles. *ACS Catal.* **2017**, *7* (4), 2791-2799.

(13) Ishida, R.; Hayashi, S.; Yamazoe, S.; Kato, K.; Tsukuda, T. Hydrogen-mediated electron doping of gold clusters as revealed by in Situ X-ray and UV–vis absorption spectroscopy. *J. Phys. Chem. Lett.* **2017**, *8* (11), 2368-2372.

(14) Tsui, E. Y.; Müller, P.; Sadighi, J. P. Reactions of a stable monomeric gold (I) hydride complex. *Angew. Chem. Int. Ed.* **2008**, *120* (46), 9069-9072.

(15) Escalle, A.; Mora, G.; Gagosz, F.; Mezailles, N.; Le Goff, X. F.; Jean, Y.; Le Floch, P. Cationic dimetallic gold hydride complex stabilized by a xantphos-phosphole ligand: synthesis, X-ray crystal structure, and density functional theory study. *Inorg. Chem.* **2009**, *48* (17), 8415-8422.

(16) Dhayal, R. S.; van Zyl, W. E.; Liu, C. Polyhydrido copper clusters: synthetic advances, structural diversity, and nanocluster-to-nanoparticle conversion. *Acc. Chem. Res.* **2016**, *49* (1), 86-95.

(17) Takano, S.; Hirai, H.; Muramatsu, S.; Tsukuda, T. Hydride-doped gold superatom $(Au_9H)^{2+}$: synthesis, structure, and transformation. *J. Am. Chem. Soc.* **2018**, *140* (27), 8380-8383.

(18) Yuan, S. F.; Li, J. J.; Guan, Z. J.; Lei, Z.; Wang, Q. M. Ultrastable hydrido gold nanoclusters with the protection of phosphines. *Chem. Commun.* **2020**, *56* (51), 7037-7040.

(19) Hu, G.; Wu, Z.; Jiang, D. E. Stronger-than-Pt hydrogen adsorption in a Au_{22} nanocluster for the hydrogen evolution reaction. *J. Mater. Chem. A* **2018**, *6* (17), 7532-7537.

(20) Bertino, M. F.; Sun, Z. M.; Zhang, R.; Wang, L. S. Facile syntheses of monodisperse ultrasmall Au clusters. *J. Phys. Chem. B* **2006**, *110* (43), 21416-21418.

(21) Yuan, X.; Zhang, B.; Luo, Z.; Yao, Q.; Leong, D. T.; Yan, N.; Xie, J. Balancing the rate of cluster growth and etching for gram-scale synthesis of thiolate-protected Au_{25} nanoclusters with atomic precision. *Angew. Chem. Int. Ed.* **2014**, *126* (18), 4711-4715.

Chapter 4 A Heteroleptic Gold Hydride Nanocluster for Efficient and Selective Electrocatalytic Reduction of CO_2 to CO

Portions of this chapter are adapted and/or reprinted from the following works. Copyright belongs to the publisher.

Gao, Z. H., Wei, K., Wu, T., Dong, J., Jiang, D. E., Sun, S., Wang, L. S. A Heteroleptic Gold Hydride Nanocluster for Efficient and Selective Electrocatalytic Reduction of CO_2 to CO. *J. Am. Chem. Soc*. 2022, 144, 12, 5258–5262.

4.1 Introduction

The dependence of the chemical industry on fossil fuel feedstocks has led to the overproduction of the greenhouse gas carbon dioxide. As is shown in Figure 4.1a, from 1960 to 2021, the concentration of CO_2 in the atmosphere has increased from 319 ppm to 412 ppm.[1] Being a huge threat to the survival of all the creatures, there is a urging need to advance the development of CO_2 ultilization. Electrochemical CO_2 reduction reaction (CO_2RR) has been considered as a very promising strategy to convert CO_2 to value-added chemcials and to balance the carbon cycle (Figure 4.1b).[2, 3]

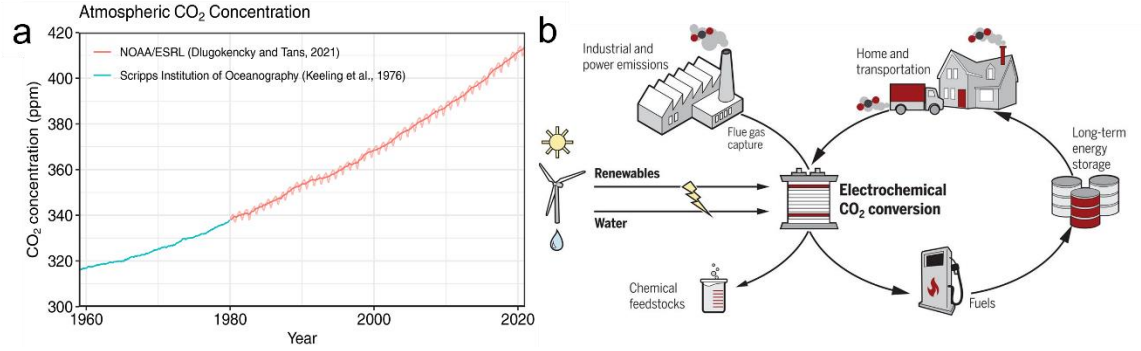

Figure 4.1 a) Surface average atmospheric CO_2 concentration (ppm) from 1960 to 2021.[1] b) Electrochemical CO_2 conversion.[2] Copyright © 2019 The American Association for the Advancement of Science.

Gold-based nanomaterials have been one of the most widely studied catalysts for electrochemical conversion of CO_2 to CO with high selectivity and relatively low overpotentials.[4-6] In 2013, Zhu et al. reported the electrocatalytic CO_2 reduction properties of on monodisperse Au NPs with different sizes. Among 4, 6, 8 and 10 nm Au NPs tested, the 8 nm Au NPs show the highest selectivity towards CO with faradaic efficiency (FE) reaching 90% at -0.67 V. The 4 nm Au NPs exhibit the highest mass activity of 14 A/g_{Au}

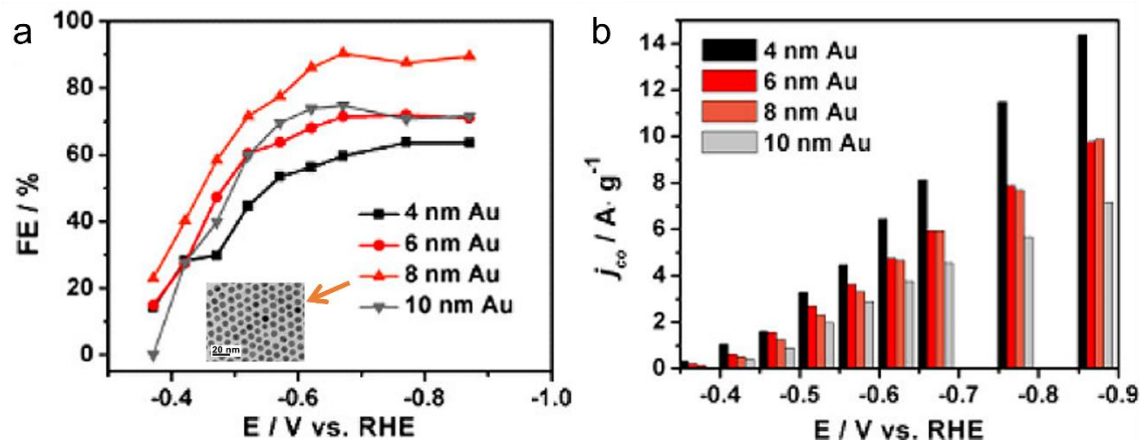

Figure 4.2 Potential-dependent a) FEs and b) Current densities for different-size Au NPs at various potentials.[6] Copyright © 2013 American Chemical Society.

at -0.9 V. Theoretical calculations indicate that the edge sites favor CO formation and the presence of a relatively higher density of edge sites on 4 nm NPs (10-13%) contributes to the higher mass activity. Despite the tremendous progress in producing monodisperse Au nanoparticles with appreciable activity and selectivity,[7-10] their surface structure cannot be precisely resolved and well-defined, making it difficult to investigate the structure-activity relationship.[11, 12] Hence, it is highly desirable to achieve synthetic control in the coordination environments of surface Au atoms to create well-defined active centers for the eluciation of the structure-activity relationship of Au nanocatalysis.

In this quest, atomically precise Au nanoclusters have attracted intensive interest because they possess high molecular purity, well-defined structures, and high surface-to-volume ratios.[13-23] With more and more Au NCs being structurally characterized, researchers have spent more efforts in applying Au NCs as ideal model systems for understanding catalytic properties at the atomic level. And Au NCs have been proved to be an important component in catalysis science, including heterogeneous catalysis,

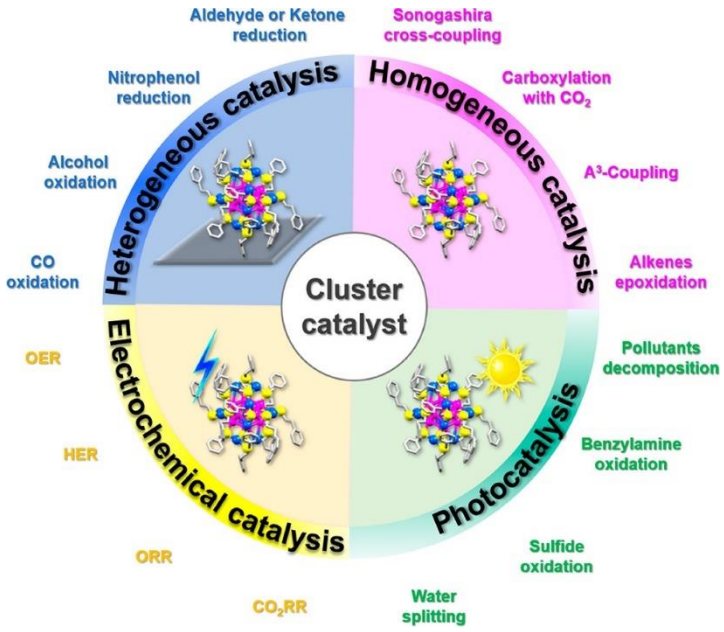

Figure 4.3 Various catalytic applications of atomically precise Au NCs.[28] Copyright © 2022 American Chemical Society.

homogeneous catalysis, electrochemical catalysis, and photocatalysis (Figure 4.3).[24-28] In particular, a series of thiolate-protected Au nanoclusters have been studied for CO_2RR,[29-33] although the detailed catalytic mechanisms are not well understood and are controversial.[31, 34]

An ideal Au-nanocluster model catalyst should be atomically precise with uncoordinated Au (*uc*Au) sites serving as *in situ* catalytic active centers. Our focus has been on the Au_{20} pyramid, which is known to have all its atoms on the cluster surface.[35] We have tried to synthesize the Au_{20} pyramid using different phosphine ligands with the hope of creating *uc*Au sites with suitable ligands.[36-38] The use of diphosphine ligands led to the synthesis of $Au_{22}(dppo)_6$ [dppo = 1,8-bis(diphenylphosphino)octane], which was the first atom-precise Au nanocluster with 8 *uc*Au sites[36] and was found to be able to catalyze the CO oxidation reation at mild condtions,[22] as well as being a good catalyst for H_2

activation.[37] Further investigations led to the discovery of three Au nanohydride clusters with *uc*Au, $[Au_{22}H_4(dppo)_6]^{2+}$, $[Au_{22}H_3(dppee)_7]^{3+}$ and $[Au_{22}H_3(dppb)_7]^{3+}$, where the *uc*Au sites are bridged by the H atoms.[39, 40] The steric effects produced by mixed bulky ligands[41-44] provide another strategy to control the interfacial chemistry of Au nanoclusters to create catalytic active sites, which inspired us to consider mixing bidentate and monodentate phosphine ligands to try to synthesize the Au_{20} pyramid.

Here we report the synthesis and catalysis of a new heteroleptic $[Au_{22}H_3(dppe)_3(PPh_3)_8]^{3+}$ trihydride cluster [dppe = 1,2-bis(diphenylphosphino)ethane, PPh_3 = triphenyl phosphine], when we used a mixture of dppe and PPh_3 (Figure 1a). A combination of experimental and theoretical studies revealed that the $Au_{22}H_3$ core consists of two Au_{11} units that are bonded together via two triangular faces with the three H atoms bridging six *uc*Au atoms at the interface. We have found that $[Au_{22}H_3(dppe)_3(PPh_3)_8]^{3+}$ exhibits excellent performance for the selective electro-catalytic reduction of CO_2 to CO with a 92.7% Faradaic efficiency (FE) at -0.6 V [vs reversible hydrogen electrode (RHE)], high mass activity (134 A/g_{Au}), and high stability. The catalytic performance is among the best Au-based catalysts for electrochemical reduction of CO_2 to CO. The current study demonstrates the possibility of designing catalytically active centers using Au nanohydrides for potential applications.

4.2 The synthesis of a heteroleptic $[Au_{22}H_3(dppe)_3(PPh_3)_8]^{3+}$ trihydride cluster

4.2.1 Chemicals

The chemicals listed below were used as received. Dichloro(DPPE)digold(I) ($Au_2(dppe)Cl_2$, ≥96%, Sigma-Aldrich), Chloro(triphenylphosphine)gold(I) (PPh_3, ≥99.5%, Sigma-Aldrich), sodium borohydride ($NaBH_4$, ≥98.0%, Sigma-Aldrich), sodium borodeuteride ($NaBD_4$, 98 atom % D, Sigma-Aldrich), methylene chloride (≥99.5%, Certified ACS, Fisher Scientific), ethanol (≥99.5%, 200 proof, ACS reagent, Sigma-Aldrich), ethanol-OD (≥99.5% atom %D, Sigma-Aldrich), methanol (≥99.6%, Sigma-Aldrich), Potassium bicarbonate (≥99.99% trace metals basis, 99.7- 100.5% dry basis, Sigma-Aldrich), Toray Carbon Paper (TGP-H-60, Alfa Aesar). Polyvinylidene fluoride (PVDF, MTI corporation).

4.2.2 Synthetic methods

Synthesis of the $[Au_{11}(dppe)_5]^{3+}$ nanoclusters:

A sample of 20 mg (0.024 mmol) of $Au_2(dppe)Cl_2$ was first added to a flask containing 4 mL CH_2Cl_2. The solution was stirred at 900 rpm for 5 minutes. Then, 9 mg (0.24 mmol) of $NaBH_4$ dissolved in 1.5 mL ethanol (EtOH) was quickly added to the solution. The color of the solution quickly changed to black. The reaction was allowed to proceed for 2 hours at room temperature in the dark. After the removal of all solvents by a rotary evaporator, the dark brown residue was washed by a 10 mL CH_2Cl_2/hexane (1/5 ratio) mixed solution for three times to get rid of the excess phosphine ligands. The remained solid was then dissolved into a minimum amount of CH_2Cl_2 and purified by silica-gel column chromatography. A sample of 9.1 mg brown powder was obtained after solvent evaporation. If all counter anions were assumed as chloride, a relatively high yield of 50% was obtained on the basis of the initial amount of Au in $Au_2(dppe)Cl_2$. ^{1}H-NMR

(600.0 MHz, $CDCl_2$): δ 6.24-8.34 (m, 20H), 1.83 (s, 4H). ESI-MS: observed *m/z* = 1386.1052, calculated *m/z* ($Au_{11}C_{130}H_{120}P_{10}$) = 1386.1029.

Synthesis of the $[Au_{22}H_3(dppe)_3(PPh_3)_8]^{3+}$ hydride nanocluster:

A sample of 10 mg (0.012 mmol) of $Au_2(dppe)Cl_2$ and 11.6 mg (0.023 mmol) of $Au_2(dppe)Cl_2$ were initially dissolved in 3.5 mL CH_2Cl_2. The solution was stirred at 900 rpm for 5 minutes. Then, 9 mg (0.24 mmol) of $NaBH_4$ dissolved in 1.5 mL ethanol (EtOH) was quickly added to the solution. The color of the solution quickly changed to black. The reaction was carefully sealed with nitrogen and stirred for 3 hours in the dark. After the removal of all solvents by a rotary evaporator, the dark brown residue was washed by a 10 mL CH_2Cl_2/hexane (1/5 ratio) mixed solution for three times to get rid of the excess phosphine ligands. The remained solid was then dissolved into a minimum amount of CH_2Cl_2 and purified by silica-gel column chromatography. A sample of 5.8 mg brown powder was obtained after solvent evaporation. If all counter anions were assumed as chloride, a yield of 35% was obtained on the basis of the initial amount of Au in two precursors. ^{1}H-NMR (600.0 MHz, $CDCl_2$): δ 14.06-14.12 (t, 3H), 6.60-7.91 (m, 194H), 2.83-0.22 (m, 13H). ESI-MS: observed *m/z* = 2543.1391, calculated *m/z* ($Au_{22}C_{192}H_{220}P_{12}$) = 2543.1408.

4.3 The characterizations on $[Au_{22}H_3(dppe)_3(PPh_3)_8]^{3+}$ trihydride cluster

4.3.1 Techniques

UV-vis Absorption Spectroscopy: UV-vis absorption spectra were recorded on a Varian Cary 50 Bio spectrometer with a spectral range between 300 to 800 nm at 298 K. The

quartz cuvette used for all measurements had 1.0 cm optical path length. Background subtractions were done using appropriate solvents as blanks.

Electrospray Ionization Mass Spectrometry (ESI-MS): Positive ionization mode ESI mass spectra were measured on an Agilent 6530 Accurate Mass Q-TOF LC-MS system (with Agilent 1260 HPLC). The CH_2Cl_2 solution of the sample (*ca.* 1.0 mg mL^{-1}) was introduced into the system through a stainless steel needle via flow injection. Acetonitrile/water (1/1 ratio) was used as the mobile phase at a flow rate of 200 µL min^{-1}. The source temperature was kept at 130 °C. The fragmentor voltage was set at 50 V, skimmer at 65 V, and the capillary voltage at 3500 V. The measuring mass range was 0 to 20,000 m/z units. All spectra were recorded at a rate of 1 spectrum s^{-1}. Different species were assigned using isotopic distributions in the high-resolution spectra by comparing with simulated spectra.

NMR Spectroscopy: ^{1}H and ^{31}P-NMR were obtained on a 600 MHz Bruker Ultrashield spectrometer using CD_2Cl_2 as the solvent. Unless further noted, the NMR spectra were measured at 298 K. Chemical shifts (δ) are reported in ppm and referenced to internal solvent resonances for ^{1}H and external 85% H_3PO_4 for ^{31}P-NMR. Coupling constants (*J*) are reported in Hertz (Hz). All data were processed using the MestreNova software.

Computational Methods

First-principles calculations were carried out using DFT[45] and the all-electron projected augmented wave (PAW)[46] method as implemented in the Vienna ab initio simulation package (VASP).[47] For the exchange correlation energy, we used the Perdue-Burke-Ernzerhof (PBE) version of the generalized gradient approximation (GGA) for geometry optimization.[48] The revised Perdue-Burke-Ernzerhof (RPBE) functional was

used to improve the accuracy of adsorption energy calculation. The lattice constants and atomic positions were optimized with a cutoff energy of 400 eV for the plane-wave basis. The van der Waals interactions were included using the empirical correction in Grimme's scheme (DFT-D3).[49] The total energies and Hellmann-Feynman forces acting on atoms were converged below 10^{-5} eV per atom and smaller than 0.05 eV $Å^{-1}$, respectively. The Brillouin zone was sampled using only Γ point. For the experimental complex, $[Au_{11}(dppe)_5]^{3+}$ and $[Au_{22}(dppe)_3(PPh_3)_8H_3]^{3+}$, the phenyl groups were replaced by the H atoms in theoretical computations. The $[Au_{11}]^{3+}$ or $[Au_{22}H_3]^{3+}$ nanocluster was placed in an oorthogonal box with dimensions of 20 × 20 × 25 $Å^3$. In addition, a uniform background charge was added to the unit cell to balance the charges. The optimized structures are in good agreement with the experiment for the starting cluster structures (Table S1).

The reaction free energies of the electrochemical steps were calculated using the computational hydrogen electrode proposed by Nørskov et al.[50] Gibbs free energies (ΔG) for all the electrochemical or non-electrochemical steps were computed by the following equation:

$$\Delta G = \Delta E + \Delta E_{zpe} - T\Delta S,$$

where ΔE is the difference of the DFT total energy, ΔE_{zpe} is the zero-point energy difference calculated from the vibrational frequencies, and ΔS is the entropy difference between the products and the reactants. The entropies of the free molecules at 298 K and 1 atm were taken from the NIST database, while the vibrational entropy was computed for the adsorbed species.

TD-DFT calculations:

To simulate the UV-vis spectrum, linear-response time-dependent (TD-DFT) calculations are carried out using the Gaussian 16 software package.[51] The theoretical method was the popular hybrid functional B3LYP,[52-54] and the 6-31+G(d) basis set for C, H, P, and the LANL2DZ scalar relativistic pseudopotential basis set for Au.[55-57] The first 600 singlet transitions are considered in the simulation. Orbital composition analyses were done using the Multiwfn 3.7 software.[58] For the experimental complex, $[Au_{11}(dppe)_5]^{3+}$ and $[Au_{22}H_3(dppe)_3(PPh_3)_8]^{3+}$, the phenyl groups were replaced by the H atoms in theoretical computations.

4.3.2 Characterization results

The $[Au_{22}H_3(dppe)_3(PPh_3)_8]^{3+}$ cluster (abbreviated as $[Au_{22}H_3]^{3+}$ hereafter) was synthesized by reacting excess amount of $NaBH_4$ with a mixture of $Au_2(dppe)Cl_2$ and $Au(PPh_3)Cl$ precursors. And the highest cluster yield could be achieved when the ratio of these two precursors were 2:1. After purificaition with column chromatography, the final product showed a distinct peak at around 2543 Da in the ESI mass spectrum. As is shown in Figure 4.4top, the experimental isotope distribution profile matched perfectly with the simulated result. To confirm that the acetic acid used during the electrospray process didn't contribute to the three H atoms, we performed isotopic labelling experiment by using $NaBD_4$ instead. The resulting isotope distribution profile had exactly 1Da shift compared to the $[Au_{22}H_3]^{3+}$ cluster, indicating three H atoms were original to the cluster. The $[Au_{22}H_3]^{3+}$ cluster peak could also be observed in the spectra when $Au(PPh_3)Cl$ and dppe

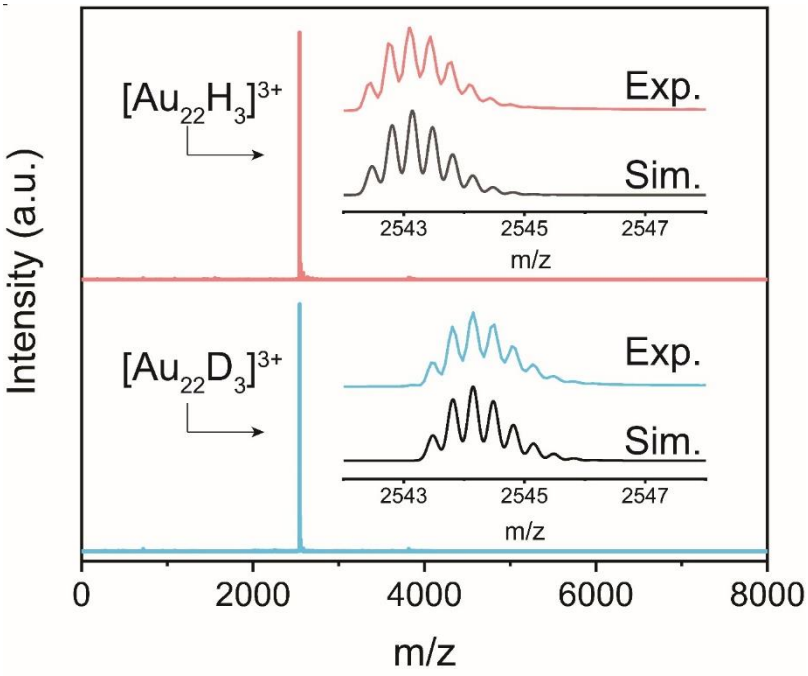

Figure 4.4 ESI-MS spectra of $[Au_{22}H_3]^{3+}$ and $[Au_{22}D_3]^{3+}$; the insets show the experimental and simulated isotopic distributions.

ligand were used as precursor materials, but the ratio was not optimized to get the highest yield of this hydride cluster.

The controlled experiments were also performed by using the precursor alone. It was discovered that a Au_{11} cluster could be obtained when $Au_2(dppe)Cl_2$ was reduced with an excess amounts of $NaBH_4$. The Au_{11} cluster could also be purified with column chromatography to give a spectrum as in Figure 4.5. The prominent peak around 1386 Da could be assgined to $[Au_{11}(dppe)_5]^{3+}$, which was confirmed by the simulated result. Instead, by using the $Au(PPh_3)Cl$ precursor alone, the $[Au_{10}(dppe)_8]^{2+}$cluster peak could be observed with relatively high intensity. However, the cluster was not stable on the SiO_2 column, preventing us from purifying the cluster.

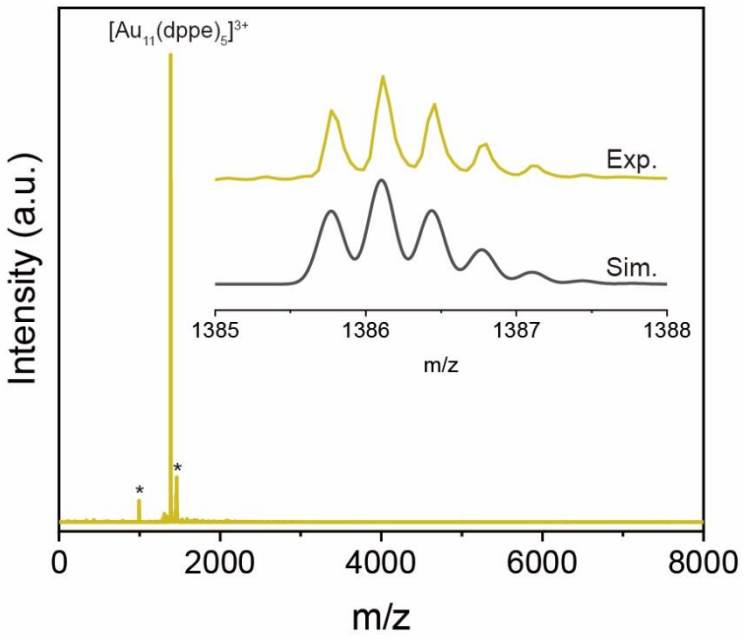

Figure 4.5 The ESI-MS spectrum of $[Au_{11}(dppe)_5]^{3+}$ nanocluster. Inset: comparison of the experimental and simulated isotopic distributions. The minor peaks labeled with * (from right to left) are: $[Au_{12}(dppe)_5Cl]^{3+}$ and $[Au(dppe)_2]^{+}$.

Then the $[Au_{22}H_3(dppe)_3(PPh_3)_8]^{3+}$ cluster was further characterized with NMR spectroscopy. As is shown in Figure 4.6a, three peaks were observed in ^{1}H-NMR spectrum

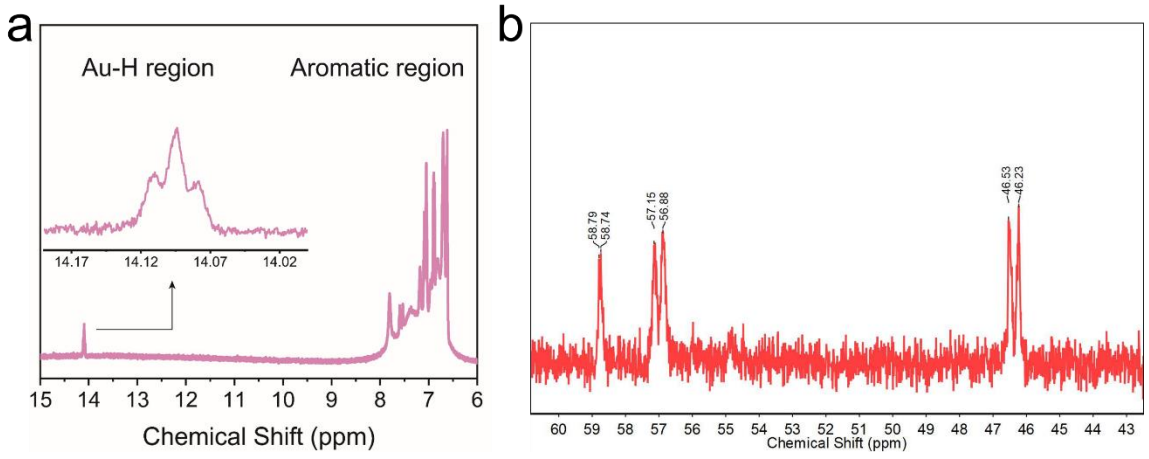

Figure 4.6 a) The ^{1}H-NMR spectrum of $[Au_{22}H_3]^{3+}$; the inset shows the enlarged signal in the Au-H region. b) The ^{31}P-NMR spectrum of $[Au_{22}H_3]^{3+}$.

at 14.1 ppm. The ratio of the integrated area for these hydride peaks to that of the 180 aromatic H atoms on the eleven phosphine ligands (6.6~7.9 ppm) is about 3:194. The observed chemical shift suggests that the three H atoms are directly bonded to Au, similar to those observed in previous Au-H nanoclusters: ~15.1 ppm in $[Au_9H(PPh_3)_8]^{2+}$,[59] ~15.5 ppm in $[Au_{22}H_4(dppo)_6]^{2+}$ [39], ~14.8 ppm in $[Au_{22}H_3(dppb)_7]^{3+}$ and ~15 ppm in

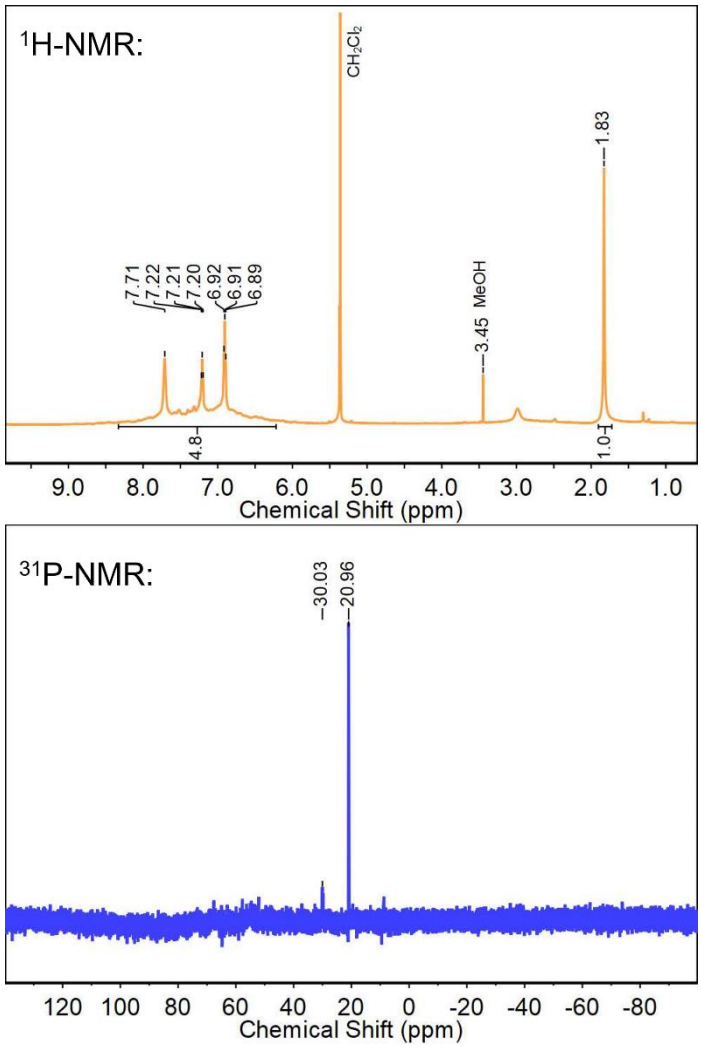

Figure 4.7 Top: The ^{1}H-NMR spectrum of the $[Au_{11}(dppe)_5]^{3+}$ cluster. Bottom: The ^{31}P-NMR spectrum of the $[Au_{11}(dppe)_5]^{3+}$ cluster. The small peak at 30.03 ppm is due to the $Au_2(dppe)Cl_2$ precursor.

$[Au_{22}H_3(dppee)_7]^{3+}$.[40] The ^{31}P-NMR spectrum of the $[Au_{22}H_3]^{3+}$ cluster, however, displayed multiple peaks in the range of 45-60 ppm (Figure 4.6b), suggesting the complexity of the phosphine environments. Similarly, the corresponding NMR spectra were also taken for the $[Au_{11}(dppe)_5]^{3+}$ cluster. In the ^{1}H-NMR spectrum, the ratio of integrated area of aromatic H to alkyl H is about 4.8:1 which corresponds to the 5:1 ratio for different hydrogens on dppe ligand. The ^{31}P-NMR spectrum showed that the phosphorus environments are much simpler on $[Au_{11}(dppe)_5]^{3+}$ cluster. Only one peak at 20.96 ppm was originated from the cluster, suggesting all the ten P atoms are identical on the cluster. And the small peak at 30.03 ppm was from the $Au_2(dppe)Cl_2$ precursor, which was evidenced on ESI mass spectrum at the same time (Figure 4.5).

To gain more insights into the structure of this unique heteroleptic hydride cluster, we have tried our best effort under various conditions to grow crystals of

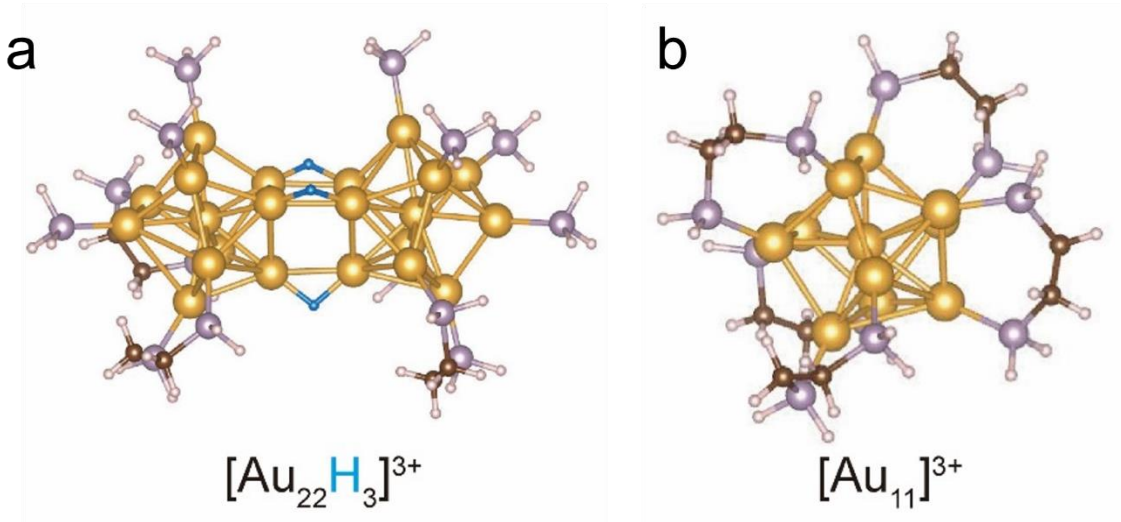

Figure 4.8 The DFT optimized structures of (a) $[Au_{11}(dppe)_5]^{3+}$ and (b) $[Au_{22}H_3(dppe)_3(PPh_3)_8]^{3+}$ clusters. Colors: Au = yellow; C = brown; P = purple; Hydride = blue; H on the ligands = white.

$[Au_{22}H_3(dppe)_3(PPh_3)_8]^{3+}$ for SC-XRD. There are two possible reasons for our inability to grow high quality crystals suitable for SC-XRD: 1) The two different phosphine ligands could be one possible cause. During crystal growth in solution, there could be ligand rearrangements or different ligand configurations, making it more difficult for crystal growth. 2) There is a very slow decomposition process by the cluster in solution, which is also not conducive for the slow crystallization process. Therefore, DFT calculations were performed to find the optimized structures for both clusters. The optimized structures for $[Au_{11}]^{3+}$ and $[Au_{22}H_3]^{3+}$ are shown in Figure 4.8. $[Au_{11}]^{3+}$ is fully capped with five diphosphine ligands. However, the the kernel of $[Au_{22}H_3]^{3+}$ cluster could be viewed as the dimer of two Au_{11} units sharing a triangular facet. The three H atoms bridge the six *uc*Au sites, whereas the remaining fourteen surface Au atoms are coordinated by the phosphine ligands (Figure 4.9). More interestingly, an experiment was performed by using the purified $[Au_{11}]^{3+}$ and $Au(PPh_3)Cl$ as precursors. The reduction of the mixture by $NaBH_4$ led to the appearance of the $[Au_{22}H_3(dppe)_3(PPh_3)_8]^{3+}$ peak in the mass spectrum. However, the yield of the hydride cluster was low and there was $Au_2(dppe)Cl_2$ precursor impurities

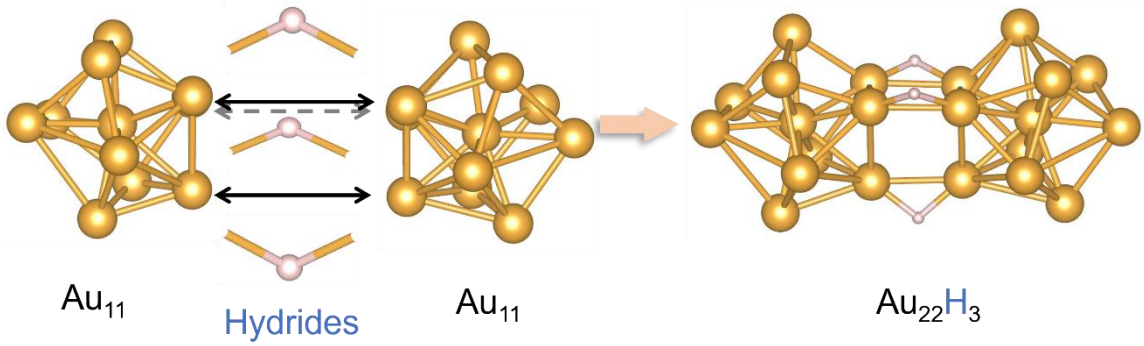

Figure 4.9 The proposed $Au_{22}H_3$ metal core consisting of two Au_{11} units fused by two triangular faces and three bridging H atoms.

in the $[Au_{11}]^{3+}$ (though the amount was little), making the conclusion of the fusion experiment not that solid. Nevertheless, I believe it will still be intriguing if such dimerization from Au_{11} cluster could be verified on any of these Au_{22} clusters, which suggests a novel method to synthesize more hydride/uncoordinated sites containing clusters.

Table 4.1 Comparison of the Au-Au bond distances (Å) between the DFT optimized structures and the experiment. The $[Au_{11}(dppe)_5]^{3+}$ cluster in the DFT model is compared to the experimental $[Au_{11}(dppp)_5]^{3+}$ cluster[60] while the $[Au_{22}H_3(dppe)_3(PPh_3)_8]^{3+}$ cluster in the DFT model is compared to the experimental $[Au_{22}(dppo)_6]^{2+}$ cluster.[61]

	$[Au_{11}]^{3+}$	$[Au_{22}H_3]^{3+}$
DFT	2.72-3.24	2.67-3.23
Experiment	2.67-3.09 [60]	2.63-3.23 [61]

We compared the Au-Au bond lengths between our DFT calculations and the experimental results of ($[Au_{11}(dppp)_5]^{3+}$ and $[Au_{22}(dppo)_6]^{2+}$), both agreeing well with the reported crystal data (Table 4.1). The $[Au_{11}]^{3+}$ cluster also shares similar bond lengths as the Au_{11} unit in the $[Au_{22}H_3]^{3+}$ cluster.

To gain more insights into their electronic structures, we measured the UV-Vis absorption spectra of these two clusters. We compared the UV-Vis absorption spectra with those of $[Au_{22}H_4(dppo)_6]^{2+}$, $[Au_{22}H_3(dppb)_7]^{3+}$, and $[Au_{22}H_3(dppee)_7]^{3+}$ (Figure 4.10) and

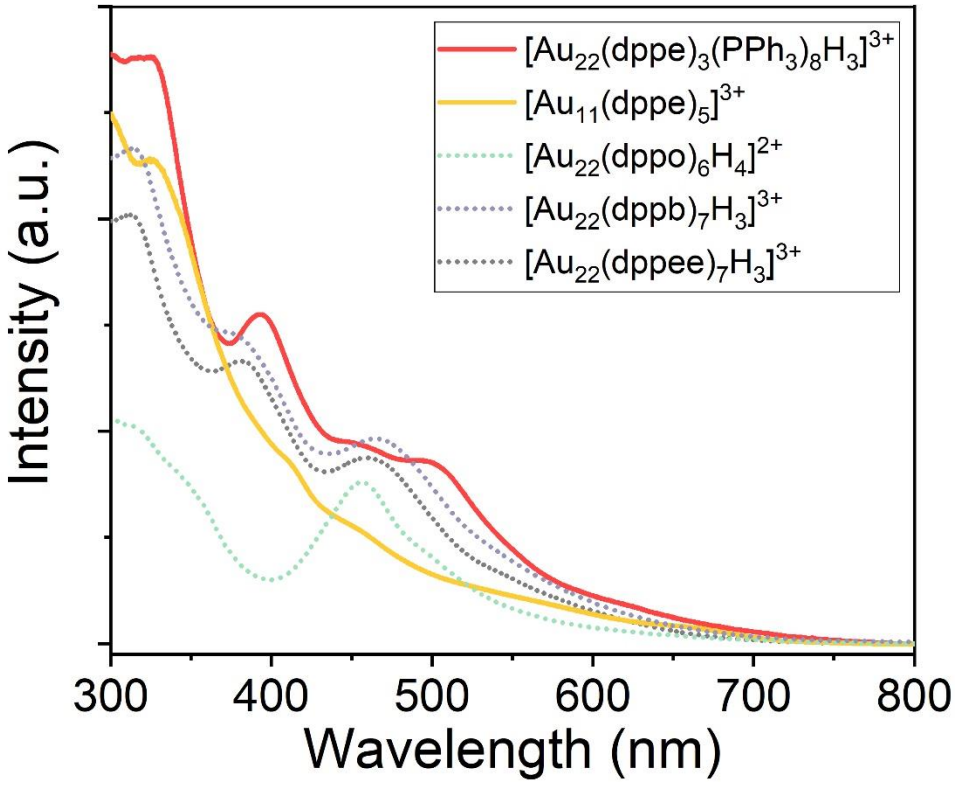

Figure 4.10 Comparison of the UV-Vis absorption spectra of $[Au_{22}H_3]^{3+}$, $[Au_{11}]^{3+}$, $[Au_{22}H_4(dppo)_6]^{2+}$, $[Au_{22}H_3(dppb)_7]^{3+}$, and $[Au_{22}H_3(dppee)_7]^{3+}$.

found that the three $Au_{22}H_3$ clusters share similar absorption features at around 323 nm, 394 nm, and 446 nm (Figure 4.10). These features from the absorition spectra again indicated the purity of the sample. The $[Au_{11}]^{3+}$ cluster exhibits analogous features at around 324 nm and 400 nm. To interpret these absorption features, we simulated the optical absorption spectra of the $[Au_{22}H_3]^{3+}$ and $[Au_{11}]^{3+}$ clusters using time-dependent density functional theory (TD-DFT). Overall, good agreement between the experiment and the simulation has been found for both clusters (Figure 4.11). For $[Au_{22}H_3]^{3+}$, the 323 nm band involves many close excitations of Au d→sp (Table 4.2), the 394 nm band is assigned mainly to the HOMO-7 → LUMO+1 transition (Au d/s → sp excitation), and the 446-nm band is assigned to HOMO → LUMO+9 transition (Au sp → p excitation). The frontier

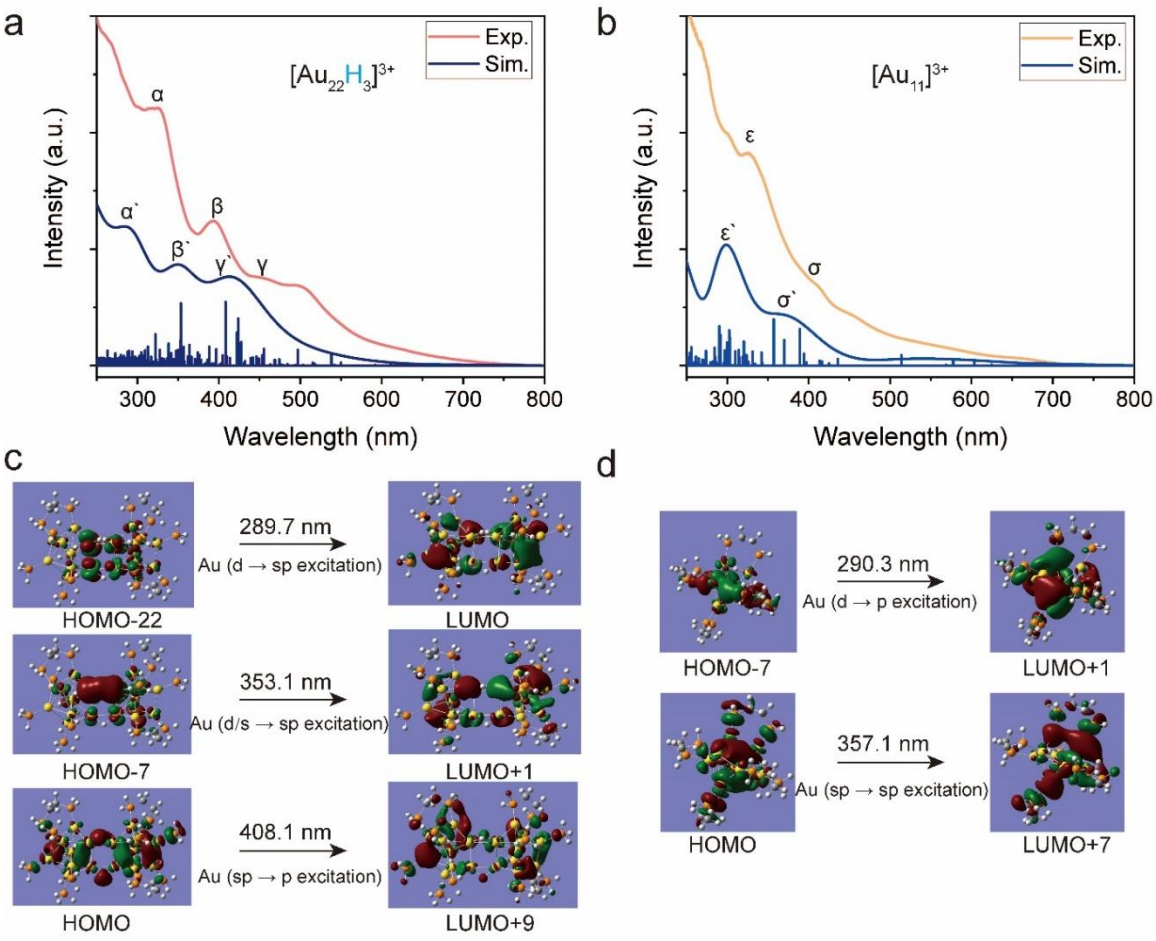

Figure 4.11 Comparison of simulated and experimental UV-vis absorption spectra: (a) $[Au_{22}H_3(dppe)_3(PPh_3)_8]^{3+}$; (b) $[Au_{11}(dppe)_5]^{3+}$. Main transitions and orbitals involved for the major peaks in the simulated absorption spectra: (c) $[Au_{22}H_3]^{3+}$; (d) $[Au_{11}]^{3+}$.

orbitals of $[Au_{22}H_3]^{3+}$ involved in the transitions all show features along the rod-shaped structure of the cluster (Figure 4.11). For comparison, the 324 nm band of the $[Au_{11}]^{3+}$ cluster also invovlves many close excitations of mainly Au d→p (Table 4.3), while its 400 nm band has just a few strong transitions (Au sp → sp). The ligands are more involved in the frontier orbitals of the $[Au_{11}]^{3+}$ cluster (Figure 4.11). The results indicate that the Au_{22} core in $[Au_{22}H_3]^{3+}$ may also be composed of two Au_{11} units bonded via Au atoms and the Au_{11} units may have similar structures with the $[Au_{11}]^{3+}$ cluster.

Table 4.2 Electronic excitation wavelengths, energies, oscillator strengths, and main transitions for the $[Au_{22}H_3(dppe)_3(PPh_3)_8]^{3+}$ cluster from TD-DFT simulation.

Wavelength (nm)	Energy (eV)	Oscillator Strength	Main transition
423.7	2.927	0.201	HOMO-1→LUMO+5
422.3	2.936	0.142	HOMO-1→LUMO+6
408.1	3.038	0.273	HOMO→LUMO+9
363.8	3.408	0.089	HOMO-5→LUMO+5
353.1	3.512	0.267	HOMO-7→LUMO+1
352.7	3.516	0.106	HOMO-6→LUMO+2
293.7	4.222	0.060	HOMO-1→LUMO+18
289.7	4.280	0.063	HOMO-22→LUMO
288.1	4.304	0.060	HOMO→LUMO+21

Table 4.3 Electronic excitation wavelengths, energies, oscillator strengths, and main transitions for the $[Au_{11}(dppe)_5]^{3+}$ cluster from TD-DFT simulation.

Wavelength (nm)	Energy (eV)	Oscillator Strength	Main transition
389.4	3.184	0.157	HOMO-1→LUMO+3
370.1	3.350	0.109	HOMO-2→LUMO+4
357.1	3.472	0.199	HOMO→LUMO+7
303.4	4.087	0.120	HOMO→LUMO+10
302.4	4.101	0.151	HOMO-6→LUMO
290.3	4.271	0.168	HOMO-7→LUMO+1

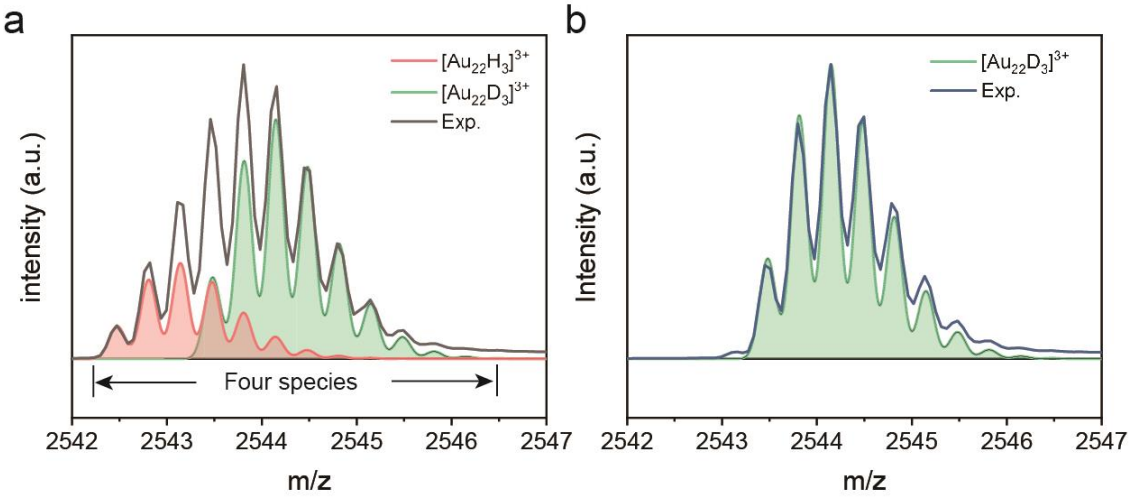

Figure 4.12 The isotopic distributions of $[Au_{22}H_3(dppe)_3(PPh_3)_8]^{3+}$ after addition of excess amounts of $NaBD_4$ and (a) React for 3h, (b) React for 3 days. Comparison with simulated isotope patterns revealed isotope scrambling due to hydride exchange between $[Au_{22}H_3(dppe)_3(PPh_3)_8]^{3+}$ and $NaBD_4$.

We also studied the hydride exchange properties of this hydride cluster. As is shown in Figure 4.12, the addition of excess amounts of $NaBD_4$ in the $[Au_{22}H_3]^{3+}$ cluster sample resulted in the broadening of the peak at around 2544 m/z, which was due to the incomplete hydride exchange. Four species $[Au_{22}H_xD_{3-x}(dppe)_3(PPh_3)_8]^{3+}$ (x = 3, 2, 1, 0) coexisted after 3 hours reaction. After 1d, the cluster peak continued shifting to higher mass range and became narrower, which was a result of near complete exchange reaction and the forming of $[Au_{22}D_3(dppe)_3(PPh_3)_8]^{3+}$ cluster. The reverse reaction by adding $NaBH_4$ in the $[Au_{22}D_3]^{3+}$ cluster had similar outcomes and indicated that the hydride exchange reaction was not rapid. However, the three H atoms on the cluster were not exchangeable with the proton in ethanol. In Figure 4.13, the addition of EtOD in the $[Au_{22}H_3]^{3+}$ cluster sample had no affect on the cluster peak at around 2543 m/z. Therefore, the hydrogen atoms on $[Au_{22}H_3]^{3+}$ cluster are similar to those from $[Au_{22}H_4(dppo)_6]^{2+}$ and $[Au_{22}H_3(dppb)_7]^{3+}$

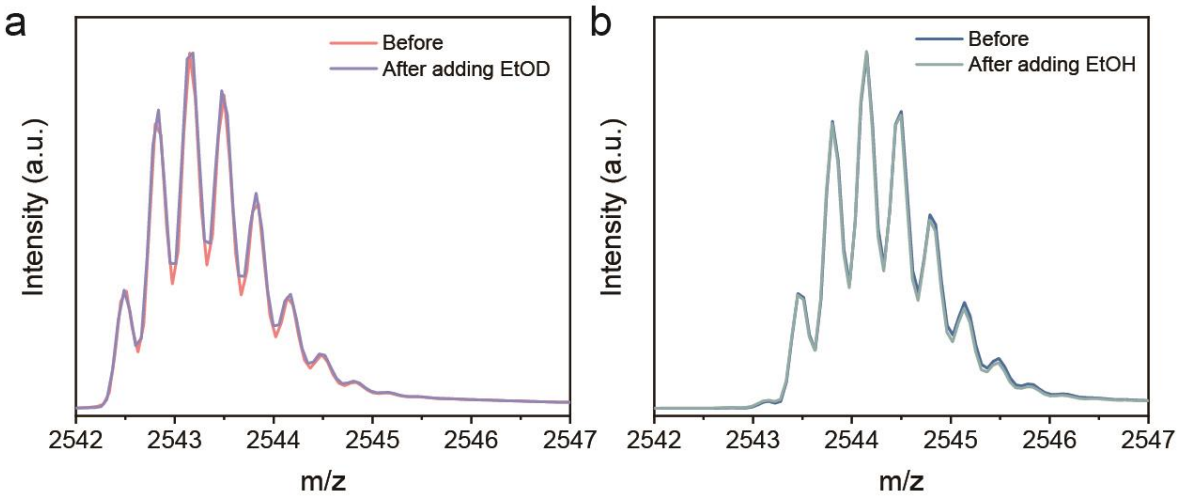

Figure 4.13 The isotopic distributions of (a) $[Au_{22}H_3(dppe)_3(PPh_3)_8]^{3+}$ and (b) $[Au_{22}D_3(dppe)_3(PPh_3)_8]^{3+}$ before and after the addition of ethanol (EtOD/EtOH), showing that the gold hydride cluster does not exchange D/H with ethanol.

clusters in terms of hydride exchange properties. They are only exchangable with the hydrides from $NaBH_4$ instead of protons from the solvent.

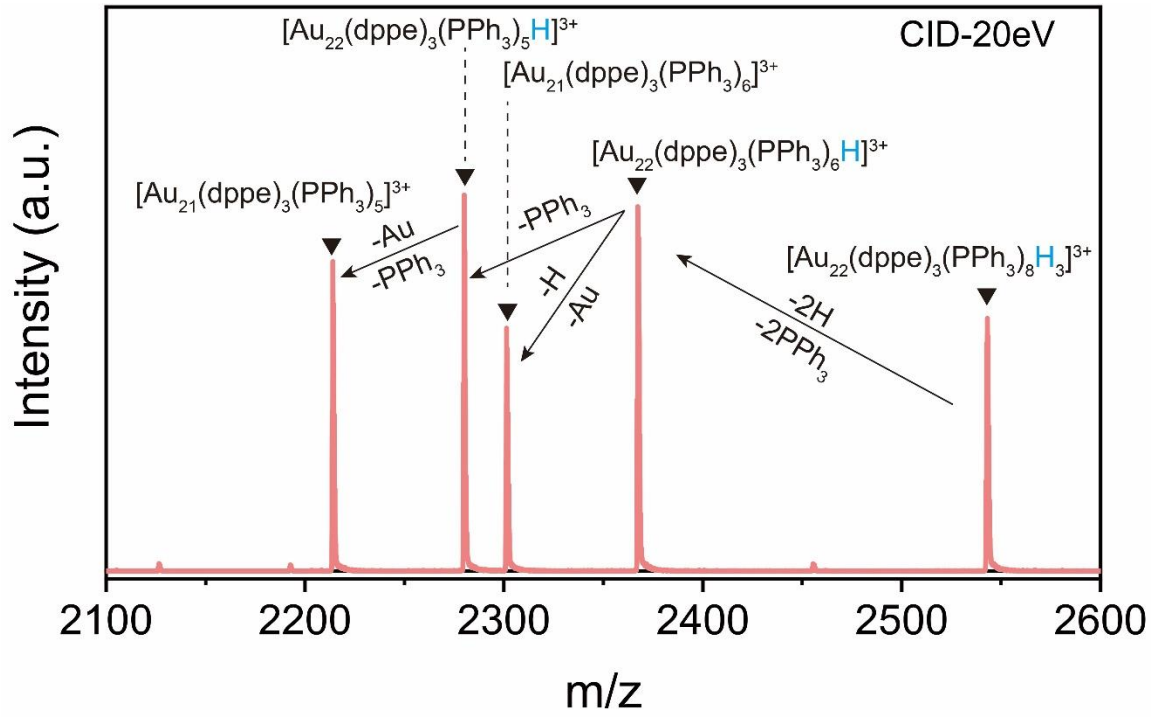

Figure 4.14 CID of $[Au_{22}H_3]^{3+}$ cluster under 20 eV.

After these characterizations, we went on studying the stability of this hydride cluster under various conditions. Firstly, CID was performed on $[Au_{22}H_3]^{3+}$ cluster to induce the colloision with neutral N_2 molecules in the gas phase. We still used mass spectrometer to check the fragments under 20 eV and the spectrum is shown in Figure 4.14. The spectrum was much more complicated than the case with $[Au_{22}H_3(dppb)_7]^{3+}$ cluster.

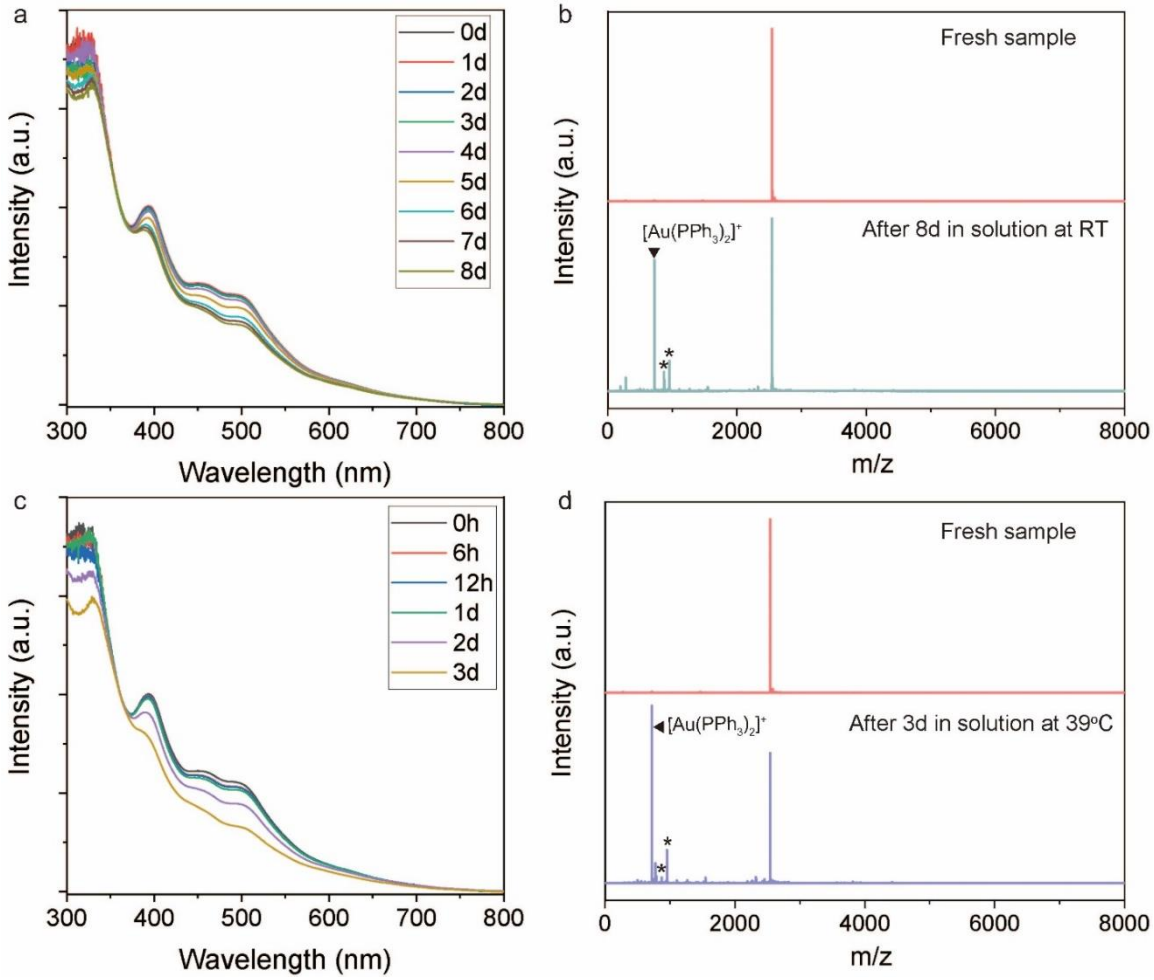

Figure 4.15 Stability test of the $[Au_{22}H_3]^{3+}$ cluster in dichloromethane (2 x 10^{-5} M): UV-Vis absorption spectra at room temperature (a) and 39 °C (c). (b) and (d): ESI-MS results for the final solutions, peaks labelled with * are $[Au(PPh_3)(dppe)]^+$ with some attached solvent molecules.

Several cluster peaks could be observed and assigned based on the isotope distribution patterns. The original cluster peak at 2543 m/z could initially loss 2 H atoms and 1 PPh_3 ligand to form $[Au_{22}H(dppe)_3(PPh_3)_6]^{3+}$, then it could loss the last H atom, 1 Au atom and one more PPh_3 ligand to form $[Au_{21}(dppe)_3(PPh_3)_5]^{3+}$, and these processes were accompanied by the appearance of $[Au(PPh_3)_2]^+$ peak at 721 m/z. The result also suggests that the binding of the monodentate PPh_3 ligand is poorer than the bidentate dppe ligand.

Then the stability of the $[Au_{22}H_3]^{3+}$ cluster was studied in solution phase at room temperature and 39 ^oC. As is shown in Figure 4.15a, at room tempearture the cluster could slowly decompose with decreasing intensitis for both 394 nm and 500 nm peaks. At elevated temperature, such decompostion could be greatly accelerated and the cluster was not stable for 3d in solution under 39 ^oC (Figure 4.15 c,d). These results are also similar to the $[Au_{22}H_3(dppb)_7]^{3+}$ cluster. However, the cluster was suprisingly stable at solid state and ambient conditions. The UV-Vis absorption spectra were measured and compared after six months (Figure 4.16). The three main absorption features remain prominent with only a slight decrease, suggesting the mixed ligand Au nanohydride cluster is very stable. The

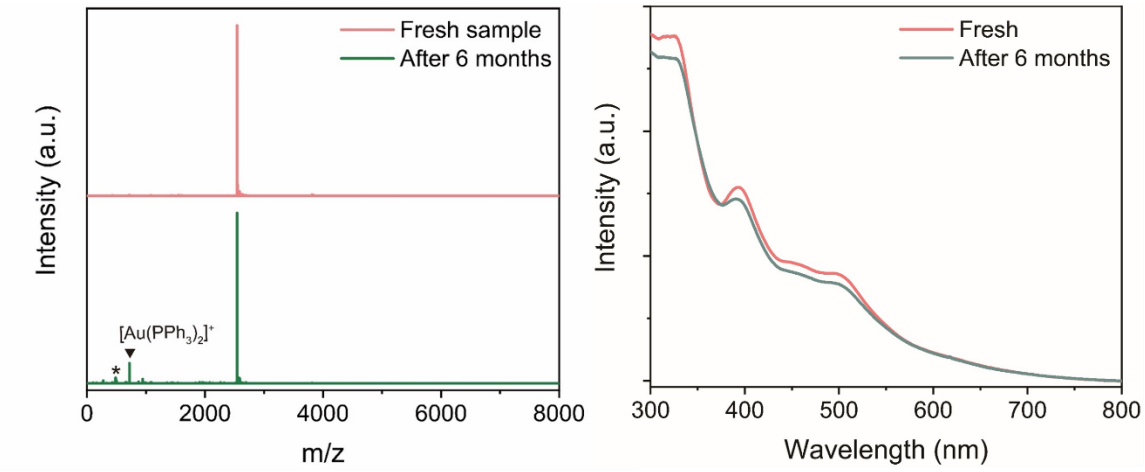

Figure 4.16 The stability test of solid $[Au_{22}H_3]^{3+}$ cluster for 6 months.

ESI mass spectra also agree well with the absorption spectra, confirming its high stability in the solid state.

4.4 Electrocatalytic CO_2RR on $[Au_{22}H_3]^{3+}$ trihydride cluster

4.4.1 Methods

Catalyst Preparation:

20 mg NCs were deposited onto 20 mg Ketjen Carbon (C) (EC300J) by sonicating the mixture of NC dispersion in 60 mL CH_2Cl_2 in ice bath. The carbon loaded catalyst was separated from CH_2Cl_2 by centrifugation under 9000 rpm for 1 min. To remove excess ligand, the catalyst was further washed by CH_2Cl_2 twice and dried under vacuum.

Electrode Preparation:

10 mg of the dried catalyst powder was ground with 2 mg polyvinyli-dene fluoride (PVDF) (industrial adhesive) with a few drops of 1-methyl-2-pyrrolidone (MP) (solvent) to produce catalyst paste that was painted directly onto a 1.0 cm x 1.0 cm carbon paper (Toray TGP-H-060). The catalyst-decorated carbon paper was dried in a vacuum-oven overnight and served as a working electrode.

Electrochemical CO_2RR Test:

An EC-Lab VSP Ultimate electrochemical workstation was used to conduct CO_2 reduction experiments in aqueous 0.5 M $KHCO_3$ (pH = 7.2 when saturated with CO_2, pH = 8.8 when saturated with N_2). A 99.9% platinum wire was used as counter electrode. All potentials were measured against an Ag/AgCl reference electrode (4.0 M KCl, Pine instrument) and were converted to those against a RHE reference: E (vs. RHE) = E (vs.

Ag/AgCl) + 0.63 V. All potentials were used without IR correction. The experiments were performed in a gas-tight cell with two-compartments separated by an anion exchange membrane (Nafion® 212). Each compartment contained 10 mL electrolyte with approximately 10 mL headspace.

4.4.2 Charaterizations and products analyses

Inductively coupled plasma-atomic emission spectroscopy (ICP-AES):

The (ICP-AES) results were obtained on a JY2000 Ultrace ICP atomic emission spectrometer equipped with a JY AS 421 autosampler and 2400 g/mm holographic grating.

X-ray Photoelectron Spectroscopy (XPS):

XPS spectra were collected by a Thermo Scientific K-Alpha system that equipped with an Al k-Alpha excitation source (1486.6 eV). During the measurement, the analysis chamber pressure was pumped down below 10^{-7} mBar with the electron flood gun on to reduce possible sample charging. The X-ray spot size was set at 400 μm, pass energy at 50 eV and energy step size at 0.1 eV. Samples were positioned at the electron take-off angle normal to the surface relative to the analyzer.

Product Analyses:

Before the experiment, the electrolyte in the cathode compartment was saturated with CO_2 by bubbling CO_2 gas for at least 20 min and was stirred at 900 rpm. CO_2 gas was delivered at an average rate of 12 mL/min (at room temperature and ambient pressure) and routed directly into the gas sampling loop of a gas chromatograph (Agilent 7890A). The gas phase composition was analyzed by GC every 30 min. The GC analysis was set up to

split the gas sample into two aliquots whereof one aliquot was routed through a packed Mole-Sieve 5A column and a packed HP-PLOT Q column before passing a thermal conductivity detector (TCD) for CO quantification. Argon (Corp Brother, 99.9999%) and Helium (Corp Brother, 99.9999%) were employed as carrier or make-up gases respectively. The second aliquot was routed through a packed HP-PLOT Q + PT column equipped with a flame ionization detector (FID) for analyzing C1 to C3 hydrocarbons. The GC was calibrated using commercially available calibration standards from JJS Technical Services. 1H NMR was employed at the end of experiments to characterize any liquid products. To be specific, 700 μL aliquot of the electrolyte was mixed with 35 μL dimethyl sulfoxide (DMSO) as internal standard solution (20 mM DMSO in D_2O). 1H NMR spectra were recorded on Bruker DRX 400 Avance and 600 Avance MHz spectrometers. No liquid products were detected at all tested potentials.

4.4.3 Surface redox properties for $[Au_{11}]^{3+}$ and $[Au_{22}H_3]^{3+}$

The thorough characterizations of the $[Au_{22}H_3]^{3+}$ trihydride cluster prepared it for some applcations. And considering its excellent solid-state stability, we thought it might be a good candiate for heterogeneous catalysis. The previous reported thiolate-protected Au_{25} clusters have been proved as an efficent catalyst for electrocatalytic CO_2RR.[30] However, all the surface Au atoms of such Au_{25} cluster are fully protected with thiolate ligands as well as some -SR-Au-SR-Au-SR- staple motifs, preventing the absorption of CO_2 molecules. The corresponding theoretical results indicate that the removal of one thiolate ligand from the cluster is critical for generating active sites for CO_2 reduction. Therefore, even though the cluster iteself is atomically precise, the catalytic process

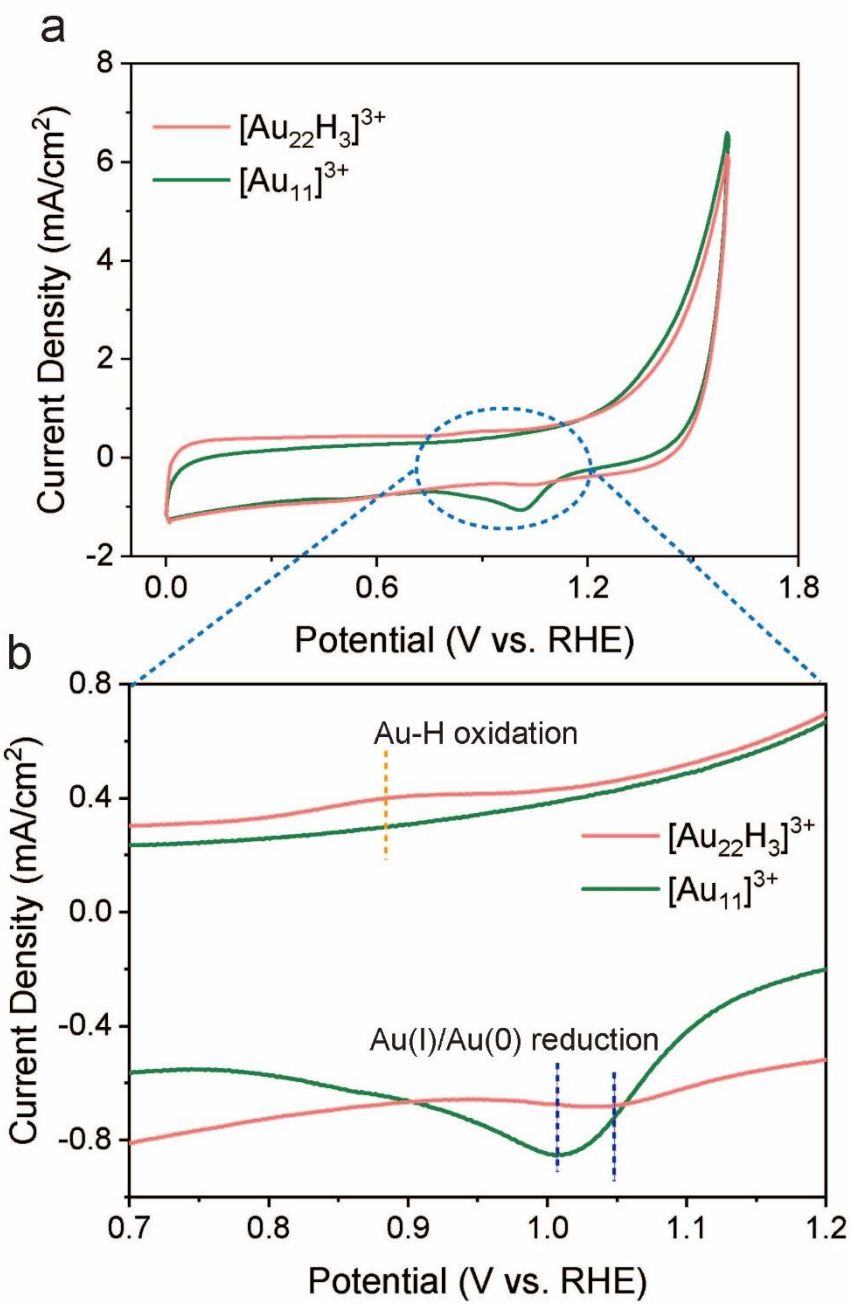

Figure 4.17 (a) CVs of $[Au_{22}H_3(dppe)_3(PPh_3)_8]^{3+}$ and $[Au_{11}(dppe)_5]^{3+}$ clusters deposited on Ketjen Carbon in N_2 saturated 0.5 M $KHCO_3$. Scan rate: 100 mv/s. (b) The enlarged spectra show that the Au-H leads to the occurrence of an oxidation peak at 0.88 V and shifts the Au(I)/Au(0) reduction peak from 1.02 to 1.05 V.

remains a mystery and it can hardly be treated as a model catalyst to provide more information. As a comparison, we now have two clusters in hand. The $[Au_{11}]^{3+}$cluster is fully protected with phosphine ligands without accessible catalytic sites on the surface. The $[Au_{22}H_3]^{3+}$ cluster could be viewed as a dimer of $[Au_{11}]^{3+}$cluster, while the fourteen Au atoms on both sides are coordinated with phosphine ligands just like $[Au_{11}]^{3+}$cluster, the center six atoms are easily accessible. Therefore, these two clusters form great comparison group, and the active sites are perceptible if they show different selectivity or activity towards some catalytic reactions.

We began with studying the surface redox properties of $[Au_{22}H_3]^{3+}$, in comparison with those of $[Au_{11}]^{3+}$. We first tested the cyclic voltammetry (CV) of the two clusters, as shown in Figure 4.17. It demonstrates that the existence of H atoms in the $[Au_{22}H_3]^{3+}$

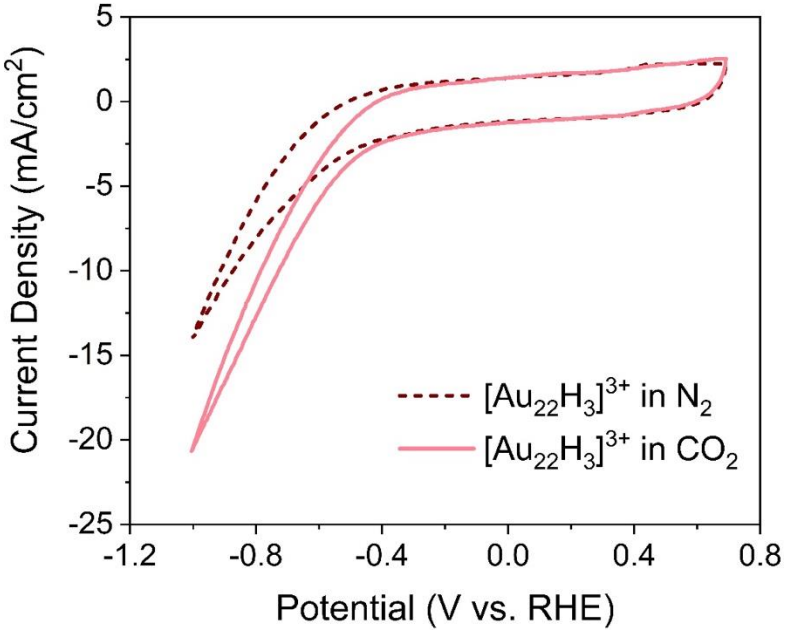

Figure 4.18 CVs of $[Au_{22}H_3(dppe)_3(PPh_3)_8]^{3+}$ cluster deposited on Ketjen Carbon in N_2/CO_2 saturated 0.5 M $KHCO_3$. Scan rate: 100mv/s.

cluster leads to a unique oxidation peak at 0.88 V and shifts the Au(I)/Au(0) reduction peak from 1.02 to 1.05 V relative to $[Au_{11}]^{3+}$.

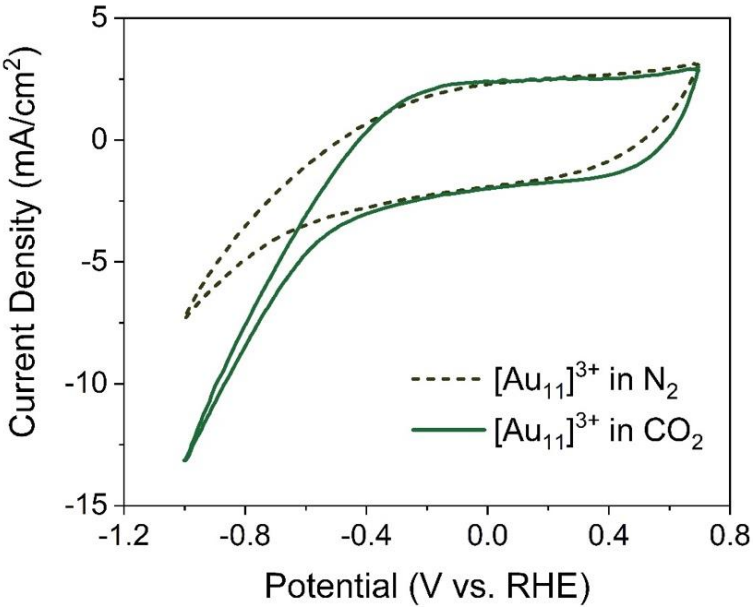

Figure 4.19 CVs of $[Au_{11}(dppe)_5]^{3+}$ cluster deposited on Ketjen Carbon in N_2/CO_2 saturated 0.5 M $KHCO_3$. Scan rate: 100mv/s.

After that, the CVs of $[Au_{22}H_3]^{3+}$ were taken in N_2- and CO_2-saturated 0.5 M $KHCO_3$. In Figure 4.18 The current density starts to increase as the potential reaches approximately -0.3 V in the N_2-saturated electrolyte, due to the hydrogen evolution reaction (HER) and CO_2RR. In CO_2-saturated solution, the current density starts to increase at lower potential compared to that in N_2-saturated electrolyte. And under the same potential, the current density is higher in CO_2-saturated solution, indicating the $[Au_{22}H_3]^{3+}$ cluster can effectively catalyze the electroreduction of CO_2. The CVs of $[Au_{11}]^{3+}$cluster were also taken under the same conditions. The result in Figure 4.19 also confirmed that $[Au_{11}]^{3+}$cluster can catalyze the electroreduction of CO_2.

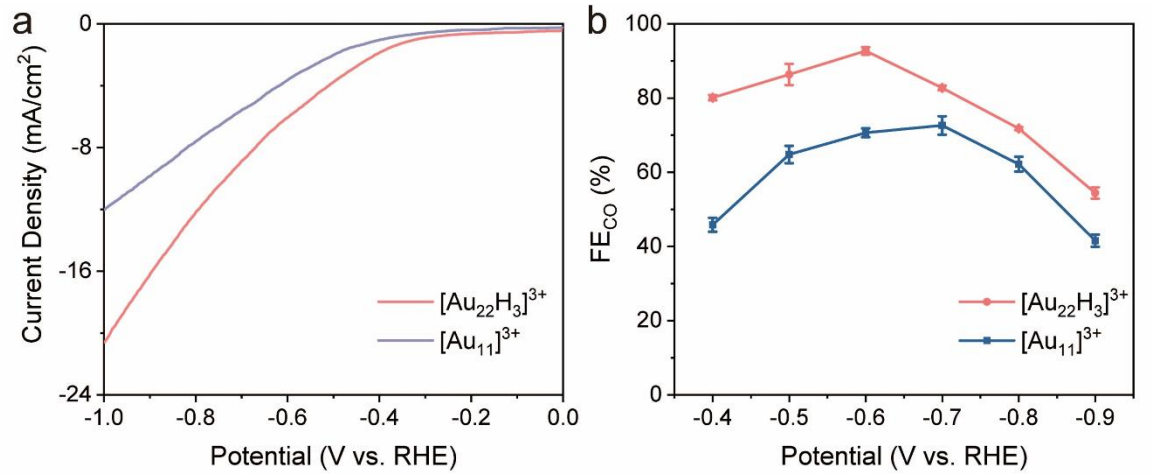

Figure 4.20 (a) LSV curves and (b) FE_{CO} of $[Au_{22}H_3]^{3+}$ and $[Au_{11}]^{3+}$ in the electrocatalytic reduction of CO_2 to CO.

The electrocatalytic reduction of CO_2 was studied by linear sweep voltammetry (LSV) in the CO_2-saturated 0.5 M $KHCO_3$ (Figure 4.20a) to obtain the potentials required to reduce CO_2. The $[Au_{22}H_3]^{3+}$ cluster shows a lower onset potential and higher current

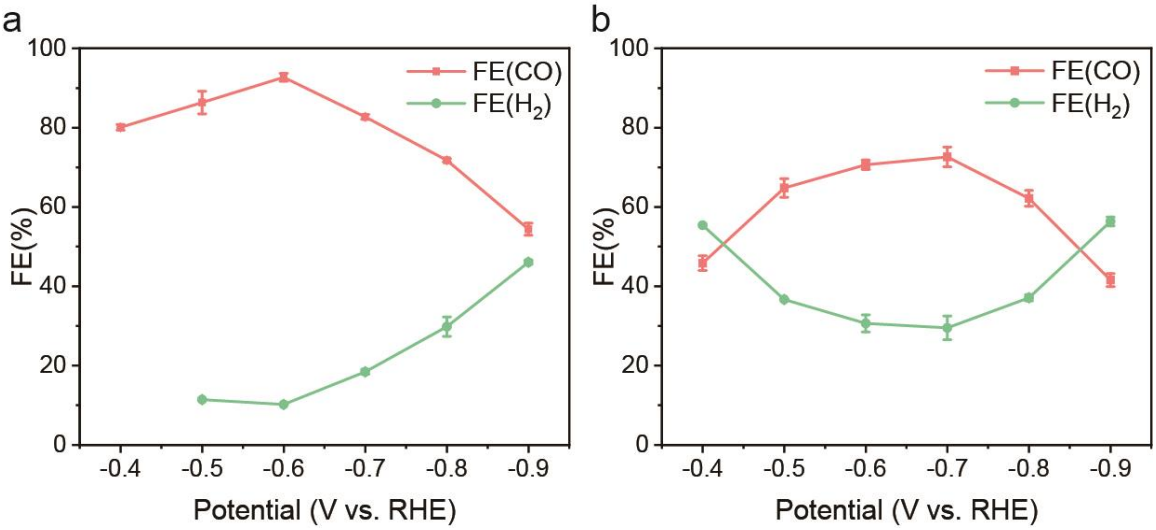

Figure 4.21 Potential-dependent FEs of CO and H_2 in CO_2 saturated 0.5 M $KHCO_3$ of (a) $[Au_{22}H_3]^{3+}$ and (b) $[Au_{11}]^{3+}$ clusters.

density relative to $[Au_{11}]^{3+}$. In the subsequent electrolysis test at a constant potential, only H_2 and CO were detected in all our expeirments (as described in Figure 4.21).

Figure 4.20b and Figure 4.21 compare the potential dependent FEs for the formation of CO and H_2 over $[Au_{22}H_3]^{3+}$ and $[Au_{11}]^{3+}$. We found that the $[Au_{22}H_3]^{3+}$ cluster shows higher FE toward CO than the $[Au_{11}]^{3+}$ cluster under all voltages. When more negative potentials are applied, the FE first increases and then decreases, reaching a maximum at about –0.6 V. This trend is similar to the recently reported phosphine/thiolate co-protected Au_{55} cluster.[62] The best catalytic performance of $[Au_{22}H_3]^{3+}$ was observed at -0.6 V with a FE_{CO} of 92.7 %, which is significantly higher than that of the thiolate-protected Au_{25} cluster at a similar potential.[30] For the competing HER, the FE towards H_2 was less than 10% at -0.6 V, followed by an increasing to almost 50% at -0.9 V.

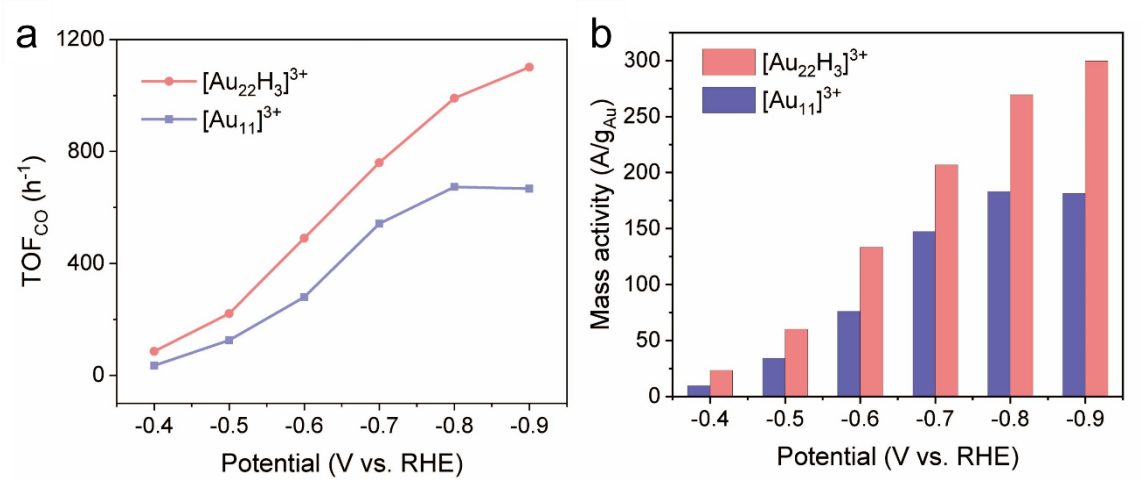

Figure 4.22 (a) TOF_{CO} clusters. (b) Potential-dependent mass activity of the of the $[Au_{22}H_3]^{3+}$ and $[Au_{11}]^{3+}$ clusters.

Furthermore, the $[Au_{22}H_3]^{3+}$ cluster also shows a very high turnover frequency (TOF) of 488 h^{-1} and mass activity of 134 A/g_{Au} at -0.6 V (Figure 4.22), which is much higher than the values of Au nanoparticles[7-9] at the same potential due to the higher ratio

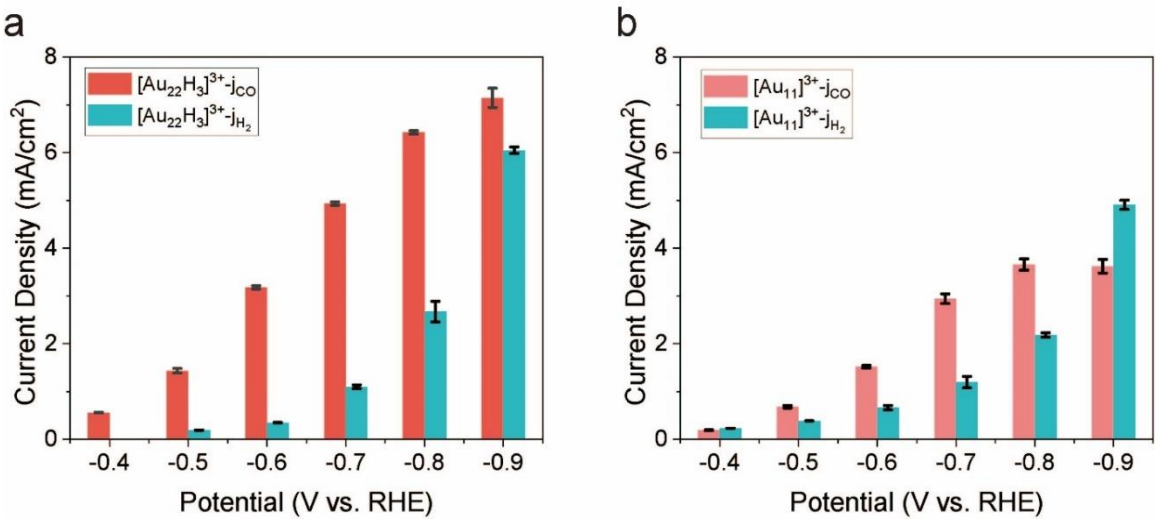

Figure 4.23 The individual partial current density for H_2 and CO_2RR product under different potentials. a) $[Au_{22}H_3]^{3+}$ cluster, b) $[Au_{11}]^{3+}$ cluster.

of surface atoms. And both TOF and mass activity kept increasing with larger overpotential. Mass activity reached nearly 300 A/g_{Au} at -0.9 V. For comparison, the $[Au_{11}]^{3+}$ cluster has a FE_{CO} of 70.6 % at -0.6 V, which is close to the reported value for $[Au_{11}(PPh_3)_8Cl_2]^+$.[63] Relative to that of $[Au_{22}H_3]^{3+}$, the current densities of $[Au_{11}]^{3+}$ at all potentials are lower (Figure 4.23). In addition, the TOF value of 276 h^{-1} and mass activity of 75.8 A/g_{Au} at -0.6 V suggest a much lower activity of the $[Au_{11}]^{3+}$ cluster than the $[Au_{22}H_3]^{3+}$ cluster. The catalytic results of the cluster were also compared with the state-of-art gold based catalysts, as shown in Table 4.4 below. Therefore, we can conclude that the $[Au_{22}H_3]^{3+}$ cluster is among the best catalysts for electrocatalytic CO_2 reduction reaction in terms of both selectivity and activity.

Table 4.4 A summary of the electrochemical CO_2RR performance of different Au-based catalysts reported in aqueous solution under ambient conditions. [a] The potential at which the CO Faradaic efficiency reaches the maximum over the above corresponding catalyst.

Catalysts	electrolyte	Potential (V vs. RHE)[a]	Faradic efficiency (FE_{CO2}, %)	Mass activity (A/g)	References
$[Au_{22}H_3(PPh_3)_8(dppe)_3]Cl_3$	0.5 M $KHCO_3$	-0.6	92.7	134	This work
$[Au_{11}(dppe)_5]Cl_3$	0.5 M $KHCO_3$	-0.6	70.6	75.8	This work
Au Nanoparticles	0.5 M $KHCO_3$	-0.52	97	3	Ref.[7]
Au nanowires	0.5 M $KHCO_3$	-0.35	94	1.84	Ref.[8]
$[Au_{55}(p\text{-}MBT)_{24}(Ph_3P)_6](SbF_6)_3$	0.1 M $KHCO_3$	-0.6	94.1	150	Ref.[62]
$[Au_{11}(PPh_3)_8Cl_2]Cl$	0.5 M $KHCO_3$	-0.8	79	4	Ref.[63]
$[Au_{11}(PPh_3)_7(NHC^{Me})Cl_2]Cl$	0.5 M $KHCO_3$	-0.8	93	13	Ref.[63]
$Au_{19}Cd_2(SR)_{16}$	0.5 M $KHCO_3$	-0.67	96	NA at this potential	Ref.[33]
$Au_{23}(SR)_{16}$	0.5 M $KHCO_3$	-0.67	64	NA at this potential	Ref.[33]
Au_{25} nanosphere	0.5 M $KHCO_3$	-0.57	73.7	NA	Ref.[30]
Au_{25} nanorod	0.5 M $KHCO_3$	-0.85	55	NA	Ref.[30]
$[Au_{28}(Ph\text{-}form)_{12}](OTf)_2$	0.5 M $KHCO_3$	-0.57	96.5	80	*Angew. Chem. Int. Ed*. 2021, 60, 14345 –14349
$Pd_1Au_{24}(SR)_{18}$	0.1 M $KHCO_3$	-0.8	~100	700	Ref.[31]
$Au_{47}Cd_2(TBBT)_{31}$	0.5 M $KHCO_3$	-0.57	83	55.6	*Angew. Chem. Int. Ed*. 2020, 59, 3073-3077
$Au_{25}(PET)_{18}$	1 M $KHCO_3$	-0.4	75	NA	*ACS Catal.* 2021, 11, 18, 11551–11560
$Au_{24}Cd_1(PET)_{18}$	1 M $KHCO_3$	-0.5	90	68.5	*ACS Catal.* 2021, 11, 18, 11551–11560

$Au_{19}Cd_3(S\text{-}tol)_{18}$	1 M $KHCO_3$	-0.5	65	NA	*ACS Catal.* 2021, 11, 18, 11551–11560
$[Au_{24}(NHC)_{14}Cl_2H_3]^{3+}$	0.1 M $KHCO_3$	NA	90	1360	*J. Am. Chem. Soc. 2022, 144, 9000−9006*

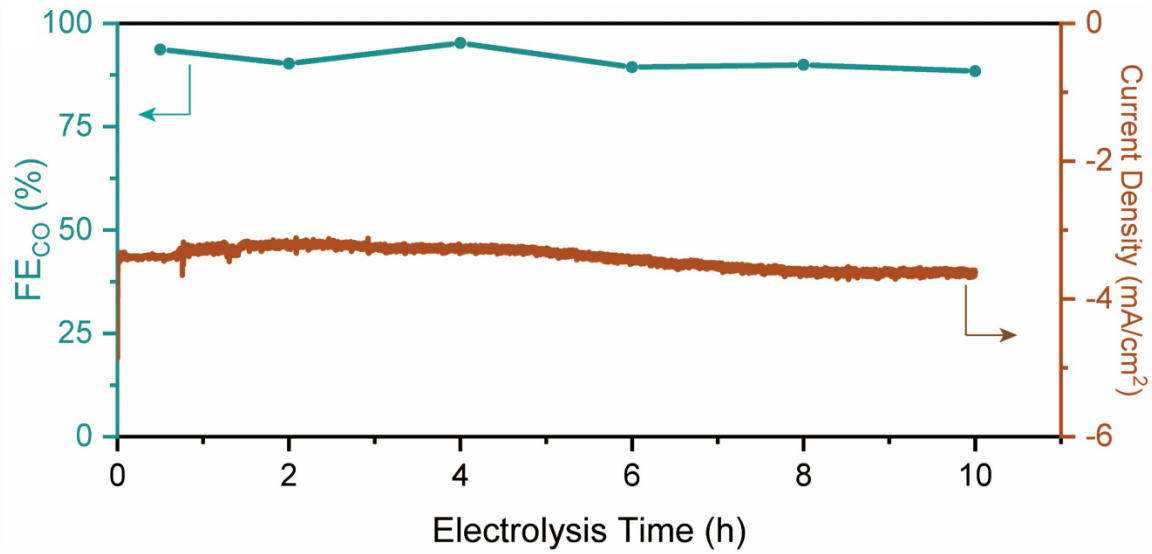

Figure 4.24 Stability test of $[Au_{22}H_3]^{3+}$ for electrolysis at -0.6 V.

It is noteworthy that the $[Au_{22}H_3]^{3+}$ cluster not only exhibits promising selectivity and activity towards CO_2RR, but also remians stable during the electrochemical CO_2RR. The stability test results in Figure 4.24 indicate the current density stays steady at -3.5 $mAcm^{-2}$ during the 10 h electrolysis at -0.6 V, with the FE_{CO} only dropping slightly (5.6 %). The good stability indicates that the $[Au_{22}H_3]^{3+}$ cluster can remain intact on the electrode under -0.6 V for over 10 h.

Besides the indirect evidences from the FE and current density measurement of the cluster catalyst before and after electrolysis, it's of great interest to study the changes of cluster during this process. Still, ESI mass spectroscopy should be the best characterization method for this quest, as it can directly provide information on the cluster's formula which

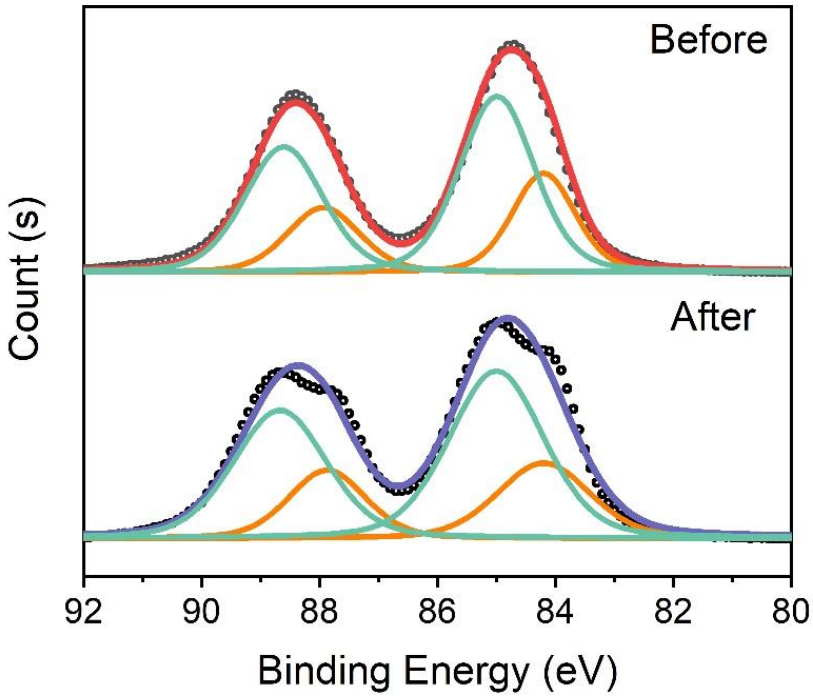

Figure 4.25 XPS profiles of intact $[Au_{22}H_3(dppe)_3(PPh_3)_8]^{3+}$ cluster for Au 4*f* before (top) and after (bottom) electrochemical activation at -0.6 V vs. RHE for 10h. All spectra were background-corrected. Experimental data (black dots) are shown with envelops and component fitting of Au(0) 4*f* (orange lines), Au(I) 4*f* (cyan lines).

can be used to interpret the fate of the three H atoms during electrolysis. Unfortunately, the cluster sample was ground with PVDF adhesive on the working electrode and could't redissolve in DCM for the measurements. Due to such limitation, the characterization could only be done in the solid state before and after the electrolysis. XPS is a powerful tool to characterize the charge state of the elements that esist within a material. And the XPS profiles of the intact cluster sample were taken before and after the electrolysis, as shown in Figure 4.25. The Au(0)/Au(I) ratio before and after the catalysis could be measured based on the peak area, which decreases only a little from 0.47 to 0.44 after the process. The little change on the charge state of Au in $[Au_{22}H_3]^{3+}$ cluster catalyst confirms the good

stability of the cluster sample. The higher Au(I) ratio might come from the slight decomposition of catalyst during electrolysis. The performance of the $[Au_{22}H_3]^{3+}$ electrode was measured even after one month of storage in air, the FE_{CO} at -0.6 V only drops 3.4 % (Figure 4.26). All these results prove that the $[Au_{22}H_3]^{3+}$ cluster is a stable CO_2RR catalyst.

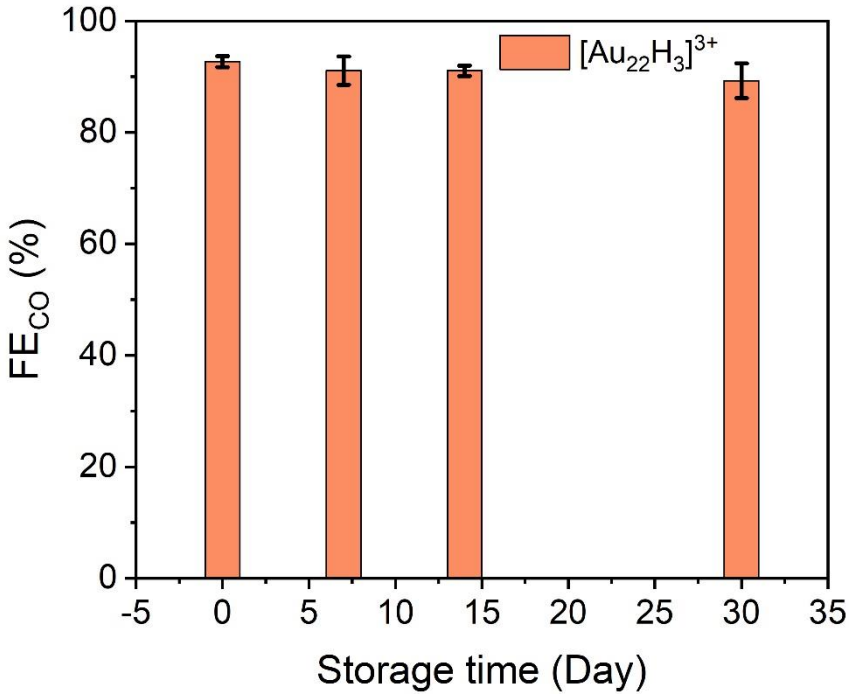

Figure 4.26 FE(CO) @ -0.6 V (vs. RHE) performance after 7, 14, 30 days storage of the $[Au_{22}H_3(dppe)_3(PPh_3)_8]^{3+}$ electrode in air (92.7 % to 89.3 %).

4.5 Mechanism study of the electrocatalytic CO_2RR on $[Au_{22}H_3]^{3+}$ and $[Au_{11}]^{3+}$ clusters

The size effect for NP suggests that higher mass activity can usually be achieved by decreasing the size of target NP, which is due to the more exposed surface/edge active sties. However, with the atomically precise $[Au_{22}H_3]^{3+}$ and $[Au_{11}]^{3+}$Au NCs, the smaller size

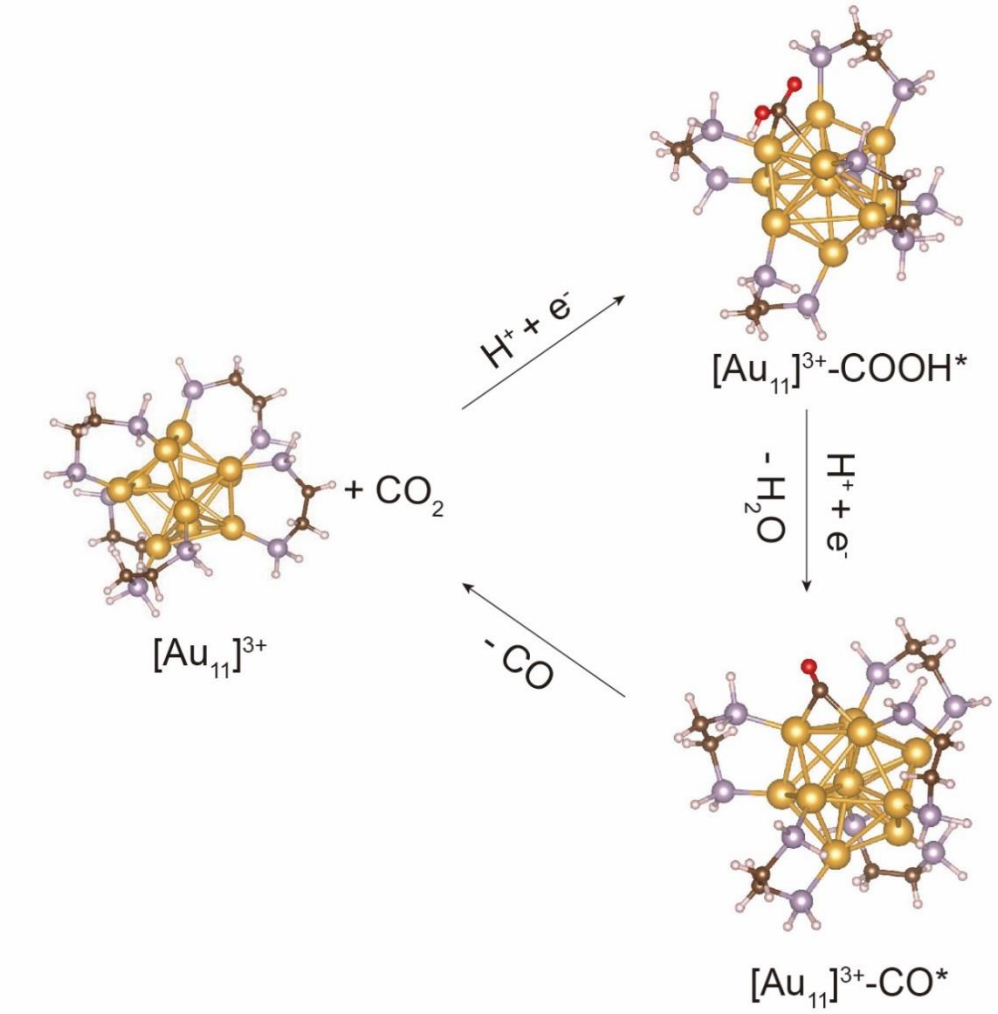

Figure 4.27 DFT-optimized structures of the CO_2 reduction to CO cycle on $[Au_{11}(dppe)_5]^{3+}$. Color code: Au = yellow; C = brown; P = purple; Hydride = blue; H on the ligands = white; O = red.

$[Au_{11}]^{3+}$ cluster doesn't result in better performance. The better electrocatalytic CO_2RR performance of the $[Au_{22}H_3]^{3+}$ cluster indicate that the surface coordination mode may matter more than the size effect. To provide more insights on the understanding of the catalytic mechanisms, DFT calculations were carried out. The reaction pathways for the $[Au_{11}]^{3+}$ are shown in Figure 4.27: all the surface Au atoms of $[Au_{11}]^{3+}$ are cooridnated with the bulky phosphine ligands, the CO_2 molecule requires proton reduction from the

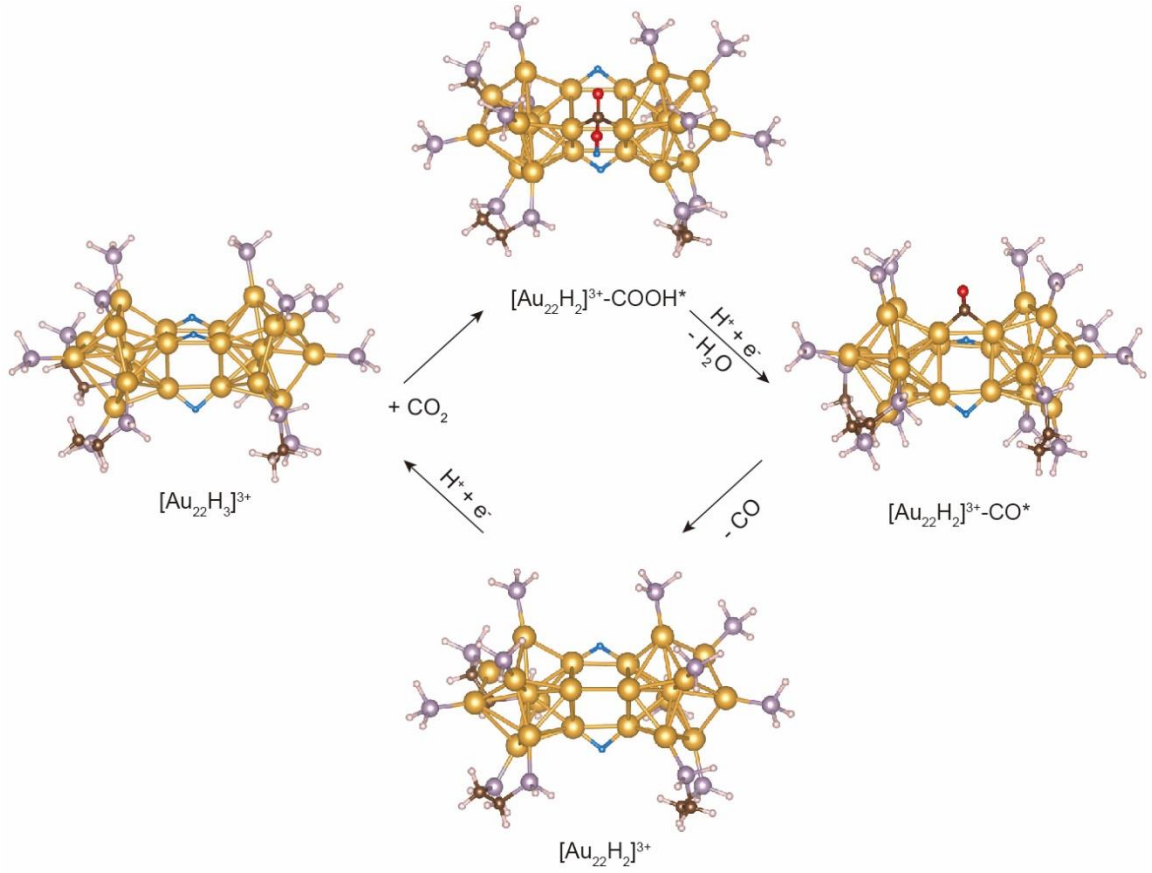

Figure 4.28 DFT-optimized structures of the CO_2 reduction to CO cycle on the $[Au_{22}H_3(dppe)_3(PPh_3)_8]^{3+}$ cluster. Color code: Au = yellow; C = brown; P = purple; Hydride = blue; H on the ligands = white; O = red.

electrolyte as well as electrode to form the $[Au_{11}]^{3+}$-COOH* intermediate with the C atom coorinated to two adjacent Au atoms. Then such intermediate could react with another proton and electron, followed by losing one H_2O molecule to form $[Au_{11}]^{3+}$-CO* intermediate. Finally, the $[Au_{11}]^{3+}$cluster catalyst could be regenerated with the leaving of CO molecule. Such catalytic cycle for $[Au_{22}H_3]^{3+}$ cluster is much more interesting: We found that the bridge H atom in $[Au_{22}H_3]^{3+}$ could directly hydrogenate CO_2 to form adsorbed *COOH (Figure 4.28) with a Gibbs free energy (ΔG) change of 0.85 eV (Figure

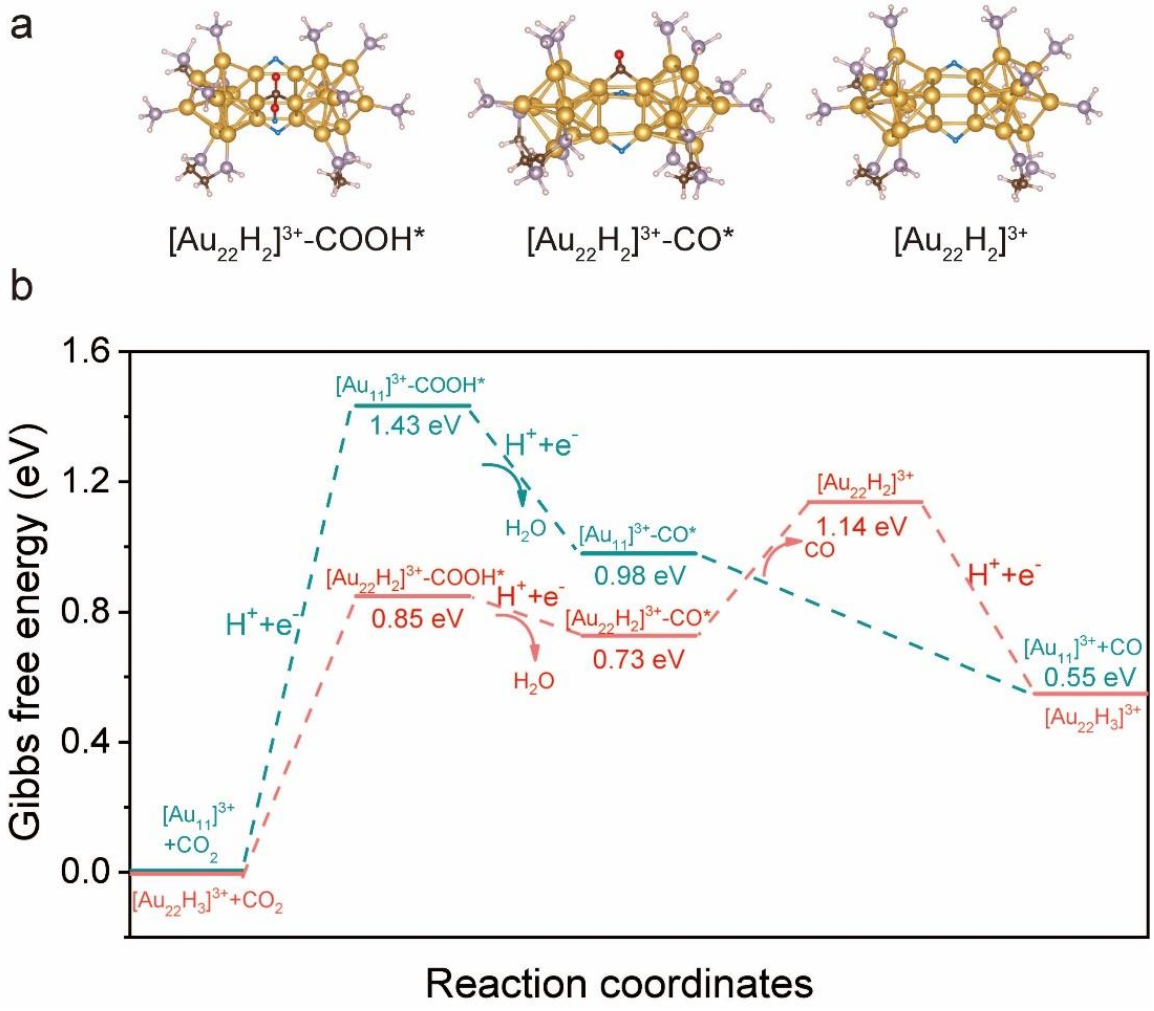

Figure 4.29 DFT structures and energetics of CO_2RR. (a) Optimized structures of the intermediates on $[Au_{22}H_3]^{3+}$ for *COOH and *CO and after CO desorption. Color code: Au = yellow; C = brown; P = purple; Hydride = blue; H on the ligands = white; O = red. (b) Free energy profiles of CO_2RR on the $[Au_{11}]^{3+}$ (cyan lines) and $[Au_{22}H_3]^{3+}$ (red lines) clusters at 0 V vs. RHE.

4.29). Then, an electrochemical proton reduction proccess takes place on *COOH, leading to the formation of adsorbed CO* and H_2O. Although CO desorption has a higher

barrier on $[Au_{22}H_2]^{3+}$ than on $[Au_{11}]^{3+}$, the formation of the key *COOH intermediate is much more difficult on $[Au_{11}]^{3+}$ than on $[Au_{22}H_2]^{3+}$. This is because the $[Au_{11}]^{3+}$ cluster requires proton reduction from the elctrolye to form COOH* (Figure 4.27). As a result, the DFT profiles in Figure 4.29 indicate that it is much more favorable to form CO on $[Au_{22}H_2]^{3+}$ than on $[Au_{11}]^{3+}$, in agreement with our experimental observations (Figure 4.20). Moreover, Figure 4.29 shows that the H vacancy in $[Au_{22}H_2]^{3+}$ can be readily recovered by

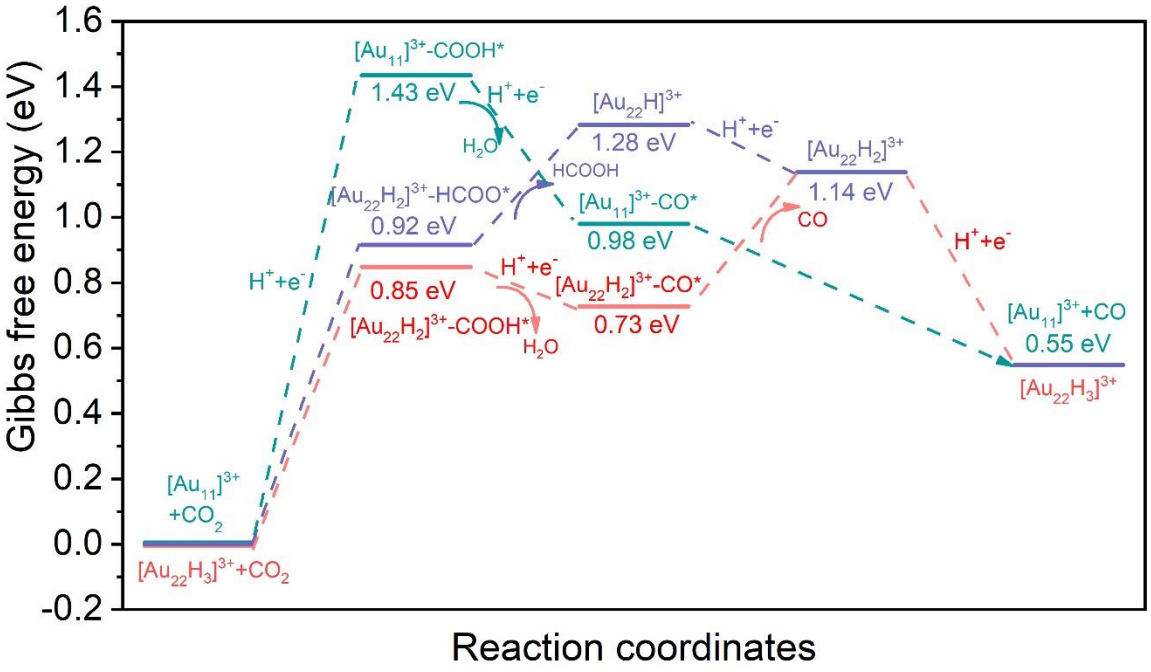

Figure 4.30 DFT-optimized Free energy profiles of CO_2RR on the $[Au_{11}]^{3+}$ (cyan lines) and two different reaction pathways for $[Au_{22}H_3]^{3+}$ clusters at 0 V vs. RHE. Red lines: The more feasible reaction pathway with one bridge H atom to form absorbed *COOH. Purple lines: The alternative reaction pathway with two bridge H atoms participating in. The Gibbs free energy (ΔG) change is 0.92 eV to form absorbed HCOO* and an extra 0.38 eV is needed for the second hydride from the cluster to release HCOOH. The higher energy requirement for HCOOH formation via the hydride addition further confirms our conclusion that CO is the preferred CO_2RR product on the $[Au_{22}H_3]^{3+}$ cluster.

proton reduction (Figure 4.28), completing the catalytic cycle. Although the CO_2RR pathway on $[Au_{22}H_3]^{3+}$ shown in Figure 4.29 resembles the lattice-hydride mechanism of CO_2RR on copper-hydride nanoclusters,[64] an important difference is in selectivity, because HCOOH is preferred over CO on the latter. We have also computed the ΔG for HCOOH formation via hydride addition and the *HCOO intermediate on $[Au_{22}H_2]^{3+}$ but found that it is less favorable than CO formation (Figure 4.30). In other words, the lattice hydrides in $[Au_{22}H_3]^{3+}$ behave very differently from those in the Cu-H systems.

4.6 Summary

To summarize, we have synthesized a new heteroleptic Au trihydride nanocluster, $[Au_{22}H_3(dppe)_3(PPh_3)_8]^{3+}$. The use of the mixed ligands provides the cluster with both Au-H active sites and good stability. The cluster is found to be an excellent electrochemical CO_2RR catalyst, which exhibits high reactivity and selectivity to CO (92.7 % FE and 134 A/g_{Au} mass activity at -0.6 V) and long-term stability. DFT studies of the CO_2RR mechanisms revealed that the Au nanohydride cluster facilitates the formation of the key *COOH intermediate, thereby favoring the CO product. The current work uncovers a unique Au nanohydride cluster with well-defiend *in situ* catalytic centers for CO_2RR and suggests new approaches to design nanocatalysts for understanding structure-activity relationships and energy applications.

References

(1) Friedlingstein, P.; Jones, M. W.; O'Sullivan, M.; Andrew, R. M.; Bakker, D. C.; Hauck, J.; Le Quéré, C.; Peters, G. P.; Peters, W.; Pongratz, J. Global carbon budget 2021. *Earth Syst. Sci. Data* **2022**, *14* (4), 1917-2005.

(2) Turner, J. A. A realizable renewable energy future. *Science* **1999**, *285* (5428), 687-689.

(3) De Luna, P.; Hahn, C.; Higgins, D.; Jaffer, S. A.; Jaramillo, T. F.; Sargent, E. H. What would it take for renewably powered electrosynthesis to displace petrochemical processes? *Science* **2019**, *364* (6438).

(4) Hori, Y.; Murata, A.; Kikuchi, K.; Suzuki, S. Electrochemical reduction of carbon dioxides to carbon monoxide at a gold electrode in aqueous potassium hydrogen carbonate. *J. Chem. Soc., Chem. Commun.* **1987**, (10), 728-729.

(5) Haruta, M. Size-and support-dependency in the catalysis of gold. *Catal. Today* **1997**, *36* (1), 153-166.

(6) Wang, G.; Chen, J.; Ding, Y.; Cai, P.; Yi, L.; Li, Y.; Tu, C.; Hou, Y.; Wen, Z.; Dai, L. Electrocatalysis for CO_2 conversion: from fundamentals to value-added products. *Chem. Soc. Rev.* **2021**.

(7) Zhu, W.; Michalsky, R.; Metin, O.; Lv, H.; Guo, S.; Wright, C. J.; Sun, X.; Peterson, A. A.; Sun, S. Monodisperse Au nanoparticles for selective electrocatalytic reduction of CO_2 to CO. *J. Am. Chem. Soc.* **2013**, *135* (45), 16833-16836.

(8) Mistry, H.; Reske, R.; Zeng, Z.; Zhao, Z. J.; Greeley, J.; Strasser, P.; Cuenya, B. R. Exceptional size-dependent activity enhancement in the electroreduction of CO_2 over Au nanoparticles. *J. Am. Chem. Soc.* **2014**, *136* (47), 16473-16476.

(9) Zhu, W.; Zhang, Y. J.; Zhang, H.; Lv, H.; Li, Q.; Michalsky, R.; Peterson, A. A.; Sun, S. Active and selective conversion of CO_2 to CO on ultrathin Au nanowires. *J. Am. Chem. Soc.* **2014**, *136* (46), 16132-16135.

(10) Souza, M. L.; Lima, F. H. Dibenzyldithiocarbamate-Functionalized Small Gold Nanoparticles as Selective Catalysts for the Electrochemical Reduction of CO_2 to CO. *ACS Catal.* **2021**, *11* (19), 12208-12219.

(11) Chakraborty, I.; Pradeep, T. Atomically precise clusters of noble metals: emerging link between atoms and nanoparticles. *Chem. Rev.* **2017**, *117* (12), 8208-8271.

(12) Naveen, M. H.; Khan, R.; Bang, J. H. Gold Nanoclusters as Electrocatalysts: Atomic Level Understanding from Fundamentals to Applications. *Chem. Mater.* **2021**, *33* (19), 7595-7612.

(13) Chen, M. S.; Goodman, D. W. The structure of catalytically active gold on titania. *Science* **2004**, *306* (5694), 252-255.

(14) Li, G.; Jin, R. Atomically precise gold nanoclusters as new model catalysts. *Acc. Chem. Res.* **2013**, *46* (8), 1749-1758.

(15) Jin, R.; Zeng, C.; Zhou, M.; Chen, Y. Atomically Precise Colloidal Metal Nanoclusters and Nanoparticles: Fundamentals and Opportunities. *Chem. Rev.* **2016**, *116* (18), 10346-10413.

(16) Levi-Kalisman, Y.; Jadzinsky, P. D.; Kalisman, N.; Tsunoyama, H.; Tsukuda, T.; Bushnell, D. A.; Kornberg, R. D. Synthesis and characterization of Au102(p-MBA)44 nanoparticles. *J. Am. Chem. Soc.* **2011**, *133* (9), 2976-2982.

(17) Yan, N.; Xia, N.; Liao, L.; Zhu, M.; Jin, F.; Jin, R.; Wu, Z. Unraveling the long-pursued Au144 structure by x-ray crystallography. *Sci Adv* **2018**, *4* (10), eaat7259.

(18) Zhu, M.; Aikens, C. M.; Hollander, F. J.; Schatz, G. C.; Jin, R. Correlating the crystal structure of a thiol-protected Au_{25} cluster and optical properties. *J. Am. Chem. Soc.* **2008**, *130* (18), 5883-5885.

(19) Negishi, Y.; Nakazaki, T.; Malola, S.; Takano, S.; Niihori, Y.; Kurashige, W.; Yamazoe, S.; Tsukuda, T.; Hakkinen, H. A critical size for emergence of nonbulk electronic and geometric structures in dodecanethiolate-protected Au clusters. *J. Am. Chem. Soc.* **2015**, *137* (3), 1206-1212.

(20) Zeng, C.; Chen, Y.; Liu, C.; Nobusada, K.; Rosi, N. L.; Jin, R. Gold tetrahedra coil up: Kekule-like and double helical superstructures. *Sci Adv* **2015**, *1* (9), e1500425.

(21) Konishi, K.; Iwasaki, M.; Shichibu, Y. Phosphine-ligated gold clusters with core+ exo geometries: Unique properties and interactions at the ligand–cluster interface. *Acc. Chem. Res.* **2018**, *51* (12), 3125-3133.

(22) Yuan, S. F.; Xu, C. Q.; Li, J.; Wang, Q. M. A Ligand‐Protected Golden Fullerene: The Dipyridylamido Au_{32}^{8+} Nanocluster. *Angew. Chem. Int. Ed.* **2019**, *58* (18), 5906-5909.

(23) Kang, X.; Wei, X.; Liu, X.; Wang, S.; Yao, T.; Wang, S.; Zhu, M. A reasonable approach for the generation of hollow icosahedral kernels in metal nanoclusters. *Nat. Commun.* **2021**, *12* (1), 6186.

(24) Wu, Z.; Hu, G.; Jiang, D. E.; Mullins, D. R.; Zhang, Q. F.; Allard Jr, L. F.; Wang, L. S.; Overbury, S. H. Diphosphine-protected Au_{22} nanoclusters on oxide supports are active for gas-phase catalysis without ligand removal. *Nano Lett.* **2016**, *16* (10), 6560-6567.

(25) Kwak, K.; Lee, D. Electrochemistry of Atomically Precise Metal Nanoclusters. *Acc. Chem. Res.* **2019**, *52* (1), 12-22.

(26) Cai, X.; Hu, W.; Xu, S.; Yang, D.; Chen, M.; Shu, M.; Si, R.; Ding, W.; Zhu, Y. Structural Relaxation Enabled by Internal Vacancy Available in a 24-Atom Gold Cluster Reinforces Catalytic Reactivity. *J. Am. Chem. Soc.* **2020**, *142* (9), 4141-4153.

(27) Hasegawa, S.; Takano, S.; Harano, K.; Tsukuda, T. New Magic Au_{24} Cluster Stabilized by PVP: Selective Formation, Atomic Structure, and Oxidation Catalysis. *JACS Au* **2021**, *1* (5), 660-668.

(28) Cai, X.; Li, G.; Hu, W.; Zhu, Y. Catalytic Conversion of CO_2 over Atomically Precise Gold-Based Cluster Catalysts. *ACS Catal.* **2022**, *12* (17), 10638-10653.

(29) Kauffman, D. R.; Alfonso, D.; Matranga, C.; Qian, H.; Jin, R. Experimental and computational investigation of Au_{25} clusters and CO_2: a unique interaction and enhanced electrocatalytic activity. *J. Am. Chem. Soc.* **2012**, *134* (24), 10237-10243.

(30) Zhao, S.; Austin, N.; Li, M.; Song, Y.; House, S. D.; Bernhard, S.; Yang, J. C.; Mpourmpakis, G.; Jin, R. Influence of atomic-level morphology on catalysis: The case of sphere and rod-like gold nanoclusters for CO_2 electroreduction. *ACS Catal.* **2018**, *8* (6), 4996-5001.

(31) Li, S.; Alfonso, D.; Nagarajan, A. V.; House, S. D.; Yang, J. C.; Kauffman, D. R.; Mpourmpakis, G.; Jin, R. Monopalladium substitution in gold nanoclusters enhances CO_2 electroreduction activity and selectivity. *ACS Catal.* **2020**, *10* (20), 12011-12016.

(32) Seong, H.; Efremov, V.; Park, G.; Kim, H.; Yoo, J. S.; Lee, D. Atomically Precise Gold Nanoclusters as Model Catalysts for Identifying Active Sites for Electroreduction of CO_2. *Angew. Chem. Int. Ed.* **2021**.

(33) Li, S.; Nagarajan, A. V.; Alfonso, D. R.; Sun, M.; Kauffman, D. R.; Mpourmpakis, G.; Jin, R. Boosting CO_2 Electrochemical Reduction with Atomically Precise Surface Modification on Gold Nanoclusters. *Angew. Chem. Int. Ed.* **2021**, *60* (12), 6351-6356.

(34) Alfonso, D. R.; Kauffman, D.; Matranga, C. Active sites of ligand-protected Au25 nanoparticle catalysts for CO_2 electroreduction to CO. *J. Chem. Phys.* **2016**, *144* (18), 184705.

(35) Li, J.; Li, X.; Zhai, H. J.; Wang, L. S. Au_{20}: a tetrahedral cluster. *Science* **2003**, *299* (5608), 864-867.

(36) Zhang, H.-F.; Stender, M.; Zhang, R.; Wang, C.; Li, J.; Wang, L.-S. Toward the solution synthesis of the tetrahedral Au_{20} cluster. *J. Phys. Chem. B* **2004**, *108* (33), 12259-12263.

(37) Chen, J.; Zhang, Q. F.; Williard, P. G.; Wang, L. S. Synthesis and structure determination of a new Au_{20} nanocluster protected by tripodal tetraphosphine ligands. *Inorg. Chem.* **2014**, *53* (8), 3932-3934.

(38) Zhang, Q. F.; Chen, X.; Wang, L. S. Toward solution syntheses of the tetrahedral Au_{20} pyramid and atomically precise gold nanoclusters with uncoordinated sites. *Acc. Chem. Res.* **2018**, *51* (9), 2159-2168.

(39) Dong, J.; Gao, Z. H.; Zhang, Q. F.; Wang, L. S. The Synthesis, Bonding, and Transformation of a Ligand‐Protected Gold Nanohydride Cluster. *Angew. Chem. Int. Ed.* **2021**, *60* (5), 2424-2430.

(40) Dong, J.; Gao, Z. H.; Wang, L. S. The synthesis and characterization of a new diphosphine-protected gold hydride nanocluster. *J. Chem. Phys.* **2021**, *155* (3), 034307.

(41) de Silva, N.; Ha, J. M.; Solovyov, A.; Nigra, M. M.; Ogino, I.; Yeh, S. W.; Durkin, K. A.; Katz, A. A bioinspired approach for controlling accessibility in calix[4]arene-bound metal cluster catalysts. *Nat. Chem.* **2010**, *2* (12), 1062-1068.

(42) Das, A.; Li, T.; Nobusada, K.; Zeng, Q.; Rosi, N. L.; Jin, R. Total structure and optical properties of a phosphine/thiolate-protected Au_{24} nanocluster. *J. Am. Chem. Soc.* **2012**, *134* (50), 20286-20289.

(43) Yuan, S. F.; Lei, Z.; Guan, Z. J.; Wang, Q. M. Atomically Precise Preorganization of Open Metal Sites on Gold Nanoclusters with High Catalytic Performance. *Angew. Chem. Int. Ed.* **2021**, *60* (10), 5225-5229.

(44) Wang, X.; Wang, S.; Qian, S.; Liu, N.; Dou, X.; Yuan, X. Mechanistic insights into the two-phase synthesis of heteroleptic Au nanoclusters. *Nanoscale* **2021**, *13* (6), 3512-3518.

(45) Kohn, W.; Sham, L. J. Self-consistent equations including exchange and correlation effects. *Phys. Rev.* **1965**, *140* (4A), A1133.

(46) Blöchl, P. E. Projector augmented-wave method. *Phys. Rev. B Condens. Matter* **1994**, *50* (24), 17953.

(47) Kresse, G.; Furthmüller, J. Efficient iterative schemes for ab initio total-energy calculations using a plane-wave basis set. *Phys. Rev. B Condens. Matter* **1996**, *54* (16), 11169.

(48) Perdew, J. P.; Burke, K.; Ernzerhof, M. Generalized gradient approximation made simple. *Phys. Rev. Lett.* **1996**, *77* (18), 3865.

(49) Grimme, S.; Antony, J.; Ehrlich, S.; Krieg, H. A consistent and accurate *ab* initio parametrization of density functional dispersion correction (DFT-D) for the 94 elements H-Pu. *J. Chem. Phys.* **2010**, *132* (15), 154104.

(50) Nørskov, J. K.; Rossmeisl, J.; Logadottir, A.; Lindqvist, L.; Kitchin, J. R.; Bligaard, T.; Jonsson, H. Origin of the overpotential for oxygen reduction at a fuel-cell cathode. *J. Phys. Chem. B* **2004**, *108* (46), 17886-17892.

(51) Frisch, M.; Trucks, G.; Schlegel, H.; Scuseria, G.; Robb, M.; Cheeseman, J.; Scalmani, G.; Barone, V.; Petersson, G.; Nakatsuji, H. Gaussian 16. Gaussian, Inc. Wallingford, CT: 2016.

(52) Becke, A. D. Density‐functional thermochemistry. III. The role of exact exchange. *J. Chem. Phys.* **1993**, *98* (7), 5648-5652.

(53) Lee, C.; Yang, W.; Parr, R. G. Development of the Colle-Salvetti correlation-energy formula into a functional of the electron density. *Phys. Rev. B.* **1988**, *37* (2), 785.

(54) Devlin, F.; Finley, J.; Stephens, P.; Frisch, M. Ab initio calculation of vibrational absorption and circular dichroism spectra using density functional force fields: a comparison of local, nonlocal, and hybrid density functionals. *J. Chem. Phys.* **1995**, *99* (46), 16883-16902.

(55) McLean, A.; Chandler, G. Contracted Gaussian basis sets for molecular calculations. I. Second row atoms, Z= 11–18. *J. Chem. Phys.* **1980**, *72* (10), 5639-5648.

(56) Krishnan, R.; Binkley, J. S.; Seeger, R.; Pople, J. A. Self‐consistent molecular orbital methods. XX. A basis set for correlated wave functions. *J. Chem. Phys.* **1980**, *72* (1), 650-654.
(57) Hay, P. J.; Wadt, W. R. Ab initio effective core potentials for molecular calculations. Potentials for the transition metal atoms Sc to Hg. *J. Chem. Phys.* **1985**, *82* (1), 270-283.
(58) Lu, T.; Chen, F. Multiwfn: a multifunctional wavefunction analyzer. *J. Comput. Chem.* **2012**, *33* (5), 580-592.
(59) Takano, S.; Hirai, H.; Muramatsu, S.; Tsukuda, T. Hydride-Doped Gold Superatom $(Au_9H)(^{2+})$: Synthesis, Structure, and Transformation. *J. Am. Chem. Soc.* **2018**, *140* (27), 8380-8383.
(60) Konishi, K. Phosphine-coordinated pure-gold clusters: diverse geometrical structures and unique optical properties/responses. *Gold Clusters, Colloids and Nanoparticles I* **2014**, 49-86.
(61) Chen, J.; Zhang, Q. F.; Bonaccorso, T. A.; Williard, P. G.; Wang, L. S. Controlling gold nanoclusters by diphospine ligands. *J. Am. Chem. Soc.* **2014**, *136* (1), 92-95.
(62) Wan, X. K.; Wang, J. Q.; Wang, Q. M. J. A. C. Ligand‐Protected Au_{55} with a Novel Structure and Remarkable CO_2 Electroreduction Performance. *Angew. Chem. Int. Ed.* **2021**, *60* (38), 20748–20753.
(63) Narouz, M. R.; Osten, K. M.; Unsworth, P. J.; Man, R. W. Y.; Salorinne, K.; Takano, S.; Tomihara, R.; Kaappa, S.; Malola, S.; Dinh, C. T.; et al. N-heterocyclic carbene-functionalized magic-number gold nanoclusters. *Nat. Chem.* **2019**, *11* (5), 419-425.

Chapter 5 Conclusions and Outlooks

Cluster science focuses on the study of size-selected atomic clusters atom-by-atom and forms the foundation of nanoscience. The discovery of the conspicuous T_d Au_{20} pyramidal cluster in the gas phase has motivated efforts to the syntheses of this special cluster with protecting ligands in the solution phase. The bulk syntheses of such cluster with appropriate ligand would allow the investigation of its special optical and site-specific catalytic properties. My PhD studies focus on gold-ligand interactions and exploring different synthetic methods towards this aim. Along this direction, several novel hydride-containing gold nanoclusters are discovered, and their properties are characterized. Most interestingly, the use of a combination of phosphine ligands with different steric hindrance results in a stable gold hydride nanocluster, which was revealed to be an efficient electrochemical CO_2 reduction catalyst.

More specifically, in Chapter 2, the halogen effects on the gold nanocluster were investigated. The containing of halide ions in most of the gold phosphine precursors makes it impossible to ignore the gold halogen interactions during the formation of gold nanoclusters. It's discovered that the halide exchange reaction can take place on the Au_{13} cluster and halogens have stronger influences on the electronic structures compared to phosphine ligands. The periodicity was also summarized in terms of energy gap and structure. In Chapter 3, two hydride containing clusters $[Au_{22}H_4(dppo)_6]^{2+}$ and $[Au_{22}H_3(dppb)_7]^{3+}$ were synthesized. The hydrogen exchange reactions and hydrogen loss processes were thoroughly studied on $[Au_{22}H_4(dppo)_6]^{2+}$ cluster. In terms of $[Au_{22}H_3(dppb)_7]^{3+}$ cluster, different controlled experiments were performed and revealed that the ratio, reducing power and different reducing agent could lead to the formation of completely distinct Au clusters. The research indicates that the gold clusters are extremely

sensitive to some reaction conditions and the results could facilitate the discovery of novel gold clusters. In Chapter 5, the combination of monodentate and bidentate phosphine ligands was selected to create undercoordinated sites on gold clusters. The resulting heteroleptic $[Au_{22}H_3(dppe)_3(PPh_3)_8]^{3+}$ was fully characterized and the hydride exchange reactions were also studied. The good stability as well as easily accessible Au-H sites make us to investigate its catalytic property. The experimental results proved it to be an efficient electrocatalyst towards CO_2 reduction reaction. And the theoretical calculations suggested the participation of the lattice hydrides creates a different reaction mechanism compared to the fully coordinated $[Au_{11}(dppe)_5]^{3+}$cluster.

For the outlooks and future directions, still, a lot could be done towards the synthesis of Au_{20} pyramid cluster. For example, the selection of other phosphine ligands and different reducing agents could be attempted. Just recently, Fetzer et al. reported a crystal structure of the $Au_{20}(^tBu_3P)_8$ cluster, which possesses O_h-symmetry and the core resembles the face centered cubic packing of bulk gold.[1] It proves that the phosphine ligands are suitable for producing high symmetric Au clusters. With the proper selection of phosphine ligands and reducing agents, the T_d Au_{20} pyramid cluster may be realized. The combination of different ligands could also be attempted, such as the combination of halogen ligands with phosphine ligands or the combination of phosphine ligands with different steric hindrance. Also recently, another hydride gold cluster $[Au_{24}(NHC)_{14}Cl_2H_3]^{3+}$ was reported with crystal structure by Kulkarni et al.[2] The combination of carbene ligand and halogen ligand resulted in a novel hydride containing cluster.

Apart from the synthesis, the potential applications of hydride containing gold nanoclusters in different catalytic reactions could be further explored. The gold hydride clusters have only been reported to be powerful electrocatalysts for CO_2 reduction reaction. Jia et al. recently discovered a $[Au_{11}HCl(dppee)_4]^+$ cluster that provided atomic-level insights into the mechanisms of a class of alkyne semihydrogenation reactions.[3] The existing hydride-containing gold nanoclusters could also be promising in some other hydrogen engaged reactions such as hydrogen evolution reactions, nitrogen reduction reactions or other hydrogenation reactions.

References

(1) Fetzer, F.; Pollard, N.; Michenfelder, N. C.; Strienz, M.; Unterreiner, A. N.; Clayborne, A. Z.; Schnepf, A. $Au_{20}(t Bu_3P)_8$: A Highly Symmetric Metalloid Gold Cluster in Oxidation State 0. *Angew. Chem., Int. Ed.* **2022**, *61* (36), e202206019.

(2) Kulkarni, V. K.; Khiarak, B. N.; Takano, S.; Malola, S.; Albright, E. L.; Levchenko, T. I.; Aloisio, M. D.; Dinh, C. T.; Tsukuda, T.; Häkkinen, H. N-Heterocyclic Carbene-Stabilized Hydrido Au_{24} Nanoclusters: Synthesis, Structure, and Electrocatalytic Reduction of CO_2. *J. Am. Chem. Soc.* **2022**.

(3) Dong, J.; Robinson, J. R.; Gao, Z. H.; Wang, L. S. Selective Semihydrogenation of Polarized Alkynes by a Gold Hydride Nanocluster. *J. Am. Chem. Soc*. **2022**, *144* (27), 12501-12509.